

DOT/FAA/AR-00/44

Office of Aviation Research
Washington, D.C. 20591

Impact Damage Characterization and Damage Tolerance of Composite Sandwich Airframe Structures

January 2001

Final Report

DISTRIBUTION STATEMENT A
Approved for Public Release
Distribution Unlimited

This document is available to the U.S. public
through the National Technical Information
Service (NTIS), Springfield, Virginia 22161.



20010328 078

U.S. Department of Transportation
Federal Aviation Administration

NOTICE

This document is disseminated under the sponsorship of the U.S. Department of Transportation in the interest of information exchange. The United States Government assumes no liability for the contents or use thereof. The United States Government does not endorse products or manufacturers. Trade or manufacturer's names appear herein solely because they are considered essential to the objective of this report. This document does not constitute FAA certification policy. Consult your local FAA aircraft certification office as to its use.

This report is available at the Federal Aviation Administration William J. Hughes Technical Center's Full-Text Technical Reports page: actlibrary.tc.faa.gov in Adobe Acrobat portable document format (PDF).

1. Report No. DOT/FAA/AR-00/44		2. Government Accession No.		3. Recipient's Catalog No.	
4. Title and Subtitle IMPACT DAMAGE CHARACTERIZATION AND DAMAGE TOLERANCE OF COMPOSITE SANDWICH AIRFRAME STRUCTURES				5. Report Date January 2001	
				6. Performing Organization Code	
7. Author(s) Tomblin, John S., Raju, K.S., Liew, J., and Smith, B.L.				8. Performing Organization Report No.	
9. Performing Organization Name and Address Wichita State University 1845 Fairmount Wichita KS 67260-0093				10. Work Unit No. (TRAIS)	
				11. Contract or Grant No.	
12. Sponsoring Agency Name and Address U.S. Department of Transportation Federal Aviation Administration Office of Aviation Research Washington, DC 20591				13. Type of Report and Period Covered Final Report	
				14. Sponsoring Agency Code ACE-110	
15. Supplementary Notes The Federal Aviation Administration William J. Hughes Technical Center Technical Manager was Peter Shyprykevich.					
16. Abstract The use of composite sandwich construction is rapidly increasing in current and future airframe designs. Typically, these sandwich constructions use thin gage composite facesheets (0.020" to 0.045") which are co-cured to honeycomb and foam cores. Due to the nature of these structures, damage tolerance is more complex than conventional laminated structures. Besides typical damage concerns such as through penetration and delamination, additional modes including core crushing and facesheet debonding must also be addressed. This complicates the certification process by introducing undefined Allowable Damage Limits (ADL) and Critical Damage Thresholds (CDT) as related to the ultimate and limit load carrying capability of the structure. In this report, the preliminary results of the damage resistance and tolerance experiments on sandwich panels are presented. The testing capabilities developed at the Wichita State University to support this program are presented in detail. The effect of impactor size on the impact resistance and residual strength properties was investigated. The effectiveness of traditional nondestructive inspection (NDI) methods in detecting and quantifying the damage distribution in the sandwich panels was studied and the salient results were presented. The damage metrics used for quantifying the damage distributions are planar damage area and residual indentation depth. The use of residual indentation in conjunction with a typical visual inspection protocol for preliminary damage detection was appraised. The characteristic damage states due to different impactor sizes were identified using destructive inspection and further correlated with the NDI damage metrics. The effects of different damage states were quantified by conducting uniaxial edgewise-compressive tests on the impacted specimens. The failure mechanisms governing the sandwich panels with different damage modes were identified and reported. The impacted specimens were inspected for damage using NDI methods. Planar damage area (using Through Transmission Ultrasonic C-scan) and residual indentation depths were used to implicitly quantify the damage state. The results indicated that larger diameter impactor produces a very benign appearing damage state, wherein, no surface fracture/cracks nor visually perceptible levels of indentation exist, but the NDI did indicate a very large damaged region. A select number of impact experiments were repeated, the energy levels chosen from the current experience and the specimens were subjected to destructive sectioning to study the true nature of the damage. It was observed that for specimens impacted with larger diameter impactor, the sandwich core had undergone localized crushing close to the impacted skin over a considerable area. However, the impacted skin which had not suffered any noticeable damage, thus retaining most of its original stiffness (and aided by the now more compliant damaged core), had sprung back close to its original state. This damage scenario proved to be the most elusive when the impacted specimens were inspected using a typical visual inspection protocol. It is conclusively shown that the visual inspection methods are very misleading and the residual indentation cannot be used as a reliable damage metric for static ultimate strength and damage tolerance criteria of sandwich structures.					
17. Key Words Composites, Sandwich, Honeycomb, Damage tolerance, Impact, Residual strength			18. Distribution Statement This document is available to the public through the National Technical Information Service (NTIS), Springfield, Virginia 22161.		
19. Security Classif. (of this report) Unclassified		20. Security Classif. (of this page) Unclassified		21. No. of Pages 181	
22. Price					

TABLE OF CONTENTS

	Page
EXECUTIVE SUMMARY	xi
1. INTRODUCTION	1
2. OBJECTIVES AND TEST PLAN	5
2.1 Material Systems	6
2.2 Experimental Program	7
2.2.1 Damage Resistance	7
2.2.2 Impact Damage Evaluation	7
2.2.3 Damage Tolerance	7
3. GRAVITY-ASSISTED IMPACT-TEST MACHINE	9
3.1 General Description	9
3.2 Specifications	11
3.3 Data Acquisition	17
3.4 Data Acquisition Program	20
3.5 Data Reduction and Analysis	21
4. IMPACT TESTING OF SANDWICH PANELS	23
4.1 Impact Test Procedure	23
4.2 Impact Test Results	25
5. DAMAGE EVALUATION IN IMPACTED SANDWICH PANELS	34
5.1 Nondestructive Evaluation of Damage	34
5.1.1 Planar Damage Area Measurement Using Through Transmission Ultrasonic C-Scan (TTU)	35
5.1.2 Calibration Standard Development For Sandwich Panels	37
5.2 Impact Resistance Characterization Based on Planar Damage Area	41
5.3 Residual Indentation Distribution	44
5.4 Visual Inspection of Damage in Sandwich Panels	47
5.5 Destructive Evaluation of Damage in Impacted Sandwich Panels	52
6. COMPRESSION AFTER IMPACT (CAI) TESTING OF SANDWICH PANELS	60
6.1 Compression Test Fixture	62

6.2	Compression After Impact Test Procedure	64
6.3	Finite Width and Length Effects in CAI Specimens	66
6.3.1	Case-I: Sandwich Panel Impacted With 1.00" Impactor	67
6.3.2	Case-II: Specimen Impacted With 3.00" Diameter Impactor	75
6.4	Compression After Impact Testing of Impacted Sandwich Panel—Results	83
6.5	Correlation of CAI Strength With Damage Metrics	85
7.	CONCLUSIONS AND RECOMMENDATIONS	90
8.	REFERENCES	92

Appendices

A—Detailed Drawings of Impact Tups

B—Through Transmission Ultrasonic (TTU) C-Scan Damage Maps of Impacted Sandwich Panels

C—Destructive Inspection of Selected Sandwich Panels

D—Force Resultant Versus Strain Gage Rendering Plots

LIST OF FIGURES

Figure		Page
1	Composite Sandwich Applications in Raytheon Premier-I	1
2	Damage Tolerance Philosophy	2
3	Impact Energy Levels and Ranges Used in Previous Investigations	4
4	Impact Velocity Levels and Ranges Used in Previous Investigations	4
5	Typical Impactor Diameters Used in Previous Investigations	5
6	Summary of the Experimental Program	8
7	Major Components of the Impact Test Machine	10
8	Details of the Base Platen Used for Mounting Fixtures and Sensor Accessories	13
9	Typical Specimen Mounted on Fixture to Simulate Clamped End Boundary Conditions	13
10	Typical Clamping Plate for Clamped-Clamped Boundary Condition	14
11	Low Weight Impactor Assembly	15
12	Heavy Weight Impactor Assembly-I	15
13	Heavy Weight Impactor Assembly-II	15
14	Rebound-Catch Mechanism Assembled With the Fixture and its Relative Configuration at the Instant of Impact	16
15	Arrest of the Impactor Assembly by the Rebound-Catch Mechanism	17
16	Typical Impact Tups Used With the Impactor Assembly	17
17	Typical Force Signal During an Impact Test	18
18	Arrangement for Data Acquisition	18
19	Schematic Shows Functioning of the Photoelectric Fork Sensor	19
20	Flag Arrangement for Triggering and Velocity Measurement	19
21	Typical Sensor Voltage Pulses Produced During an Impact Test	20

22	Screen Display for the Data Acquisition Program	20
23	Typical Raw Data File Obtained From the Data Acquisition Program	21
24	Typical Reduced Data File	22
25	Typical Microsoft® Excel Summary Spreadsheet	22
26	Boundary Conditions Imposed on the Test Sections of the Sandwich Specimens	23
27	Impact Test Section Relative to the Overall Specimen Geometry	24
28	Picture Shows Specimen Clamped Between Two Plates of the Fixture	25
29a	Typical Force-Time History for [90/45/Core/45/90] Sandwich Panels	26
29b	Typical Force-Displacement Curves for [90/45/Core/45/90] Sandwich Panels	26
29c	Typical Force-Time History for [(90/45) ₂ /Core/(45/90) ₂] Sandwich Panels	27
29d	Typical Force-Displacement Curves for [(90/45) ₂ /Core/(45/90) ₂] Sandwich Panels	27
29e	Typical Force-Time History for [(90/45) ₃ /Core/(45/90) ₃] Sandwich Panels	28
29f	Typical Force-Displacement Curves for [(90/45) ₃ /Core/(45/90) ₃] Sandwich Panels	28
30a	Peak Impact Force vs Impact Energy for [90/45/Core/45/90] Panels	29
30b	Peak Impact Force vs Impact Energy for [(90/45) ₂ /Core/(45/90) ₂] Panels	30
30c	Peak Impact Force vs Impact Energy for [(90/45) ₃ /Core/(45/90) ₃] Panels	30
31a	Peak Impactor Displacement vs Impact Energy for [90/45/Core/45/90] Panels	31
31b	Peak Impactor Displacement vs Impact Energy for [(90/45) ₂ /Core/(45/90) ₂] Panels	31
31c	Peak Impactor Displacement vs Impact Energy for [(90/45) ₃ /Core/(45/90) ₃] Panels	32
32a	Impact Duration vs Impact Energy for 90/45/Core/45/90 Panels	32
32b	Impact Duration vs Impact Energy for [(90/45) ₂ /Core/(45/90) ₂] Panels	33
32c	Impact Duration vs Impact Energy for [(90/45) ₃ /Core/(45/90) ₃] Panels	33
33	Typical TTU C-Scan Image of a Damaged Sandwich Panel	36
34	Summary of the TTU C-Scan Process	36
35	Layout for Artificial Flaws in Calibration Panels	37

36	Calibration Plots for [90/45/Core/45/90] Sandwich Panel With 3/4" Core	38
37	Calibration Plots for [90/45/Core/45/90] Sandwich Panel With 3/8" Core	39
38	Calibration Plots for [(90/45) ₂ /Core/(45/90) ₂] Sandwich Panel With 3/4" Core	39
39	Calibration Plots for [(90/45) ₂ /Core/(45/90) ₂] Sandwich Panel With 3/8" Core	40
40	Calibration Plots for [(90/45) ₃ /Core/(45/90) ₃] Sandwich Panel With 3/4" Core	40
41	Calibration Plots for [(90/45) ₃ /Core/(45/90) ₃] Sandwich Panel With 3/8" Core	41
42	C-Scan Images of Damage in Sandwich Panels Impacted With 1" and 3" Diameter Impactors	42
43	Planar Damage Area vs Impact Energy for [90/45/Core/45/90] Panels	42
44	Planar Damage Area vs Impact Energy for [(90/45) ₂ /Core/(45/90) ₂] Panels	43
45	Planar Damage Area vs Impact Energy for [(90/45) ₃ /Core/(45/90) ₃] Panels	43
46	Setup of Residual Indentation Depth Measurement	44
47a	Residual Indentation Distribution in a [90/45/Core/45/90] Sandwich Panel With 3/8" Thick Core, Impacted With 1.00" Diameter Impactor	45
47b	Residual Indentation Distribution in a [90/45/Core/45/90] Sandwich Panel With 3/8" Thick Core, Impacted With 3.00" Diameter Impactor	45
48	Maximum Residual Indentation vs Impact Energy for [90/45/Core/45/90] Panels	46
49	Maximum Residual Indentation vs Impact Energy for [(90/45) ₂ /Core/(45/90) ₂] Panels	46
50	Maximum Residual Indentation vs Impact Energy for [(90/45) ₃ /Core/(45/90) ₃] Panels	47
51	Visual Inspection Ranking vs Planar Damage Area for [90/45/Core/45/90] Panels With 3/8" Thick Core	48
52	Visual Inspection Ranking vs Planar Damage Area for [(90/45) ₂ /Core/(45/90) ₂] Panels With 3/8" Thick Core	49
53	Visual Inspection Ranking vs Planar Damage Area for [(90/45) ₃ /Core/(45/90) ₃] Panels With 3/8" Thick Core	49
54	Visual Inspection Ranking vs Maximum Indentation Depth for [90/45/Core/45/90] Panels With 3/8" Thick Core	50

55	Visual Inspection Ranking vs Maximum Indentation Depth for [(90/45) ₂ /Core/(45/90) ₂] Panels With 3/8" Thick Core	51
56	Visual Inspection Ranking vs Maximum Indentation Depth for [(90/45) ₃ /Core/(45/90) ₃] Panels With 3/8" Thick Core	51
57	Damaged Section and Corresponding C-Scan Damage Region for [90/45/Core/45/90] Panel, 3/4" Thick Core, Impacted With 137 lbf-in Energy Using 1.00" Diameter Impactor	53
58	Damaged Section and Corresponding C-Scan Damage Region for [90/45/Core/45/90] Panel, 3/4" Thick Core, Impacted With 136 lbf-in Energy Using 3.00" Diameter Impactor	54
59	Damaged Section and Corresponding C-Scan Damage Region for [(90/45) ₂ /Core/(45/90) ₂] Panel, 3/4" Thick Core, Impacted With 183 lbf-in Energy Using 1.00" Diameter Impactor	55
60	Damaged Section and Corresponding C-Scan Damage Region for [(90/45) ₂ /Core/(45/90) ₂] Panel, 3/4" Thick Core, Impacted With 145 lbf-in Energy Using an 3.00" Diameter Impactor	56
61	Damaged Section and Corresponding C-Scan Damage Region for [(90/45) ₃ /Core/(45/90) ₃] Panel, 3/4" Thick Core, Impacted With 183 lbf-in Energy Using an 1.00" Diameter Impactor	57
62	Damaged Section and Corresponding C-Scan Damage Region for [(90/45) ₃ /Core/(45/90) ₃] Panel, 3/4" Thick Core, Impacted With 183 lbf-in Energy Using an 3.00" Diameter Impactor	58
63	Boundary Conditions for CAI Testing of Sandwich Panels	61
64	The Unconstrained Local Out of Plane Displacement Along the Knife-Edges	62
65	Top and Front View of the CAI Fixture	63
66	The CAI Fixture Along With the Load Frame Assembly	64
67	Specimen Configuration and Strain Gage Locations on a Typical CAI Specimen	65
68	A Typical Resultant Force-Strain Plot From a CAI Test	66
69a	C-Scan Plot Showing Planar Damage Distribution in the Specimen WXC25K	67
69b	Contour Plot of Residual Dent Distribution in the Specimen WXC25K	68
70a	Strain Distributions Along the Line $y = 0$, on the Impacted Side	70

70b	Strain Distributions Along the Line $x = 0$, on the Impacted Side	71
70c	Strain Distributions Along the Line $y = 4$, on the Impacted Side	72
70d	Force Resultant vs Far-Field Strains	73
71a	Specimen WXC25K at $N_{yy} = 0.0$ lbf/in	74
71b	Specimen WXC25K at $N_{yy} \sim 1812$ lbf/in	74
71c	Backside of the Panel (WXC25K) After Failure	74
72a	C-Scan Plot Showing Planar Damage Distribution in the Specimen WXC29L	75
72b	Contour Plot of Residual Dent Distribution in the Specimen WXC29L	76
73a	Strain Distributions Along the Line $y = 0$, on the Impacted Side	77
73b	Strain Distributions Along the Line $y = 4$, on the Impacted Side	78
73c	Strain Distributions Along the Line $y = 0$, on the Backside	79
73d	Strain Distributions Along the Line $y = 4$, on the Backside	80
73e	Force Resultant vs Far-Field Strains	81
74a	Specimen WXC29L at $N_{yy} = 0.0$ lbf/in	82
74b	Specimen WXC29L at $N_{yy} \sim 1352$ lbf/in	82
74c	Backside of the Panel (WXC29L) After Failure	82
75	Compression After Impact Strength Values as a Function of Impact Energy for [(90/45)/Core/(45/90)] Panels	83
76	Compression After Impact Strength Values as a Function of Impact Energy for [(90/45) ₂ /Core/(45/90) ₂] Panels	84
77	Compression After Impact Strength Values as a Function of Impact Energy for [(90/45) ₃ /Core/(45/90) ₃] Panels	84
78a	Maximum Dent Depth vs Planar Damage Area for [(90/45)/Core/(45/90)] Panels	85
78b	Maximum Dent Depth vs Planar Damage Area for [(90/45) ₂ /Core/(45/90) ₂] Panels	86
78c	Maximum Dent Depth vs Planar Damage Area for [(90/45) ₃ /Core/(45/90) ₃] Panels	86
79a	Compression After Impact Strength vs Planar Damage Area for [(90/45)/Core/(45/90)] Panels	87

79b	Compression After Impact Strength vs Planar Damage Area for [(90/45) ₂ /Core/(45/90) ₂] Panels	88
79c	Compression After Impact Strength vs Planar Damage Area for [(90/45) ₃ /Core/(45/90) ₃] Panels	88
80a	Compression After Impact Strength vs Maximum Dent Depth for [(90/45)/Core/(45/90)] Panels	89
80b	Compression After Impact Strength vs Maximum Dent Depth for [(90/45) ₂ /Core/(45/90) ₂] Panels	89
80c	Compression after Impact Strength vs Maximum Dent Depth for [(90/45) ₃ /Core/(45/90) ₃] Panels	90

LIST OF TABLES

Table		Page
1	Test Matrix Used in the Current Investigation	8
2	Visual Inspection Ranking	48
3	Test Plan for Destructive Testing	52
4	Summary Results of Destructive Testing for 3/8" Core Panels	59
5	Summary Results of Destructive Testing for 3/4" Core Panels	60

EXECUTIVE SUMMARY

The use of composite sandwich construction is rapidly increasing in current and future airframe designs. Typically, these sandwich constructions use thin gage composite facesheets (0.020" to 0.045") which are cocured to honeycomb and foam cores. Due to the nature of these structures, damage tolerance is more complex than conventional laminated structures. Besides typical damage concerns such as through penetration and delamination, additional modes including core crushing and facesheet debonding must also be addressed. This complicates the certification process by introducing undefined Allowable Damage Limits (ADL) and Critical Damage Thresholds (CDT) as related to the ultimate and limit load carrying capability of the structure.

In this report, the preliminary results of the damage resistance and tolerance experiments on sandwich panels are presented. The testing capabilities developed at the Wichita State University to support this program are presented in detail. The effect of impactor size on the impact resistance and residual strength properties was investigated. The effectiveness of traditional nondestructive inspection (NDI) methods in detecting and quantifying the damage distribution in the sandwich panels was studied and the salient results were presented. The damage metrics used for quantifying the damage distributions are planar damage area and residual indentation depth. The use of residual indentation in conjunction with a typical visual inspection protocol for preliminary damage detection was appraised. The characteristic damage states due to different impactor sizes were identified using destructive inspection and further correlated with the NDI damage metrics. The effects of different damage states were quantified by conducting uniaxial edgewise-compressive tests on the impacted specimens. The failure mechanisms governing the sandwich panels with different damage modes were identified and reported.

The impacted specimens were inspected for damage using NDI methods. Planar damage area (using Through Transmission Ultrasonic C-Scan) and residual indentation depths were used to implicitly quantify the damage state. The results indicated that larger diameter impactor produces a very benign appearing damage state, wherein, no surface fracture/cracks nor visually perceptible levels of indentation exist, but the NDI did indicate a very large damaged region. A select number of impact experiments were repeated, the energy levels chosen from the current experience and the specimens were subjected to destructive sectioning to study the true nature of the damage. It was observed that for specimens impacted with larger diameter impactor, the sandwich core had undergone localized crushing close to the impacted skin over a considerable area. However, the impacted skin which had not suffered any noticeable damage, thus retaining most of its original stiffness (and aided by the now more compliant damaged core), had sprung back close to its original state. This damage scenario proved to be the most elusive when the impacted specimens were inspected using a typical visual inspection protocol. It is conclusively shown that the visual inspection methods are very misleading and the residual indentation by itself cannot be used as a reliable damage metric for static ultimate strength and damage tolerance criteria of sandwich structures.

1. INTRODUCTION.

Sandwich constructions are widely used in airframe structural applications due to the distinct advantages they offer over other metallic and composite (monolithic laminate) structural configurations in terms of stiffness, stability, specific strength, corrosion resistance, ease of manufacture and repair, and above all for weight savings. However, the skin-core combination is not very resilient when subjected to localized normal loads (normal to surface of the panels). Localized transverse and normal loads are prevalent during normal operational procedures, which include service and maintenance, use of service equipment, baggage handling, etc. Damage may also be inflicted by runway debris and hail impact. An understanding of the damage characteristics due to such events and the corresponding stiffness reductions is needed to quantify the effects on the long-term structural integrity of the airframe.

The damage resistance and damage tolerance of sandwich composite structures must be addressed because of the potential threat to structural integrity in both commercial and military applications. This need is further accentuated in view of the increasing use of composite sandwich configurations in general aviation (GA) aircraft where thin skins are typical. Currently, the only certified, pressurized composite sandwich construction is the Beechcraft Starship. There are a number of GA aircraft currently undergoing certification, which includes the Raytheon Premier I. The extent of composite sandwich construction use in Premier I is illustrated in figure 1.

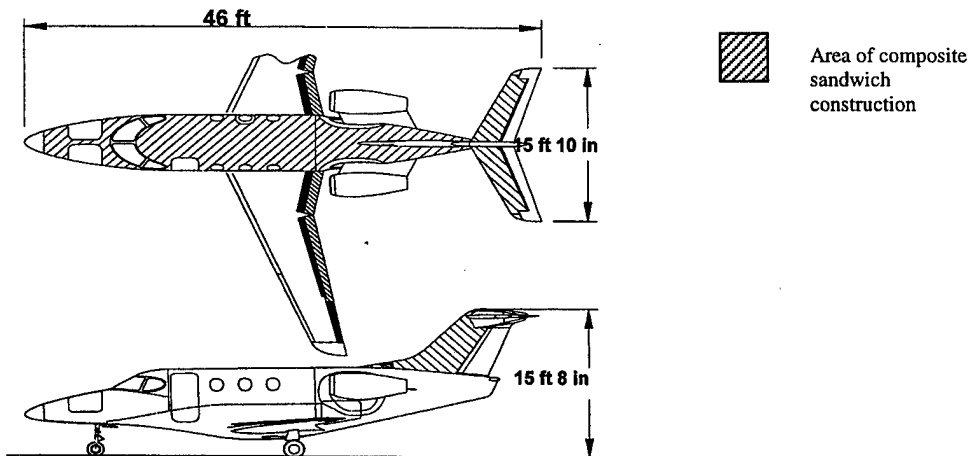


FIGURE 1. COMPOSITE SANDWICH APPLICATIONS IN RAYTHEON PREMIER-I

A limited knowledge base is available regarding the damage tolerance requirements for composite sandwich construction. Very little data exists for growth of damage inflicted by impact events. Load and damage considerations for a general damage tolerance philosophy are summarized in figure 2. The Federal Aviation Administration (FAA) has recommended this philosophy to be embedded into the design and maintenance processes.

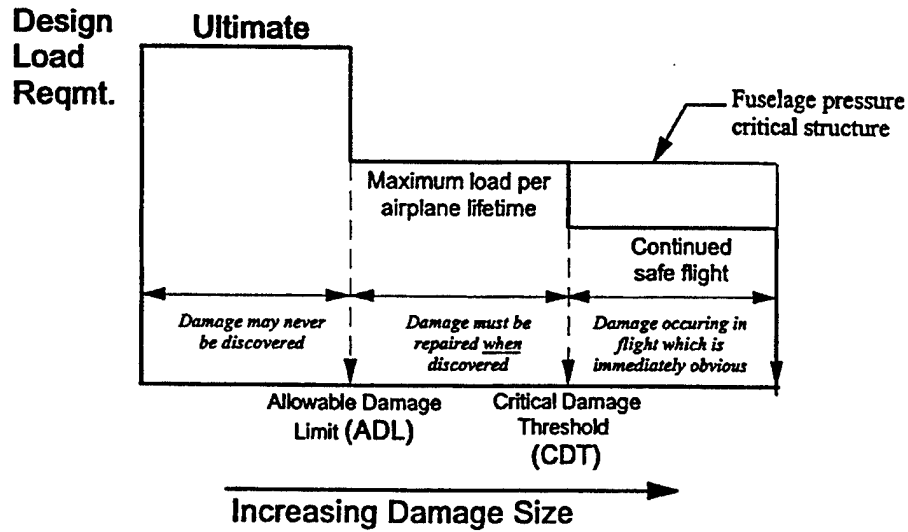


FIGURE 2. DAMAGE TOLERANCE PHILOSOPHY

A literature review, which was performed to support the current study, provided some background for the three distinct regions in figure 2. These details can be found in DOT/FAA/AR-99/49 (pages 54 and 55). In summary, the structure must carry the ultimate loads with barely visible impact damage (BVID) or damage occurring from impacts up to specified energy levels as part of static strength evaluations. As shown in figure 2, an allowable damage limit (ADL) defines the size of damage, which reduces the structure's residual strength to ultimate load levels. Any damage greater than ADL must be repaired when discovered. Further, a critical damage threshold (CDT) is defined as the damage that reduces the structure's residual strength to the limit load level. As implied by figure 2, the maintenance inspection intervals and procedures should ensure the continued airworthiness of composite structure (i.e., sufficient ADL and CDT should exist to ensure damage lowering residual strength below ultimate load will be discovered and repaired in scheduled maintenance). The final region in figure 2 is for damage that occurs in flight and is immediately obvious to the flight crew. Although such damage may be beyond the CDT, the damaged structure must be able to withstand safe flight loads for the duration of the flight and the damage repaired prior to continued aircraft operation.

The damage tolerance philosophy is well established for metallic airframes, where proven methods (structural analysis and inspection procedures) and supporting databases exist to detect damage and predict crack growth and residual strength. However, the damage characteristics, inspection procedures, analysis methods, and experimental databases are not so well understood to apply the damage tolerance philosophy to composite structure, including sandwich construction.

The state of damage is complex and dependent on a number of variables which define the intrinsic properties of the sandwich constructions and the extrinsic damage-causing event. Further, the BVID, ADL, and CDT are not clearly defined in terms of a rational damage metric. Traditionally, visual inspection procedures have been used for detecting damage in composite structures (in service) and hence, the term BVID came into existence. The current definitions of

BVID are based on the residual indentation depth, which has been clearly shown to be sandwich configuration dependent and often misleading. Another issue coupled with this, is the choice of the nondestructive inspection (NDI) techniques. The choice of NDI method dictates the damage metric defining the BVID criterion. A thorough literature review was done to summarize the various intrinsic and extrinsic variables used by different authors and identify any trends in their findings. The observations were used in planning a suitable test matrix for a thorough investigation of the damage resistance and tolerance of sandwich panels. The details of the literature review may be found in reference 1. A companion volume describing relevant analytical methods is contained in reference 2.

An experimental investigation was initiated in an effort to better understand the damage resistance and tolerance of sandwich panels. Based on the extensive literature survey, candidate material systems and sandwich configurations were chosen for the study. The sandwich skins and core types are representative of the current practices in the GA industry. Plain weave carbon fabric preimpregnated in epoxy resin (NEWPORT NB321/3K70P) was used for the skins and Nomex honeycomb cores (PLASCORE PN2-3/16-3.0) were used as the sandwich core. A flat sandwich panel geometry was selected for a baseline study, which will facilitate comparisons with curved panels in the future. The energy levels and velocities were based on the literature review. The typical impact energy levels and ranges used by previous investigators are summarized* in figure 3. In the current investigation, the energy levels were restricted to those where no surface fracture of the skin will occur. Since the previous authors seldom investigated the effects of impact velocity, it was decided that the impact velocity be maintained a constant for this preliminary test program. The impact velocities as reported by a few authors are summarized in figure 4. It is envisaged that a follow-up investigation should be conducted to investigate the effects of impact velocity and establish the range of velocity within which its effects are negligible. The other important extrinsic variables, which have received limited attention are the impactor geometry and size. The most popular impactor geometry is hemispherical or spherical in shape; the diameters used previously by various investigators are summarized in figure 5. In the current investigation, impactor diameters of 1.00" and 3.00" were selected as they compliment the previous investigations. Based on the results of the impactor diameter, effects will be investigated further.

In this report, the preliminary results of the damage resistance and tolerance experiments on sandwich panels are presented. The testing capabilities developed at the Wichita State University to support this program are presented in detail. The effect of impactor size on the impact resistance and residual strength properties was examined. The effectiveness of traditional NDI methods in detecting and quantifying the damage distribution in the sandwich panels was studied and the salient results are presented. The damage metrics used for quantifying the damage distributions are planar damage area and residual indentation depth. The use of residual indentation in conjunction with a typical visual inspection protocol for preliminary damage detection was examined. The characteristic damage states due to different impactor sizes were identified using destructive inspection and further correlated with the NDI damage metrics. The effects of different damage states were quantified by conducting uniaxial edgewise-compressive

* The summary plots contain data obtained from investigations related to sandwich panels as well as solid laminated panels.

tests on the impacted specimens. The failure mechanisms governing the sandwich panels with different damage modes were identified and are reported.

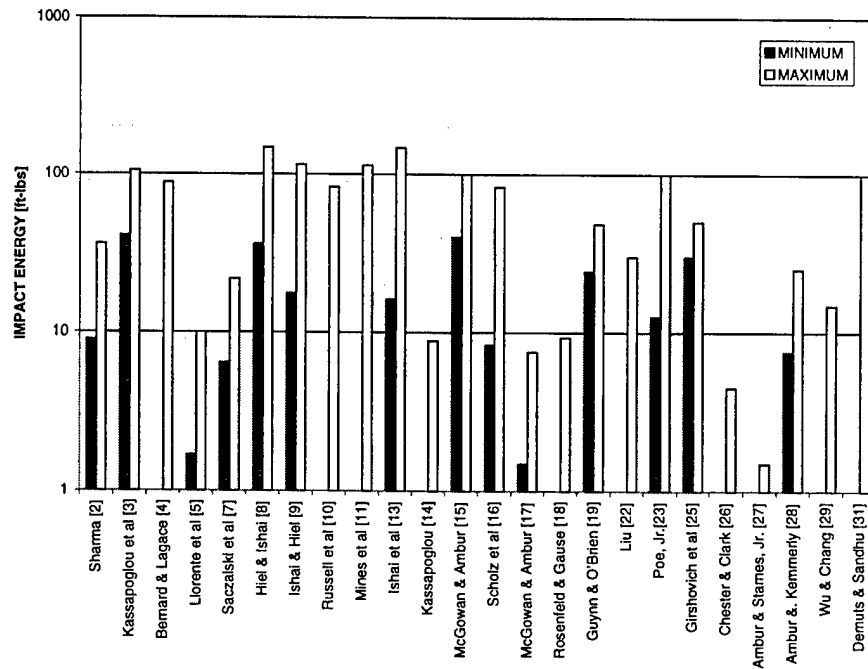


FIGURE 3. IMPACT ENERGY LEVELS AND RANGES USED IN PREVIOUS INVESTIGATIONS

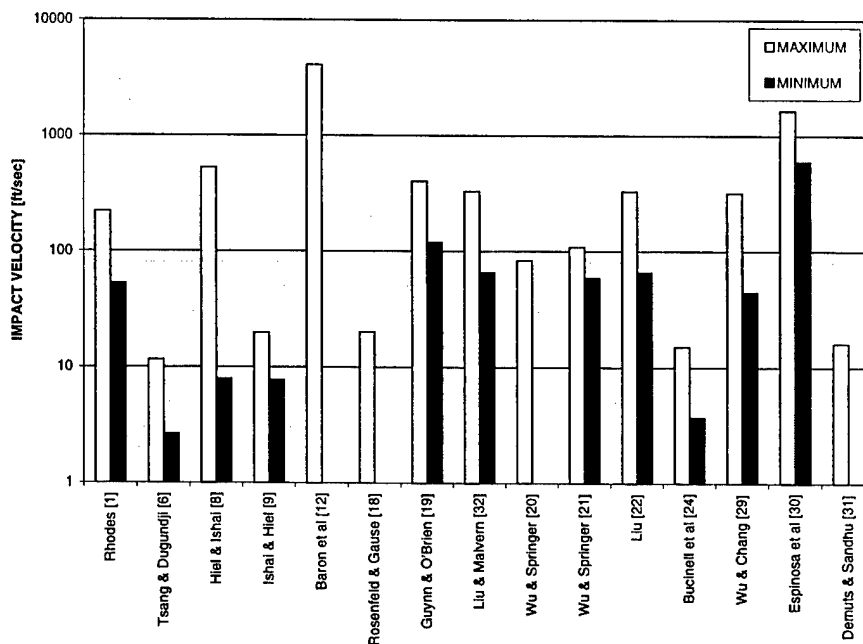


FIGURE 4. IMPACT VELOCITY LEVELS AND RANGES USED IN PREVIOUS INVESTIGATIONS

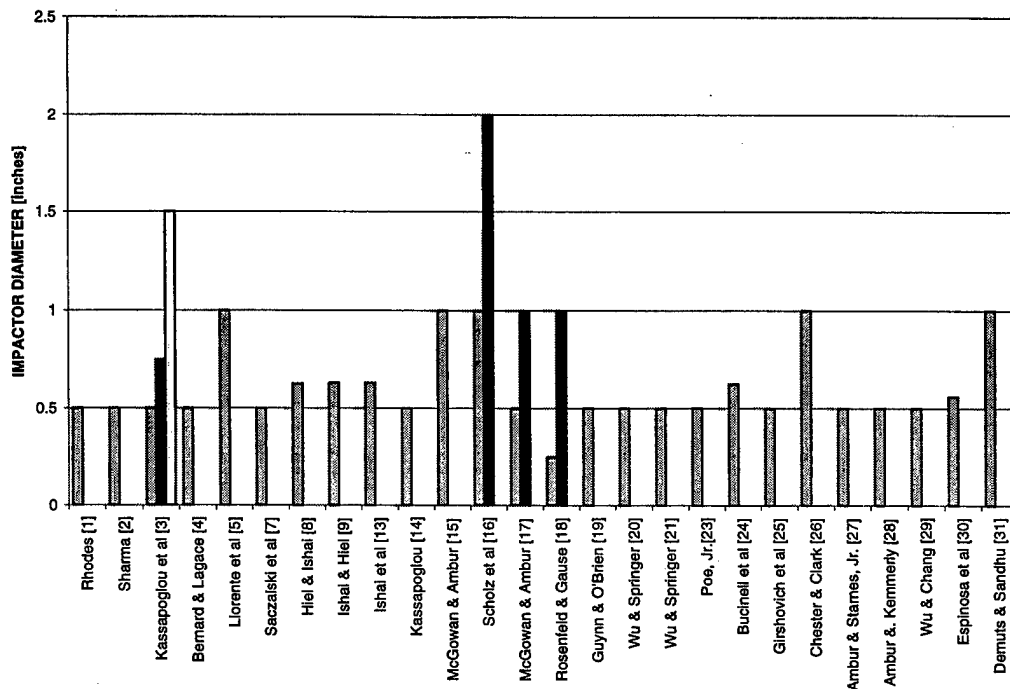


FIGURE 5. TYPICAL IMPACTOR DIAMETERS USED IN PREVIOUS INVESTIGATIONS

2. OBJECTIVES AND TEST PLAN.

In this chapter, the main concerns related to the damage resistance and damage tolerance aspects of sandwich panels are outlined. The test matrix used to address these issues is then presented and the test program is outlined.

The current investigation is aimed at understanding the nature of damage in sandwich panels constructed similarly to GA airframes, when the panels have been subjected to low-velocity impacts. Based on the extensive literature review [1-34], a number of issues were identified and are summarized as follows.

- To what extent are the parameters defining the impact response affected by impactor diameter (size)?
- Are the damage states due to different impactor diameters very different?
- How well can the damage states be detected using traditional inspection techniques and how do the measurements correlate with the actual damage?
- What are the effects of these damage states on the residual properties?

The above issues were addressed using controlled experiments. Based on the knowledge gained from the experimental program, analytical modeling will be attempted concurrently. Reference 2 describes state of the art in analysis of damaged sandwich structures. To support the

experiments, test facilities for simulating the impact event and subsequent residual loading were developed. A drop weight impact facility was designed and built at the Wichita State University. The residual properties were quantified by conducting uniaxial edgewise compression tests, popularly known as “compression after impact” (CAI) tests. A CAI test represents the most severe loading case that the sandwich structure will experience, as this mode can either introduce a pure compressive failure of the skins or a global or local stability related failure. The selection of material systems, sandwich configurations, impact scenarios (energy and velocity ranges) was based on the existing literature and current aviation industry practices.

2.1 MATERIAL SYSTEMS.

The material systems for the current investigation were selected to include a wide range of intrinsic variables. The selection of material systems was based on constitutive properties, reinforcement type, and availability of material database for constitutive properties.

- Sandwich Skins.

NEWPORT NB321/3K70P Plain weave carbon fabric was selected. The constitutive properties are listed below. All properties are room temperature, dry condition properties.

In-plane Young's modulus $E_{11}, E_{22} = 9.6$ msi

In-plane shear modulus $G_{12} = 0.62$ msi

Poisson's ratio $\nu_{12} = 0.058$

Nominal ply thickness = 0.008"

Longitudinal tensile strength $\sigma_{11}^{tu} = 89.9$ ksi

Longitudinal compressive strength $G_{22}^{su} = 69.2$ ksi

In-plane shear strength $\sigma_{12}^{su} = 16.7$ ksi.

- Core.

Plascore Nomex™ (Aramid) honeycomb cores (PN2-3/16-3.0) were used as the sandwich core due to their widespread use among the aviation industries. The selected core has a nominal cell size of 3/16" and density of 3.0 lbs/ft³. Two different core thicknesses, 3/8" and 3/4", were used for the sandwich specimens.

- Sandwich Panel Configuration.

Three different quasi-isotropic skin lay-up configurations for the skin and two thicknesses for the core were used. The skin lay-up schedules are similar to those used in some of the GA aircraft [32]. The core thicknesses used are 3/4" and 3/8". A total of six sandwich configurations were used for this study. The sandwich lay-up configurations used are:

[90/45/CORE/45/90]

[90/45/90/45/CORE/45/90/45/90]

[90/45/90/45/90/45/CORE/45/90/45/90/45/90]

2.2 EXPERIMENTAL PROGRAM.

The current investigation is subdivided into three test activities: Impact testing to determine damage resistance, impact damage evaluation, and residual compression tests to determine damage tolerance. The three test activities are illustrated by the flow chart of figure 6. The sandwich specimen configurations were fabricated and impacted according to the test matrix shown in table 1. The impacted panels were then inspected (NDI) to quantify the damage and then CAI tested to evaluate the residual properties. Additional number of specimens were fabricated and used for destructive inspections as shown on the right of figure 6. The test matrix for these panels is presented in chapter 5.

2.2.1 Damage Resistance.

To investigate the damage resistance, the sandwich panels were subjected to impact tests (impact test box in figure 6) at different energy levels, the upper bound of which corresponds to extensive damage of the impacted skin accompanied by indentation depths of the order of the skin thickness or greater. The impact velocity was held constant for all the experiments to isolate any velocity interactions in the observed results. The impact tests were conducted with two different steel impactors of diameters, 1.00" and 3.00". The effects of impactor diameters were then characterized using the parameters describing the impact response, i.e., peak impact force, peak impactor displacement, and impact duration. Sandwich panels with varying combinations of local and global stiffnesses were used.

2.2.2 Impact Damage Evaluation.

The impacted sandwich panels were inspected for damage using nondestructive inspection techniques, C-scan, indentation measurement, and visual inspection, as shown in figure 6. Also, a few impacted specimens were sectioned to observe the damage morphology and correlate it with the damage metrics, destructive evaluation box in figure 6. The planar damage area and maximum residual indentation depth were measured to quantify the damage states. The variation of damage states with the impact variables, in particular, the impactor diameter was observed. Further, a visual inspection protocol as to the determination of BVID threshold was proof tested using the same impacted sandwich specimens.

2.2.3 Damage Tolerance.

Finally, the effects of the various damage states resulting from impacts using different impactor diameters, on the residual properties of the sandwich specimens were studied using the CAI test. The failure modes governing the sandwich panels with different damage states were identified and the severity of damage states were quantified using the failure strength of the sandwich specimen.

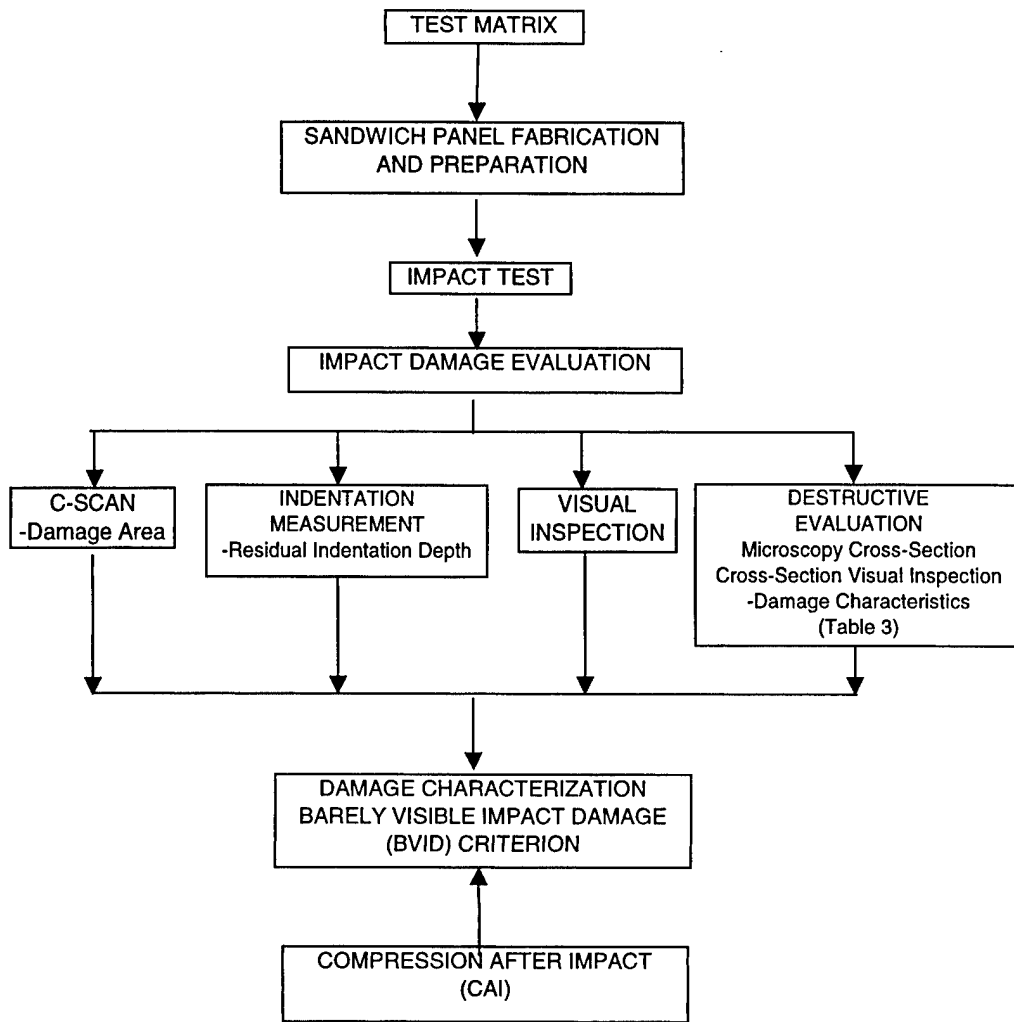


FIGURE 6. SUMMARY OF THE EXPERIMENTAL PROGRAM

TABLE 1. TEST MATRIX USED IN THE CURRENT INVESTIGATION

LAYUP SCHEDULE	PANEL I.D	BOUNDARY CONDITION	CORE THICKNESS	IMPACTOR DIAMETER	No. OF TEST SAMPLES	TOTAL SAMPLES
[90/45/CORE/45/90]	WXC1XA	CLAMPED	3/8"	1.00"	5	20
	WXC1XB	CLAMPED	3/8"	3.00"	5	
	WXC1XC	CLAMPED	3/4"	1.00"	5	
	WXC1XD	CLAMPED	3/4"	3.00"	5	
[(90/45) ₂ /CORE/(45/90) ₂]	WXC2XE	CLAMPED	3/8"	1.00"	5	20
	WXC2XF	CLAMPED	3/8"	3.00"	5	
	WXC2XH	CLAMPED	3/4"	1.00"	5	
	WXC2XG	CLAMPED	3/4"	3.00"	5	
[(90/45) ₃ /CORE/(45/90) ₃]	WXC3XM	CLAMPED	3/8"	1.00"	5	20
	WXC3XN	CLAMPED	3/8"	3.00"	5	
	WXC3XO	CLAMPED	3/4"	1.00"	5	
	WXC3XP	CLAMPED	3/4"	3.00"	5	

3. GRAVITY-ASSISTED IMPACT-TEST MACHINE.

A gravity-assisted drop-weight impact-test machine was developed to support the damage tolerance studies on composite sandwich panels. The impact tester is equipped with a state-of-the-art rebound-catch mechanism and a data acquisition computer program capable of sampling speeds up to 100 kHz. This chapter describes the details of the structural assembly of the impact test machine, electronic circuitry used in the rebound-catch mechanism, and the computer programs used for data acquisition and analysis.

3.1 GENERAL DESCRIPTION.

The gravity-assisted drop-weight apparatus was designed to inflict impact loads on test coupons and components of limited size. The salient features of the test apparatus are illustrated in figure 7. The test apparatus consists of two long guide shafts that are held in alignment between a bottom platen and a fixed top cross-head. Two aluminum tubes separate the platen and the cross-head. The impactor assembly slides down along the guide shafts from a predetermined height due to gravitational force and impacts the test coupon or the test component secured on the platen. The platen aids in mounting the fixtures which hold the test article in the path of the impactor. The impact-test machine has the following features.

- Variable impactor weight.
- Variable impactor end geometry, i.e., hemispherical with different radii, conical, etc.
- Dynamic load measurement using a piezoelectric loadcell mounted on the impactor assembly.
- Impact velocity measurement using high speed photoelectric sensors and flags.
- A pneumatic rebound-catch mechanism to avoid secondary impacts on the test coupon.
- A high-speed data acquisition system with associated software to record the force-time history of the impact event.
- A total of eight data acquisition channels, allowing the use of additional strain gages, accelerometers, etc.

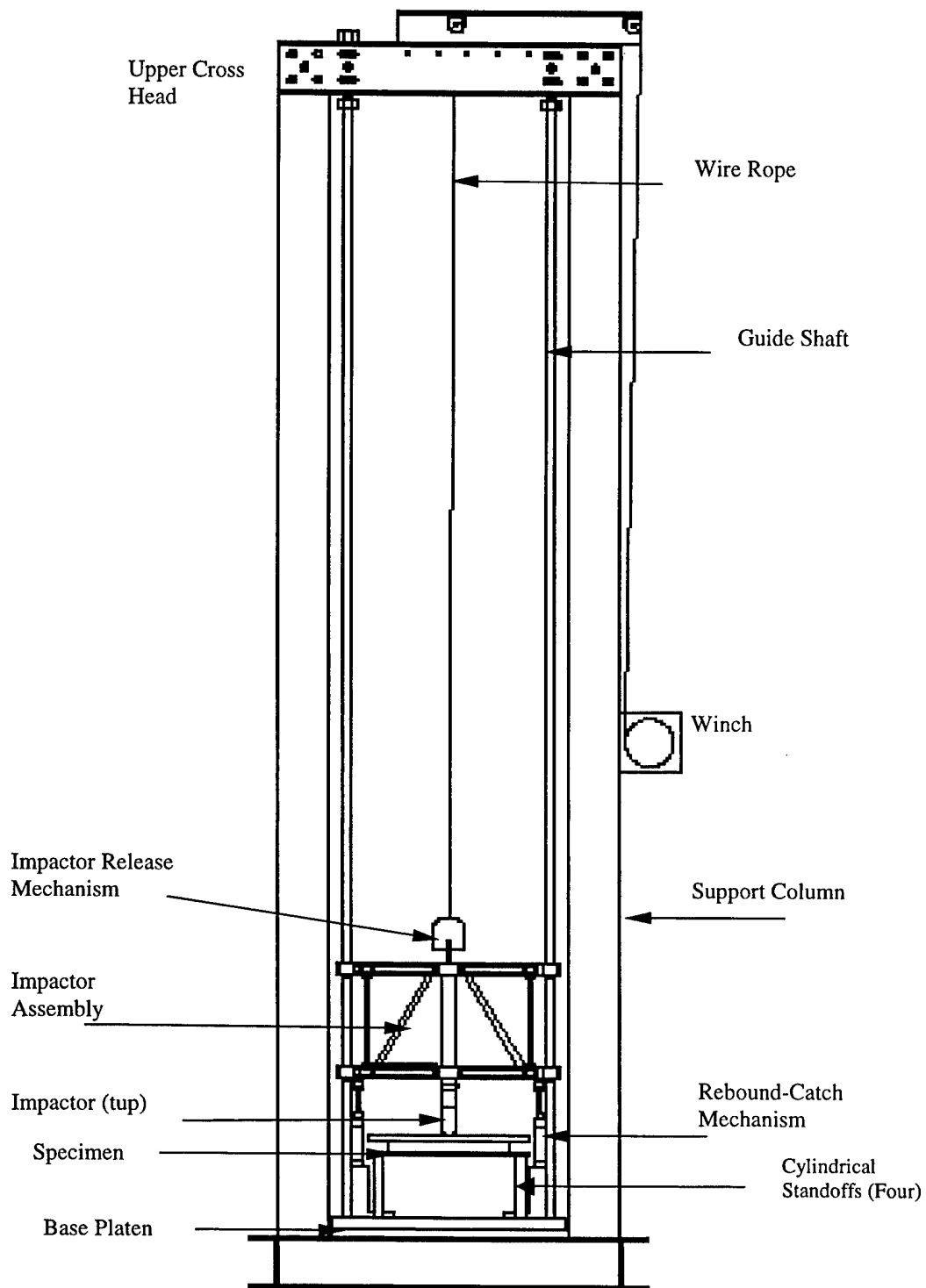


FIGURE 7. MAJOR COMPONENTS OF THE IMPACT TEST MACHINE
(Not to scale)

3.2 SPECIFICATIONS.

The following specifications apply to the impact test machine.

- Impacter Weight

Minimum: 4.5 lbs
Maximum: 50 lbs
The impacter weight can be increased in increments of ½ lbs, 1 lb, 2 lbs, and 4 lbs
- Impacter (tup) Diameter

Hemispherical 0.25", 0.50", 0.75", 1.00", 1.50", 2.00", 2.50", and 3.00"
(Note: The impacter assembly weight may not be identical with different tups)
- Drop Height

Maximum 12' (may vary with the fixture being used)
- Load Cell

Type: Piezoelectric
Capacity: 0-10000 lbf (compression only)
(Note: Load cell range can be chosen based on maximum expected loads for improved resolution)
- Rebound-Catch Mechanism

Minimum detectable/stoppable rebound height: 0.25"
- Data Acquisition

Maximum sampling frequency: 100 kHz
Number of channels: 8
Timer: Internal
Trigger: External (photoelectric)
- Fixtures

The following fixtures are available to hold test coupons in plate configuration with the following boundary conditions.
 - All edges clamped (test section 6" × 6", 8" × 8", 10" × 10", 12" × 12", and 17" × 17")
 - All edges simply supported (test section 8" × 8", 10" × 10", and 12" × 12")

The different parts of the impact test machine are described in detail in the following paragraphs.

- Support Columns.

The support columns (figure 7) are tubular and form the primary structure of the drop tower. The support columns hold the base platen and the top crosshead in place. The columns are made of $5'' \times 5'' \times 0.25''$ aluminum tubing. The winch used to hoist the impactor assembly is mounted on one of the columns.

- Guide Shafts.

The impactor assembly is guided during its descent by two guide shafts (figure 7). The guide shafts are made of stainless steel and are 0.75'' in diameter. The shafts are aligned and anchored between the upper crosshead and the base platen at the bottom. A tensile preload is introduced in the shafts by adjusting the anchor bolts at the top. The preload is intended to remove slack in the assembly and to assure the shafts are straight in the assembly.

- Base Platen.

The base platen supports all the fixtures and sensor assemblies. The base platen is a 1.5'' thick aluminum plate and is anchored at the bottom to the main frame using anchor bolts. The guide shafts pass through the base platen via recesses provided. Tapped holes are provided on the base platen for mounting the fixtures, sensor assemblies, and rebound-catch mechanism. The base platen is analogous to a bread-board used to assemble electronic circuitry. The configuration of the base platen is shown in the figure 8.

- Fixtures.

Test fixtures to hold flat square coupons of different sizes under clamped end conditions or simply supported end conditions are currently available. The fixtures consist of two aluminum plates with each plate containing an opening in the center to expose the test section of the specimen to the projectile. Fastener holes are provided for clamping and positioning the specimen. The plates are mounted on four pegs at the corners. Additional pegs can be used for increased support or foundation rigidity. The pegs screw on to the holes provided on the base platen. The maximum size of the specimen (test section) that can be accommodated is $12'' \times 12''$. The main features of the fixtures are illustrated in figures 9 and 10.

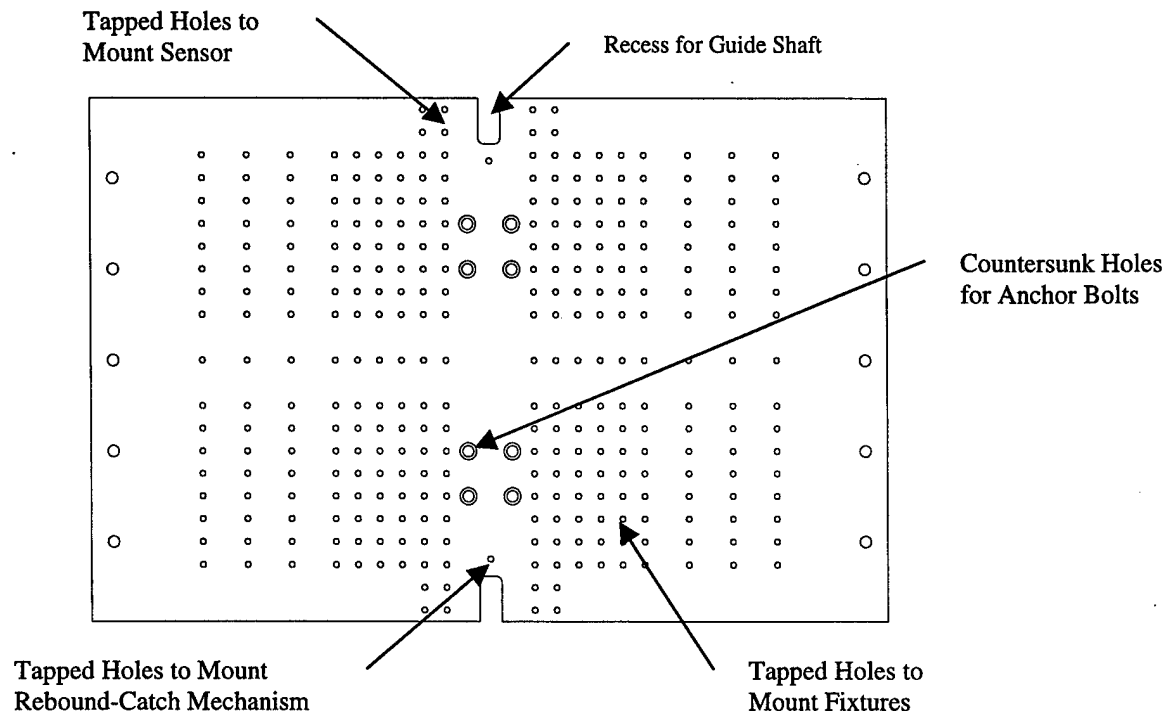


FIGURE 8. DETAILS OF THE BASE PLATEN USED FOR MOUNTING FIXTURES AND SENSOR ACCESSORIES

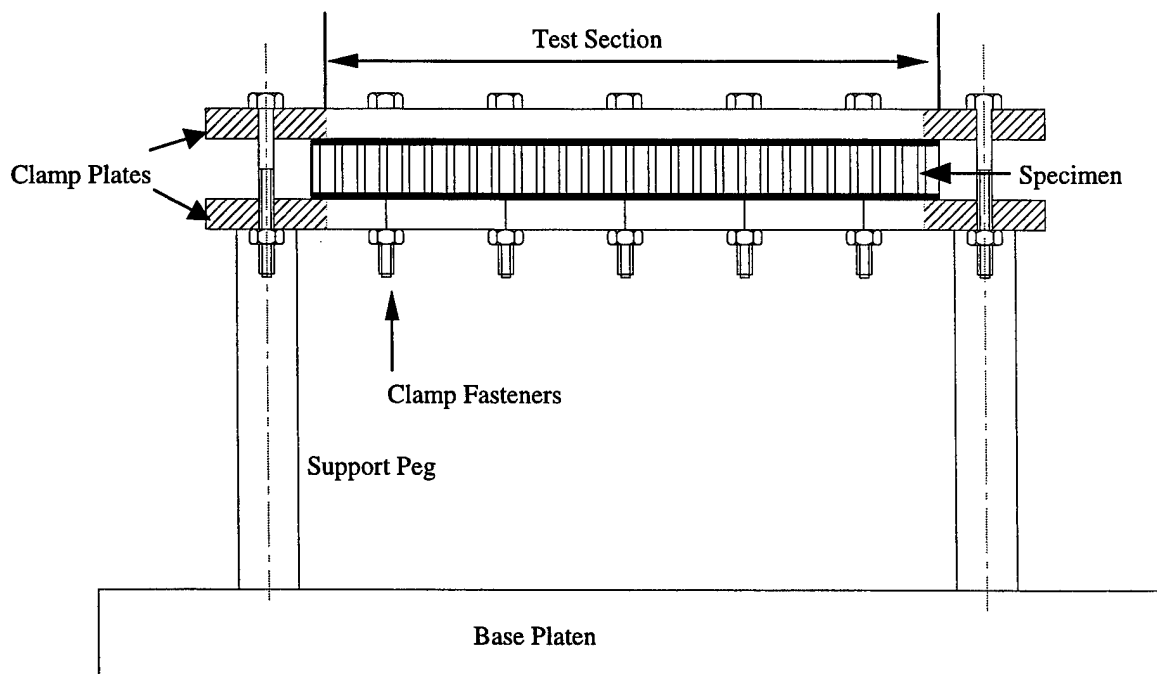


FIGURE 9. TYPICAL SPECIMEN MOUNTED ON FIXTURE TO SIMULATE CLAMPED END BOUNDARY CONDITIONS

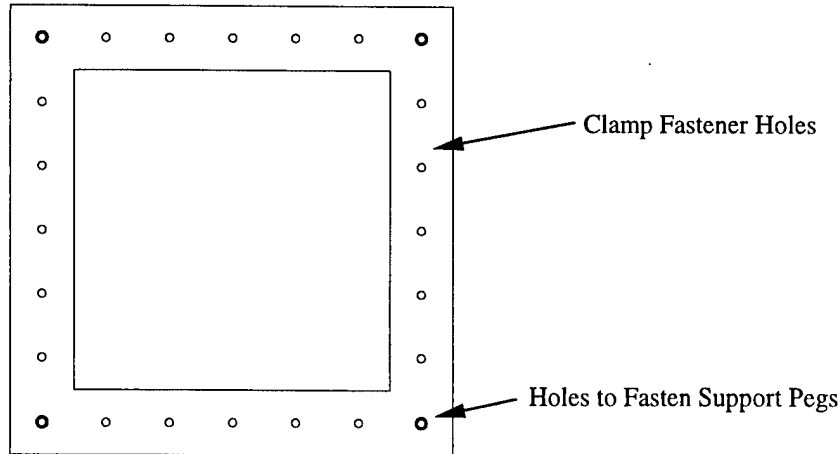


FIGURE 10. TYPICAL CLAMPING PLATE FOR CLAMPED-CLAMPED BOUNDARY CONDITION

- Impactor Assemblies.

The impactor assembly is the primary component of the test apparatus that contacts the test coupon. The impactor assemblies are designed to withstand high loads with minimal compliance in order to eliminate binding of the assembly on the guide shafts. The impactor assembly rides on the guide shafts with the aid of four bearings. Reinforced Polyamide Vespel® bearings were used. These bearings are light (3 oz), can withstand a bearing pressure of 4900 psi, and possess a very low coefficient of friction.

Depending on the weight of impact desired, a different assembly has to be used. Three assemblies were designed and built to accommodate the range of weight, strength, and compliance required. The three assemblies are the Light Weight Impactor Assembly (LWIA), Heavy Weight Impactor Assemblies I and II (HWIA-I & HWIA-II). The weight limitations of the impactor assemblies are 4.5 to 12 lbf for the LWIA, 12 to 30 lbf for HWIA-I and 16 to 50lbf for the HWIA-II. The three impactor assemblies can carry any of the tups used. All three assemblies can carry the same impactor tup and load cell, and were used for this test program. The weight differential for the LWIA and HWIA is due to the different construction.

The basic structure of LWIA and HWIA consists of two beams. The ends of the beams house the bearings. The beams are spaced apart to increase the stiffness of the assembly. The beams of the LWIA are spaced apart by a central tube, alignment rods on either side of the central tube and two inclined cross bars as shown in figure 11. The beams in the HWIA-I and II are spaced apart by two plates on either side of the assembly as shown in the figures 12 and 13. The plates are fastened to the beams and facilitate alignment of the beams. All the assemblies accommodate an eye bolt at the top beam for hoisting purposes. Sensor flags may be mounted at suitable locations on the assemblies for data acquisition and triggering purposes.

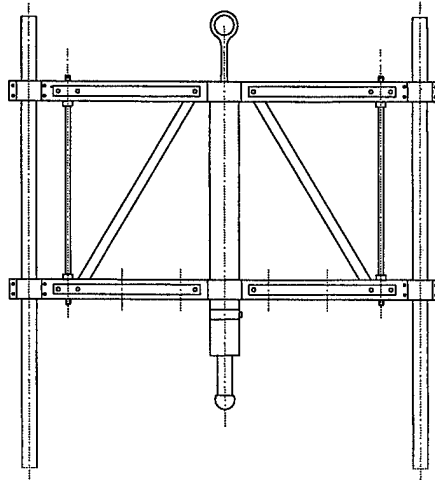


FIGURE 11. LOW WEIGHT IMPACTOR ASSEMBLY

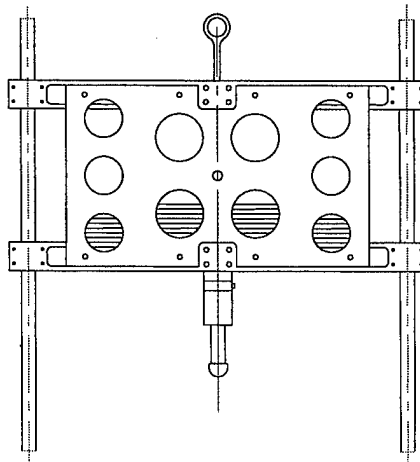


FIGURE 12. HEAVY WEIGHT IMPACTOR ASSEMBLY-I

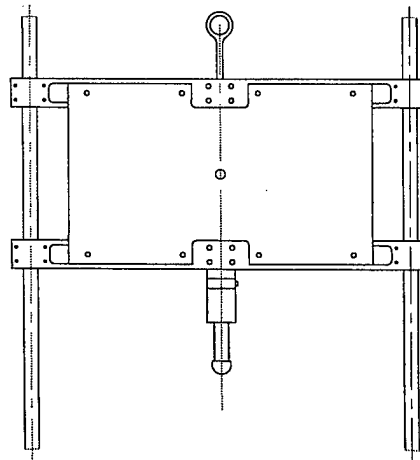


FIGURE 13. HEAVY WEIGHT IMPACTOR ASSEMBLY-II

- Rebound Catch Apparatus.

The impactor typically bounces back after its first impact with the specimen. A pneumatic rebound-catch mechanism is to prevent a secondary impact to eliminate the undesirable effects of multiple impacts. The mechanical end of the rebound-catch mechanism consists of two air cylinders located close to the guide shafts. The piston is activated using compressed air. The ends of the piston which come in contact with the impactor assembly contain a layer of resilient rubber to prevent damage to the impactor assembly. The airflow into the cylinders is controlled using a solenoid valve, which in turn is triggered by an electronic circuit which senses the rebound of the impactor assembly using photoelectric sensors. The rebound-catch assembly along with the specimen, clamping fixture, and impactor assembly is illustrated at the instant of initial impact, as seen in figure 14. The configuration of the rebound-catch mechanism after arresting the impactor assembly is shown in figure 15. The height of the mechanism can be adjusted if necessary by using extensions, which are part of the assembly.

- Impactor Tups.

The impacting end of the impactor assembly is called a “tup.” Tups are typically hemispherical in shape with various diameters. Tups can be built using different material to simulate a desired stiffness. The tups used with the current impactor assemblies are made of hardened steel. The primary constraint on the design of a tup is the weight. In order to meet the stringent weight limitations, ball bearings were ground to a suitable dimension and the remaining portions of the balls were screwed on to a steel or aluminum shank by threads machined into the balls. The shank was mounted on the impactor assembly using a threaded rod. The steel ended tups of various diameters are shown in figure 16. The detailed dimensions of the tups are given in appendix A.

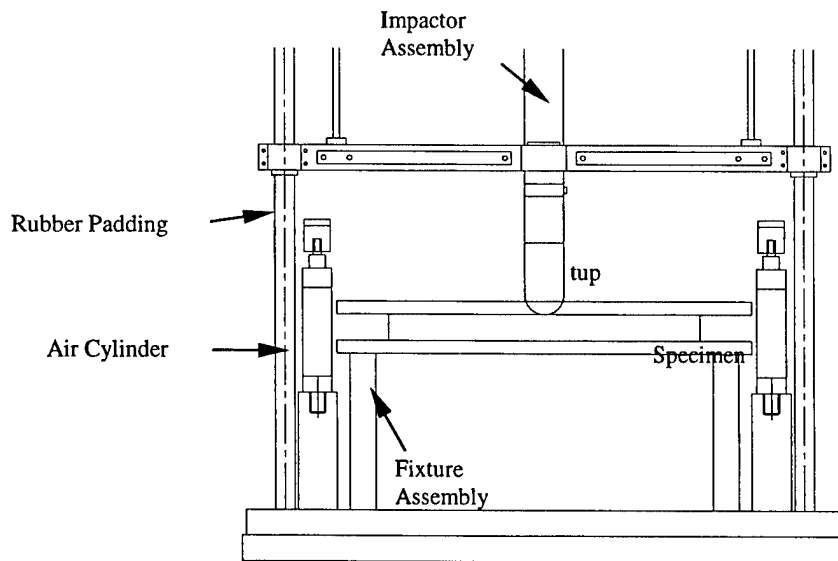


FIGURE 14. REBOUND-CATCH MECHANISM ASSEMBLED WITH THE FIXTURE AND ITS RELATIVE CONFIGURATION AT THE INSTANT OF IMPACT

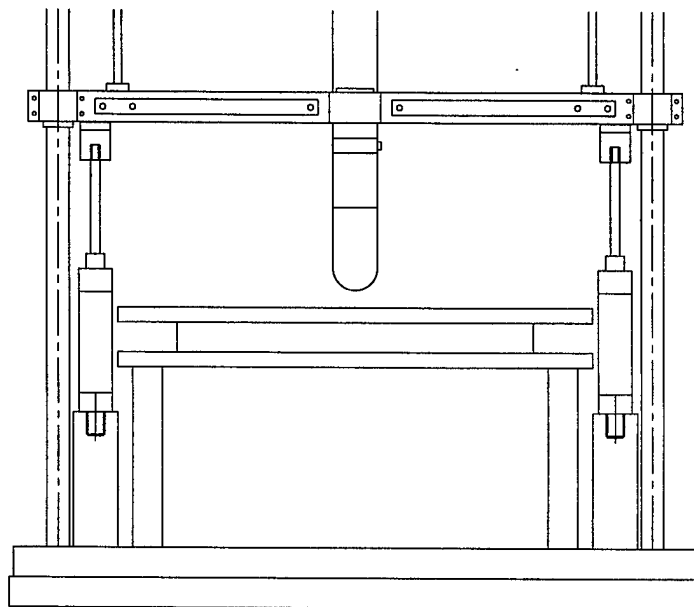


FIGURE 15. ARREST OF THE IMPACTOR ASSEMBLY BY THE REBOUND-CATCH-MECHANISM

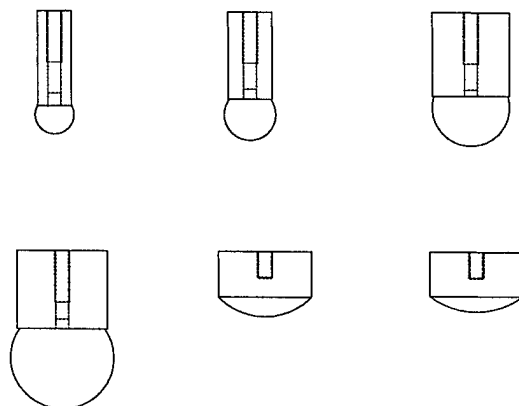


FIGURE 16. TYPICAL IMPACT TUPS USED WITH THE IMPACTOR ASSEMBLY

3.3 DATA ACQUISITION.

The duration of an impact event for which the forces are of nonzero magnitude is typically of the order of 10 to 100 milliseconds, as illustrated in figure 17. The recording of data within such small intervals of time requires a system capable of high-speed data transfer, i.e., around 10,000 to 100,000 samples per second, in order to circumvent the aliasing effect. Further, the data acquisition should be performed only for the duration of the impact to keep the amount of data to a minimum and to optimize the storage space. This requires an automated triggering device to trigger the data acquisition process upon detecting the beginning of the impact process.

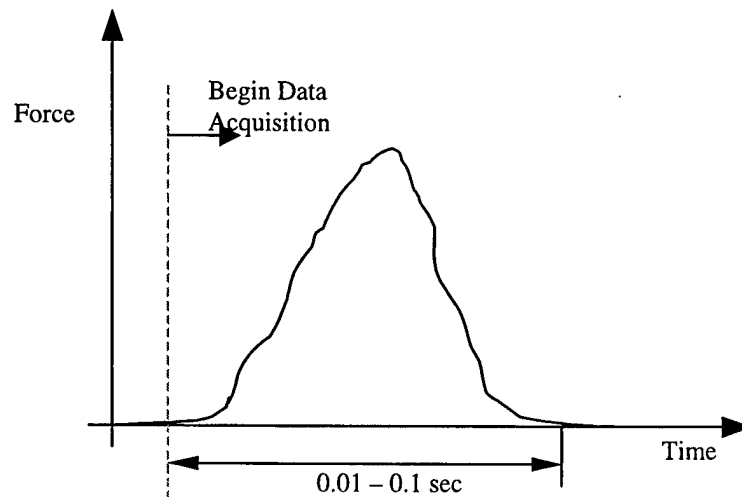


FIGURE 17. TYPICAL FORCE SIGNAL DURING AN IMPACT TEST

A high-speed data acquisition board, DT-301, supplied by DATA TRANSLATION® is used for data acquisition. The DT-301 is a multifunction data acquisition board for the peripheral component interconnect (PCI) bus. The board contains 16 single ended or 8 differential analog inputs, 23 digital input or output (I/O) lines and 4 counter/timer channels. The DT-301 board has a 12-bit resolution and a throughput speed of 150 kilo-samples/sec. The board accepts input voltages of ± 1.25 , 2.5, 5, and 10 Vdc. The finer details of the board may be obtained from the Data Translation Product Handbook. Figure 18 shows a schematic of the data acquisition system.

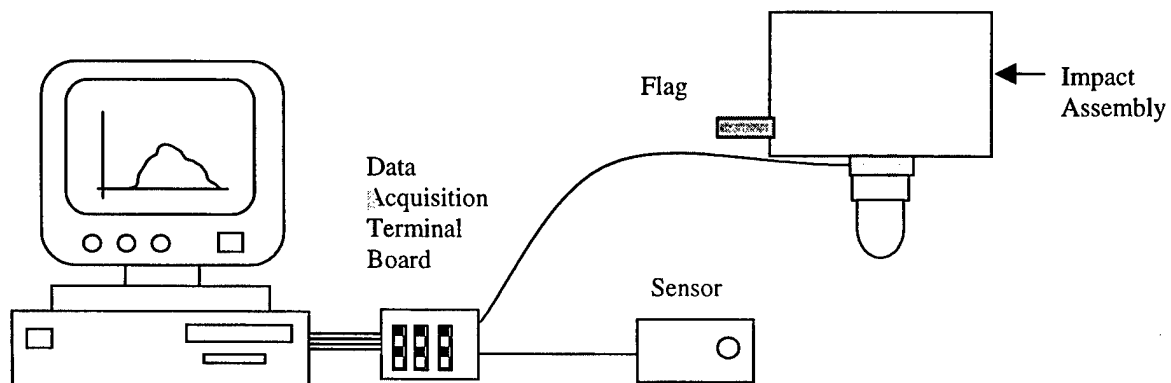


FIGURE 18. ARRANGEMENT FOR DATA ACQUISITION

The hardware set up consists of a trigger flag mounted on the impactor assembly and a photoelectric sensor* mounted close to the path of the impactor assembly. The photoelectric sensor has a "fork" construction, as illustrated in figure 19.

* Baumer Electric, Ltd., Fork sensors; model FEG 12.24.35, PNP type.

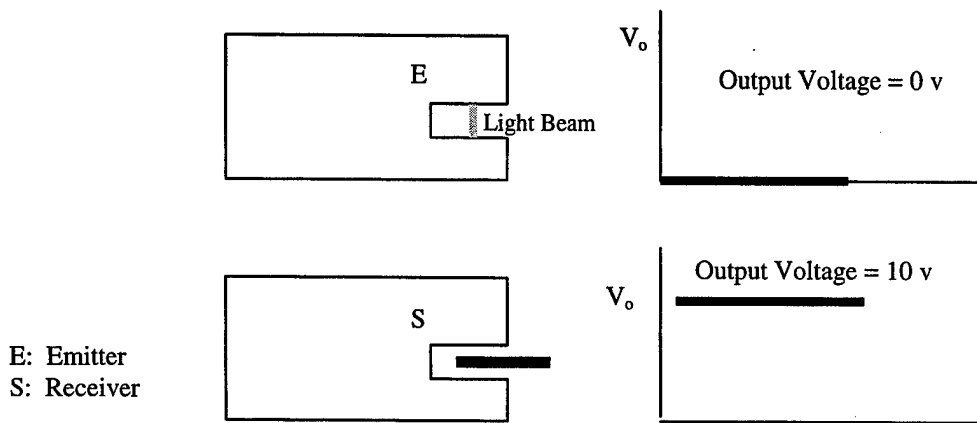


FIGURE 19. SCHEMATIC SHOWS FUNCTIONING OF THE PHOTOELECTRIC FORK SENSOR

A nonpulsating infrared beam is produced by an emitter located in one of the arms and is sensed by a receiver located in the other arm. The gap between the two arms provides the path for a flag which interrupts the light beam. When the flag passes through the gap between the two arms of the sensor, an output voltage is produced, as shown in figure 19. During the impact test, the flag blocks the light beam for a short duration and thus produces a voltage pulse. This voltage pulse can be used for two purposes. First, the pulse can be used to trigger the data acquisition and second, it can be used to measure the impact velocity, given the dimensions of the flag. The schematic of the flags used in the experiments is shown in figure 20. The first flag is used to trigger the data acquisition just before impact and the second flag is used to measure the impact velocity.

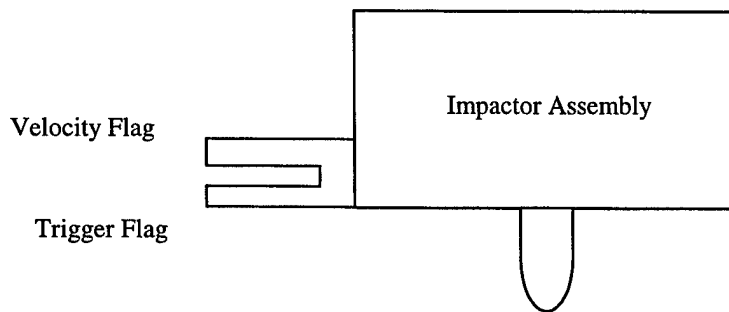


FIGURE 20. FLAG ARRANGEMENT FOR TRIGGERING AND VELOCITY MEASUREMENT

During the impact test, the trigger flag first passes through the sensor, producing a voltage pulse that starts the data acquisition. The velocity flag then passes through the sensor, producing another pulse, which is used for computing the impact velocity. The typical signals obtained during an impact test are illustrated in figure 21. It can be seen that two more voltage pulses follow the completion of impact test, the first corresponds to the rebound of the impactor and can be used to compute the rebound velocity.

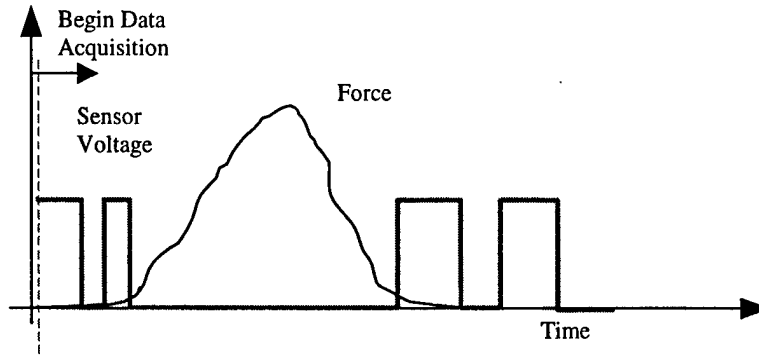


FIGURE 21. TYPICAL SENSOR VOLTAGE PULSES PRODUCED DURING AN IMPACT TEST

3.4 DATA ACQUISITION PROGRAM.

The data acquisition is done using a user-friendly computer program. The program is written in visual basic and assembled with Data Translation's data acquisition visual programming interface (DT VPI™). This program displays signals after the data acquisition is complete and also writes the acquired data into a user-specified file. A screen display of the program is shown in the figure 22. The details of the impact test may be entered in the appropriate boxes provided. The user presses the "START" button to begin the data acquisition program. The program is now armed for data acquisition and waits until the trigger pulse is supplied to start the actual acquisition of data. The program then acquires the data for a preset period of time (about 40 ms (the user can judiciously adjust this), and upon completion of this, displays the time history of the signals. The acquired data is then written into a user-specified output file in ASCII format. The structure of a typical output file is shown in figure 23.

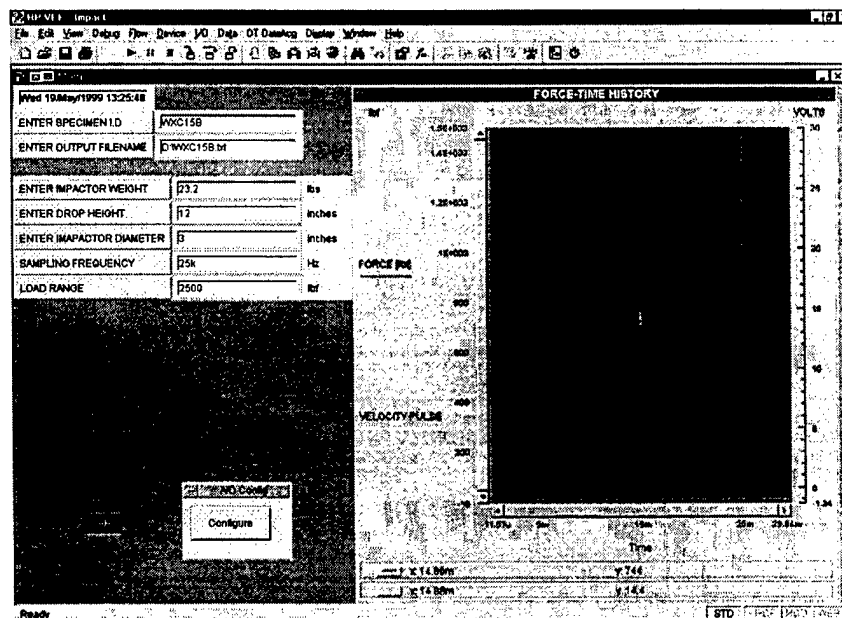


FIGURE 22. SCREEN DISPLAY FOR THE DATA ACQUISITION PROGRAM

WXC34N

IMPACTOR WEIGHT (lbf) = 15.6

IMPACTOR DIAMETER (inches) = 3

DROP HEIGHT (inches) = 12

SAMPLING FREQUENCY (hertz) = 25000

LOAD RANGE (lbf) = 2500

FORCE	VELOCITY	FLAG	VOLTAGE
0.610352	9.99756		
1.2207	9.99756		
1.2207	9.99756		
1.2207	9.99756		
1.2207	9.99756		
1.2207	9.99756		
1.2207	9.99756		
1.2207	9.99756		
1.83105	9.99756		
0	9.99756		
1.2207	9.99756		
1.83105	9.99756		
1.2207	9.99756		

FIGURE 23. TYPICAL RAW DATA FILE OBTAINED FROM THE DATA ACQUISITION PROGRAM

3.5 DATA REDUCTION AND ANALYSIS.

The raw data obtained from an impact test consists of the time histories of the sensor voltage and the force. The sensor voltage signal consists of the trigger pulse and the pulse corresponding to the impact and rebound velocities. The raw data has to be reduced to obtain the impact velocity and time histories of force, impactor velocity, impactor displacement, and energy. Since the impact velocity is readily computed using the velocity flag dimensions and the velocity voltage pulse and the mass of the impactor is known, the velocity and displacement time histories are obtained by using Newton's second law. A Matlab™ computer program was written to do the calculations and is listed in appendix C. The reduced data file contains the details of the impact event and the time histories of force, velocity, displacement, and energy. The typical reduced data file is shown in figure 24. The reduced data is then inserted into an Microsoft® Excel spreadsheet, which summarizes the reduced data for peak force, peak displacement, impact duration etc., and also can plot the time histories of various signals. The typical Microsoft® Excel spreadsheet is shown in figure 25. The Microsoft® Excel spreadsheet contains all the details pertaining to an impact test.

SPECIMEN I.D. : WXC34N				
IMPACTOR MASS : 0.04037 lb-sec ² /in				
IMPACTOR DIAMETER : 3.00000 in				
DROP HEIGHT : 12.00000 in				
TARGET IMPACT VELOCITY : 96.29953 in/sec				
MEASURED IMPACT VELOCITY : 98.48485 in/sec				
MEASURED REBOUND VELOCITY : 35.71429 in/sec				
TARGET IMPACT ENERGY : 187.20000 in-lbf				
MEASURED IMPACT ENERGY : 195.79262 in-lbf				
SAMPLING FREQUENCY : 25000.00000 Hertz				
TIME(sec)	FORCE(lbf)	DISPL(in)	VELOCITY(in/s)	ENERGY(lbf-in)
0.00000	0.00000	0.00000	98.48485	0.00000
0.00004	4.03971	0.00394	98.48285	0.00796
0.00008	20.19853	0.00788	98.47084	0.05570
0.00012	51.70820	0.01182	98.43522	0.19728
0.00016	71.90673	0.01575	98.37398	0.44057
0.00020	91.29726	0.01969	98.29313	0.76154
0.00024	114.72755	0.02362	98.19107	1.16634
0.00028	137.35022	0.02754	98.06620	1.66107
0.00032	155.93275	0.03146	97.92091	2.23586
0.00036	169.66777	0.03537	97.75961	2.87300
0.00040	174.51527	0.03928	97.58911	3.54536
0.00044	176.13154	0.04318	97.41540	4.22913
0.00048	185.01907	0.04707	97.23649	4.93212
0.00052	197.13781	0.05096	97.04718	5.67459
0.00056	197.13781	0.05484	96.85186	6.43908
0.00060	201.17784	0.05871	96.65454	7.20985
0.00064	206.02534	0.06257	96.45282	7.99619

FIGURE 24. TYPICAL REDUCED DATA FILE

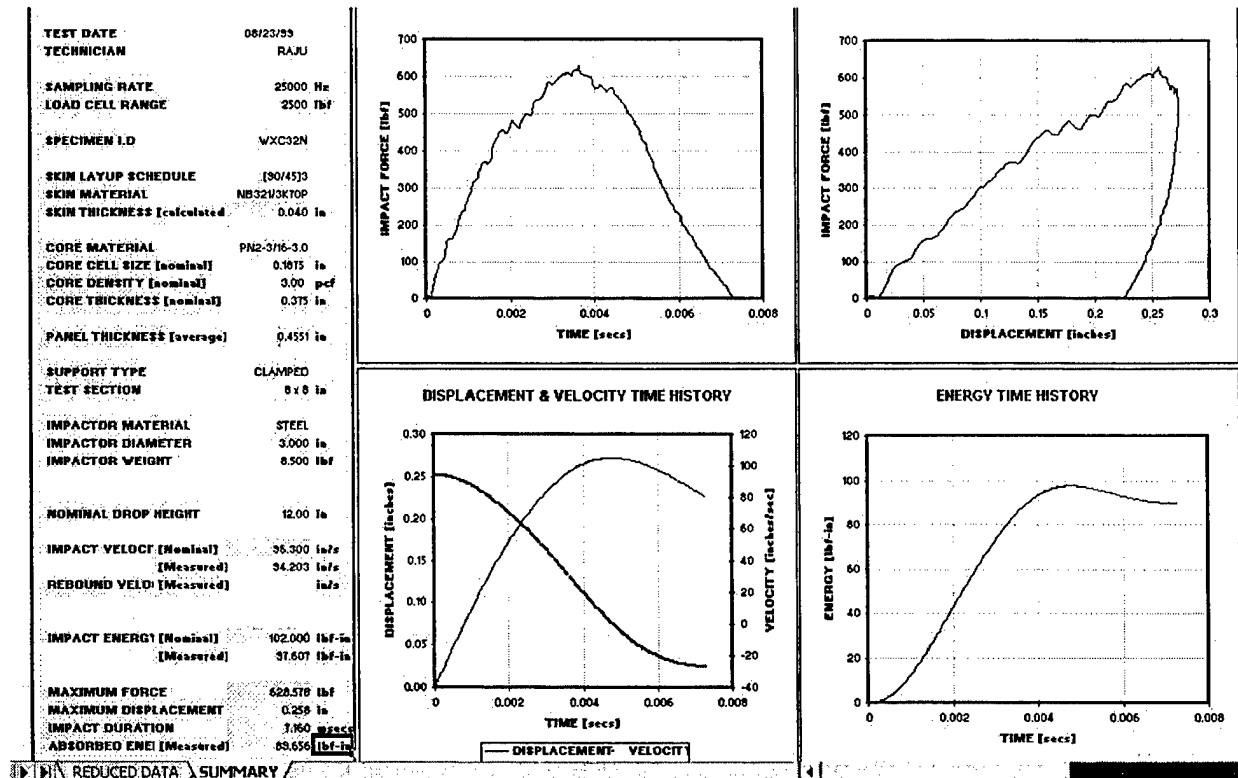


FIGURE 25. TYPICAL MICROSOFT® EXCEL SUMMARY SPREADSHEET

4. IMPACT TESTING OF SANDWICH PANELS.

The sandwich panels were impacted using the gravity-assisted impact test machine described in section 3. The specimens were impacted with steel impactors of 1.00" and 3.00" diameters*. The impact velocity was maintained at a nominal value of 96.6 in/sec, which corresponds to a drop height of 12 inches. A constant value of the impact was maintained to avoid any velocity interaction effects in the data. The typical data reported from an impact test are the time histories of force, velocity, and displacement. The variables defining an impact event are the peak impact force, peak impactor displacement, and duration of impact. The following sections describe impact test procedure, typical results, and summary of the data generated up to this point.

4.1 IMPACT TEST PROCEDURE.

The sandwich panels fabricated as described in the previous section were impacted with varying impact energy levels to inflict a range of damage states in the panels. In the present investigation, the sandwich panels were clamped along the four edges modeled, using the boundary condition equations shown in figure 26.

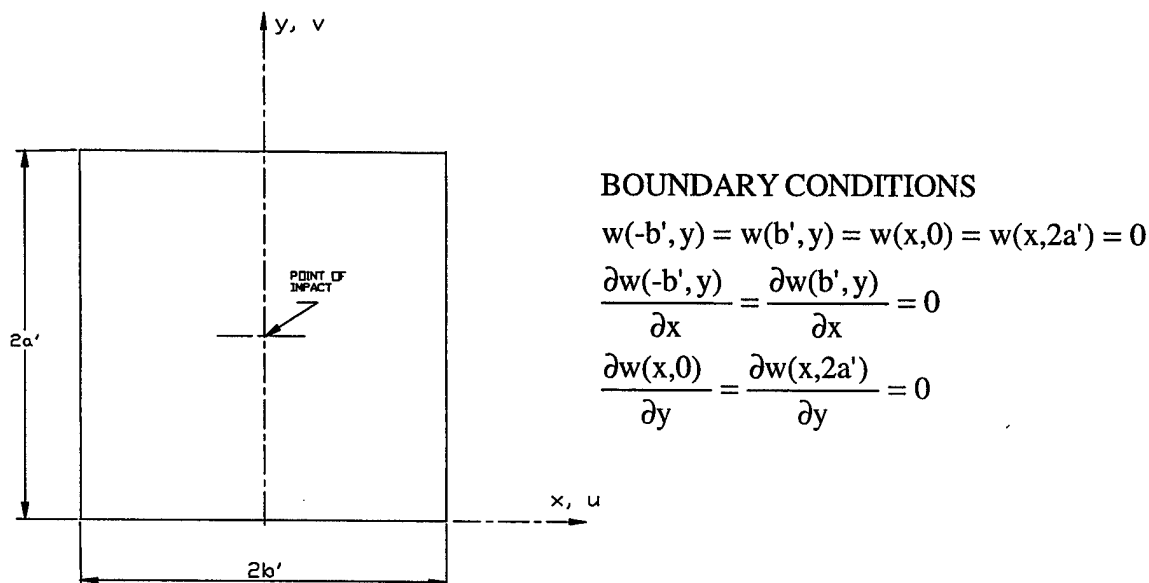


FIGURE 26. BOUNDARY CONDITIONS IMPOSED ON THE TEST SECTIONS OF THE SANDWICH SPECIMENS

It should be noted that the in-plane displacements of the specimen are not constrained in the fixture. The dimensions of the test section are $2a' = 2b' = 8.00"$. The specimen is impacted at the geometric center of the test section in the x-direction. It should be noted that the impact point does not necessarily coincide with the geometric center of the panel in the y-direction, as the test section for the following residual strength test is different than the one for impact. The position of the impact test section relative to the overall specimen is shown in figure 27.

* Henceforth, whenever a dimension is associated with an impactor, it shall refer to its diameter.

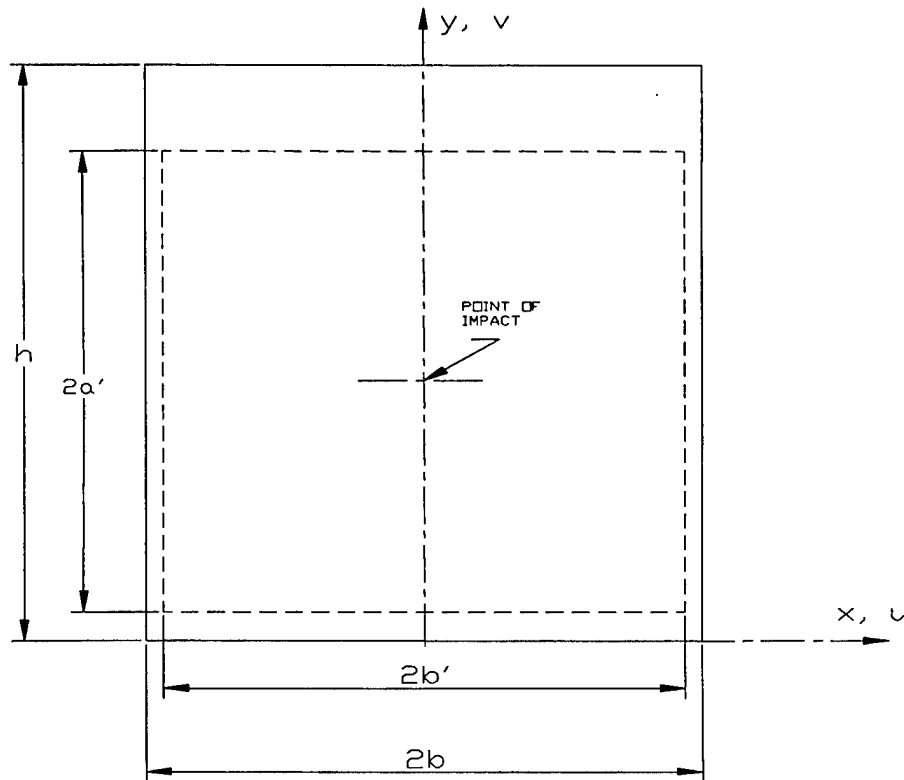


FIGURE 27. IMPACT TEST SECTION RELATIVE TO THE OVERALL SPECIMEN GEOMETRY

All sandwich test specimens have dimensions of $h = 10.5''$ and $2b = 8.5''$. The sandwich specimens are held in position by the fixture. The fixture assembly is turn mounted on four cylindrical standoffs, which elevate the assembly above the base platen of the impact test machine, described in the previous chapter. A photograph of the fixture with the test specimen is shown in figure 28. The picture frame plates are held together using fasteners, uniformly torqued*, to 8 in-lbf. It is not known whether a fully clamped condition was achieved.

The test is run and the data is collected. The test data consist of force-time histories along with the impact velocities. A Matlab® program is then used to reduce the data as described in the previous chapter to obtain time histories of force, velocity, impactor displacement, and energy. The reduced data is then summarized and plotted using an Microsoft® Excel spreadsheet.

* The applied torque was arrived at by trial and error, to avoid crushing in the clamped area.

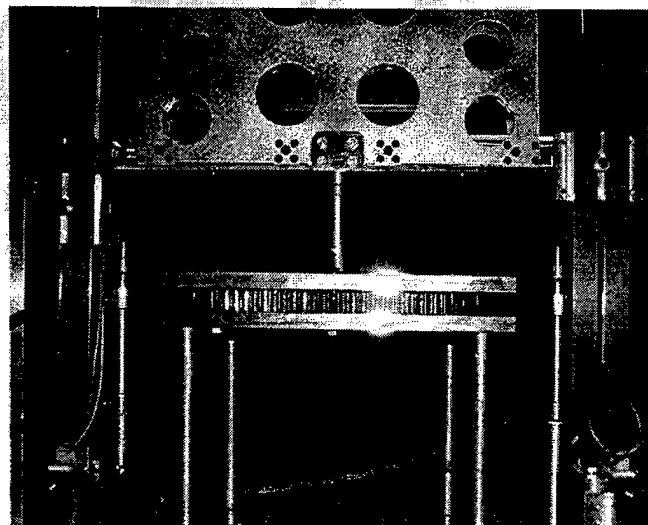


FIGURE 28. PICTURE SHOWS SPECIMEN CLAMPED BETWEEN TWO PLATES OF THE FIXTURE

4.2 IMPACT TEST RESULTS.

The performances of different sandwich panels subjected to impact scenarios at different impact energy levels are discussed in this section. The impact tests were performed with a fixed impact velocity V_0 (96.6 in/sec) and two different impactor diameters (1.00" and 3.00") as previously mentioned. The edges of the sandwich specimens were clamped along the four edges with a test section ($2a' \times 2b'$) of 8.00" \times 8.00". The impact response variables used to characterize the performance of sandwich panels are the peak impact force, maximum impactor displacement, and duration of impact.

The typical force-time and force-displacement plots for both impactor diameters for the three sandwich configurations under study are shown in figures 29a through 29f. For all three sandwich configurations the force-time history of impact tests with different impactor sizes is quite different. The smaller (1.00") impactor induces failure, i.e., core crushing, ply failure, and delaminations at a lower energy level compared to the larger (3.00") impactor. Except for the third panel, the initiation and propagation of failure is clearly indicated in the force-time history and force-displacement plots for impacts with 1.00" impactor, where the load falls sharply after the initial linear region. The larger impactor diameter produces a larger impactor force at a comparable* energy level. The higher impact force for larger impactor can be attributed to the contact phenomena at the point of impact. The induced load due to a larger impactor is distributed over a larger area, and thus the initiation of core crushing and other failure mechanisms is delayed. Further, the duration of impact was smaller for the larger impactor, indicating a stiffer system, which can again be attributed to the load distribution. It was also found that the damage states due to larger impactor was more of the subsurface kind (core crushing and core disbond only), as will be discussed in the chapter dealing with nondestructive evaluation.

* The energy levels of the impacts with different diameter impactors were not necessarily equal, due to differences in total weight of the impactor assembly. However, the typical difference was < 5 in-lbf.

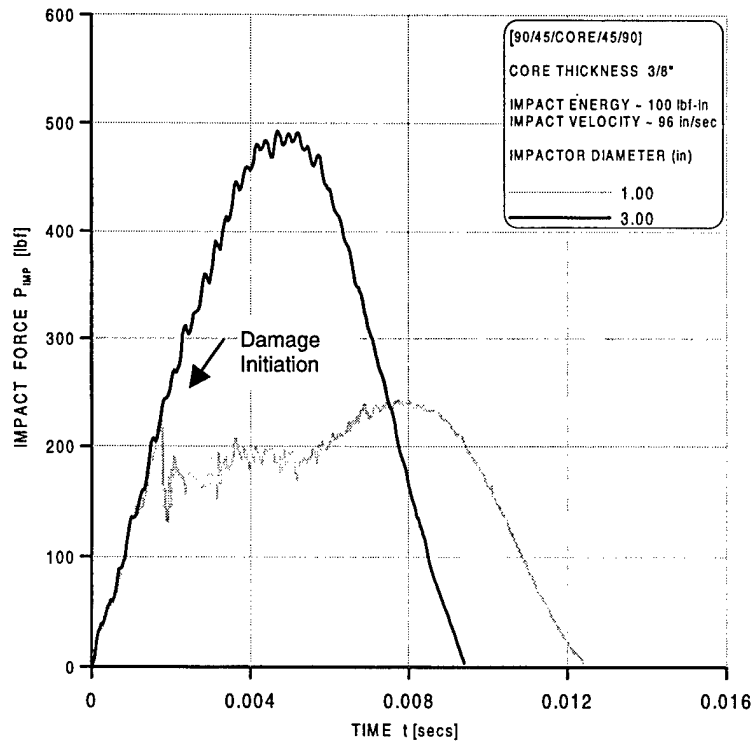


FIGURE 29a. TYPICAL FORCE-TIME HISTORY FOR [90/45/CORE/45/90] SANDWICH PANELS

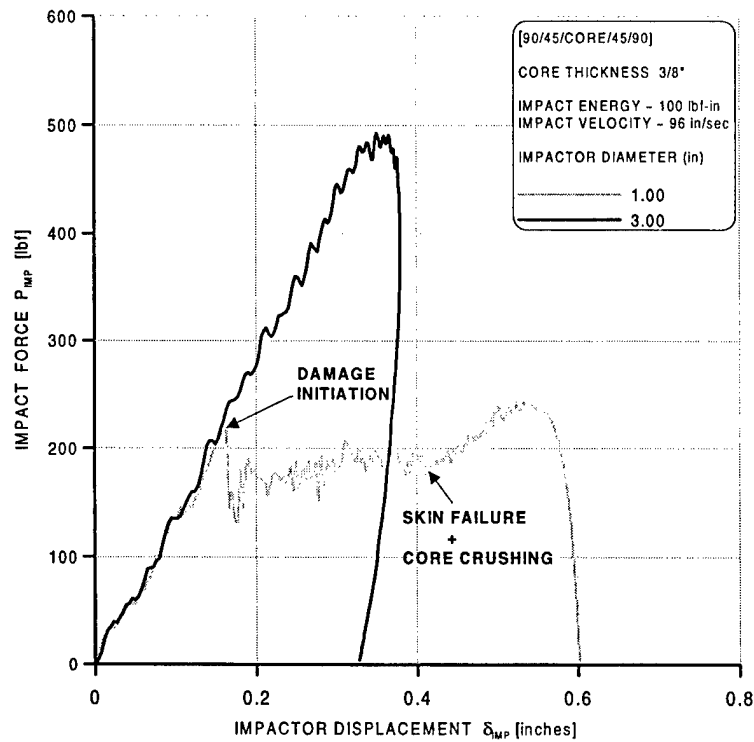


FIGURE 29b. TYPICAL FORCE-DISPLACEMENT CURVES FOR [90/45/CORE/45/90] SANDWICH PANELS

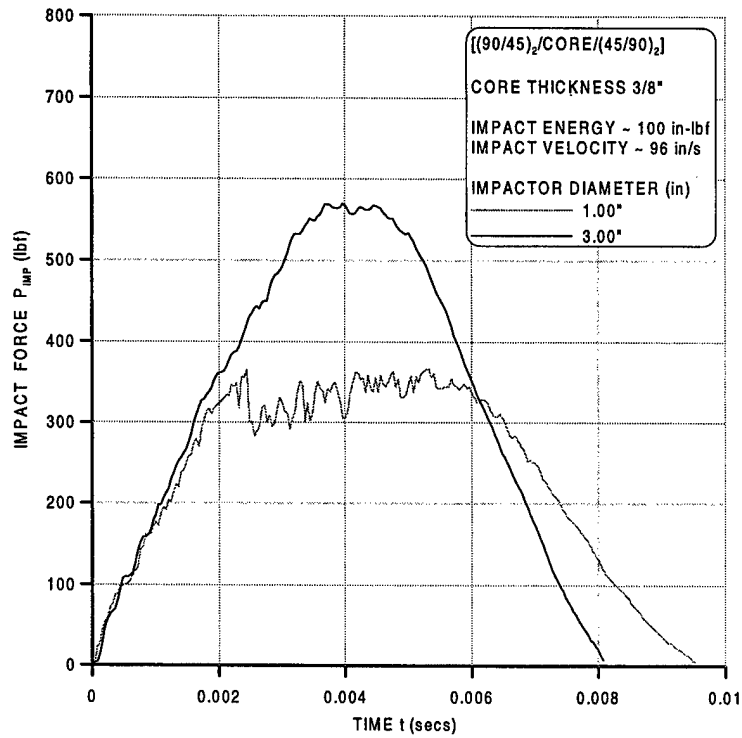


FIGURE 29c. TYPICAL FORCE-TIME HISTORY FOR $[(90/45)_2/CORE/(45/90)_2]$ SANDWICH PANELS

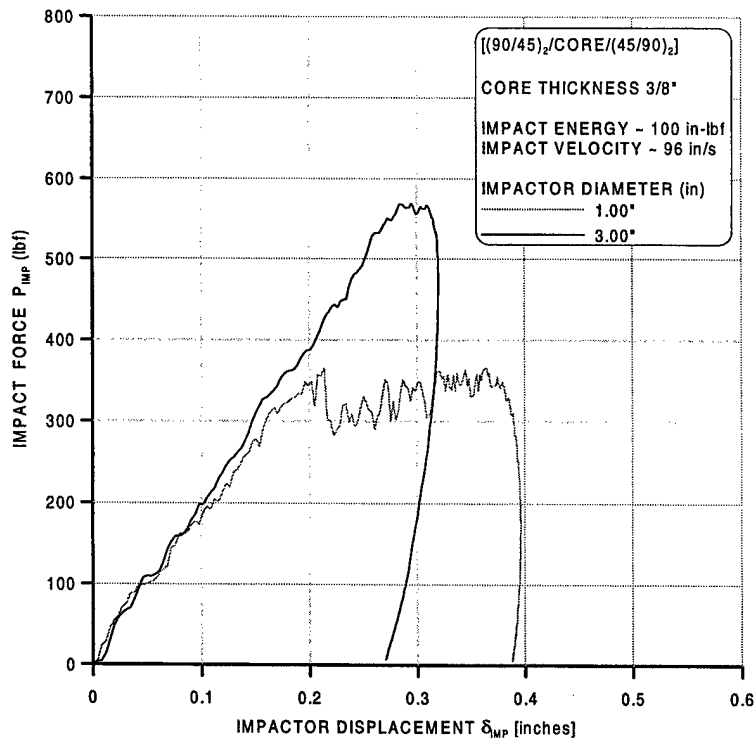


FIGURE 29d. TYPICAL FORCE-DISPLACEMENT CURVES FOR $[(90/45)_2/CORE/(45/90)_2]$ SANDWICH PANELS

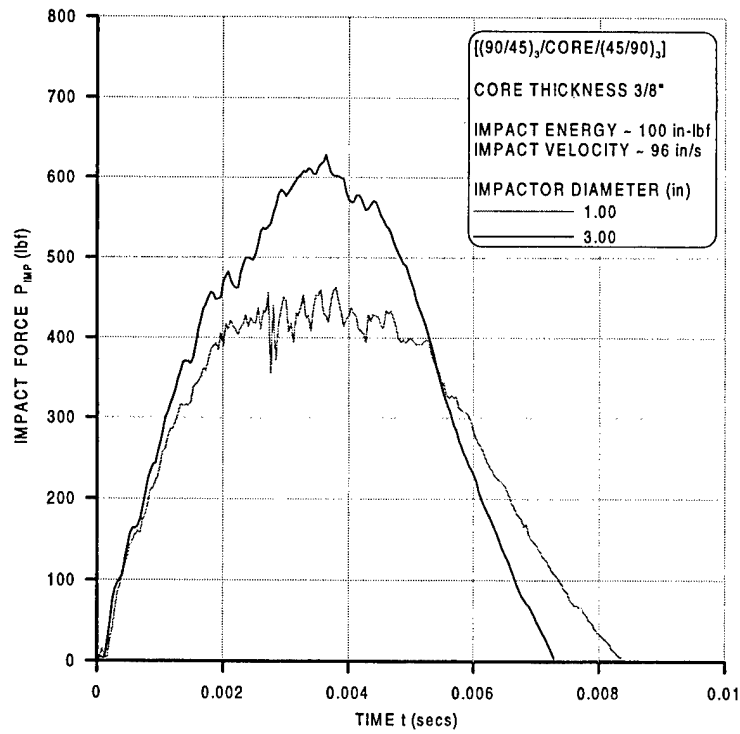


FIGURE 29e. TYPICAL FORCE-TIME HISTORY FOR $[(90/45)_3/\text{CORE}/(45/90)_3]$ SANDWICH PANELS

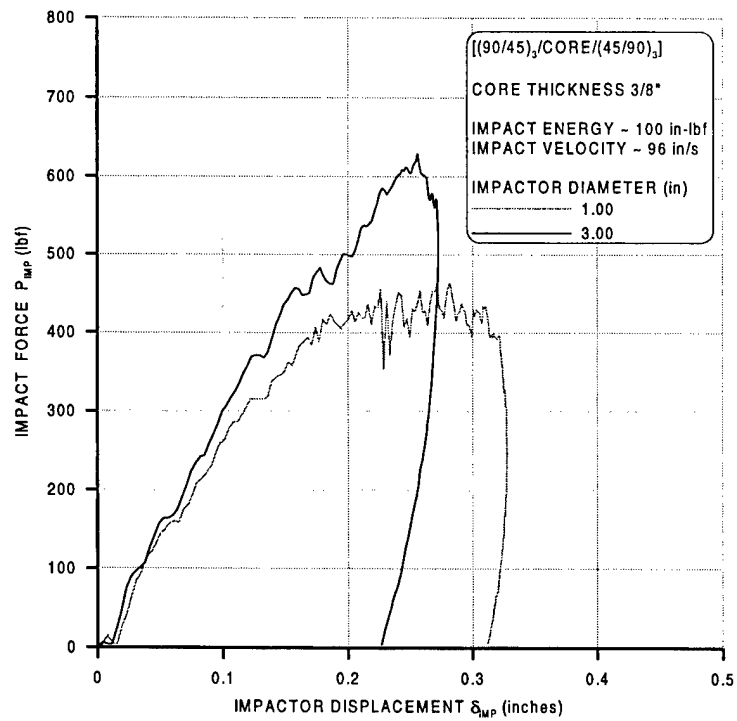


FIGURE 29f. TYPICAL FORCE-DISPLACEMENT CURVES FOR $[(90/45)_3/\text{CORE}/(45/90)_3]$ SANDWICH PANELS

The variation of peak impact force as a function of impact energy for the different sandwich configurations is plotted in the figures 30a through 30c. It can be observed that the peak impact force due to the larger impactor diameter is higher than that of the smaller impactor diameter, for reasons discussed previously. The 3/8" core panels are more compliant globally, which further increases the contact area over which the load is distributed. This should have resulted in higher impact forces for the 3/8" thick core panels than for 3/4" thick core panels. The results in figures 30a through 30c do not show that effect: the forces for the two panels are approximately equal. Also, the lower impact energy levels, the peak impact forces for the different diameter impactors tend to converge, indicating a reduction in the effects of the contact load distribution and global stiffness of the panel.

The variation of maximum impactor displacement with impact energy is plotted in figures 31a through 31c. The trends again indicate the importance of impactor diameter and associated contact load distribution at higher energy levels.

The variation of impact duration plotted in figures 32a through 32c exhibit the similar trends discussed above.

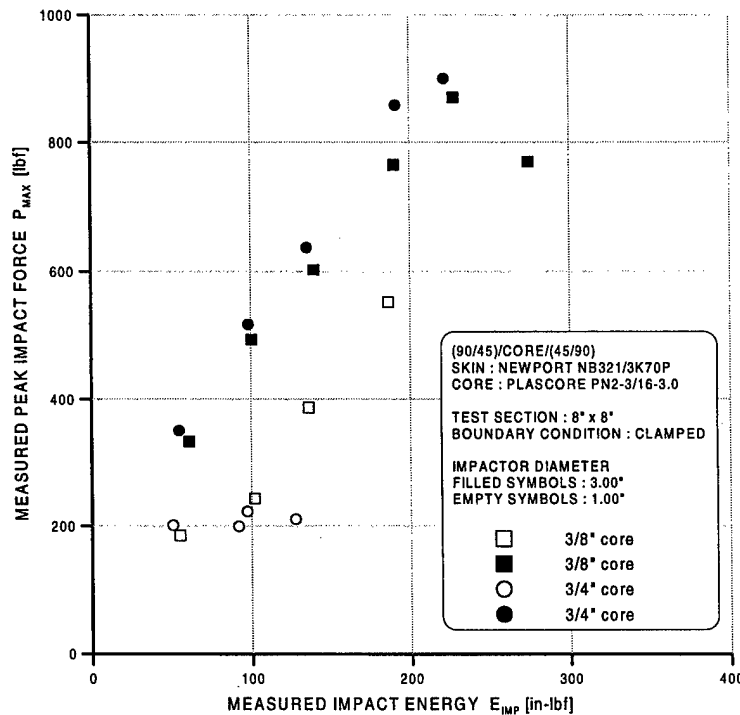


FIGURE 30a. PEAK IMPACT FORCE VS IMPACT ENERGY FOR [90/45/CORE/45/90] PANELS

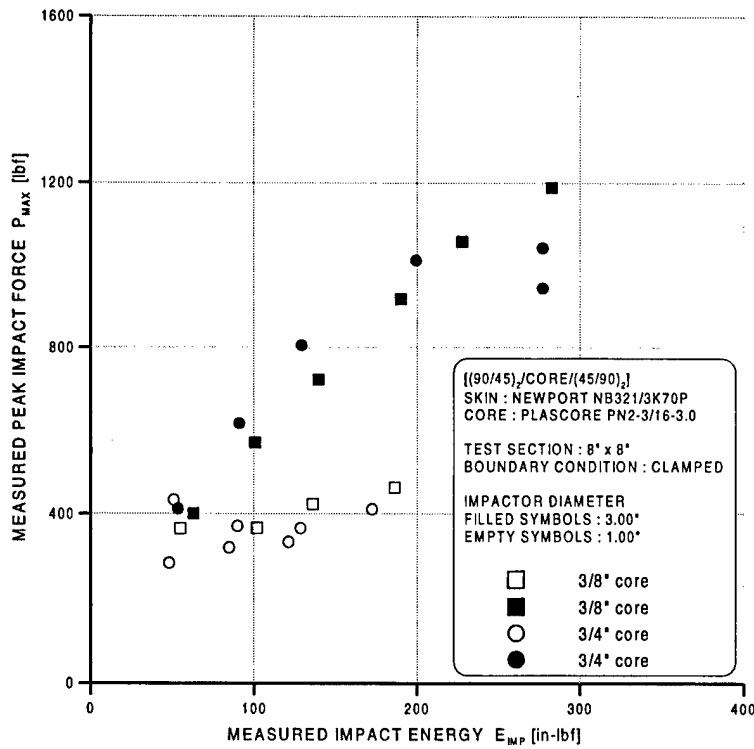


FIGURE 30b. PEAK IMPACT FORCE VS IMPACT ENERGY FOR [(90/45)₂/CORE/(45/90)₂] PANELS

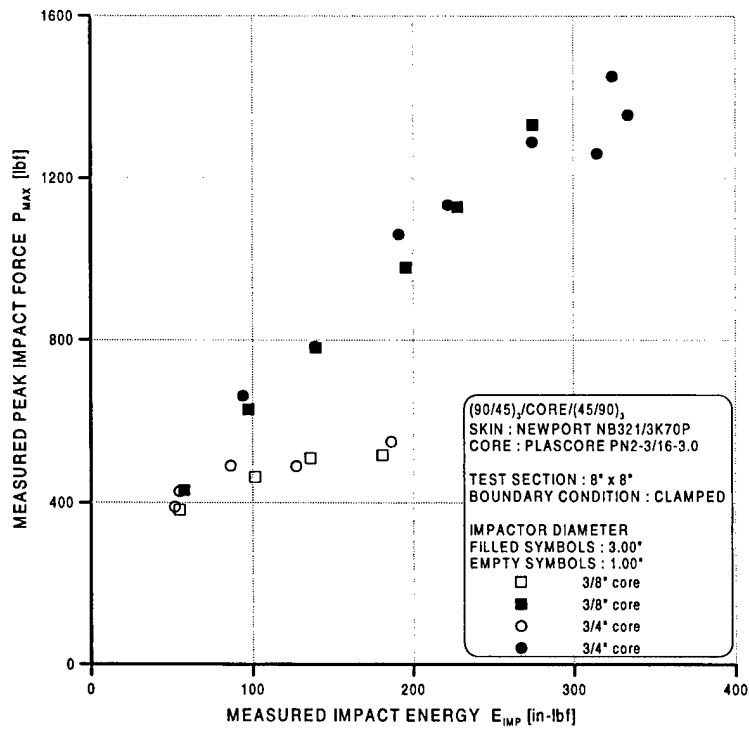


FIGURE 30c. PEAK IMPACT FORCE VS IMPACT ENERGY FOR [(90/45)₃/CORE/(45/90)₃] PANELS

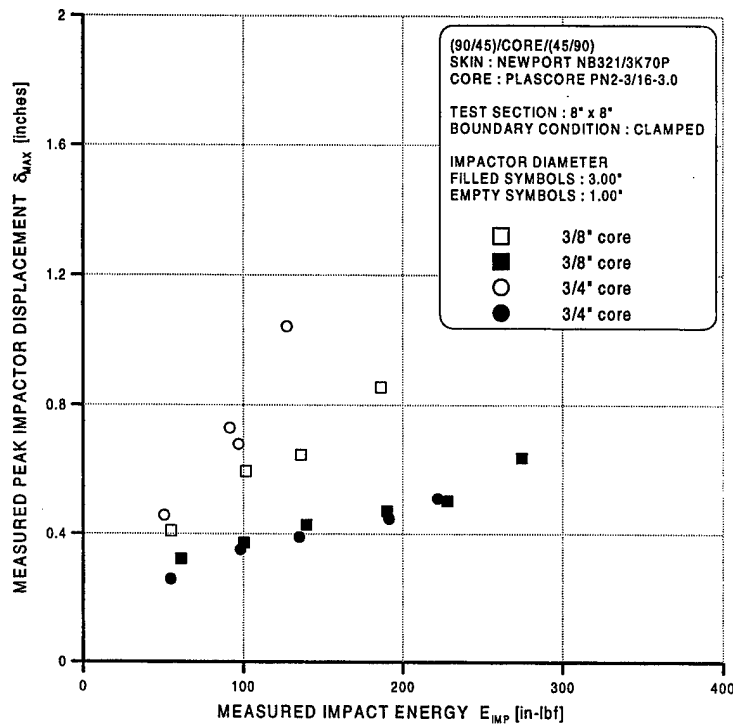


FIGURE 31a. PEAK IMPACTOR DISPLACEMENT VS IMPACT ENERGY FOR [90/45/CORE/45/90] PANELS

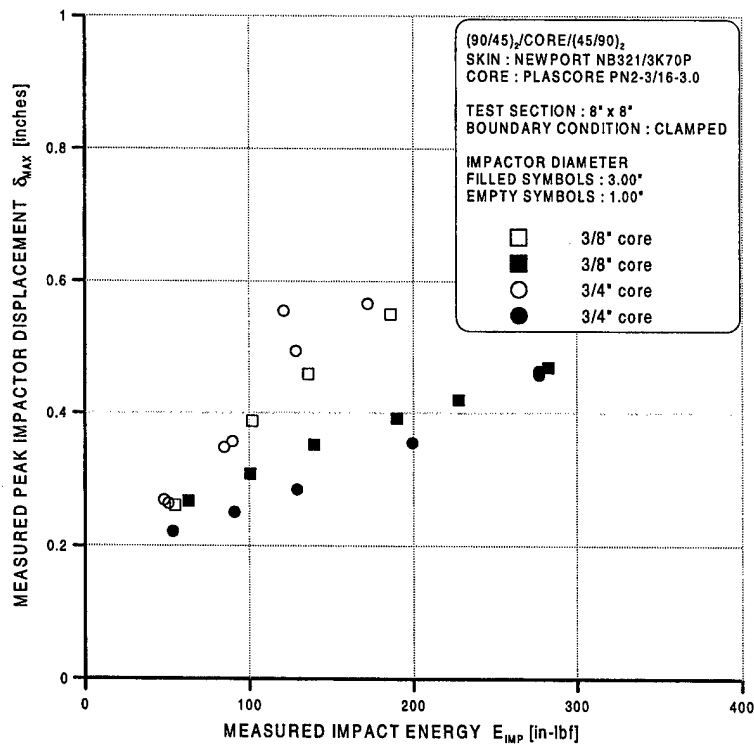


FIGURE 31b. PEAK IMPACTOR DISPLACEMENT VS IMPACT ENERGY FOR [(90/45)₂/CORE/(45/90)₂] PANELS

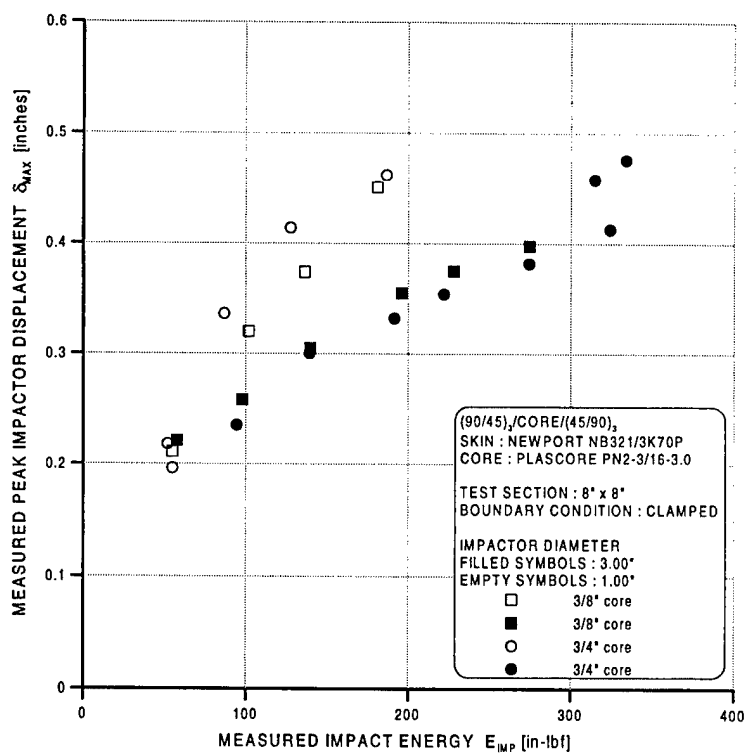


FIGURE 31c. PEAK IMPACTOR DISPLACEMENT VS IMPACT ENERGY FOR [(90/45)₃/CORE/(45/90)₃] PANELS

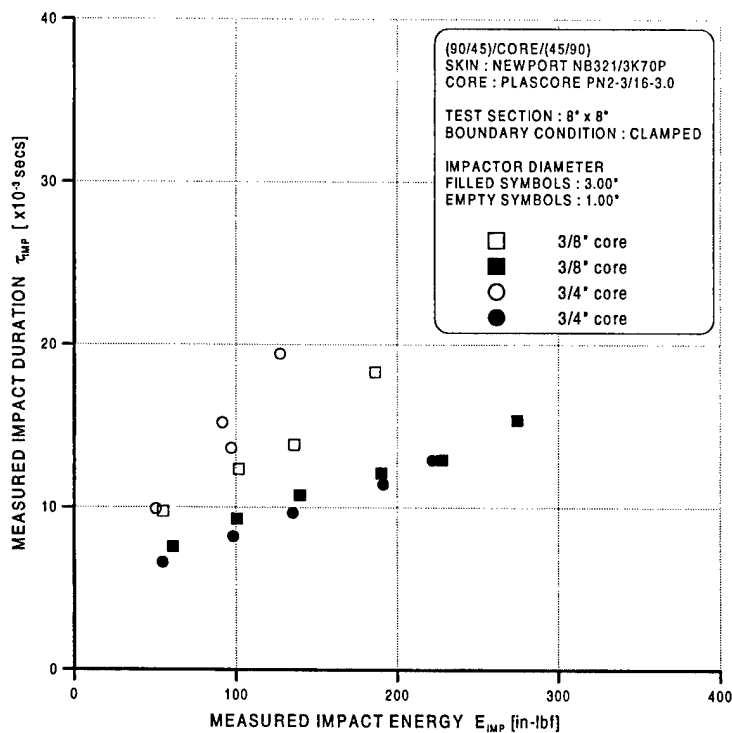


FIGURE 32a. IMPACT DURATION VS IMPACT ENERGY FOR [90/45/CORE/45/90] PANELS

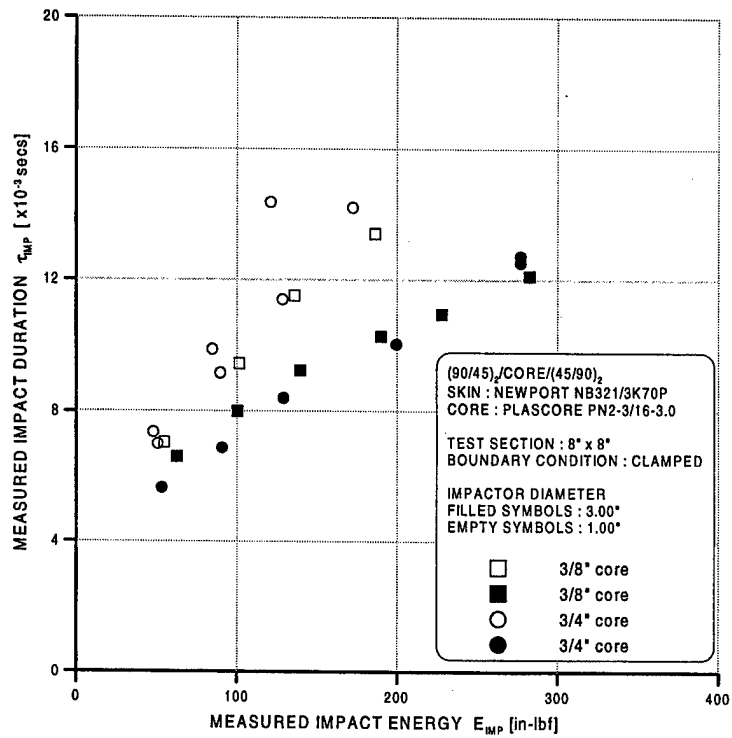


FIGURE 32b. IMPACT DURATION VS IMPACT ENERGY FOR [(90/45)₂/CORE/(45/90)₂] PANELS

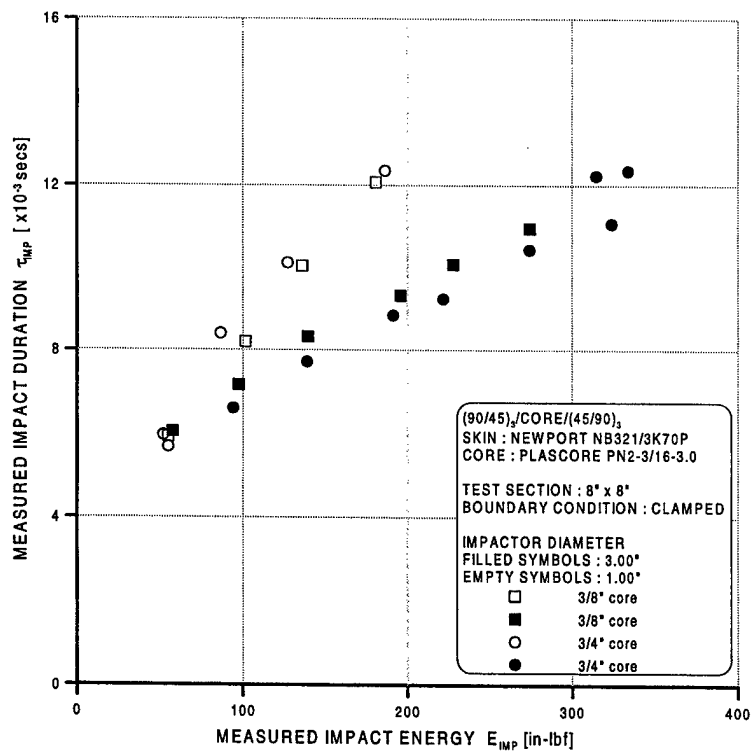


FIGURE 32c. IMPACT DURATION VS IMPACT ENERGY FOR [(90/45)₃/CORE/(45/90)₃] PANELS

The impact test results indicate the importance of the local contact phenomenon once core crushing is initiated. The core crushing significantly alters the contact load distribution, which in turn changes the local displacement field as a function of the sandwich panel stiffnesses (local and global) and the impactor geometry (diameter). However, the exact amount of indentation that occurred during the impact process cannot be estimated based on the impactor displacement alone. If the displacement of the backside of the sandwich panel, below the point of impact is measured, the actual indentation can be calculated by finding the difference between the impactor displacement and the backside displacement. This can be measured by mounting a suitable accelerometer* at that position. This enables the separation of the energy absorption components due to local indentation and global vibration of the sandwich panel. The comparison between static tests and dynamic tests can then be done effectively.

5. DAMAGE EVALUATION IN IMPACTED SANDWICH PANELS.

The damage resistance and damage tolerance programs are linked by the physical characteristics of damage. The damage morphology studies support the understanding and analytical modeling efforts in both damage resistance and tolerance programs. The study of damage state will give an insight into the competing damage mechanisms during the dynamic energy absorption process as a result of impact loading. The state of damage may also be used to model the stiffness changes in the skins and core of the sandwich panels, and the spatial distribution of this stiffness degradation which is a crucial input for any analytical model used for predicting the residual properties of the sandwich panel. Further, the success of a damage tolerance program is dependent on the nondestructive damage detection capability. Thus, it would be beneficial to correlate the damage metrics associated with popular nondestructive damage evaluation techniques (NDE) with the physical characteristics of damage.

In this investigation, nondestructive and destructive inspection techniques were used to study the extent of damage and its morphology. The damage metrics used for damage resistance and tolerance characterization are the planar damage area and residual indentation distribution. The destructive techniques were used on a few selected specimens to visualize the exact nature of the damage and correlate it with the NDE damage metrics. In the current study, ultrasonic C-scan was used to obtain the planar damage area and an indentation measurement apparatus was used for the residual indentation. Also, a visual inspection procedure is outlined and tested for its effectiveness. In this chapter, the details of the NDE and destructive inspection techniques, associated calibration and analysis methods, and significant results are presented.

5.1 NONDESTRUCTIVE EVALUATION OF DAMAGE.

The NDE techniques are important tools used to detect damage in structures without further compromising the integrity of the structure. However, due to the nature of the detection process, the exact physical characteristics of the damage cannot be directly obtained from an NDE method. Instead, a physical dimension is associated with the damaged region and the associated damage is deduced based on NDE calibration and engineering databases. The NDE calibration process involves the simulation of observed damage states in a panel by engineering a standard

* Currently, a miniature accelerometer (~ 0.02 oz) is being used in the experiments. The low mass of the accelerometer allows the use of a double sided tape for temporary mounting.

dimension for the flaw and/or applying a known impact event to a part subjected to destructive evaluations. Actual impact damage may include damage in the skins (matrix cracking, fiber breakage, delaminations), core damage (core cell wall fracture), skin-core disbonds, residual indentation due to core crushing, and combinations of the same. These damage states cannot be simulated with known dimensions without applying a standard impact to a specific structural configuration of interest. Some common engineered flaws, which may be simulated artificially, include delaminations and skin-core disbonds.

In order to get meaningful results from standard impact tests, damage metrics generated from the NDE must be correlated with additional parameters, which can be used to judge residual strength. This may include empirical strength data, measures of effective reduced stiffness, or other damage metrics (e.g., equivalent hole or notch size).

In the current study, only those defects that can be applied artificially were used to calibrate the NDE procedures. Delaminations and disbonds are typically simulated by using a layer of release film of predetermined size and geometry between two adjacent plies (ply and core for disbond) of the laminated skins. A calibration panel containing these engineered flaws is then subjected to NDE inspection and the associated damage metric is obtained. The process is repeated by varying parameters associated with the inspection technique, and calibration data is generated which can be used to correlate the observed damage metrics with the actual damage size. In the following section, the details of the Through Transmission Ultrasonic (TTU) C-scan system, the calibration process and the typical results are presented.

5.1.1 Planar Damage Area Measurement Using Through Transmission Ultrasonic C-Scan (TTU).

The TTU C-scan method was used to obtain a planar damage distribution of the cumulative damage state. The NDE process involved scanning of the impacted panel using the C-scan equipment and obtaining a grayscale image, which gives the planar distribution of damage in terms of signal attenuation levels. A typical C-scan image is shown in figure 33. The parameter used to tune the C-scan system is the wave “gain” value. The gain value determines the resolution of the resulting C-scan image. The grayscale image is then analyzed using the image analysis software, “Global Lab Image”, which computes geometrical quantities such as area, average radius, perimeter, etc., of the damaged region. During the image analysis, a digitized grayscale is used to determine the damaged regions. The grayscale is divided into 255 increments, starting at 0 (zero), which corresponds to the color white and where the value of 255 corresponds to the color black. During the image analysis, a grayscale threshold value is selected such that the shades of gray corresponding to values above the defined threshold value are treated as damaged regions and the colors corresponding to values less than that of the threshold value will be considered as undamaged regions. The two regions will then be separated into a dark colored damaged region and a light colored undamaged region. The software then computes the geometric properties of the damaged region. The NDE process using TTU C-scan is summarized in figure 34.

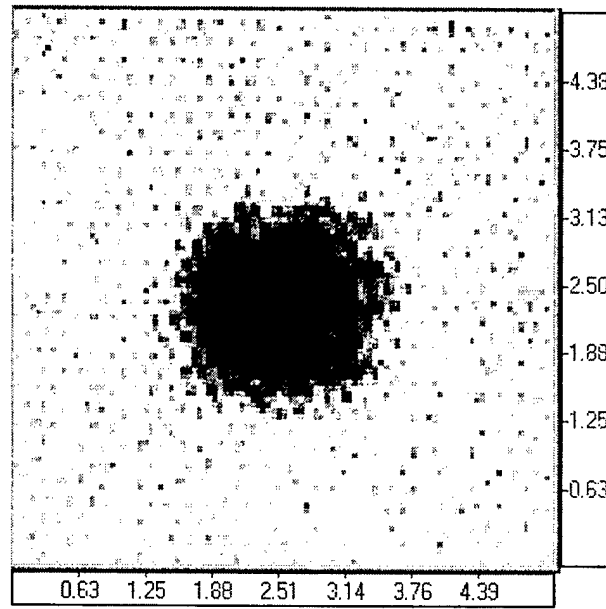


FIGURE 33. TYPICAL TTU C-SCAN IMAGE OF A DAMAGED SANDWICH PANEL

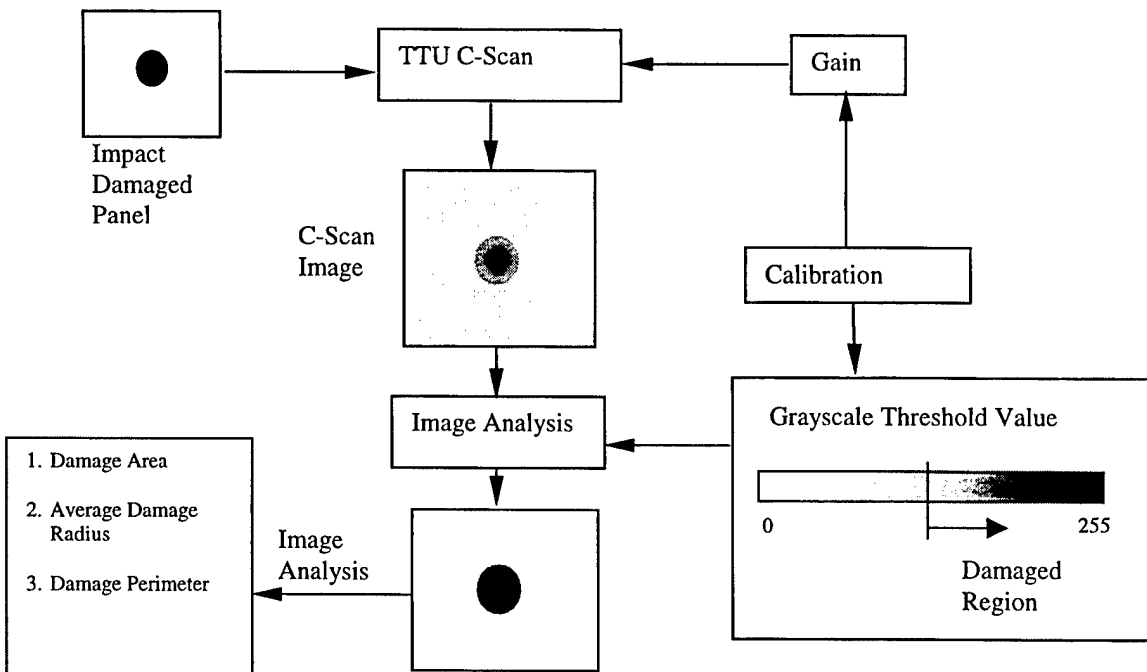


FIGURE 34. SUMMARY OF THE TTU C-SCAN PROCESS

The NDE process using TTU C-scan needs the optimum value of the gain for the C-scan and the optimum value of the grayscale threshold value. These values are obtained using a calibration process where sandwich panels with similar lay-up sequence but with engineered flaws of known dimensions are subjected to the same analysis. The calibration panels and the artificial or engineered flaws used in the investigation are illustrated in figure 35.

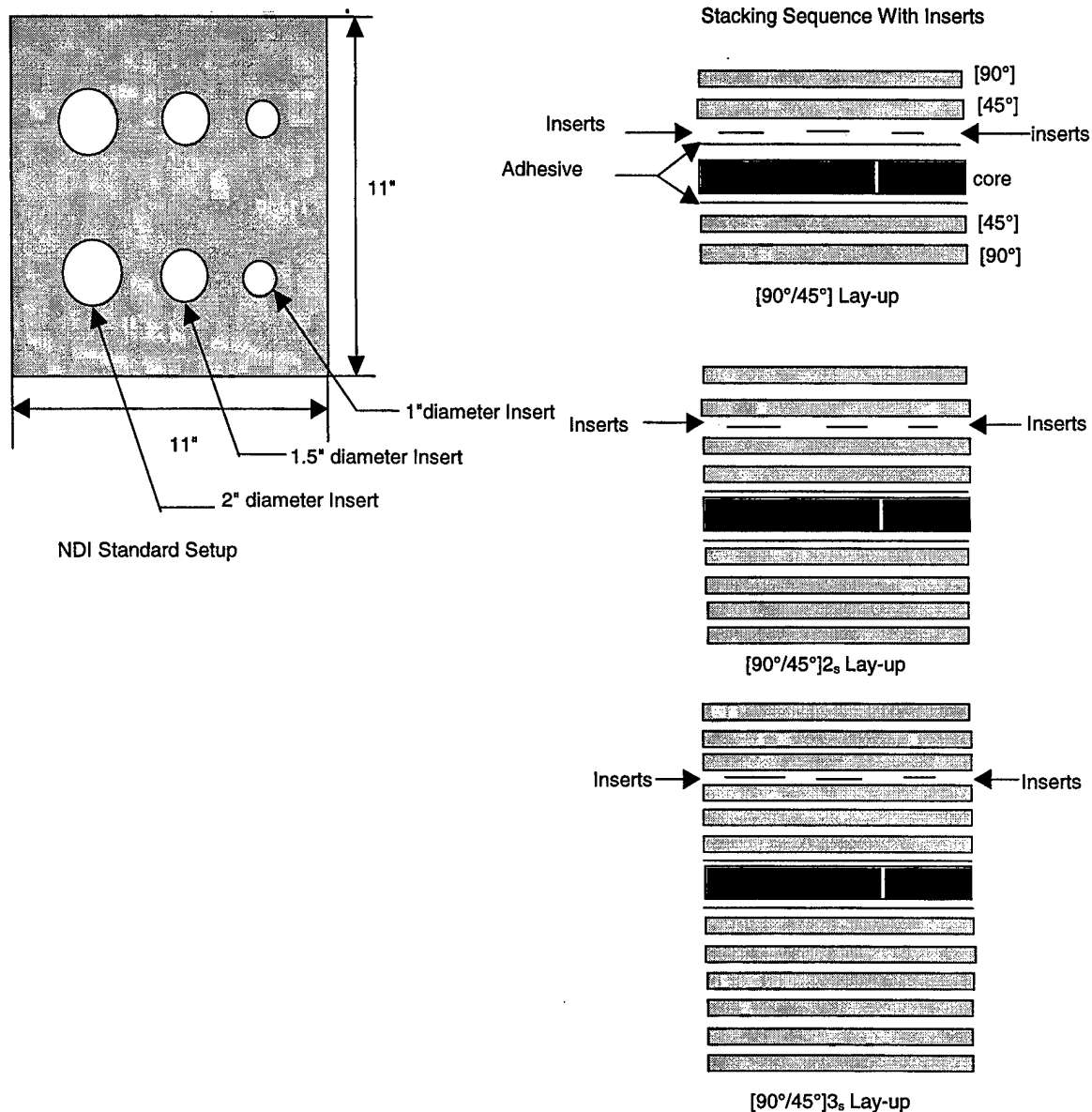


FIGURE 35. LAYOUT FOR ARTIFICIAL FLAWS IN CALIBRATION PANELS

5.1.2 Calibration Standard Development For Sandwich Panels.

The calibration data for sandwich panels was generated using sandwich panels that contained artificial flaws, which were Teflon (0.0025" thick) inserts added during the lay-up process. The Teflon inserts were circular in geometry and of known diameters. The test matrix under investigation has three different skin configurations and two different core thicknesses, thus a total of six calibration standards were developed. The lay-up sequence for standards, insert sizes, and the location of inserts for different lay-up sequence is illustrated in figure 35.

The calibration panel was first subjected to the C-scan process with an initial gain value, G_0 . The resulting C-scan image was then analyzed using the image analysis software using a range of grayscale threshold values, T_i . The geometric property, e.g., area, was recorded for each value of T_i . The threshold value was varied until the measured area exceeds $\pm 5\%$ of the actual area. The entire process was repeated for another value of gain, G . The process was repeated until a gain value was obtained, for which a wide range of threshold values could be used without incurring an error greater than 5%. The typical calibration plot for a [90/45/CORE/45/90] sandwich panel with $\frac{3}{4}$ " thick core is shown in figure 36. It can be seen that as the gain increases, the range of threshold values that can be used while keeping the error within 5%, also increases. Thus, for this sandwich configuration, a gain of 83 db and a grayscale threshold value of 180 was used. However, another set of gain and threshold could also be used, once the calibration curves are generated.

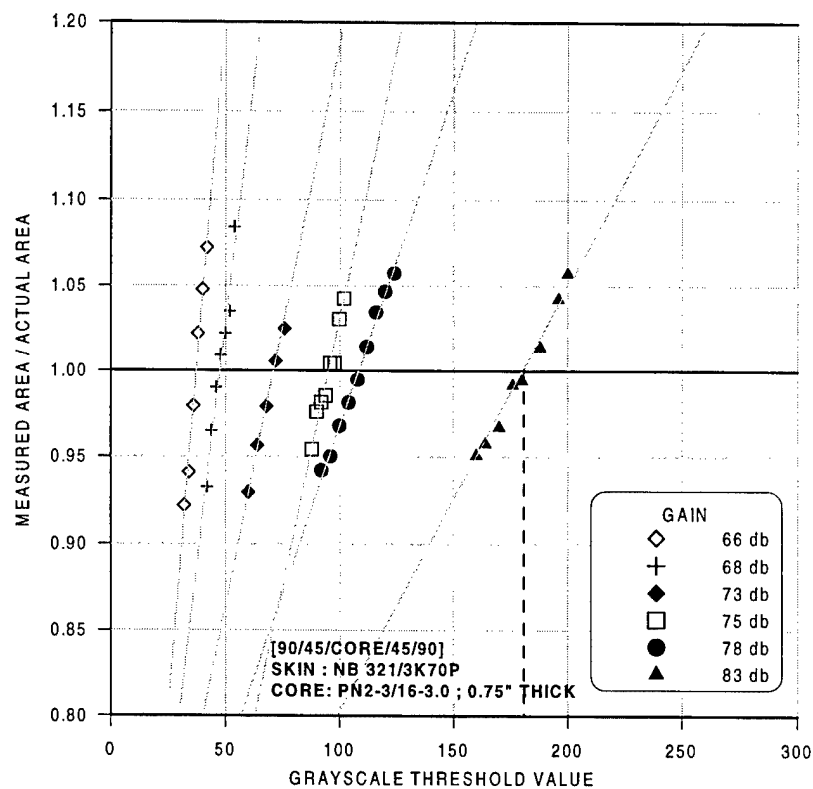


FIGURE 36. CALIBRATION PLOTS FOR [90/45/CORE/45/90] SANDWICH PANEL WITH $\frac{3}{4}$ " CORE

The calibration plots for the various sandwich configurations being investigated are shown in figures 37 through 41.

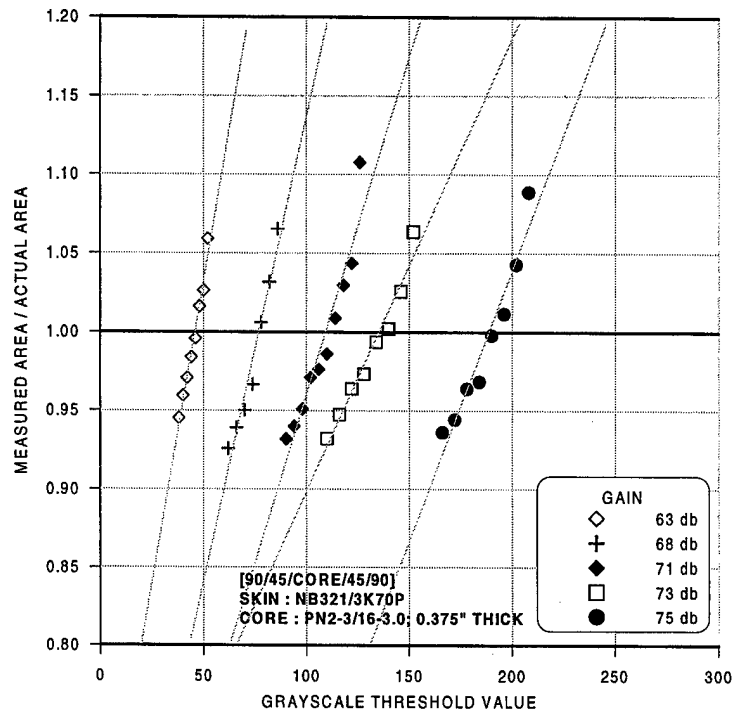


FIGURE 37. CALIBRATION PLOTS FOR [90/45/CORE/45/90] SANDWICH PANEL WITH 3/8" CORE

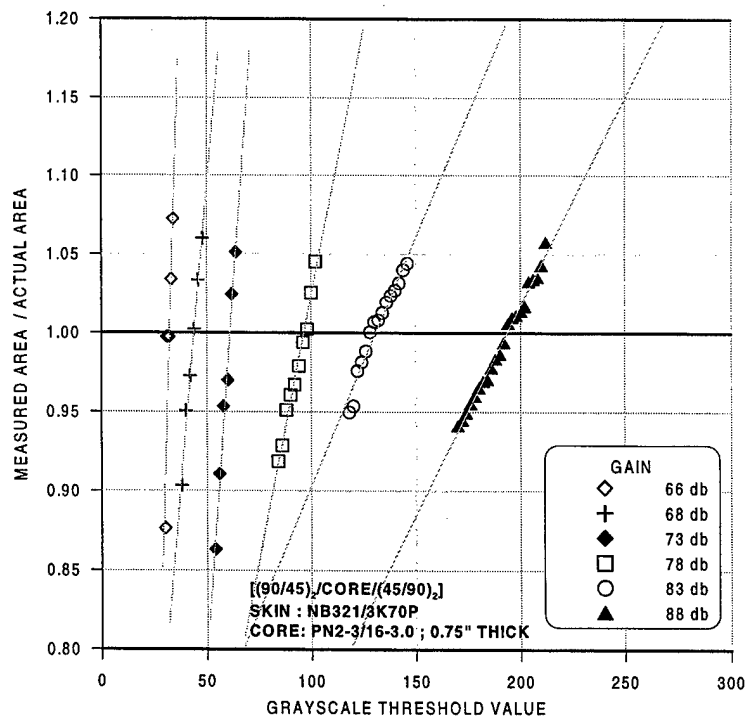


FIGURE 38. CALIBRATION PLOTS FOR [(90/45)₂/CORE/(45/90)₂] SANDWICH PANEL WITH 3/4" CORE

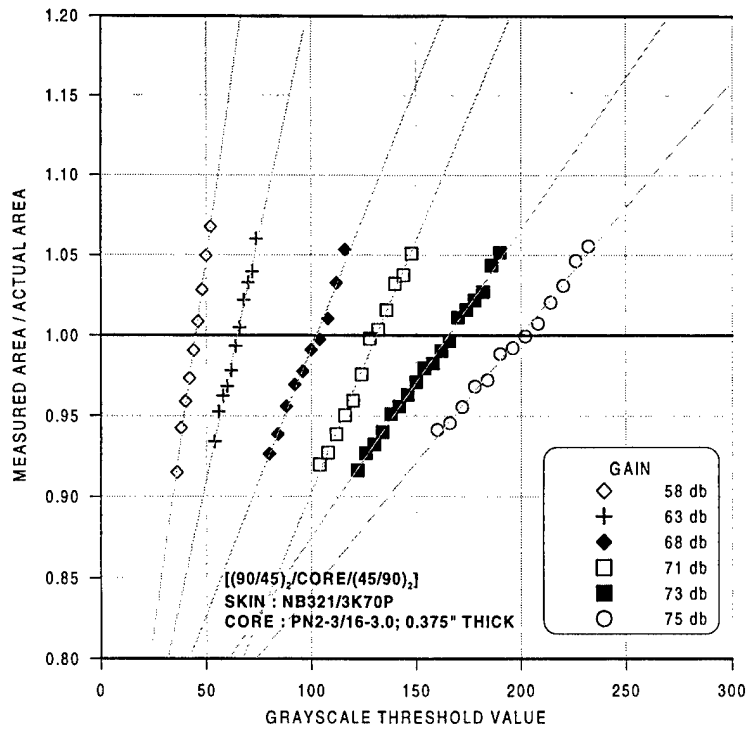


FIGURE 39. CALIBRATION PLOTS FOR [(90/45)₂/CORE/(45/90)₂] SANDWICH PANEL WITH 3/8" CORE

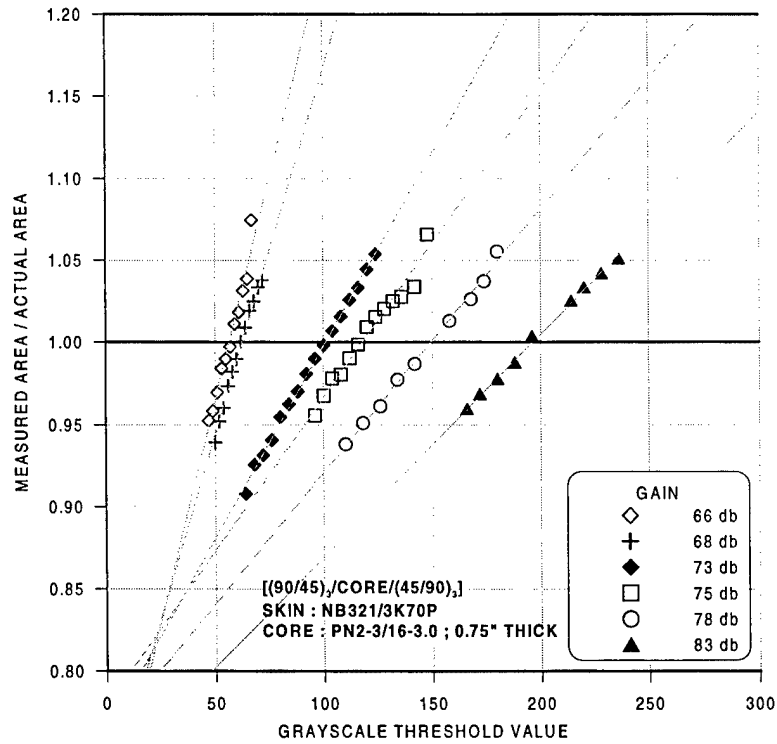


FIGURE 40. CALIBRATION PLOTS FOR [(90/45)₃/CORE/(45/90)₃] SANDWICH PANEL WITH 3/4" CORE

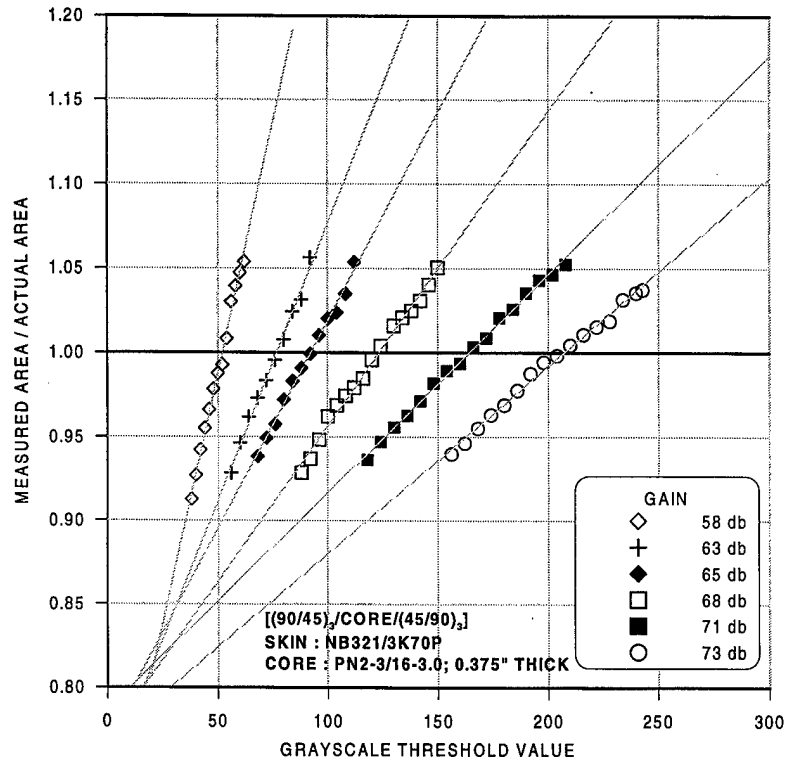


FIGURE 41. CALIBRATION PLOTS FOR $[(90/45)_3/\text{CORE}/(45/90)_3]$ SANDWICH PANEL WITH 3/8" CORE

5.2 IMPACT RESISTANCE CHARACTERIZATION BASED ON PLANAR DAMAGE AREA.

The impact damaged sandwich panels were subjected to NDE using the previously described calibration standards. The effects of the skin lay-up sequence (skin stiffness), core thickness (global stiffness), and impactor diameter were characterized using these results. The C-scan images of a sandwich panel impacted with a 1" diameter impactor and a 3" impactor are shown in figure 42. These panels were impacted at similar energy levels. It can be seen that the impact damage due to the larger* impactor size is larger than that of the smaller impactor which could indicate contrasting damage mechanisms associated with the different impactor diameters. The variation of planar damage area with impact energy for different sandwich configurations is plotted in figures 43 through 45. The C-scan images of the individual specimens are shown in appendix B. The planar damage area is significantly larger for panels that are more compliant in global bending and those which are impacted with the larger diameter impactor. This may be attributed to the impact load being distributed over a larger area for more compliant panels.

* Here, *larger* refers to 3.00" diameter impactor and *smaller* refers to 1.00" diameter impactor.

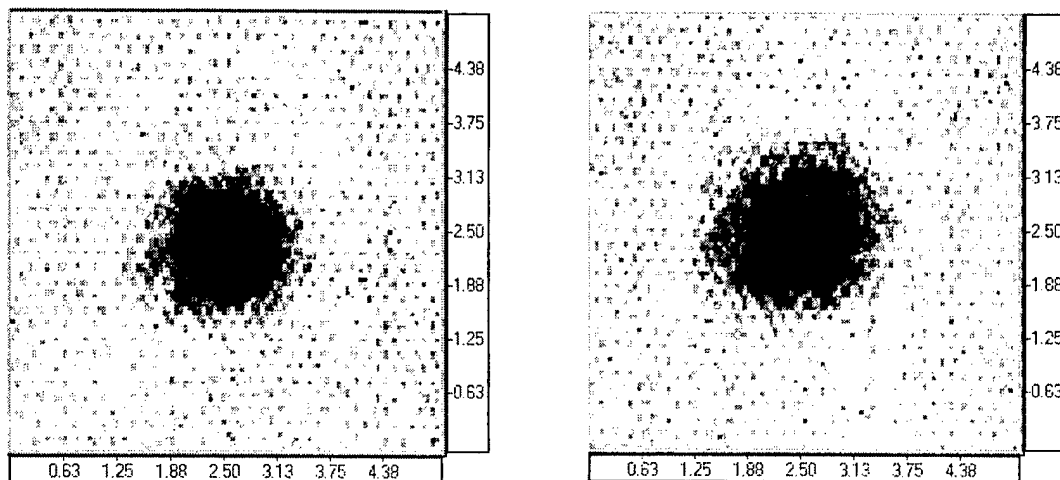


FIGURE 42. C-SCAN IMAGES OF DAMAGE IN SANDWICH PANELS IMPACTED WITH 1" AND 3" DIAMETER IMPACTORS

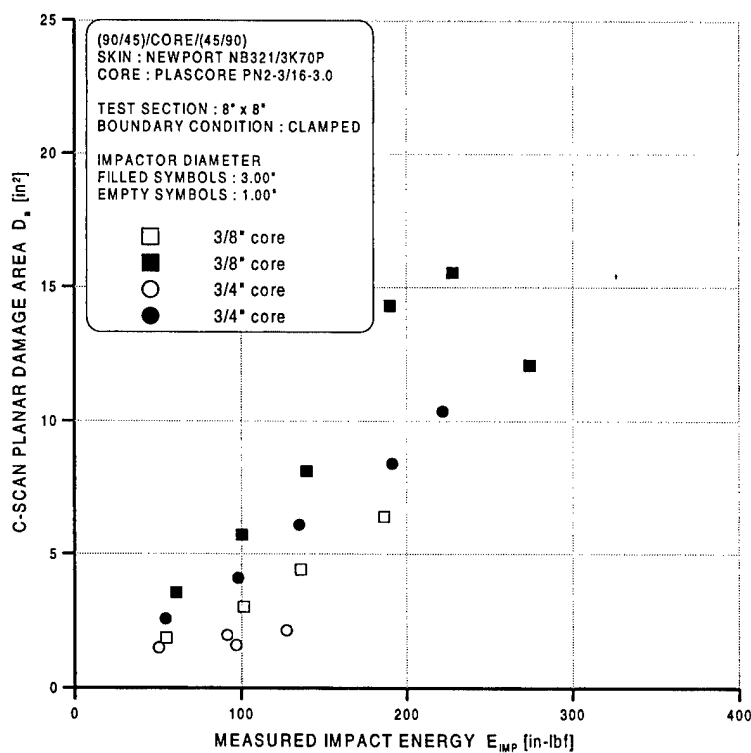


FIGURE 43. PLANAR DAMAGE AREA VS IMPACT ENERGY FOR [90/45/CORE/45/90] PANELS

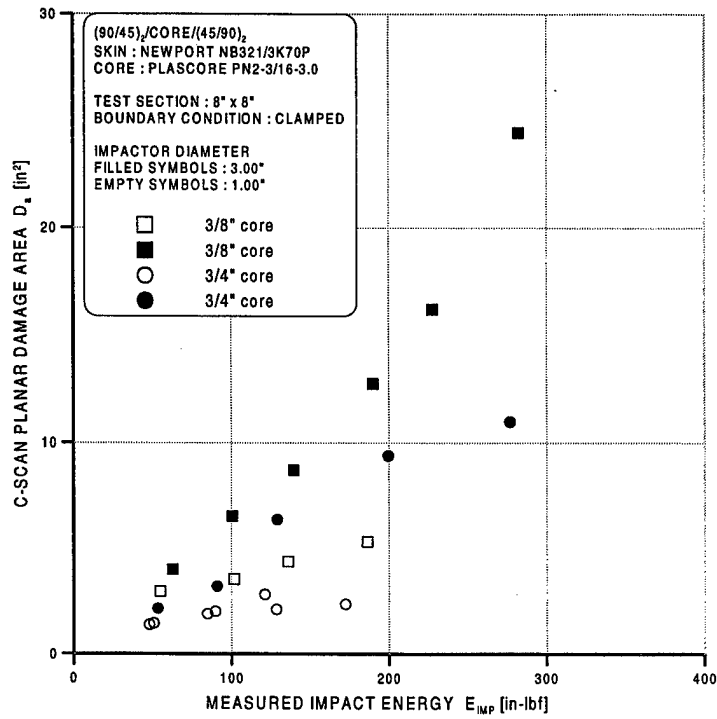


FIGURE 44. PLANAR DAMAGE AREA VS IMPACT ENERGY FOR [(90/45)₂/CORE/(45/90)₂] PANELS

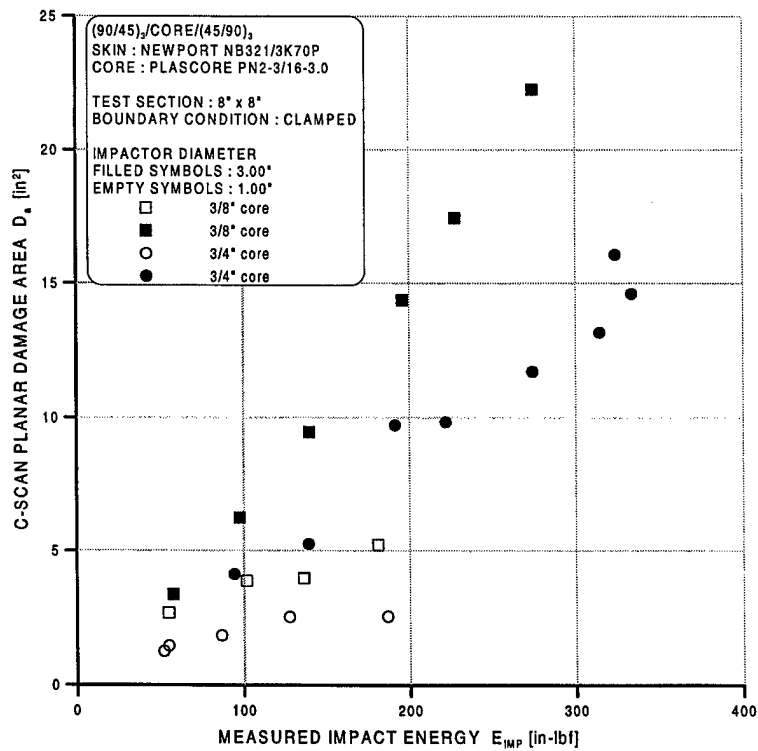


FIGURE 45. PLANAR DAMAGE AREA VS IMPACT ENERGY FOR [(90/45)₃/CORE/(45/90)₃] PANELS

5.3 RESIDUAL INDENTATION DISTRIBUTION.

The residual indentation in a sandwich panel will manifest itself as a geometric imperfection in the residual strength analysis. The stiffness degradation distribution in the core of the sandwich panel may be correlated* to the residual indentation distribution. The indentation studies in conjunction with residual strength properties will facilitate the validation of BVID criterion and also aid in the feasibility studies and potential development of a suitable visual inspection procedure.

The impact damaged sandwich panels, which were subjected to TTU C-scan, were inspected for residual indentation distribution in the vicinity of the impact point. The residual indentation depth was measured using a digital indicator. The digital indicator has a resolution of 0.0005" and a range of ± 1.0000 ". The indicator reading is recorded using a data acquisition program called APPSTAT. The indentation measurements are recorded over an area of 4.00"x 4.00" centered about the impact point, with a grid size of 0.2" in both directions. Figure 46 shows the setup of the residual indentation depth measurement. The residual indentation depth data for each specimen is stored in a spreadsheet to obtain the maximum depth of the indentation distribution on the surface. The surface plots of the indentation are generated using Golden Software's SURFER 32 computer graphing program. The surface plots for a typical impact damaged specimen is shown in figure 47a and 47b). The panels impacted with the larger impactor had a smaller maximum indentation depth but a larger indentation distribution area compared to the panels impacted with the smaller impactor. The variations of maximum indentation depth with impact energy for different sandwich configurations are shown in figures 48 through 50. The true nature of the damage underlying the indentation was revealed in the destructive testing which is described in later sections.

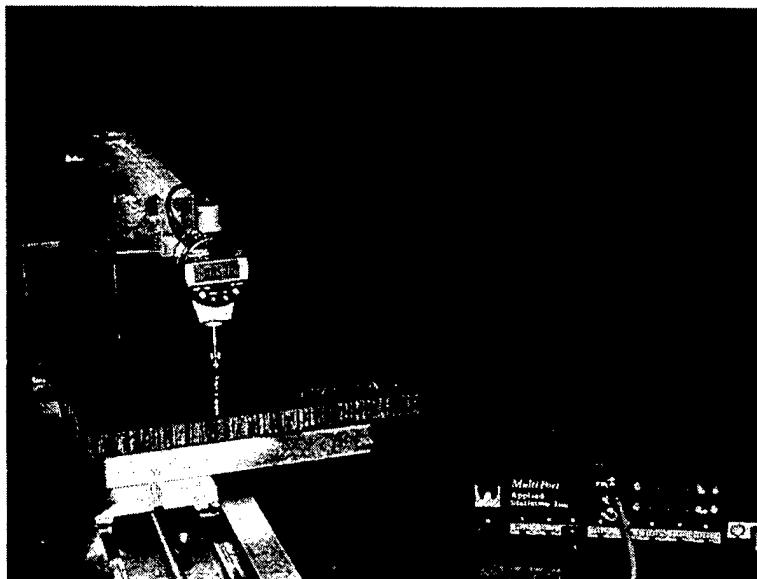


FIGURE 46. SETUP OF RESIDUAL INDENTATION DEPTH MEASUREMENT

* Indentation relaxation is currently being studied using static indentation tests.

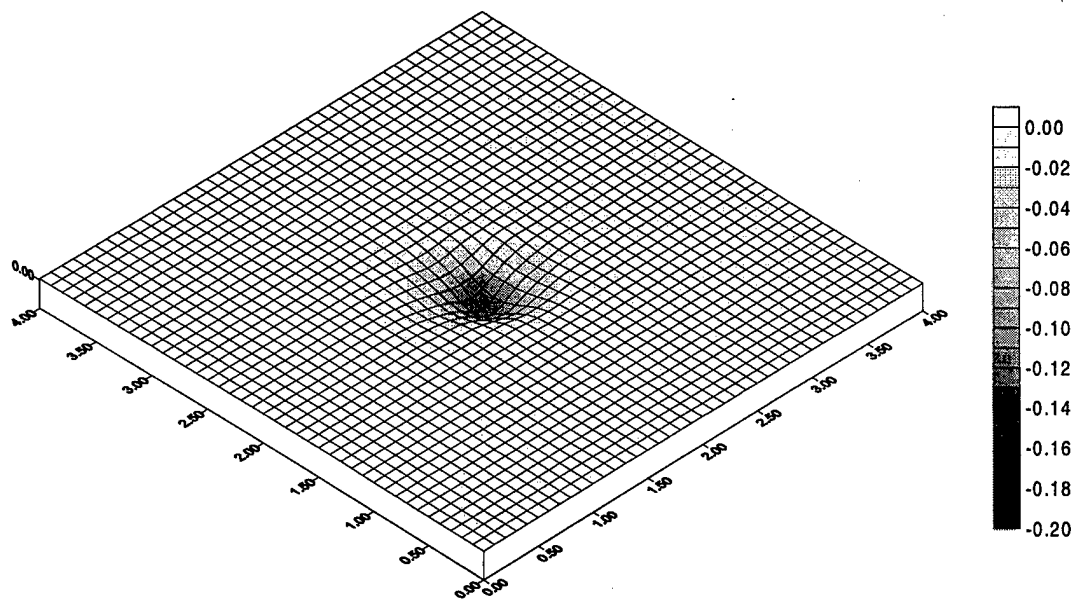


FIGURE 47a. RESIDUAL INDENTATION DISTRIBUTION IN A [90/45/CORE/45/90] SANDWICH PANEL WITH 3/8" THICK CORE, IMPACTED WITH 1.00" DIAMETER IMPACTOR

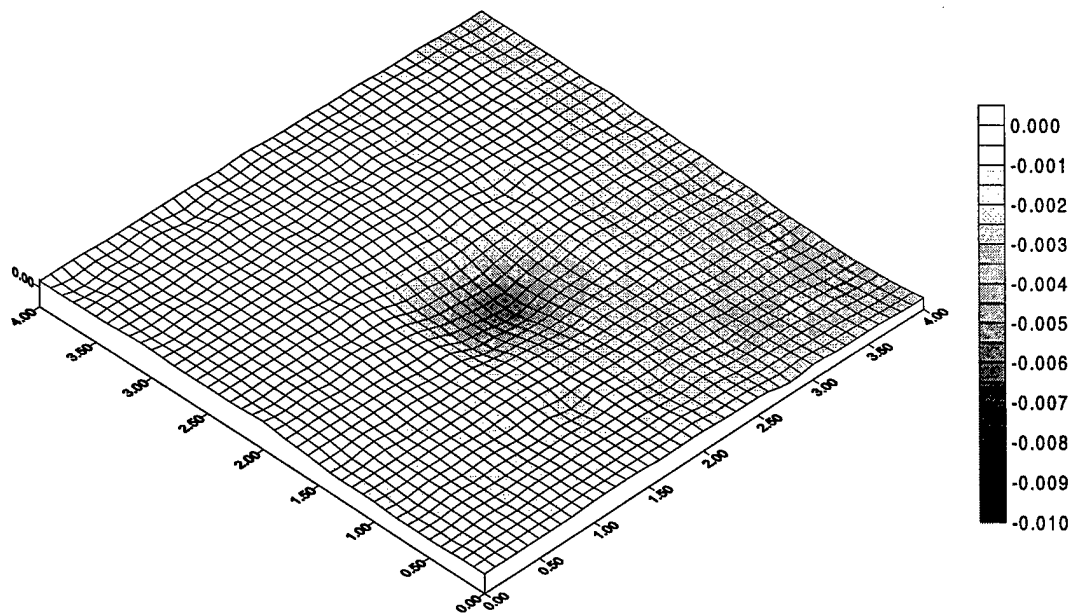


FIGURE 47b. RESIDUAL INDENTATION DISTRIBUTION IN A [90/45/CORE/45/90] SANDWICH PANEL WITH 3/8" THICK CORE, IMPACTED WITH 3.00" DIAMETER IMPACTOR

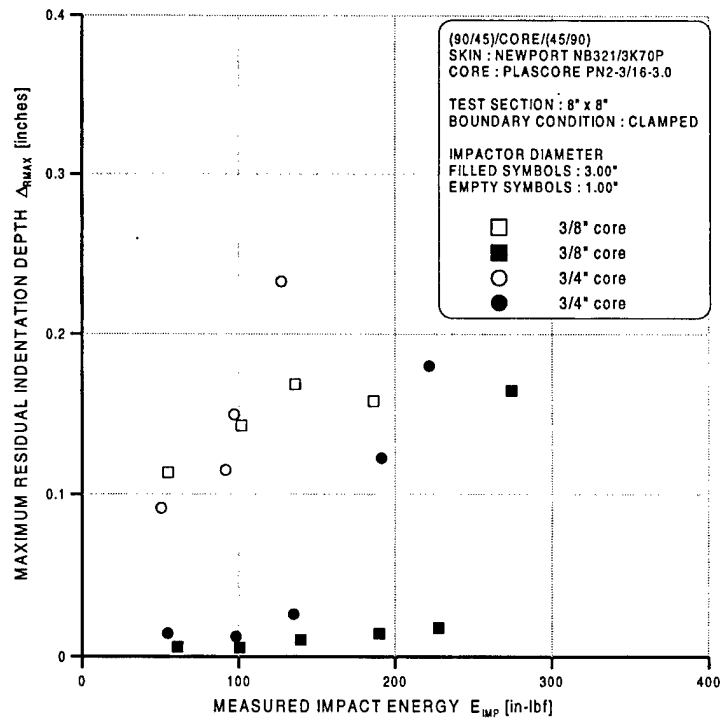


FIGURE 48. MAXIMUM RESIDUAL INDENTATION VS IMPACT ENERGY FOR [90/45/CORE/45/90] PANELS

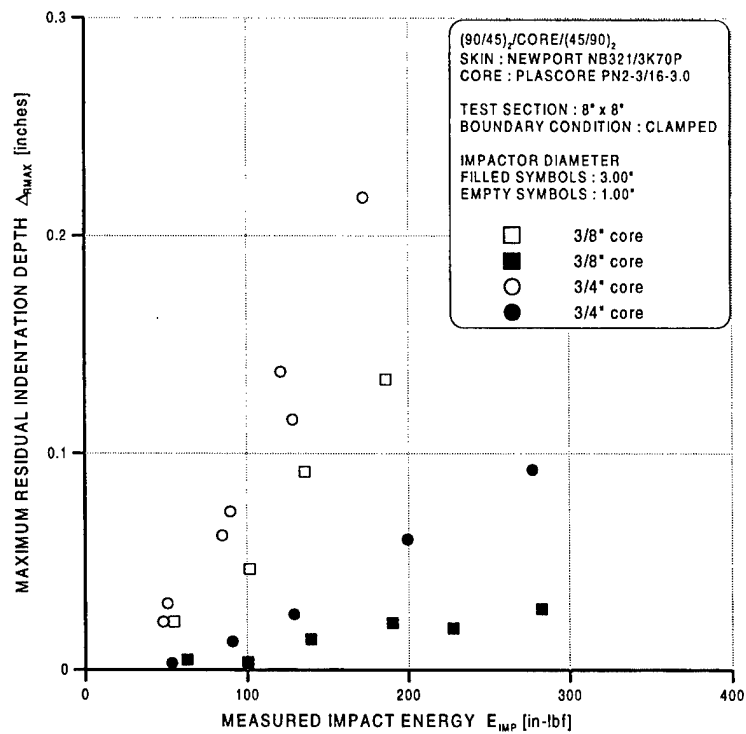


FIGURE 49. MAXIMUM RESIDUAL INDENTATION VS IMPACT ENERGY FOR [(90/45)₂/CORE/(45/90)₂] PANELS

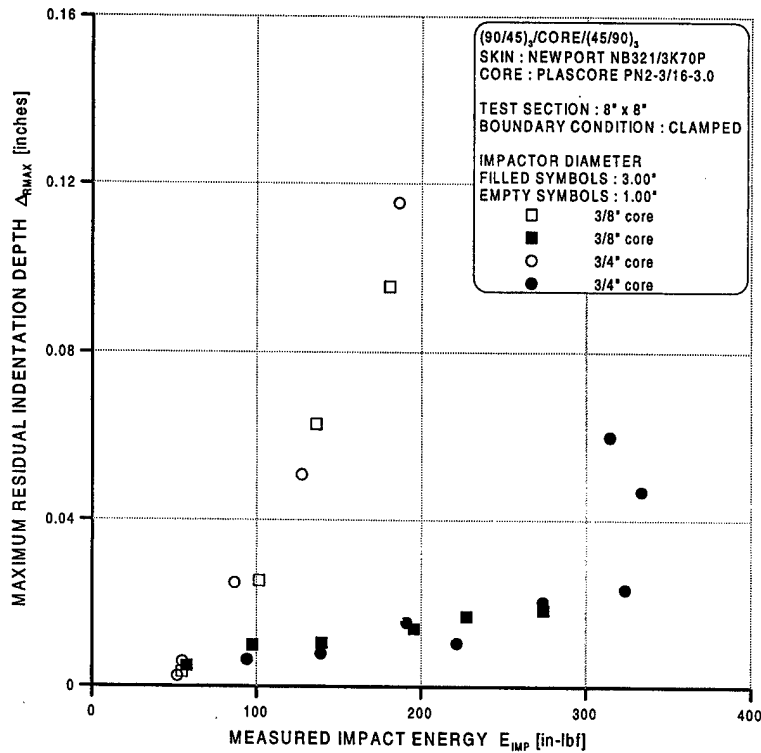


FIGURE 50. MAXIMUM RESIDUAL INDENTATION VS IMPACT ENERGY FOR [(90/45)₃/CORE/(45/90)₃] PANELS

5.4 VISUAL INSPECTION OF DAMAGE IN SANDWICH PANELS.

Visual inspection is a common NDI method used by many commercial and military aviation industries. It is one of the simplest and fastest NDI methods used to detect damage. It is used as a preamble to the more involved (and expensive) NDI methods, identifying regions containing possible damage(s) or flaws, thereby eliminating the detailed NDI of the entire structure. This common NDI method relies on the capability of the human eye and is subjective in nature. However, this method has had limited success in detecting damage in sandwich structures where the subsurface damage is prevalent with little or no residual indentation. Thus, a typical visual inspection procedure was tested against the NDI data and its limitations were identified.

In this study, a typical visual inspection protocol was developed and used for qualitative assessment of damage in the sandwich specimens. The protocol consisted of a rating scale of 0 to 10, with the most severe damage corresponding to a rating of 10. The scale was defined based on the typical surface damage observed in the sandwich panels. Table 2 shows the visual inspection ranking scale used in the current investigation.

The impacted sandwich specimens were inspected and ranked using the guidelines in table 2 by a group of individuals proficient in the area of composites. The average value of the rankings by different individuals was then used for comparison and analysis.

TABLE 2. VISUAL INSPECTION RANKING

Visual Inspection Ranking (scale 0-10)	
Scale	Scale Description
0 1	No visible surface damage of any kind
2 3	Slight to moderate surface depression on the order of the facesheet thickness. Minor facesheet crazing and/or roughness.
4 5 6	Easily visible surface indentation. Formation of localized matrix cracks and/or fiber breakage.
7 8	Maximum indentation exceeding facesheet thickness. Widespread matrix cracks and/or fiber breakage throughout the impact region. Evidence of core crushing.
9 10	Upper facesheet penetration. Dent depth a significant fraction of the overall panel thickness. Indentor outline clearly visible. Significant facesheet fracture and crushing throughout the impact zone. Significant core crushing.

The severity of damage as indicated by the visual inspection was compared with the TTU C-scan planar damage area. The plots correlating the two for different sandwich configurations are shown in figures 51 through 53. A damage detection threshold was arbitrarily defined for a visual ranking between 2 and 3. The results show that the visual inspection method is capable of detecting damage states due to the small impactor (smaller objects in general), which causes a very localized damage accompanied by indentation. However, the damage states due to the large impactor, which had no skin failure and very little or no indentation, may be difficult to discern using visual inspection as indicated by the results. Thus, large subsurface damage areas may never be discovered in service. The potential growth of such damage, assuming it can occur without becoming visible, poses a serious safety threat that must be understood.

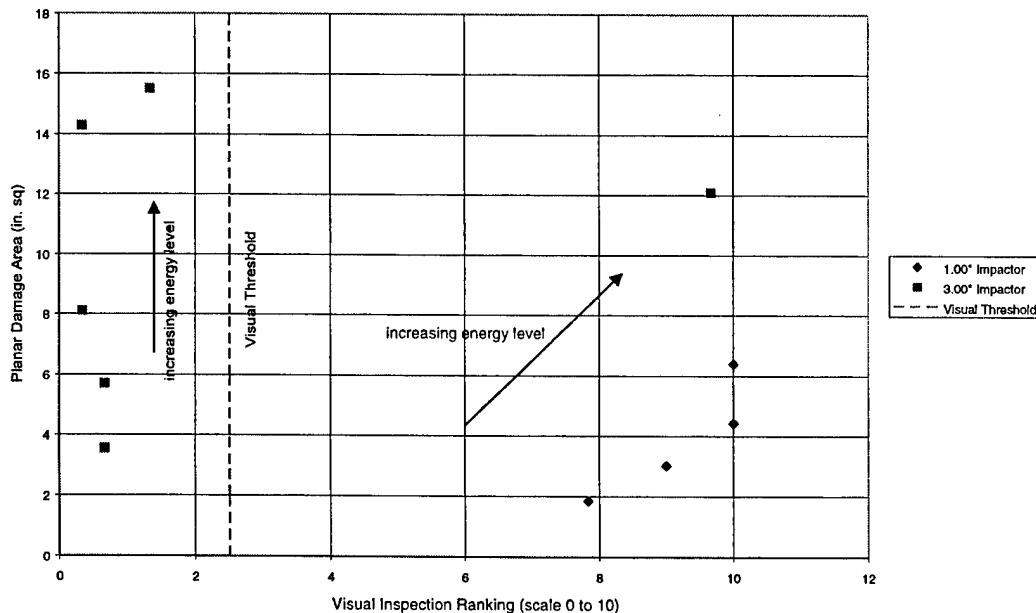


FIGURE 51. VISUAL INSPECTION RANKING VS PLANAR DAMAGE AREA FOR [90/45/CORE/45/90] PANELS WITH 3/8" THICK CORE

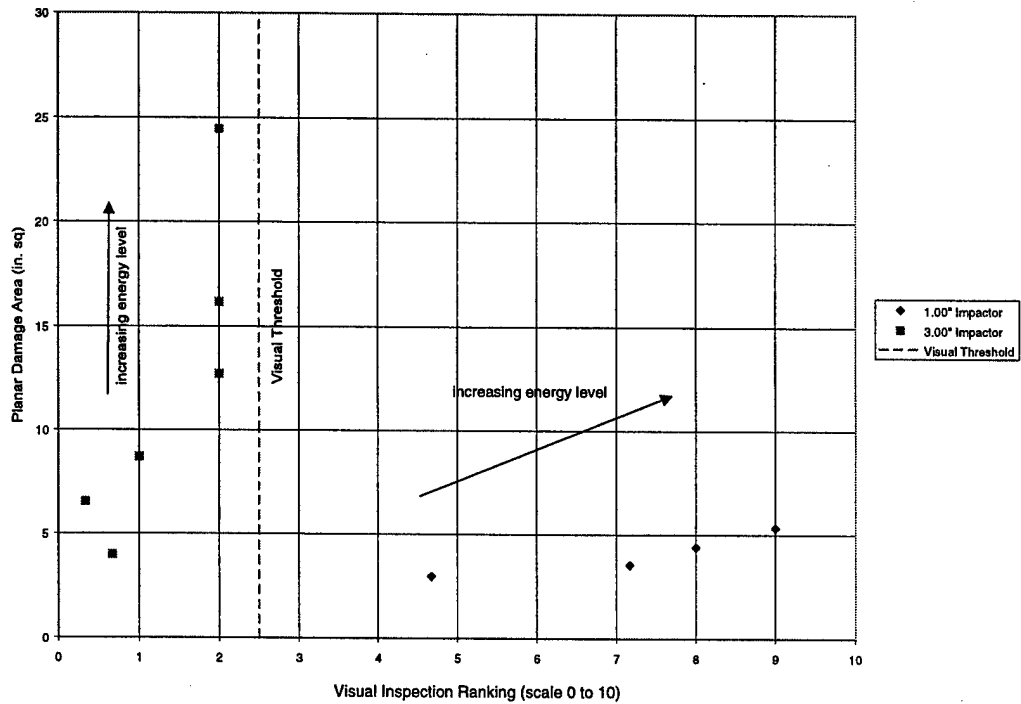


FIGURE 52. VISUAL INSPECTION RANKING VS PLANAR DAMAGE AREA FOR [(90/45)₂/CORE/(45/90)₂] PANELS WITH 3/8" THICK CORE

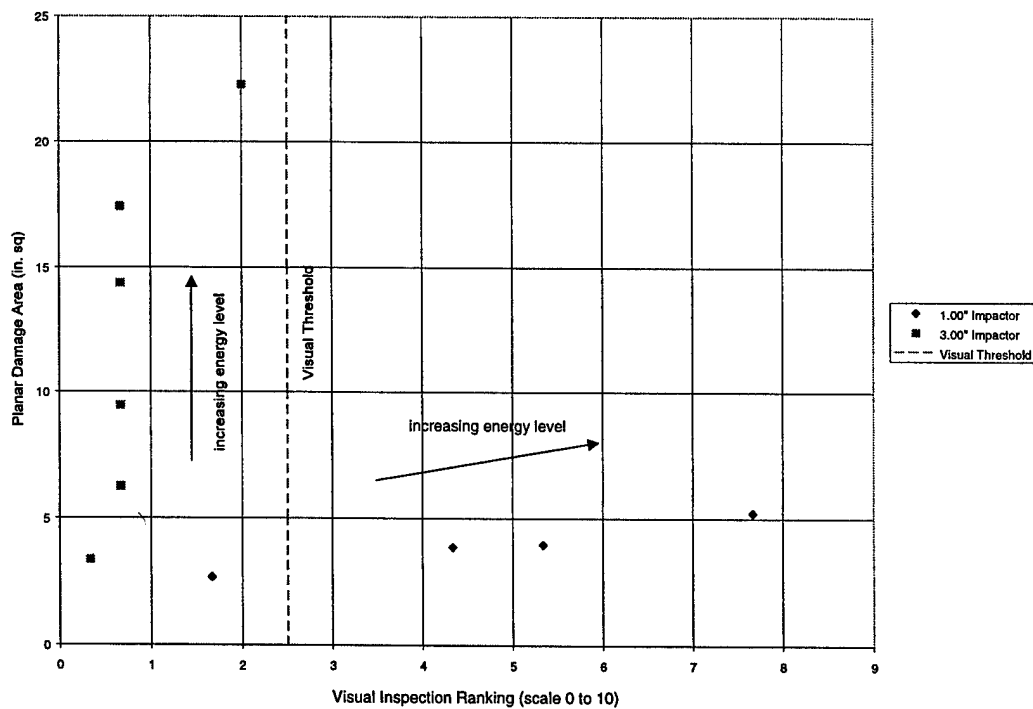


FIGURE 53. VISUAL INSPECTION RANKING VS PLANAR DAMAGE AREA FOR [(90/45)₃/CORE/(45/90)₃] PANELS WITH 3/8" THICK CORE

In addition to visual inspection, other “field type” NDI inspections techniques may also be available to characterize damage in sandwich structures. One commonly used and inexpensive technique in these “field” applications is the tap test. In the future phases of this program, the “laboratory” NDI inspection techniques will be correlated with applicable “field” related techniques.

The other damage metric that is more closely associated with the visual inspection is the residual indentation depth/distribution. The current practices define the BVID threshold as an indentation depth of 0.05". In the current investigation, a BVID threshold of 0.02" was chosen and the visual inspection rankings were compared with the indentation depth measurements for the sandwich specimens. The visual inspection rankings are plotted against the maximum residual indentation depth for different sandwich configurations, in figures 54 to 56. It is seen from these plots that the damage due to the large impactors often falls well below the BVID and visual inspection thresholds and may never be visually detected in service. Thus, it is once again seen that the visual inspection methods are better suited for damage states which are conspicuous on the surface and are accompanied by indentation depths that can be readily seen by the naked eye.

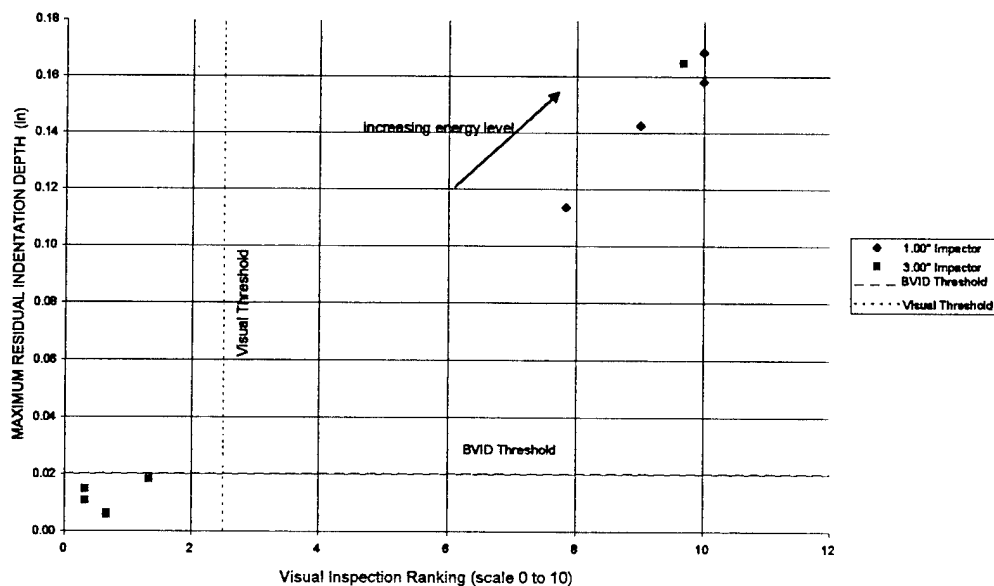


FIGURE 54. VISUAL INSPECTION RANKING VS MAXIMUM INDENTATION DEPTH FOR [90/45/CORE/45/90] PANELS WITH 3/8" THICK CORE

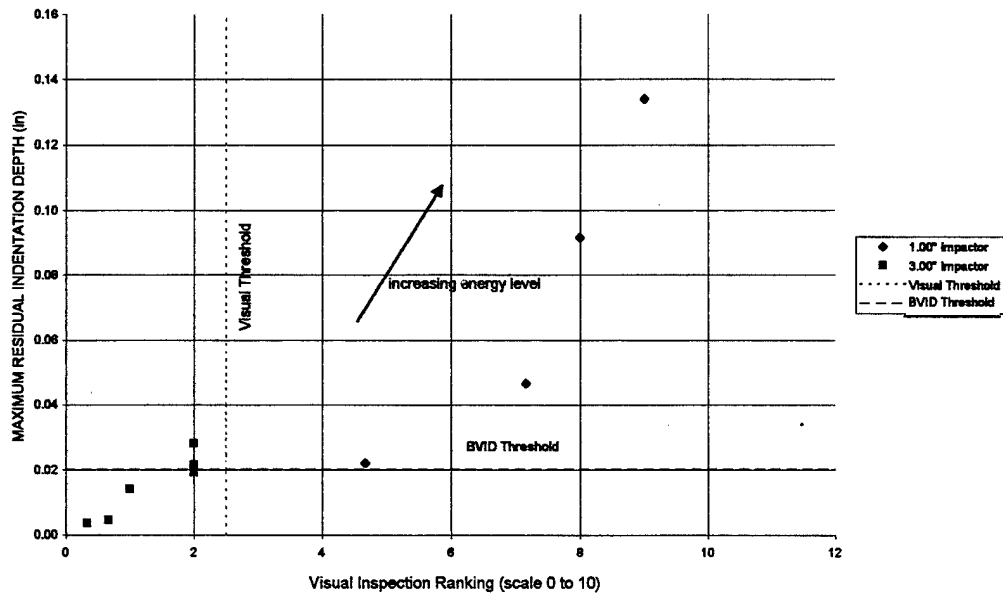


FIGURE 55. VISUAL INSPECTION RANKING VS MAXIMUM INDENTATION DEPTH FOR [(90/45)₂/CORE/(45/90)₂] PANELS WITH 3/8" THICK CORE

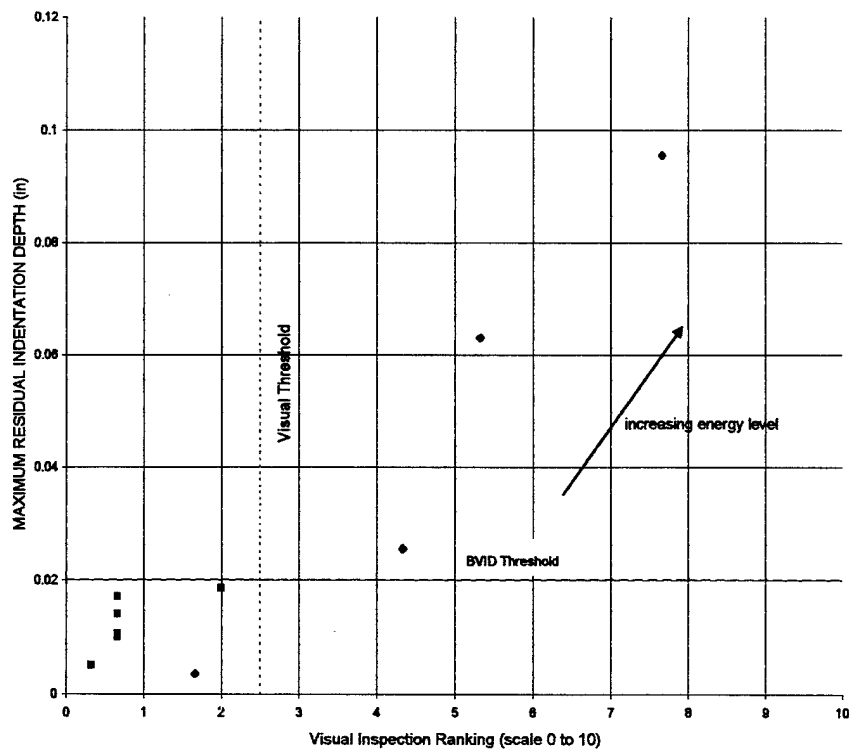


FIGURE 56. VISUAL INSPECTION RANKING VS MAXIMUM INDENTATION DEPTH FOR [(90/45)₃/CORE/(45/90)₃] PANELS WITH 3/8" THICK CORE

5.5 DESTRUCTIVE EVALUATION OF DAMAGE IN IMPACTED SANDWICH PANELS.

The damage metrics obtained using NDI methods do not explicitly give an indication of the failure mode(s) prevailing in the damaged region. The damage morphology can be studied using destructive testing. The destructive inspection* consisted of slicing or sectioning of the specimen along a plane passing through the damaged region. Visual inspection of the cross-section can observe the damage modes in the core and gross fiber/matrix fractures in the skins.

In this investigation, all configurations of sandwich panels were impacted with selected energy levels with the two different impactor sizes under study. Table 3 shows the test plan for destructive testing.

TABLE 3. TEST PLAN FOR DESTRUCTIVE TESTING

LAY-UP CONFIGURATION	IMPACT	ENERGY	LEVEL (in-lbf)	CORE SIZE	IMPACTOR DIAMETER	NUMBER OF SPECIMEN
	1	2	3			
[0°/90°/±45°]S (2 plies)	59		183.6	3/8"	1.00"	2
	63.6	181.2	279		3.00"	3
	59		137	3/4"	1.00"	2
	63.6	136	224		3.00"	3
[0°/90°/±45°]2S (4 plies)	59		183.6	3/8"	1.00"	2
	63.6	181.2	279		3.00"	3
	59		183.6	3/4"	1.00"	2
	63.6	145	318		3.00"	3
[0°/90°/±45°]3S (6 plies)	59		183.6	3/8"	1.00"	2
	63.6	181.2	279		3.00"	3
	59		183.6	3/4"	1.00"	2
	98.4	180	320		3.00"	3

Impacted specimens were visually inspected for face sheet damage, and then sectioned across the width, along a line containing the impact location. The cross-sections were then cleaned of any core debris to better see the damaged region. Each sectioned specimen was then inspected for core damage (typically core crushing) and face sheet damage. The maximum width of core damage diameter was measured and compared with the average diameter of the damage area obtained from TTU C-scan.

The visually measured core damage diameter corresponded closely with the average diameter of the damage area obtained from the C-scan. This is a strong indication that the planar damage area obtained from C-scan is core damage region. This indicates that the dominant energy absorption mechanism during an impact event is core crushing. Skin fractures were predominant in sandwich panels impacted with the small impactor. Typical damage states in sandwich panels with 3/4" thick cores as seen by sectioning are shown in figures 57 through 62. The pictures containing the sectional views of the damaged region for the sandwich panels listed in table 3 are shown in appendix C. The effects of impactor diameter can be easily seen from these pictures. The damage modes due to the small impactor contains significant amounts of core crushing and skin failures, resulting in a clearly visible indentation distribution. However, the damage state due to the large impactor, which appeared benign when visually inspected, mainly consisted of a

* Microscopic visualization for interply damage in the skins is currently in progress.

larger core area without any skin damage, with negligible residual indentation. These contrasting damage modes may be attributed to the distinct contact load distributions associated with the two different impactor sizes.

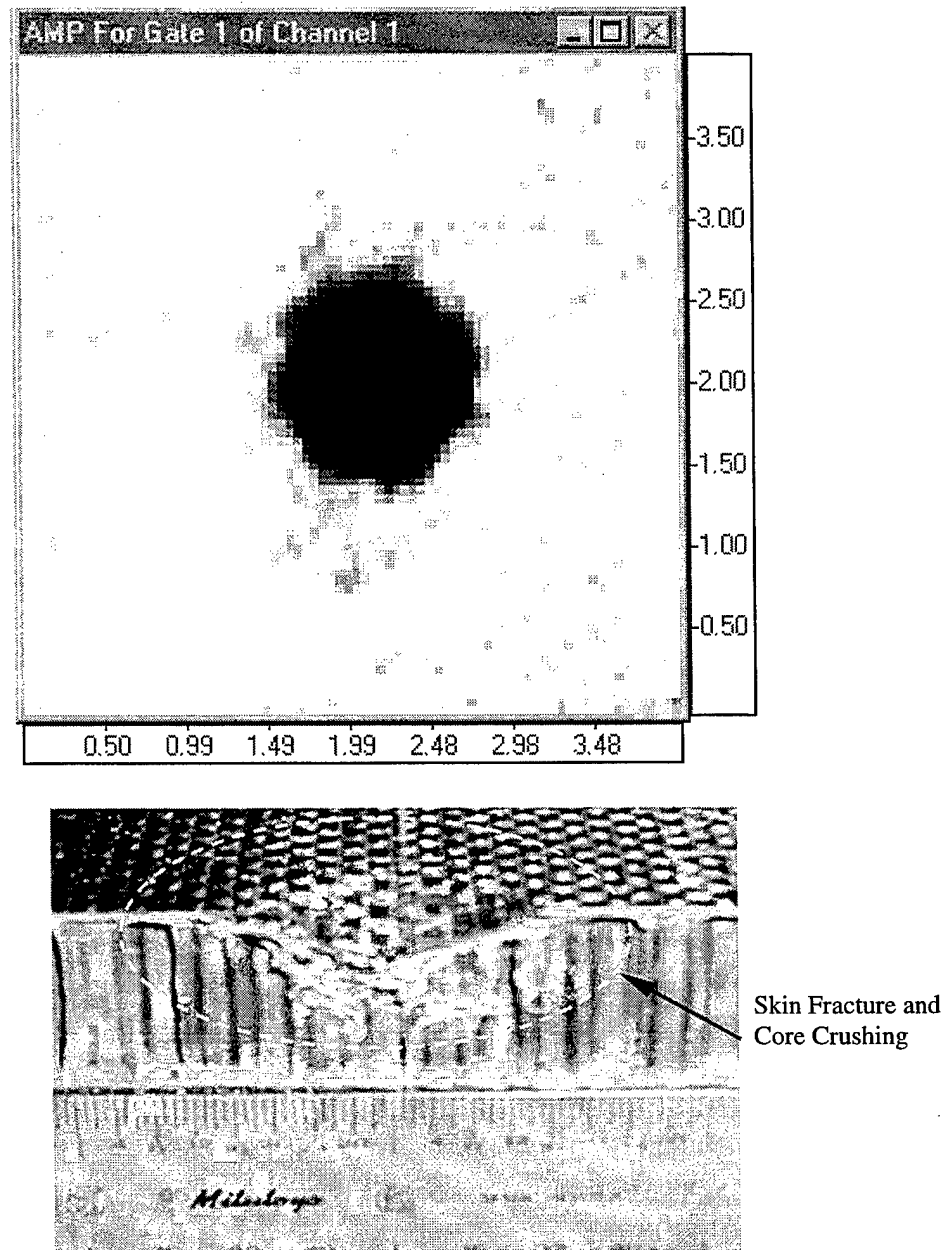


FIGURE 57. DAMAGED SECTION AND CORRESPONDING C-SCAN DAMAGE REGION FOR [90/45/CORE/45/90] PANEL, 3/4" THICK CORE, IMPACTED WITH 137 lbf-in ENERGY USING 1.00" DIAMETER IMPACTOR

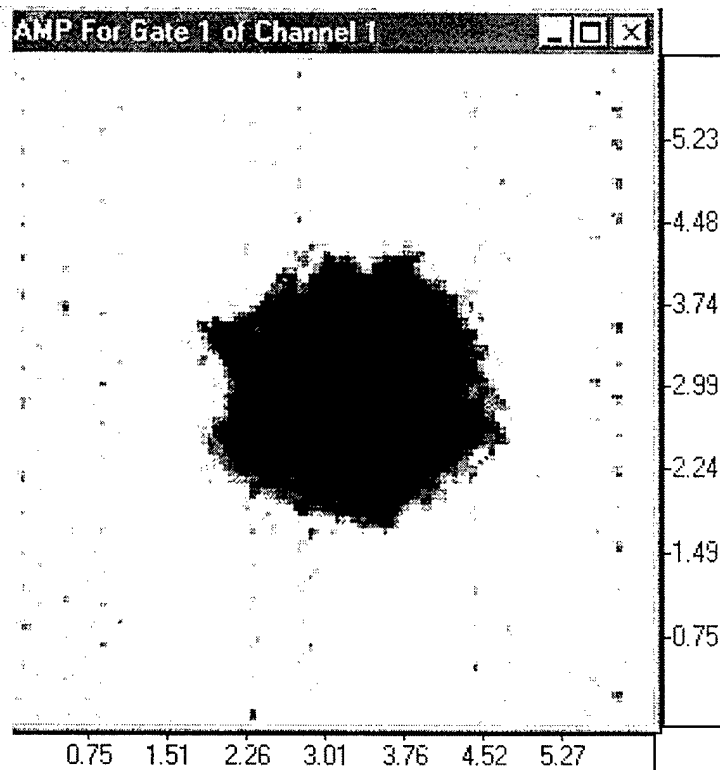
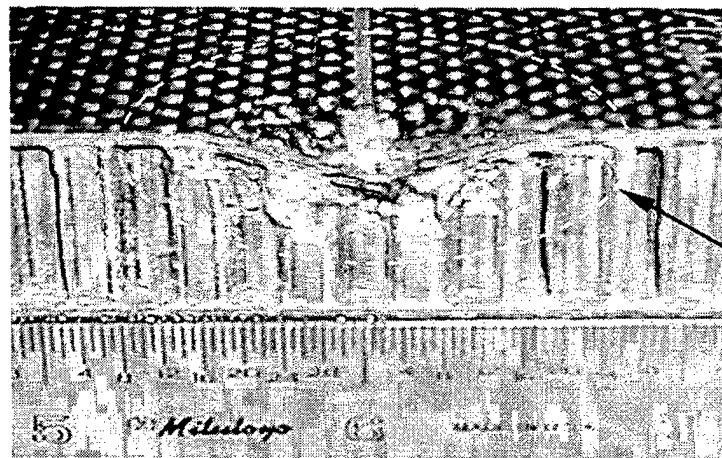
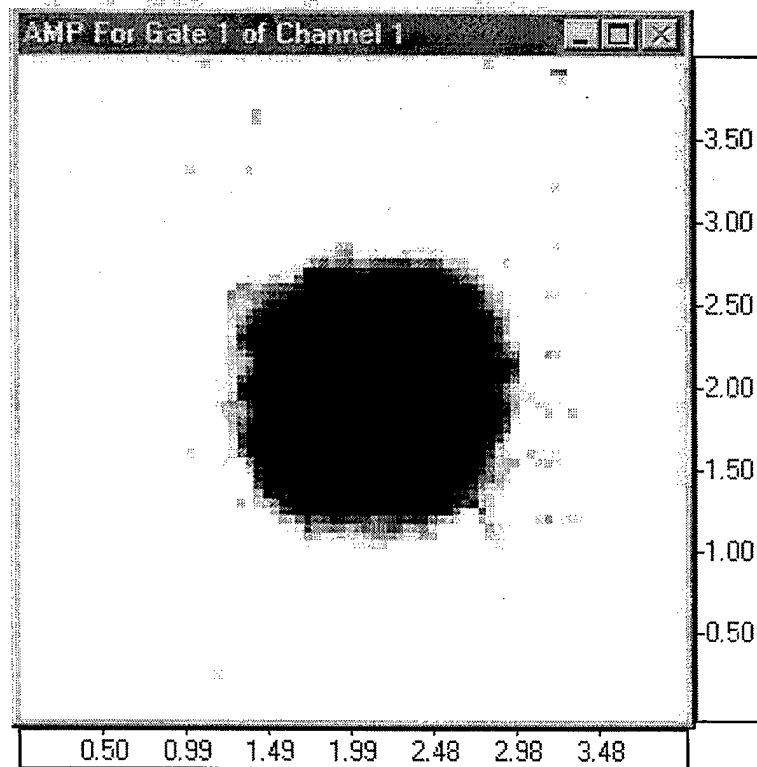


FIGURE 58. DAMAGED SECTION AND CORRESPONDING C-SCAN DAMAGE REGION FOR [90/45/CORE/45/90] PANEL, 3/4" THICK CORE, IMPACTED WITH 136 lbf-in ENERGY USING 3.00" DIAMETER IMPACTOR



Skin Fracture and
Core Crushing

FIGURE 59. DAMAGED SECTION AND CORRESPONDING C-SCAN DAMAGE REGION FOR $[(90/45)_2/\text{CORE}/(45/90)_2]$ PANEL, $3/4$ " THICK CORE, IMPACTED WITH 183 lbf-in ENERGY USING 1.00" DIAMETER IMPACTOR

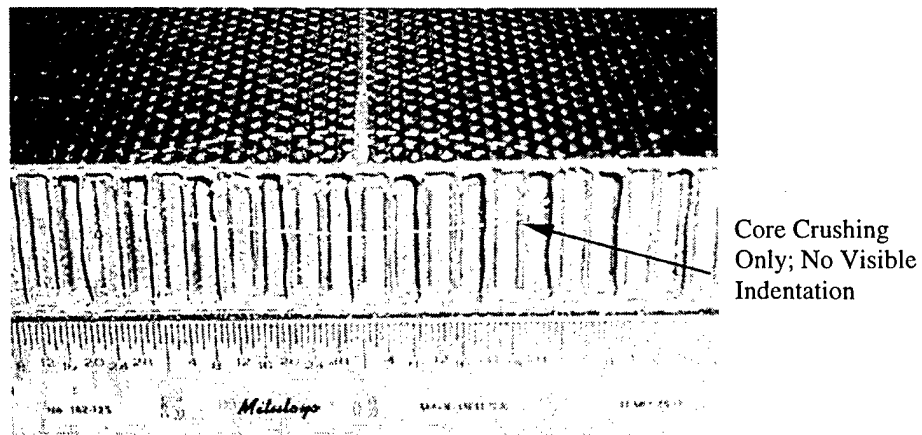
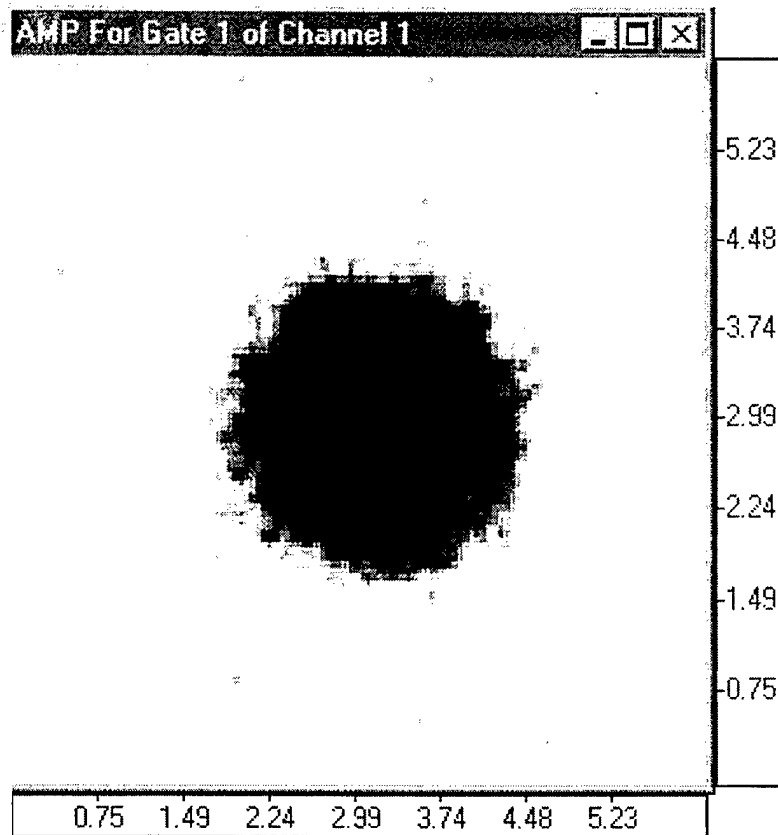


FIGURE 60. DAMAGED SECTION AND CORRESPONDING C-SCAN DAMAGE REGION FOR $[(90/45)_2/\text{CORE}/(45/90)_2]$ PANEL, $3/4$ " THICK CORE, IMPACTED WITH 145 lbf-in ENERGY USING AN 3.00" DIAMETER IMPACTOR

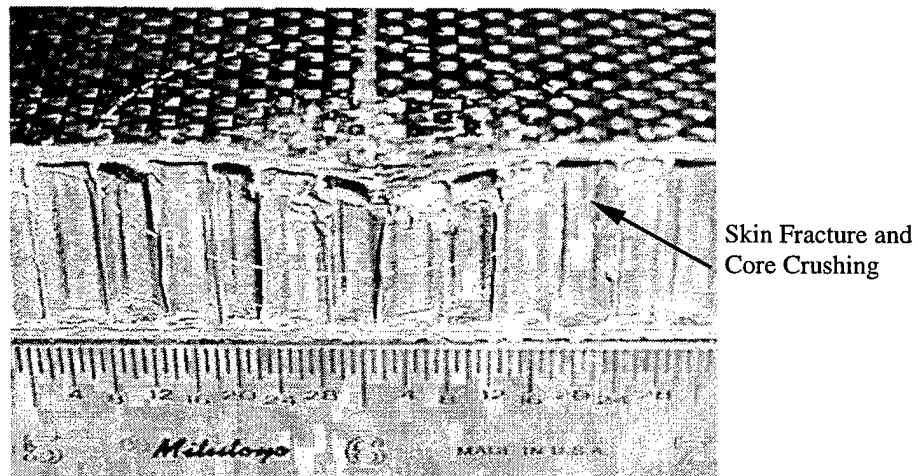
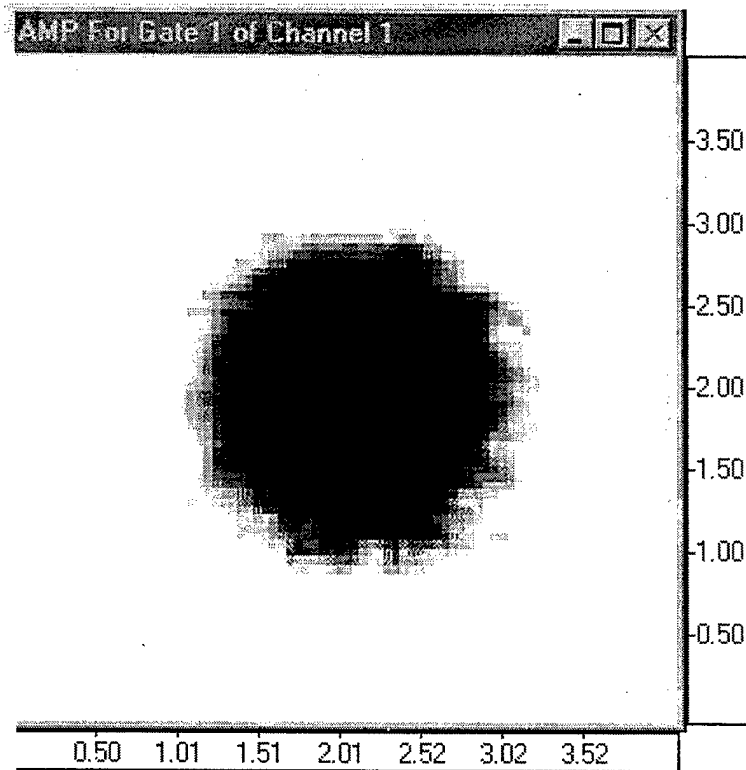


FIGURE 61. DAMAGED SECTION AND CORRESPONDING C-SCAN DAMAGE REGION FOR $[(90/45)_3/\text{CORE}/(45/90)_3]$ PANEL, $3/4$ " THICK CORE, IMPACTED WITH 183 lbf-in ENERGY USING AN 1.00" DIAMETER IMPACTOR

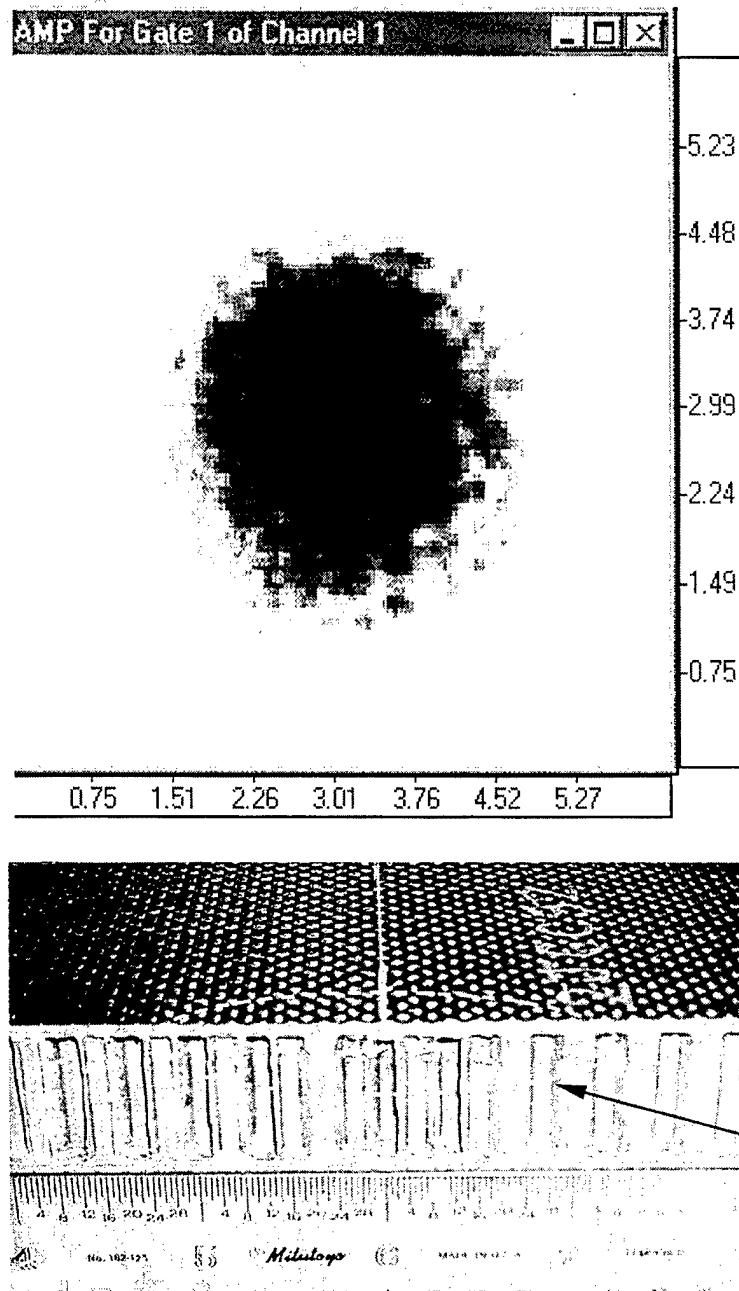


FIGURE 62. DAMAGED SECTION AND CORRESPONDING C-SCAN DAMAGE REGION FOR $[(90/45)_3/\text{CORE}/(45/90)_3]$ PANEL, $3/4$ " THICK CORE, IMPACTED WITH 183 lbf-in ENERGY USING AN 3.00" DIAMETER IMPACTOR

The descriptive summary of damage states in the sandwich specimens used for destructive inspection is given in tables 4 and 5. The tables also contain the visual inspection ratings associated with these specimens before they were sectioned. The tables show that the visual inspection correlates quite well with indention depth but is unable to assess damage area.

TABLE 4. SUMMARY RESULTS OF DESTRUCTIVE TESTING FOR 3/8" CORE PANELS

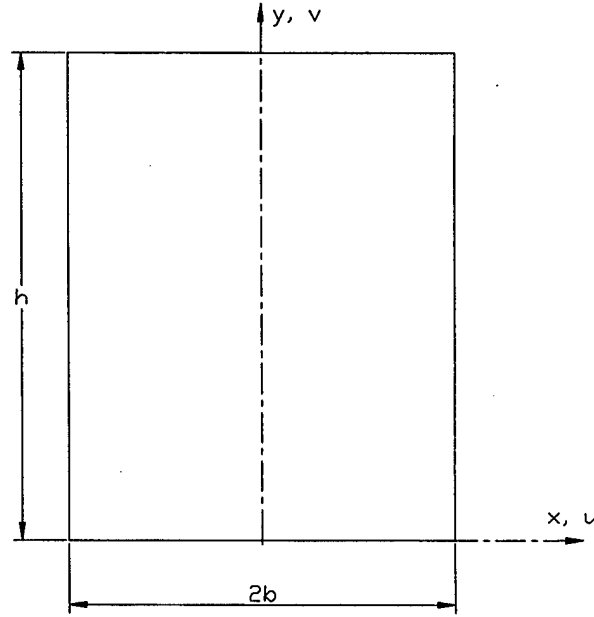
Lay-Up Sequence	Impact Energy (in-lbf)	Impactor Size (in)	Impact Damage Characteristics Morphology	Damage Metrics		
				(square in)	(in)	(scale 0-10)
				Damage Area	Indentation Depth	Visual
[0°/90°/±45°] _s (2 Plies)	59	1.00"	<ul style="list-style-type: none"> complete facesheet penetration fiber breakage/delamination/matrix cracks localized core crushing underneath facesheet 	1.4839	0.1135	7.8
	183.6		<ul style="list-style-type: none"> complete facesheet penetration fiber breakage/delamination/matrix cracks localized core crushing underneath facesheet 	5.2753	0.1580	10.0
	63.6	3.00"	• core crush region underneath the facesheet	2.1445	0.0060	0.7
	181.2		• core crush region increases underneath the facesheet	10.3633	0.0145	0.3
	279		• core crush region increases underneath the facesheet	13.7032	0.1645	9.7
[0°/90°/±45°] _{2s} (4 Plies)	59	1.00"	• core crushing underneath facesheet	1.6158	0.0220	4.7
	183.6		<ul style="list-style-type: none"> complete penetration of facesheet fiber breakage/delamination/matrix cracks localized core crushing underneath facesheet 	4.4249	0.1340	9.0
	63.6	3.00"	• core crush region underneath the facesheet	2.0928	0.0045	0.7
	181.2		<ul style="list-style-type: none"> matrix cracks/delamination core crush region underneath the facesheet 	7.7116	0.0215	2.0
	279		<ul style="list-style-type: none"> fiber breakage/delamination/matrix cracks extensive core crushing region underneath the facesheet 	17.8760	0.0280	2.0
[0°/90°/±45°] _{3s} (6 Plies)	59	1.00"	• core crushing underneath facesheet	2.4738	0.0035	1.7
	183.6		<ul style="list-style-type: none"> fiber breakage/delamination/matrix cracks localized core crushing underneath facesheet 	4.0552	0.0955	7.7
	63.6	3.00"	• core crush region underneath the facesheet	3.9981	0.0050	0.3
	181.2		• core crush region increases underneath the facesheet	13.3707	0.0140	0.7
	279		<ul style="list-style-type: none"> fiber breakage/delamination/matrix cracks extensive core crush region underneath facesheet 	21.3599	0.0185	2.0

TABLE 5. SUMMARY RESULTS OF DESTRUCTIVE TESTING FOR 3/4" CORE PANELS

Lay-Up Sequence	Impact Energy (in-lbf)	Impactor Size (in)	Impact Damage Characteristics Morphology	Damage Metrics		
				(square in) Damage Area	(in) Indentation Depth	(scale 0-10) Visual
[0°/90°/±45°] _s (2 Plies)	59	1.00"	<ul style="list-style-type: none"> • fiber breakage/delamination/matrix cracks • localized core crushing underneath facesheet 	1.0713	0.0915	4.0
	137		<ul style="list-style-type: none"> • complete penetration of facesheet • fiber breakage/delamination/matrix cracks • localized core crushing underneath facesheet 	1.565	0.233	10.0
	63.6	3.00"	• core crush region underneath the facesheet	2.865	0.0145	0.0
	136		• core crush region increases underneath the facesheet	5.4931	0.0265	1.0
	224		• core crush region increases underneath the facesheet	8.5439	0.18	1.5
[0°/90°/±45°] _{2s} (4 Plies)	59	1.00"	<ul style="list-style-type: none"> • fiber breakage/delamination/matrix cracks • localized core crushing underneath facesheet 	1.2279	0.0305	2.0
	183.6		<ul style="list-style-type: none"> • complete penetration of facesheet • fiber breakage/delamination/matrix cracks • localized core crushing underneath facesheet 	2.2618	0.2175	9.5
	63.6	3.00"	• core crush region underneath the facesheet	1.9275	0.002	0.0
	145		• core crush region increases underneath the facesheet	5.2188	0.0255	1.0
	318		<ul style="list-style-type: none"> • complete penetration of facesheet • fiber breakage/delamination/matrix cracks • extensive core crushing region underneath the facesheet 	10.6436	0.0925	5.8
[0°/90°/±45°] _{3s} (6 Plies)	59	1.00"	• localized core crushing underneath facesheet	1.7398	0.005	1.5
	183.6		<ul style="list-style-type: none"> • complete penetration of facesheet • fiber breakage/delamination/matrix cracks • localized core crushing underneath facesheet 	3.4423	0.1155	7.0
	98.4	3.00"	• core crush region underneath the facesheet	3.7516	0.0065	0.0
	180		• core crush region increases underneath the facesheet	7.9037	0.0155	1.0
	320		<ul style="list-style-type: none"> • fiber breakage/delamination/matrix cracks • extensive core crush region underneath facesheet 	10.7615	0.047	5.5

6. COMPRESSION AFTER IMPACT (CAI) TESTING OF SANDWICH PANELS.

The sandwich panels impacted at various energy levels were subjected to in-plane compression testing. The compression testing was performed to measure the relative severity of the damage states from a strength perspective at various energy levels and different impactor diameters. The specimen was end loaded in a fixture; clamped edge conditions were simulated on the loading edges and simply supported edge conditions were simulated on the other two edges of the specimen. The simply supported conditions were effected by using knifed-edged supports. The loading and boundary conditions on the specimen are illustrated in figure 63. A constant displacement was applied along the loading edges.



BOUNDARY CONDITIONS

$$v(x,0) = 0 \quad v(x,h) = v_o \quad \{\text{applied displacement}\}$$

$$w(x,0) = w(x,h) = w(b,y) = w(-b,y) = 0$$

$$\frac{\partial w(x,0)}{\partial y} = \frac{\partial w(x,h)}{\partial y} = \frac{\partial w(b,y)}{\partial y} = \frac{\partial w(-b,y)}{\partial y} = 0$$

$$\frac{\partial w(x,0)}{\partial x} = \frac{\partial w(x,h)}{\partial x} = 0$$

FIGURE 63. BOUNDARY CONDITIONS FOR CAI TESTING OF SANDWICH PANELS

It should be noted that any inward collapsing of the skins could not be prevented by knife-edged supports. Thus, the knife-edges do not strictly enforce the simply supported boundary conditions for local deformations which tend to compress the core in the thickness direction. This scenario is illustrated in figure 64. Only the local out-of-plane displacements along the positive normal direction to the panel surface are constrained.

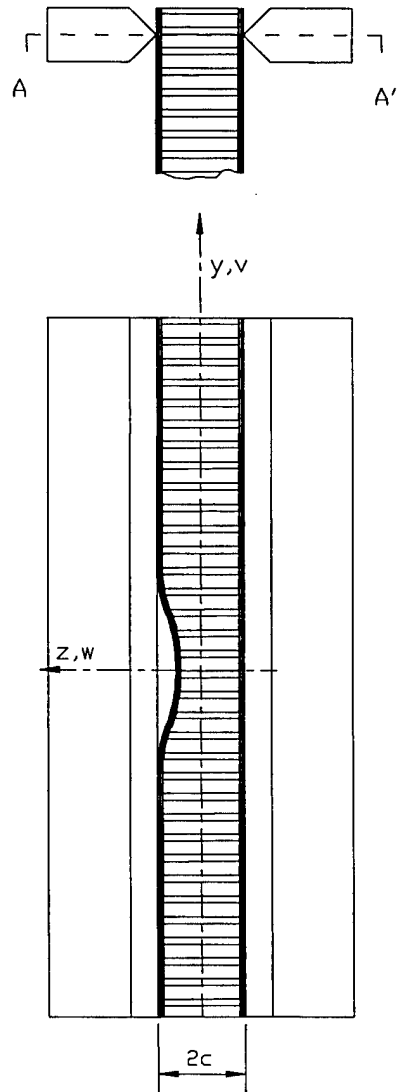


FIGURE 64. THE UNCONSTRAINED LOCAL OUT OF PLANE DISPLACEMENT ALONG THE KNIFE-EDGES

The effects of finite width and length on the CAI strength were of particular concern. The effects of different impact damage modes on the edge effects were studied by suitably mounting strain gages on the specimens. The details of this study and the test fixtures, procedures, and results are discussed in the following sections.

6.1 COMPRESSION TEST FIXTURE.

The test fixture is a modified version of the National Aeronautics and Space Administration (NASA) CAI test fixture (see reference 35). A schematic drawing of the fixture is shown in figure 65. The fixture consists of an aluminum base, which is bolted onto the floor of the lab. The base also houses a steel bearing plate that comes in contact with the bottom edge of the specimen. The steel bearing plate has tapped holes onto which the clamped edges can be fastened as shown in figure 65. Two right angle blocks carry the knife-edge lateral supports for

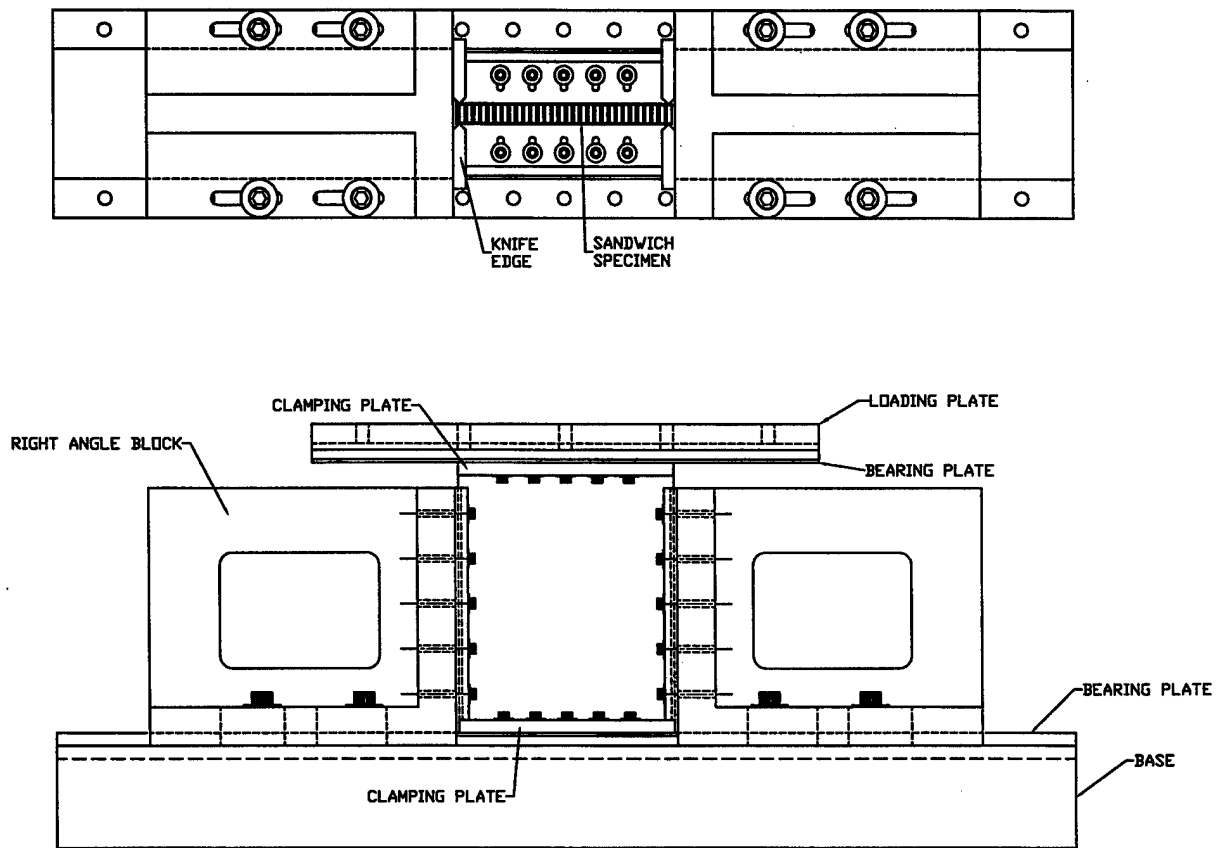


FIGURE 65. TOP AND FRONT VIEW OF THE CAI FIXTURE

the specimen. The right angle blocks slide on the aluminum base and can be fastened to the base at different locations to accommodate different specimen widths. The standard widths that can be accommodated are 8", 10", and 12". The fixture can fit a maximum specimen width of 16". The simply supported boundary conditions along the vertical edges are simulated using knife-edge supports. The knife-edges are grounded to an appropriate radius to prevent any undesired damage to the specimen. These supports do not restrict the lateral expansion (x-direction) of the specimen, thus eliminating the induced lateral stresses due to Poisson's effects. The load is introduced into the specimen by the loading plate at the top, which enforces a uniform displacement along the top edge. The loading plate which is made of aluminum, also carries a steel bearing plate that makes contact with the top edge of the specimen. The aluminum plate is fastened to the load cell that in turn is mounted on an actuator end. The schematic drawing of the compression fixture with the load frame assembly is shown in figure 66.

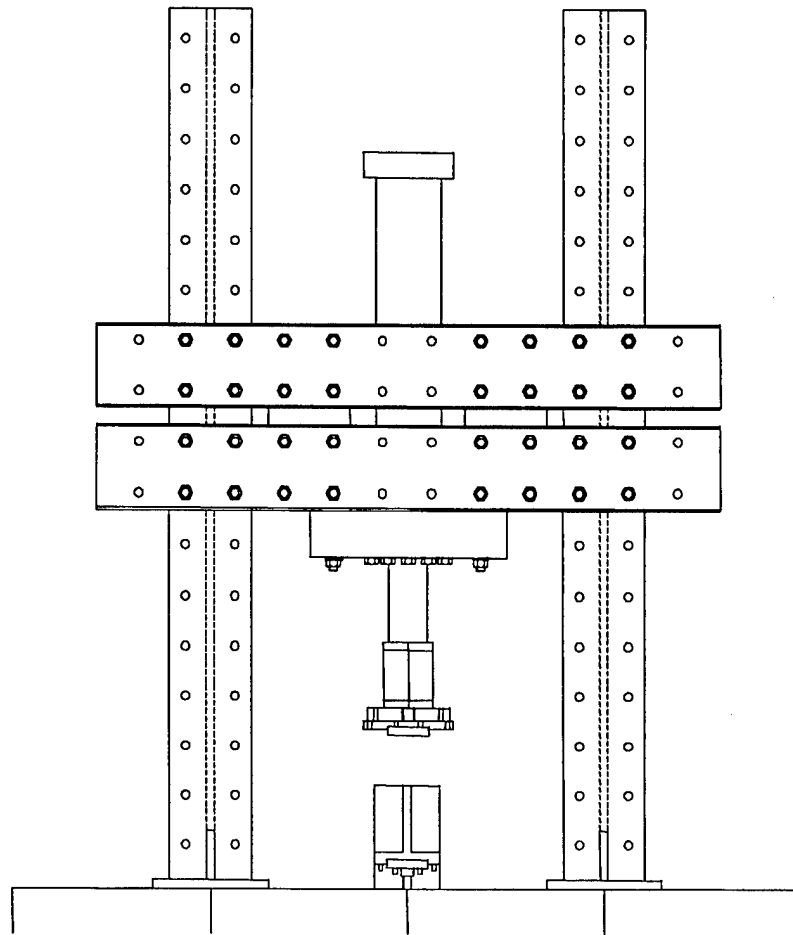


FIGURE 66. THE CAI FIXTURE ALONG WITH THE LOAD FRAME ASSEMBLY

The specimen was loaded by a 80 Kip MTS servohydraulic actuator. The actuator was controlled using the MTS Flextest-II system. The test control and data acquisition was done using the MTS Basic Testware computer program. The test was conducted under displacement control mode, at a rate of 0.05in/min. The Flextest-II system can acquire analog data on 24 channels simultaneously. The typical data acquired during a compression test are the time, actuator displacement, force, and the three strains from far-field strain gages mounted on the specimen.

6.2 COMPRESSION AFTER IMPACT TEST PROCEDURE.

The CAI strength test was performed using the fixture described in the previous section. The test specimen configuration for a typical test is shown in figure 67. A minimum of three strain gages were mounted on the specimen to monitor the loading of the specimen along the top edge. The strain gages were located at a distance of 2.50" (nominal) from the point of impact. This distance was chosen based on the typical size of the damage zones from the C-scans. Nonuniform loading from minor misalignments caused by machining tolerances were corrected using brass shims of various thicknesses (0.001" to 0.0075" typical). The misalignments were

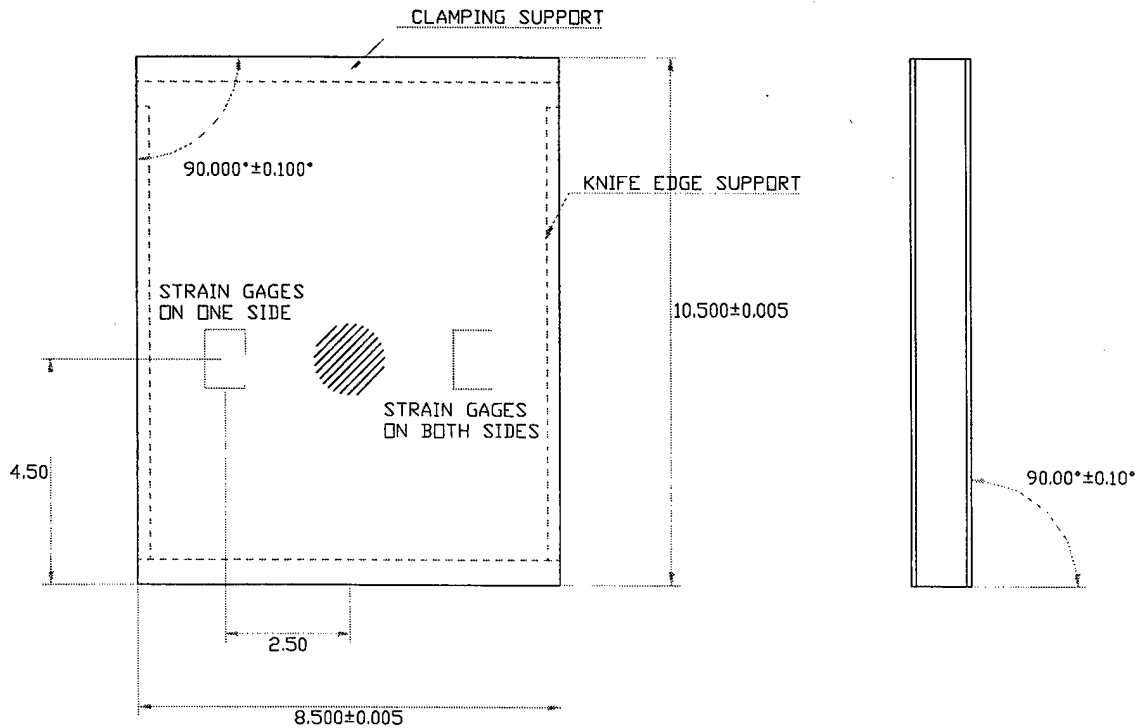


FIGURE 67. SPECIMEN CONFIGURATION AND STRAIN GAGE LOCATIONS ON A TYPICAL CAI SPECIMEN

detected by preloading the specimens to 1500 lbf (typical) and recording the differences in the strain gage readings. The top edges of the specimens were shimmed by trial and error until the differences in strain gage readings were minimal (about 50 microstrain). The stronger panels were loaded up to 3000 lbf to do the same. It was observed on more than one occasion that the strain gage readings which were close to each other at preload diverged when actual loading went past the preload during the test. The testing was not aborted at this stage because any damage growth that might have occurred during the loading might significantly affect the subsequent test results. The typical plot from a CAI test is shown in figure 68. The strains are plotted against the compressive force resultant N_{yy} defined as follows.

$$N_{yy} = \frac{\text{Applied load } P}{\text{Specimen width } 2b} (\text{lbf} / \text{in})$$

The total specimen width, which included the width outside the knife-edges (0.25" nominal, each side), was used for computing the force resultant, as that portion also contributes to the load carrying ability of the specimen. The maximum load sustained by the specimen before failing by either compression mode or some localized buckling mode was used to compute the CAI strength.

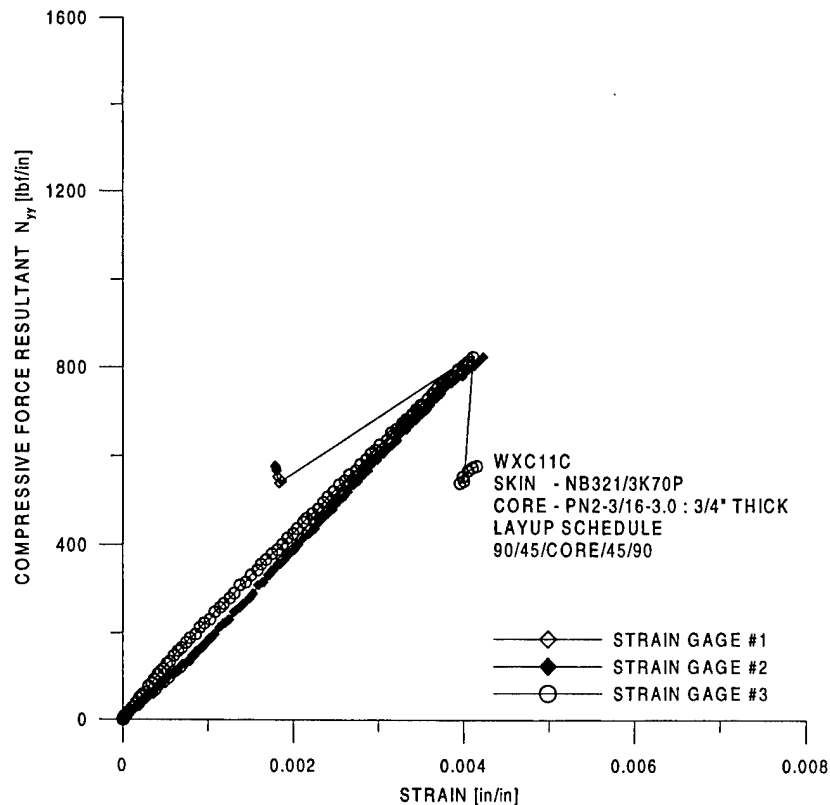


FIGURE 68. A TYPICAL RESULTANT FORCE-STRAIN PLOT FROM A CAI TEST

6.3 FINITE WIDTH AND LENGTH EFFECTS IN CAI SPECIMENS.

The existence of finite width and length effects in the CAI specimen for the chosen specimen dimensions was investigated for different impact damage states. Sandwich panels with a lay-up sequence of $[(90/45)_2/\text{core}/(45/90)_2]$ and a 0.75" thick core were chosen for this study. Two panels were impacted with impactor diameters of 1.00" and 3.00", with sufficient energy to cause visible damage. The panels impacted with the 1.00" diameter impactor suffered a localized skin failure and core crushing type damage while the specimens impacted with the 3.00" diameter impactor suffered a more distributed core damage area with minimal skin damage. The objective of this study was to ensure that the chosen specimen width and height was sufficient enough to eliminate any finite width or length effects arising due to the different damage states/sizes. Also, the apparent increase in strength due to shear-lag effect [36] as a result of insufficient length or height of the panel was investigated. Popular methods that have been employed by various investigators are strain field measurements using Moiré fringe methods, strain-gaging, and analytical modeling. Since the analytical model requires the knowledge of the damage morphology a priori [open-hole configurations have been typically used], it was decided that a series of strain gages be used on the impacted side in both horizontal and vertical directions originating from the point of impact. A limited number of strain gages were also mounted closer to the loading edge and the back (unimpacted) side of the panels. The variations of strain readings along the horizontal and vertical directions originating from point of impact were plotted at various load levels to identify any significant edge effects. Further, the specimens were photographed at different load levels during the test to visually detect the growth

of failure or instability mechanism during the test. The test results of each specimen used for this investigation will be discussed in detail individually in the following paragraphs.

6.3.1 Case-I: Sandwich Panel Impacted With 1.00" Impactor.

- Specimen I.D: WXC25K
- Impact energy: 180 in-lbf
- Impactor diameter: 1.00 inch
- C-scan planar damage area: 2.2924 sq. inches
- Maximum residual dent depth: 0.126 inches

The specimen sustained visible skin damage and substantial core crushing in the vicinity of the impact region. The C-scan damage plot is shown in figure 69a. The planar damage area has an average radius of 0.8642 inches. The dent depth distribution in the vicinity of damage was measured at equal intervals of 0.20 inches [x & y] and its contour plot shown in figure 69b. The residual indentation is localized and is much greater than the skin thickness itself. The damage manifested itself as an open hole in the impacted skin during the CAI test. The strain distributions along different sections in the specimens are shown in figures 70a to 70d.

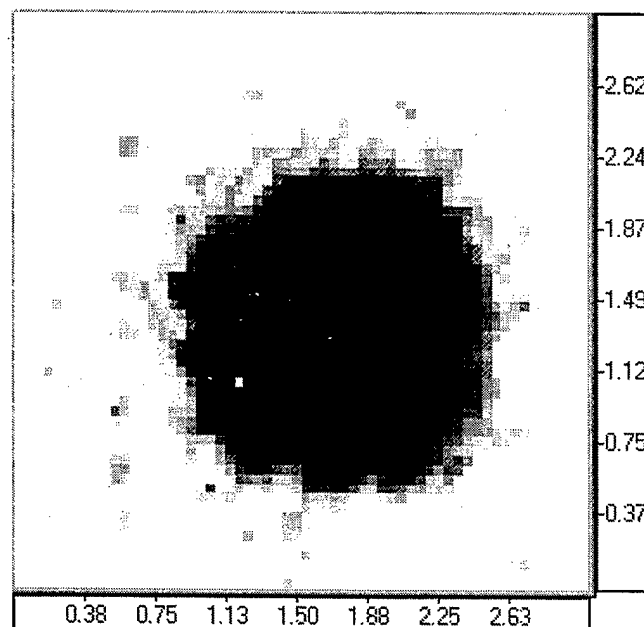


FIGURE 69a. C-SCAN PLOT SHOWING PLANAR DAMAGE DISTRIBUTION
IN THE SPECIMEN WXC25K

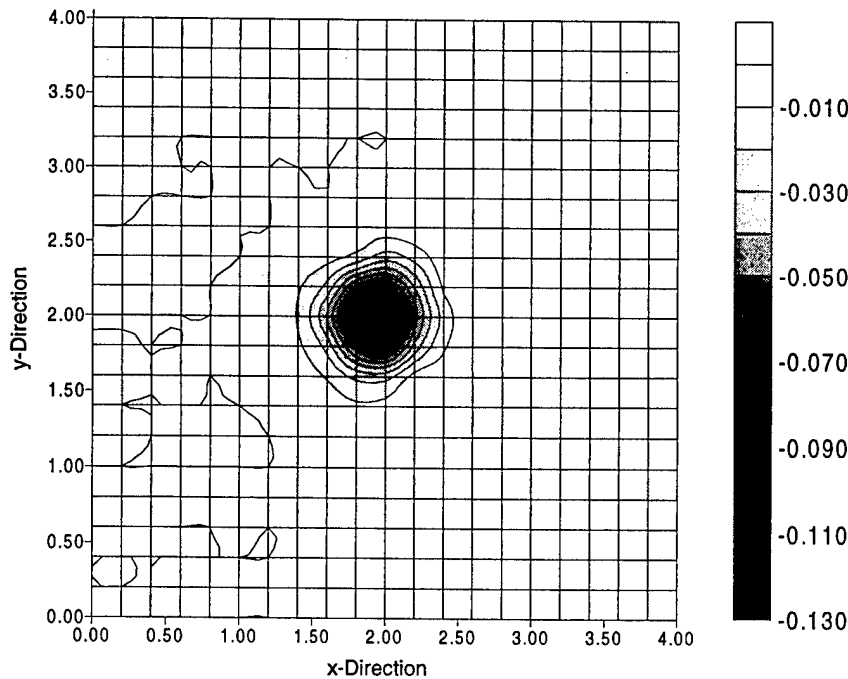


FIGURE 69b. CONTOUR PLOT OF RESIDUAL DENT DISTRIBUTION
IN THE SPECIMEN WXC25K

The following inferences are made from the observed strain distributions.

1. Strain distributions along $y = 0$, on the impact side. [See figure 70a.]

The impact damage acts like an open hole in the impacted skin. The strain values rise exponentially next to damage region and saturate to the far field strain values within about 2" inches from the damage zone. However, closer to the failure load the distance needed for the strain to saturate increases, indicating some kind of failure propagation across the panel. Thus, the finite width effects are not significant for this kind of damage.

2. Strain distributions along $x = 0$, on the impact side. [See figure 70b.]

The strain values fall steeply near the damage zone due to lack of stiffness but saturate to the far field value towards the top edge of the specimen. It can be observed that this strain gradient is much more gradual when compared to the horizontal direction. Since the strain values do reach the far-field values along $y = 0$, it can be assumed that the shear lag phenomenon is not very dominant. The fact that these "far-field" strains actually exceed those observed along $y = 0$ should be interpreted as a slight bending in the specimen, possibly related to the damage imperfection (see figure 70d).

3. Strain distributions along $y = 4$, on the impact side. [See figure 70c.]

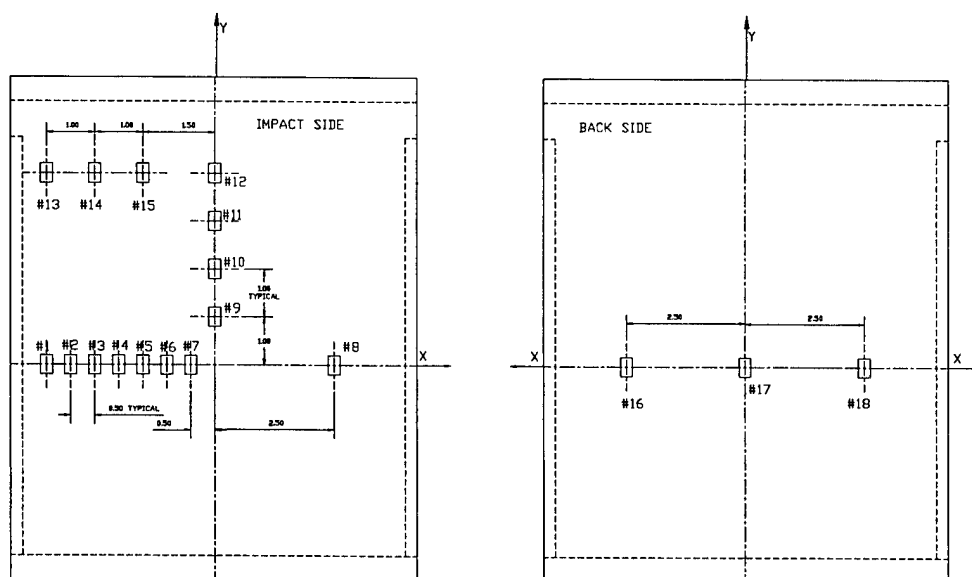
These strain reading were intended to further capture any strain gradients due to shear lag effects. There was a negligible strain gradient along $y = 4$, except close to the failure

load when some failure growth may have occurred. Thus, shear lag effects are negligible until the specimen has sustained a load that is close to its CAI strength value. Once again, the observation of strains greater than those in the far-field for $y = 0$ should be interpreted as a slight specimen bending. The height of the specimen, i.e., 10" seems adequate for the impact damage type addressed in this section.

Thus, the images of the specimen prior to testing and after failure are shown in figures 71a to 71c. Note the compressive failure mode of the skins in figures 71b and 71c. The sandwich skins failed in a compressive mode across the section containing the impact damage as shown. The gridlines drawn on the specimen were intended to visually identify any local buckling that might occur during the test. No local buckling of the skin was visible during the test. It was observed during the experiments that the failure/crack propagated from the impact point outwards on both sides. The far-field strain values were in the vicinity of 4000 micro-strain at failure. Thus, the specimen size chosen for the investigation does not exhibit any finite width & length effects for damage states resembling an open-hole, with diameter around 1.00".

4. Axial strain measurements versus applied loading. [See figure 70d.]

These strain readings were recorded and plotted against the axial load, N_{xx} . This plot shows the load and corresponding strain on the front and back surfaces of the panel. This figure indicates no global buckling or bending of the panel during the testing.



70

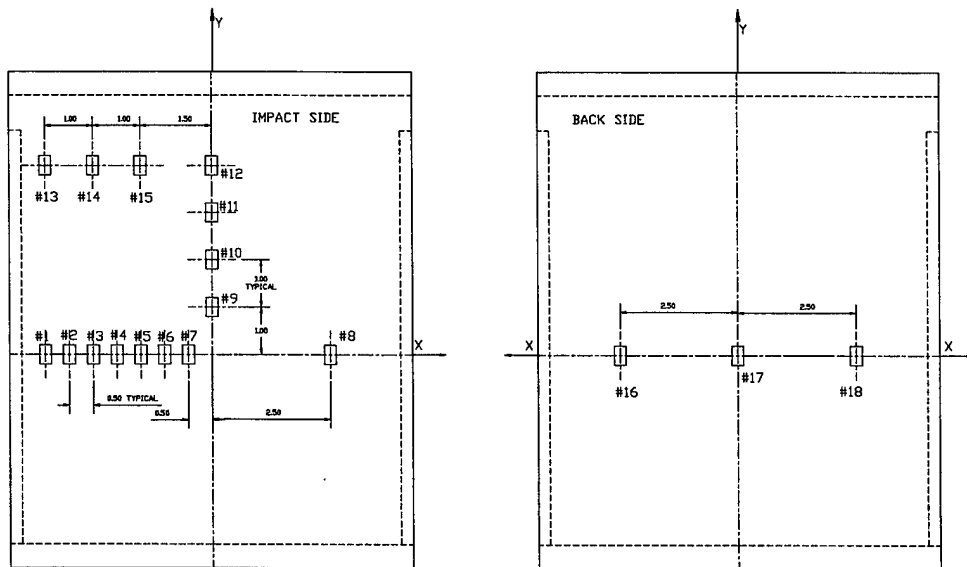
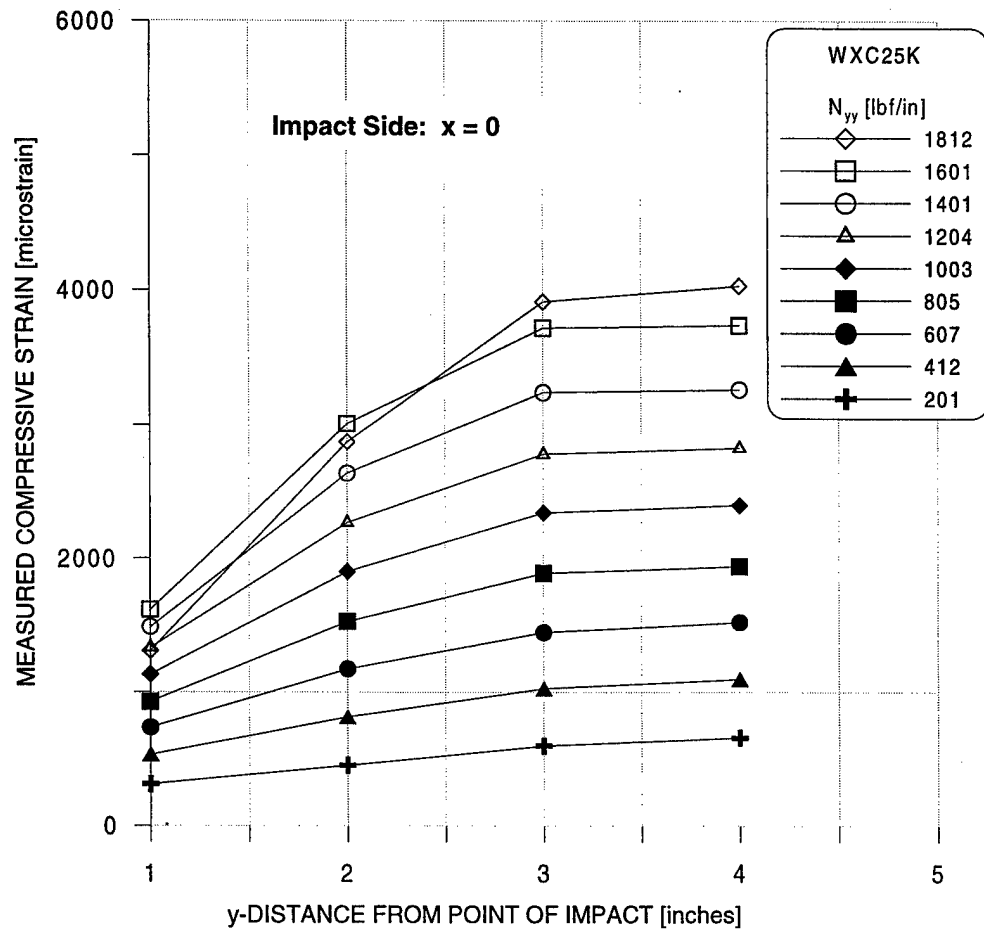


FIGURE 70b. STRAIN DISTRIBUTIONS ALONG THE LINE $x = 0$, ON THE IMPACTED SIDE

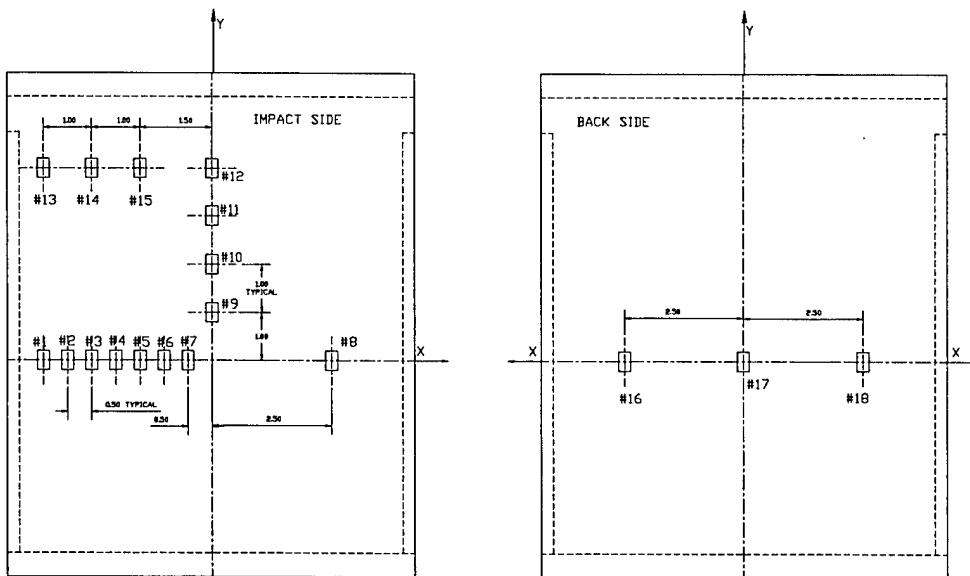
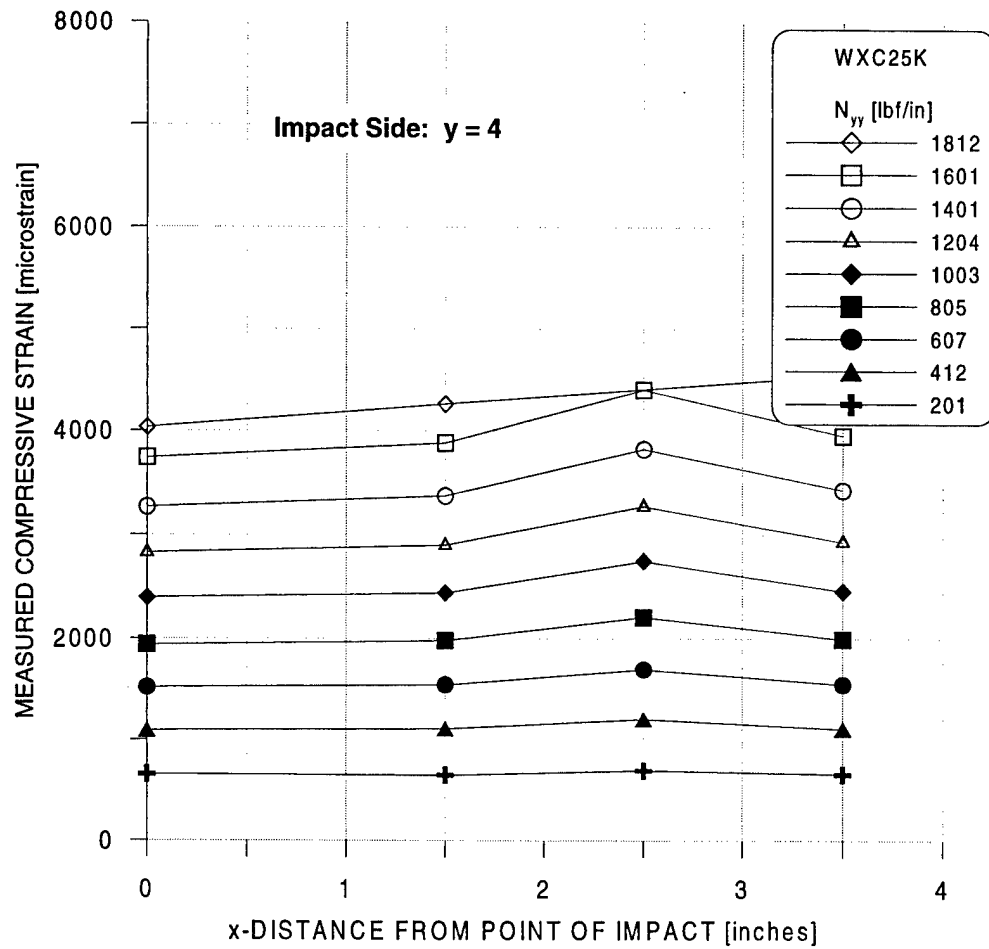
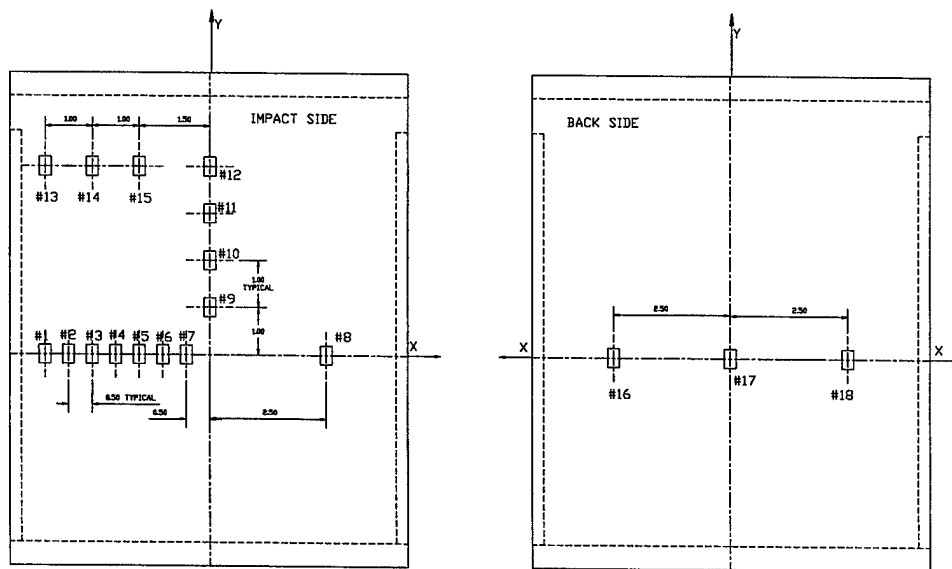


FIGURE 70c. STRAIN DISTRIBUTIONS ALONG THE LINE $y = 4$, ON THE IMPACTED SIDE



73

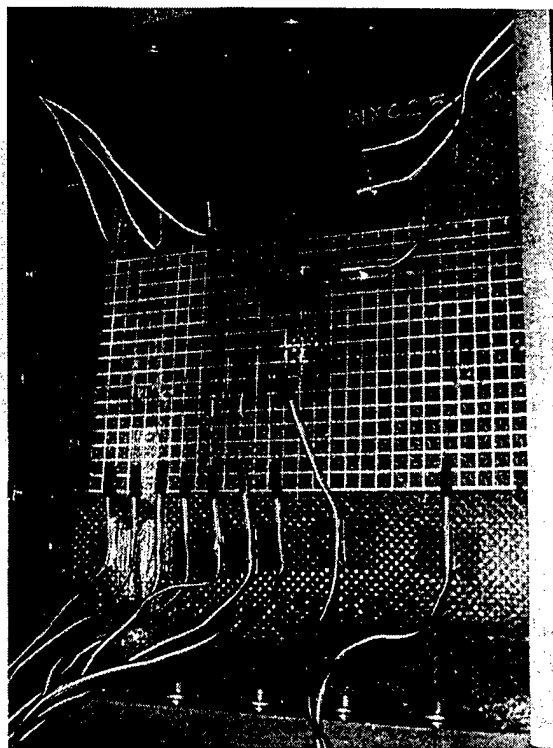


FIGURE 71a. SPECIMEN WXC25K AT
 $N_{yy} = 0.0$ lbf/in

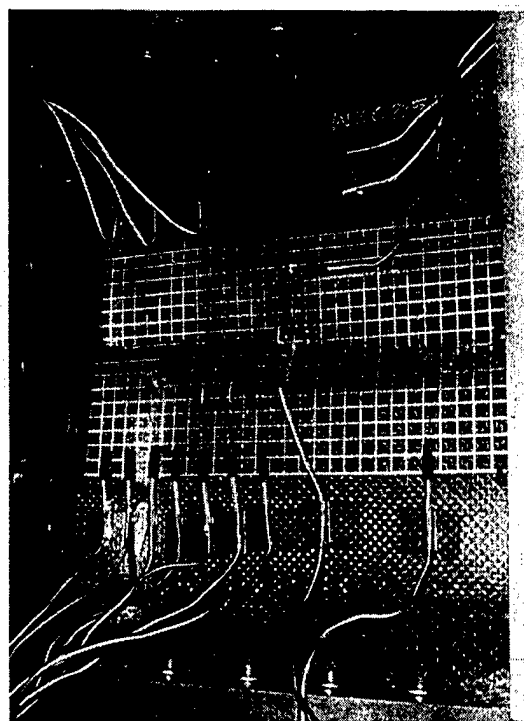


FIGURE 71b. SPECIMEN WXC25K AT
 $N_{yy} \sim 1812$ lbf/in

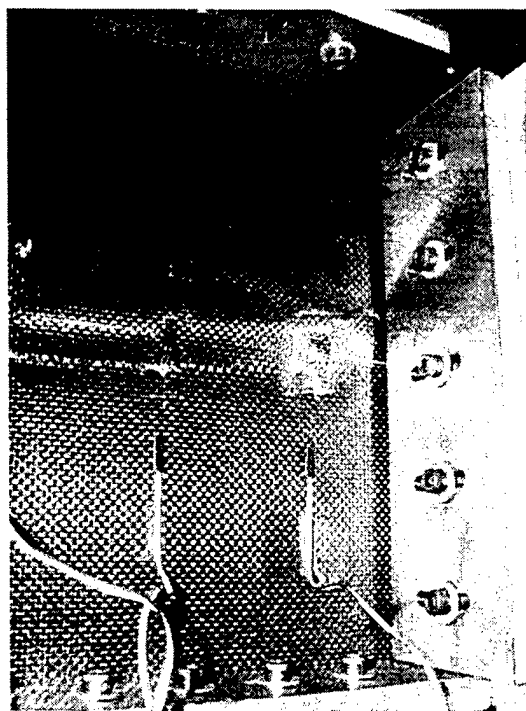


FIGURE 71c. BACKSIDE OF THE PANEL (WXC25K) AFTER FAILURE

6.3.2 Case-II: Specimen Impacted With 3.00" Diameter Impactor.

- Specimen I.D: WXC29L
- Impact energy: 250 in-lbf
- Impactor diameter: 3.00"
- C-scan planar damage area: 11.5497 sq. inches
- Maximum residual dent depth: 0.165 inches

In this case, the specimen was impacted with a 3.00" diameter impactor with considerable impact energy, enough to cause visible residual indentation and skin failure in the vicinity of the impact point. The C-scan damage plot is shown in figure 72a. The planar damage area has an average radius of 1.9305 inches. The dent depth distribution in the vicinity of damage was measured at equal intervals of 0.20 inches [x and y] and its contour plot shown in figure 72b.

The specimen had strain gages along the lines $y = 0$ and $y = 4$ on both sides of the panel. On the impact side, along the line $y = 0$, at least two strain gages were within the indentation region. The strain distributions and pictures of the specimen at certain loads are shown in the figures 73a to 73e.

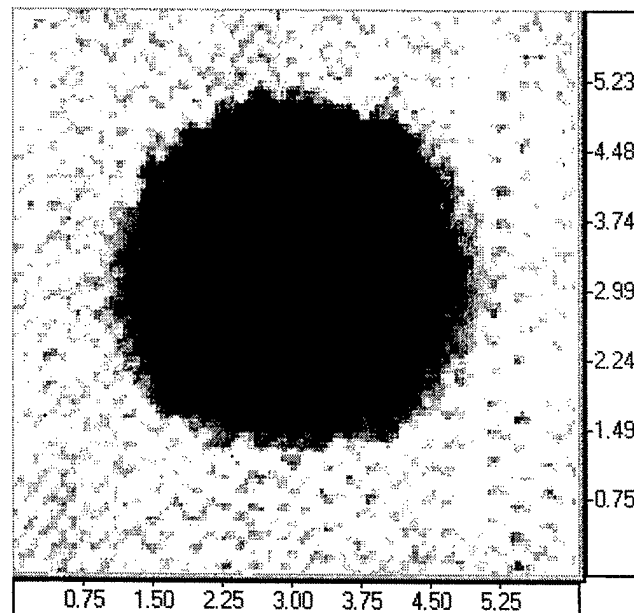


FIGURE 72a. C-SCAN PLOT SHOWING PLANAR DAMAGE DISTRIBUTION
IN THE SPECIMEN WXC29L

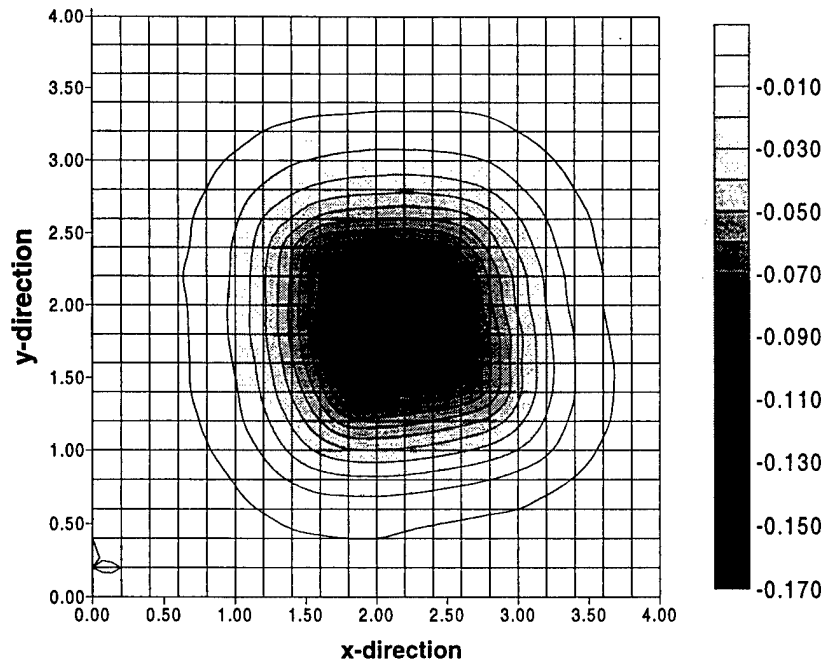


FIGURE 72b. CONTOUR PLOT OF RESIDUAL DENT DISTRIBUTION IN THE SPECIMEN WXC29L

The following inferences can be drawn based on the observed strain distributions.

1. Strain distribution along $y = 0$, on the impact side [see figure 73a].

The strain distributions clearly indicate that the skin was transferring some load through the damage (6.indentation) region unlike the previous case. The maximum strain value was reached about 1.5" from the point of impact (may not be the actual maxima due to the coarse strain gage spacing). The strain distributions exhibit a slight finite width effects at lower loads while strain distributions are more pronounced closer to the failure load which can be attributed to the growth of the indentation in the lateral direction.

2. Strain distribution along $y = 4$, on the impact side [see figure 73b].

A small strain gradient was observed at the initial stages, which grew with the load indicating the presence of shear lag effects.

3. Strain distributions along $y = 0$, on the backside [see figure 73c].

The strain distributions did not indicate any finite width effects as they picked up some tensile loading due to the buckling induced strains in the back facesheet.

4. Strain distributions along $y = 4$, on the backside [see figure 73d].

No shear lag effects were indicated in the strain distributions on the backside.

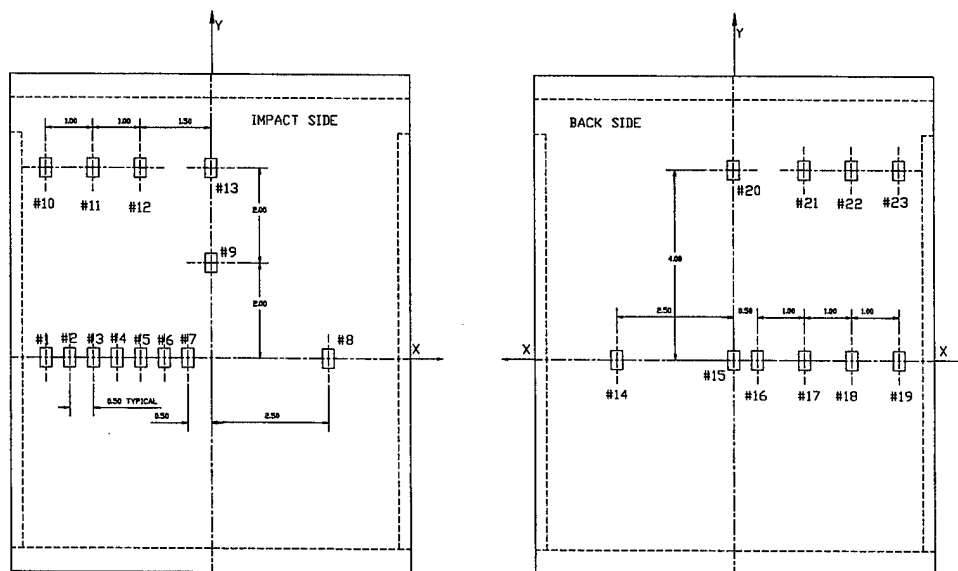
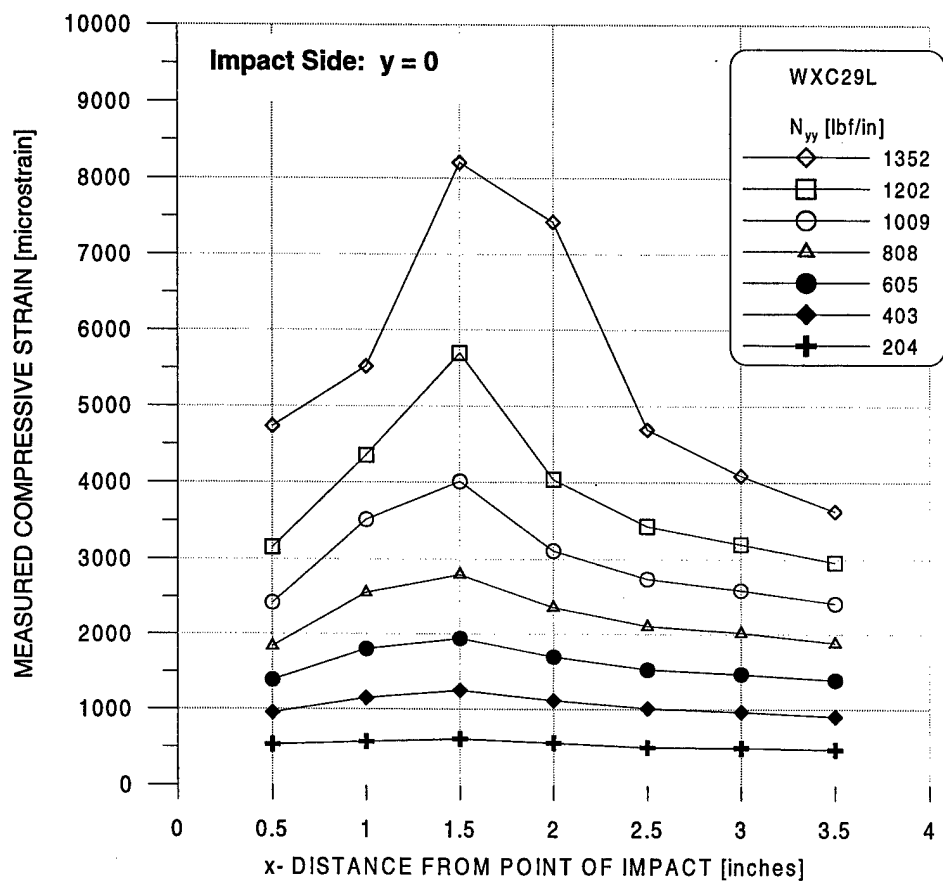


FIGURE 73a. STRAIN DISTRIBUTIONS ALONG THE LINE $y = 0$, ON THE IMPACTED SIDE

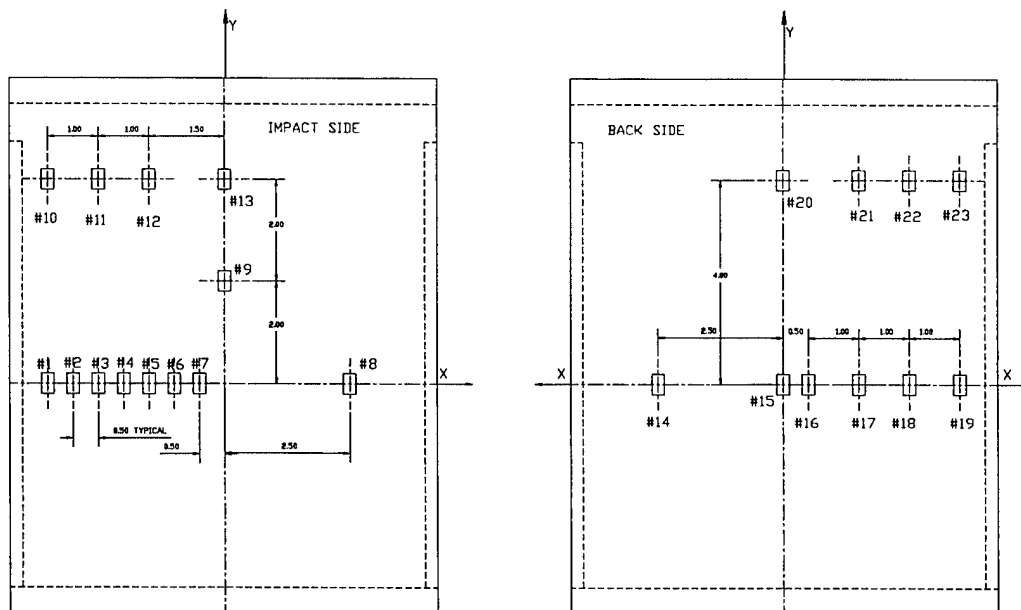
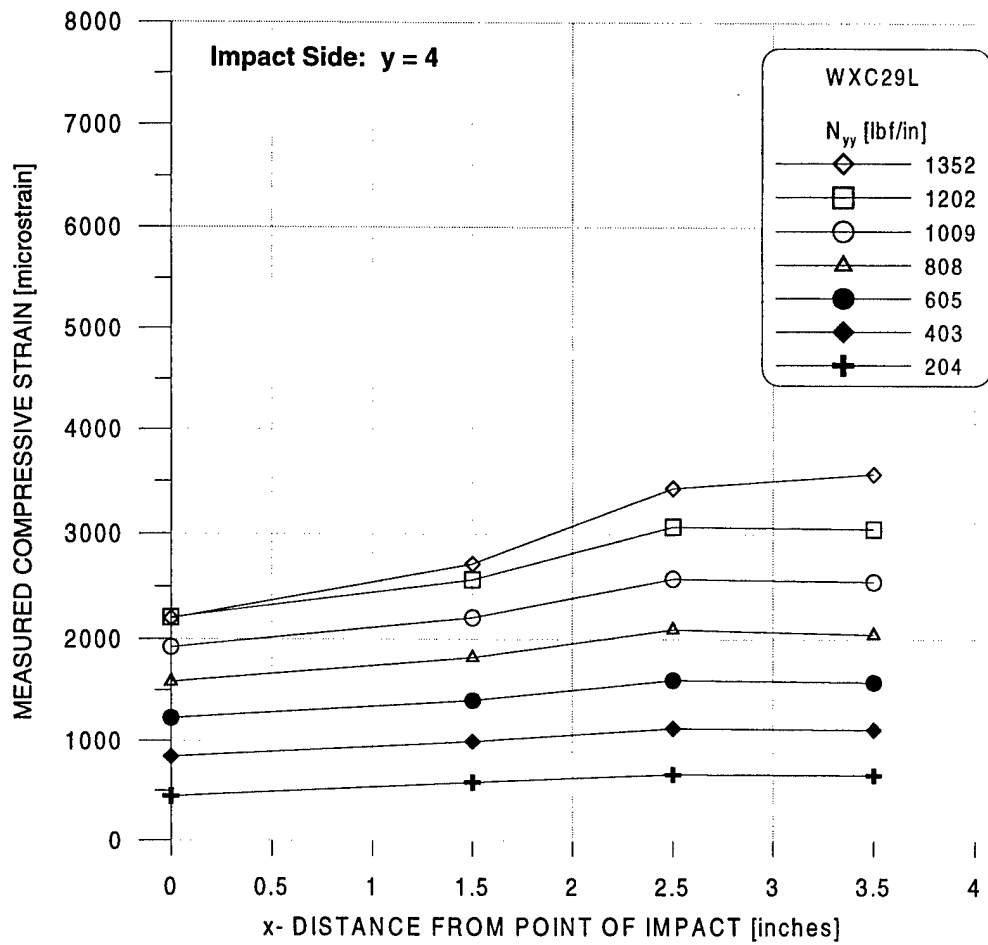


FIGURE 73b. STRAIN DISTRIBUTIONS ALONG THE LINE $y = 4$, ON THE IMPACTED SIDE

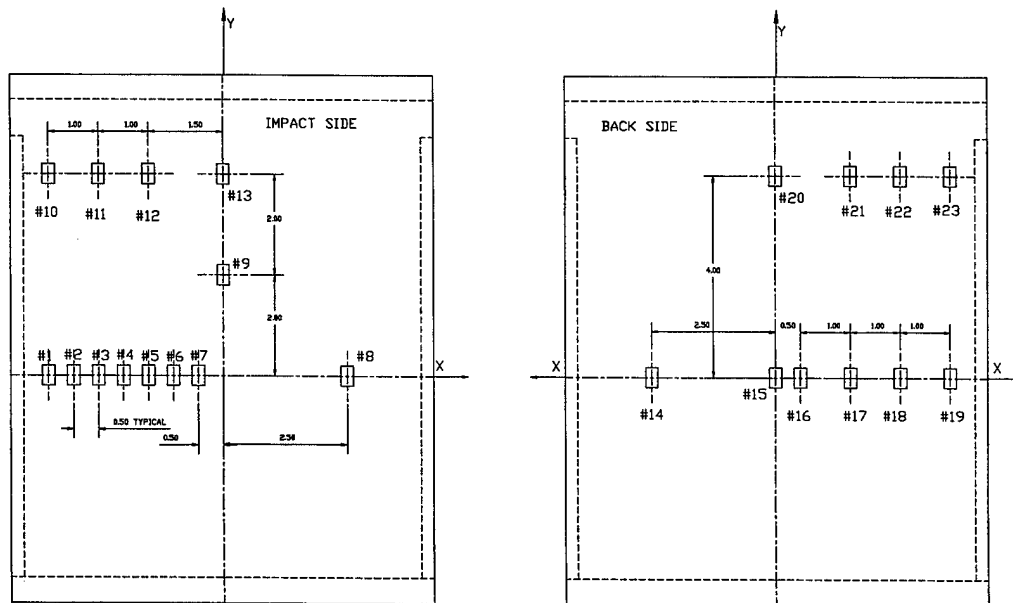
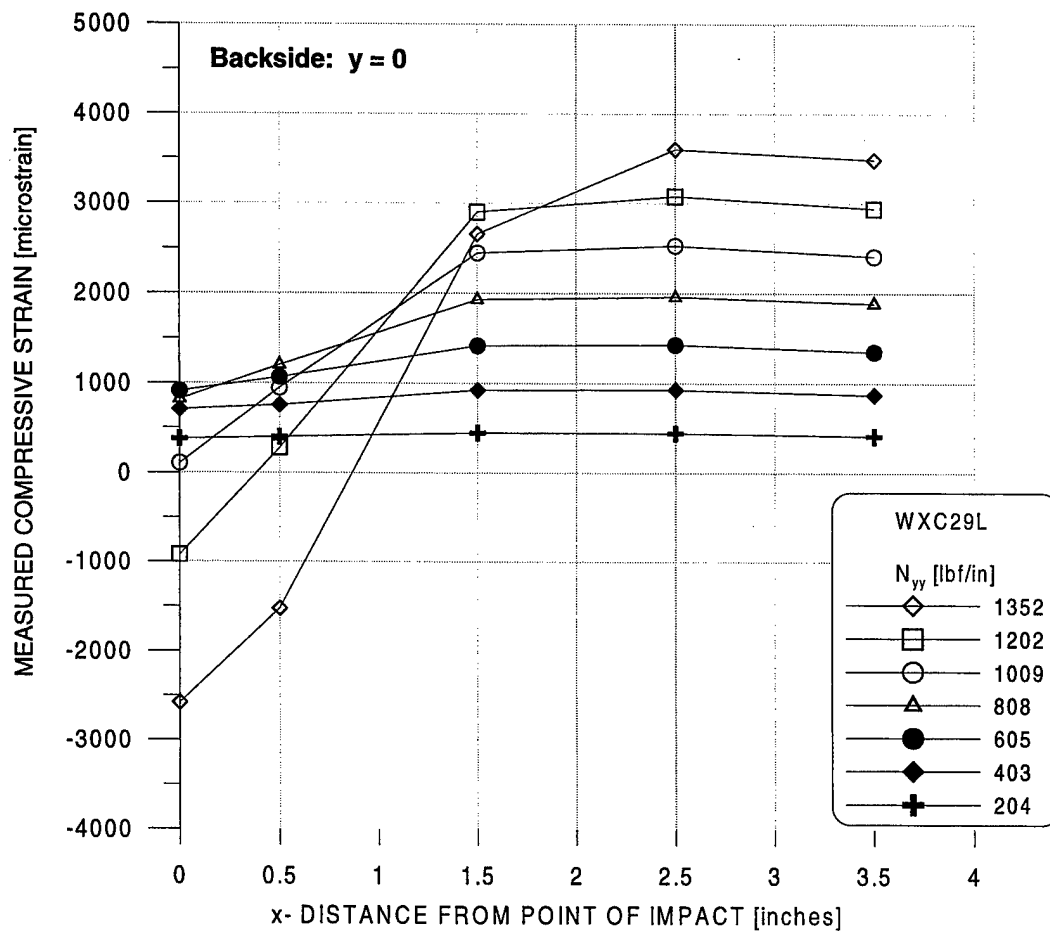


FIGURE 73c. STRAIN DISTRIBUTIONS ALONG THE LINE $y = 0$, ON THE BACKSIDE

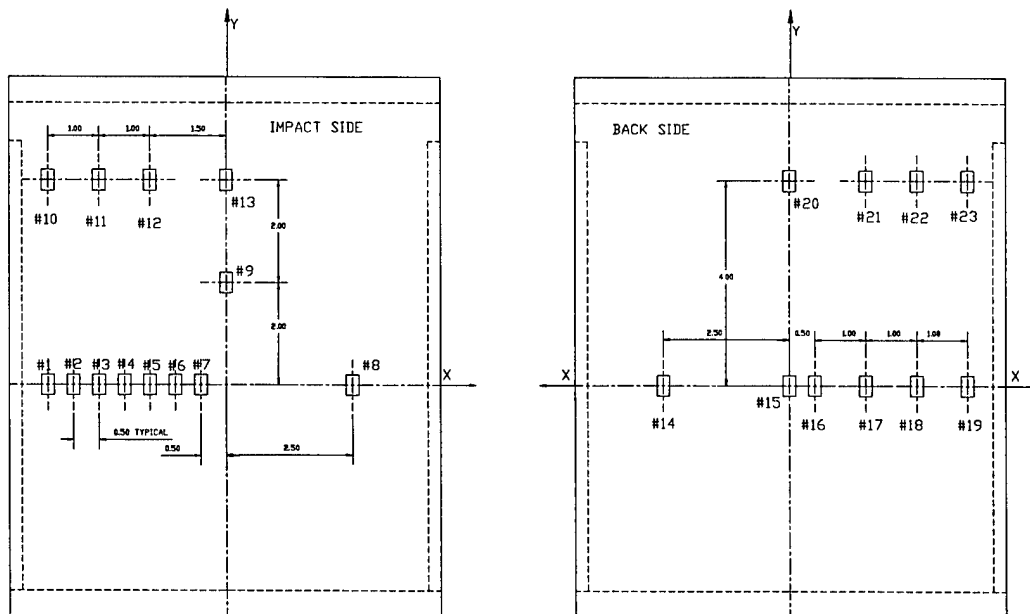
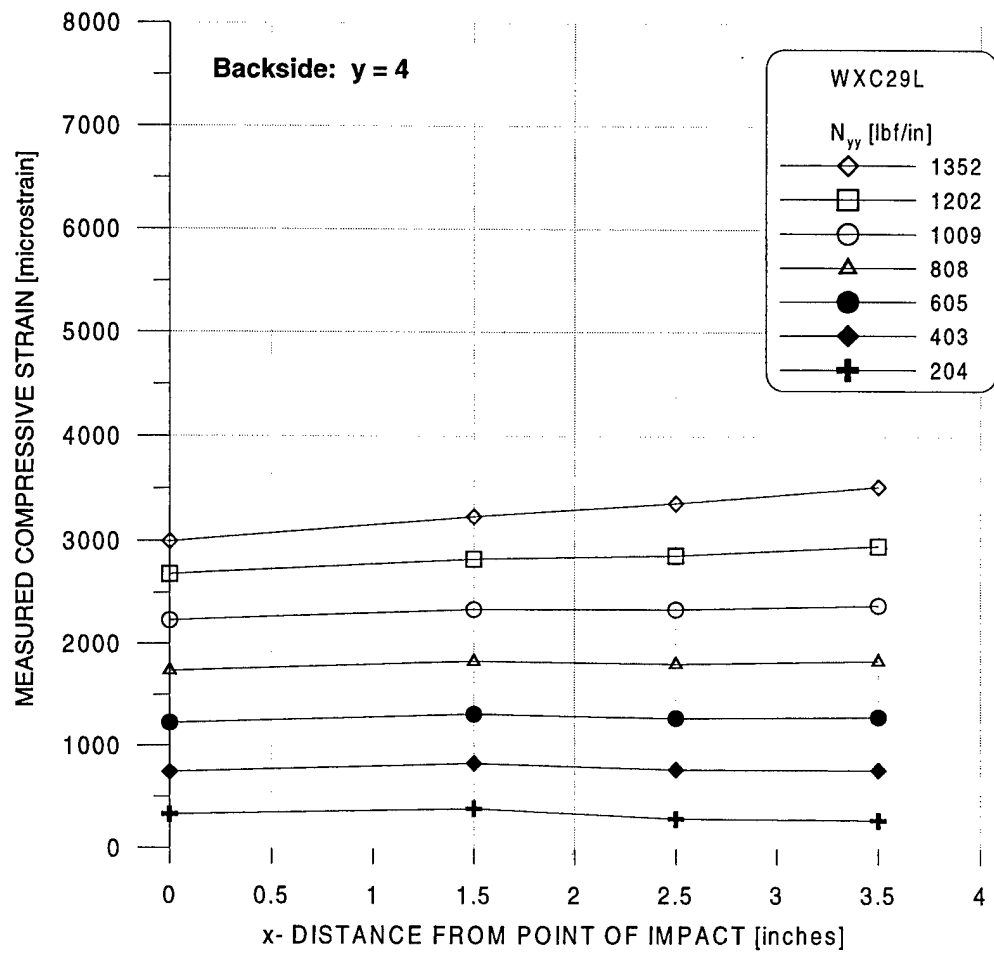


FIGURE 73d. STRAIN DISTRIBUTIONS ALONG THE LINE $y = 4$, ON THE BACKSIDE

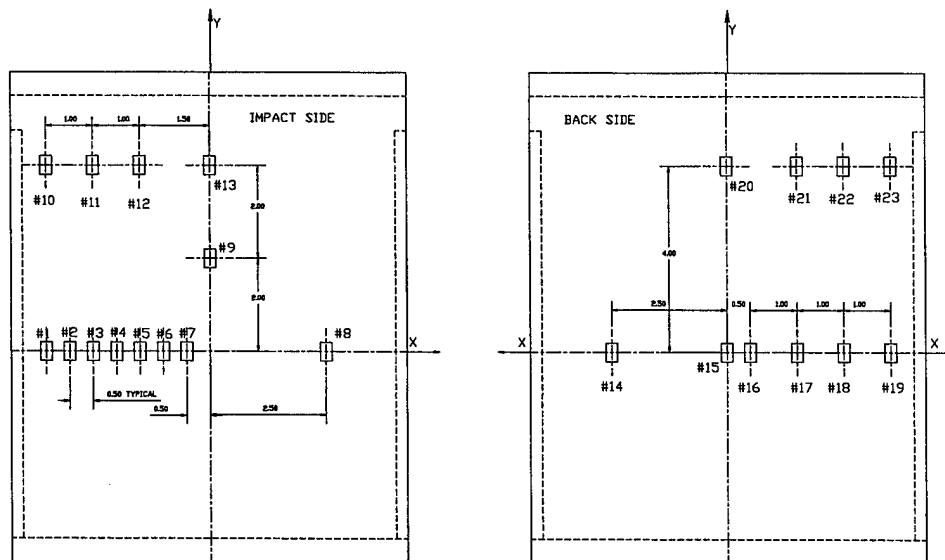
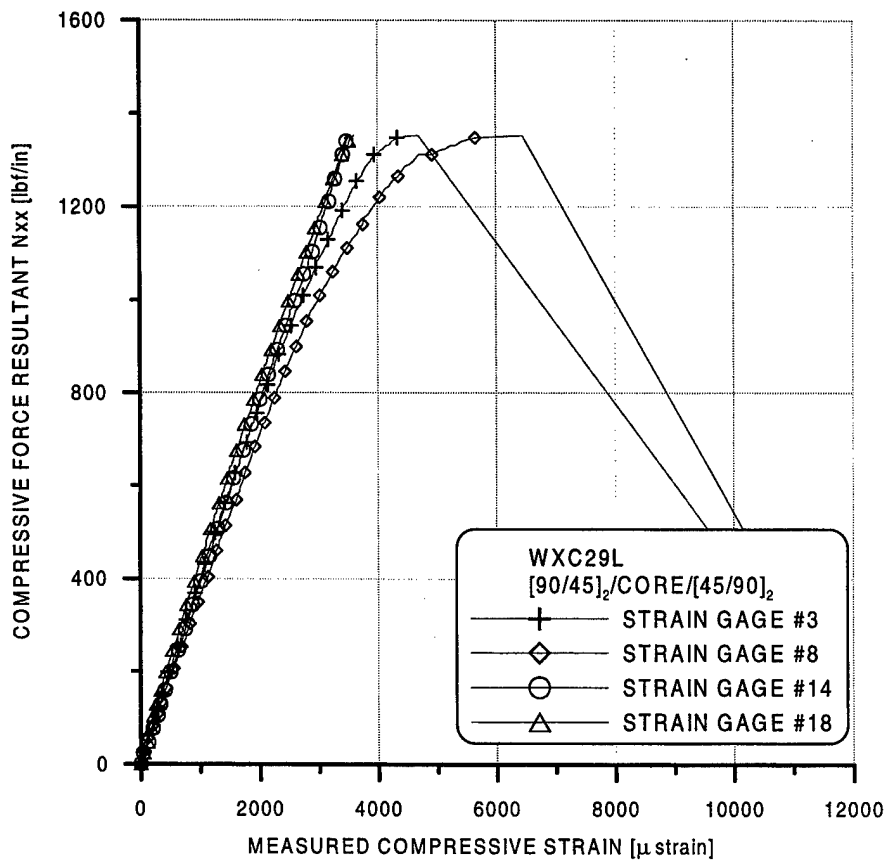


FIGURE 73e. FORCE RESULTANT VS FAR-FIELD STRAINS

The pictures of the specimen in figures 74a to 74c show the typical failure mode associated with panels impacted with the large impactor. The local buckling of the skin across the width of the panel is shown in figure 74b.

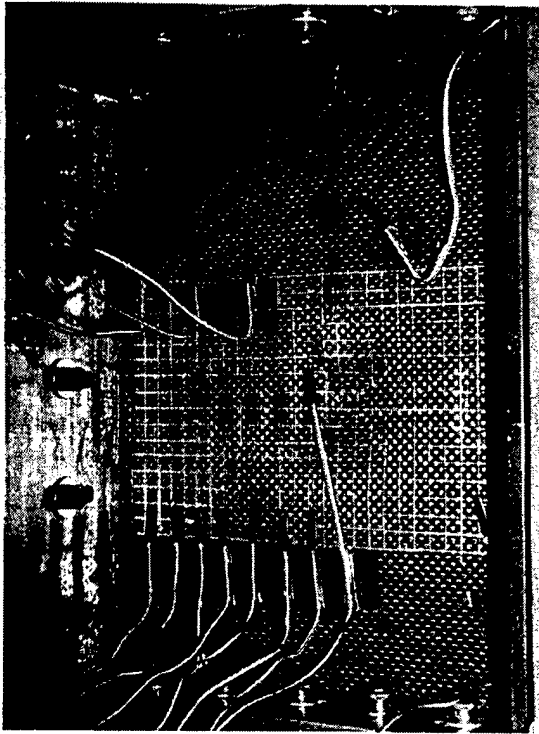


FIGURE 74a. SPECIMEN WXC29L AT
 $N_{yy} = 0.0 \text{ lbf/in}$

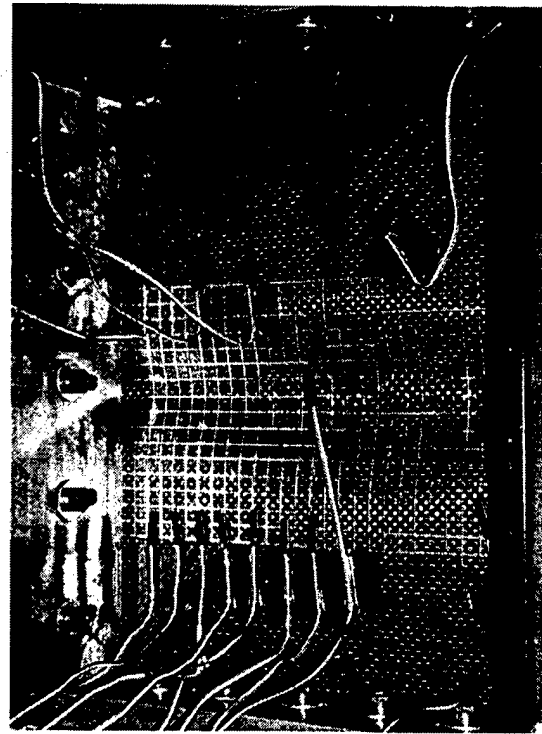


FIGURE 74b. SPECIMEN WXC29L AT
 $N_{yy} \sim 1352 \text{ lbf/in}$



FIGURE 74c. BACKSIDE OF THE PANEL
(WXC29L) AFTER FAILURE

The specimen configuration chosen for the current investigation does not exhibit any significant finite width or length effects based on experimental observations. The results are limited to open-hole type damages with diameters in the range of 1.00" and excessive indentation and visible skin failure region with diameters in the range of 3.00". Further, these observations were made for only one sandwich lay-up configuration, as the experiments are very expensive due to the number of strain gages involved. At present, work is in progress to test panels with widths of 10" and 12". An analytical model would be more appropriate for such investigations, but care should be taken to suitably represent the damage state and distribution in the panel. Destructive tests are currently being used to investigate the damage characteristics resulting from different impact scenarios.

6.4 COMPRESSION AFTER IMPACT TESTING OF IMPACTED SANDWICH PANEL—RESULTS.

The sandwich panels that were impacted and inspected by nondestructive methods were subjected to compression testing to assess their residual strength. The load, displacement, and strain gage readings were recorded during each test. The plots of force resultant versus strain gage readings can be seen in appendix D. The variation of residual strength with impact energy is summarized in figures 75 through 77 for all the sandwich configurations that were tested. Most results indicate that the specimens impacted with the 3.00" impactor had a lower CAI strength compared to the specimens impacted with the 1.00" impactor at a given (comparable) energy level.

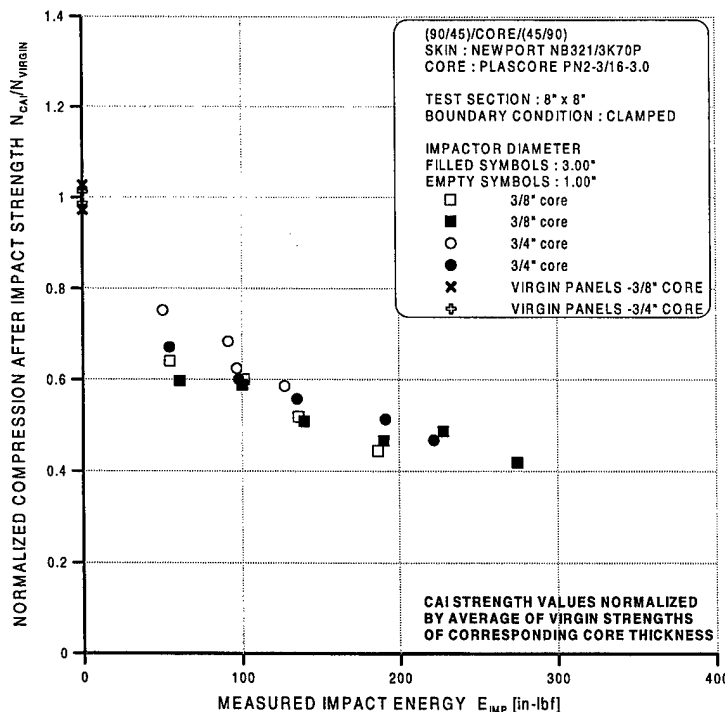


FIGURE 75. COMPRESSION AFTER IMPACT STRENGTH VALUES AS A FUNCTION OF IMPACT ENERGY FOR [(90/45)/CORE/(45/90)] PANELS

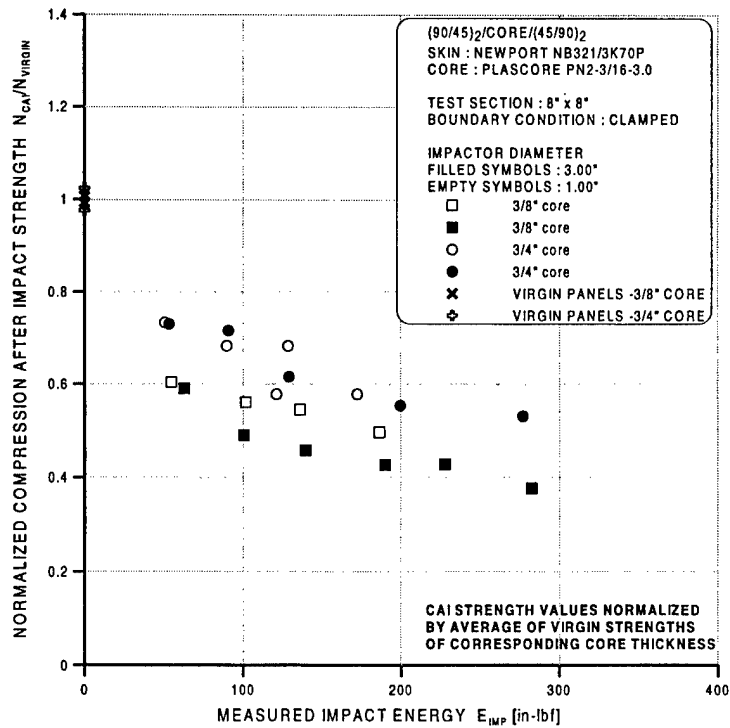


FIGURE 76. COMPRESSION AFTER IMPACT STRENGTH VALUES AS A FUNCTION OF IMPACT ENERGY FOR [(90/45)₂/CORE/(45/90)₂] PANELS

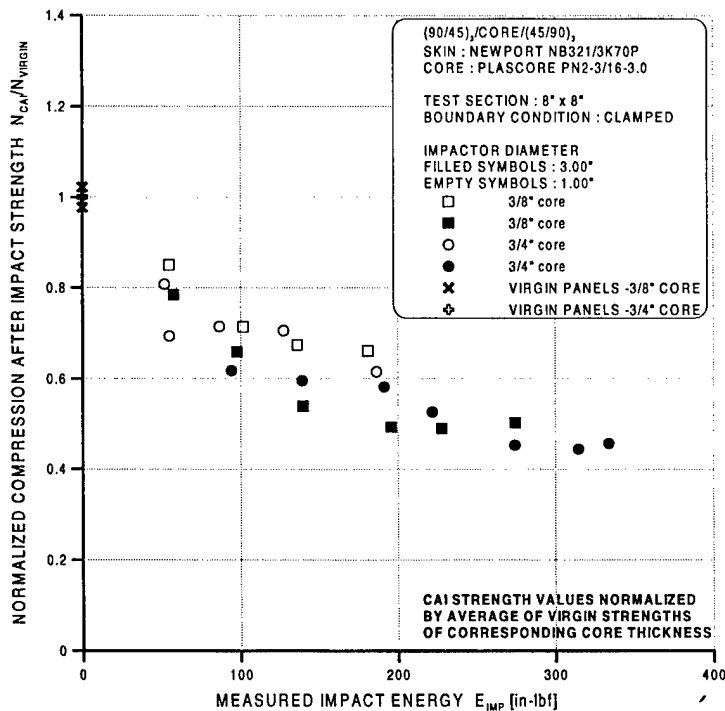


FIGURE 77. COMPRESSION AFTER IMPACT STRENGTH VALUES AS A FUNCTION OF IMPACT ENERGY FOR [(90/45)₃/CORE/(45/90)₃] PANELS

The reader must exercise caution when comparing CAI strengths of panels impacted with different impactor diameters as the failure modes are different. The open-hole type damage states induced by the 1.00" diameter impactor produced compressive failures of the skin, with the failure propagating from the damage site towards the edges of the specimen. The damage state produced by the 3.00" impactor, characterized by large indentation areas with minimal skin damage, produced a local buckling initiated failure. The dimple produced by inward buckling of the skin within the damage area grew outwards to the lateral edges at which point the panel becomes unstable resulting in failure.

6.5 CORRELATION OF CAI STRENGTH WITH DAMAGE METRICS.

The correlation of damage metrics to the CAI properties is important from a damage tolerance perspective. The damage metrics that have been investigated in this program are the planar damage area obtained using an ultrasonic C-scan technique and maximum residual indentation depth. At any given impact energy level these damage metrics were found to be strongly dependent on the impactor diameter and the sandwich configuration. The combinations of planar damage area and maximum dent depth for the three sandwich configurations are summarized in figures 78a to 78c. The sandwich panels with thinner core (3/8" thick) and panels impacted with the large (3.00" diameter) impactor had significantly smaller dent depths for a given planar damage area. The trends are very well defined for the [(90/45)₂/core/(45/90)₂] and [(90/45)₃/core/(45/90)₃] panels.

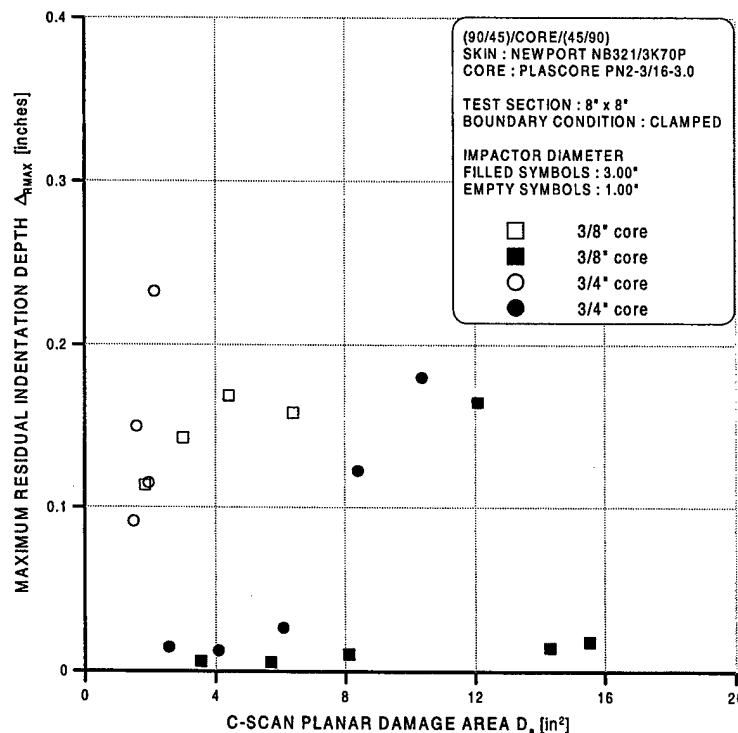


FIGURE 78a. MAXIMUM DENT DEPTH VS PLANAR DAMAGE AREA FOR [(90/45)/CORE/(45/90)] PANELS

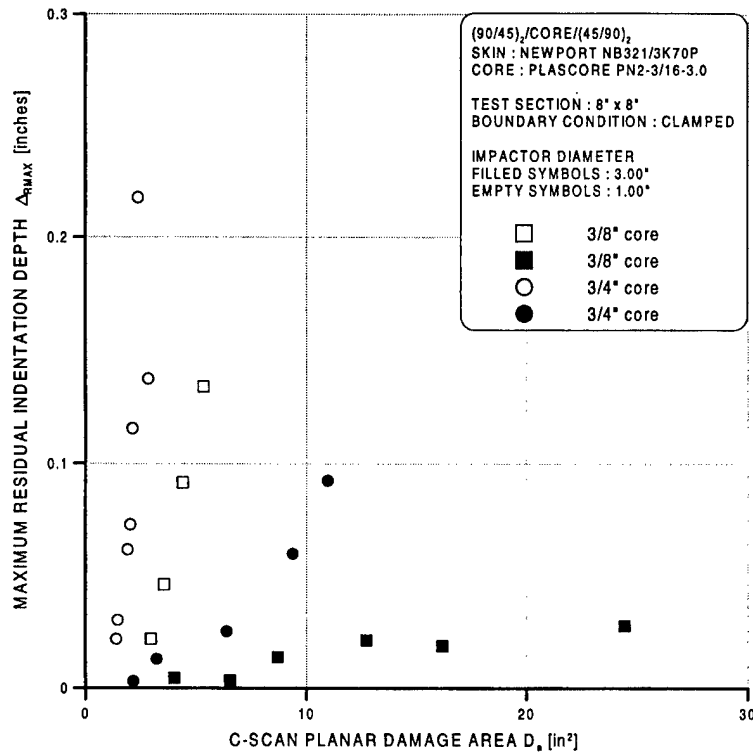


FIGURE 78b. MAXIMUM DENT DEPTH VS PLANAR DAMAGE AREA FOR [(90/45)₂/CORE/(45/90)₂] PANELS

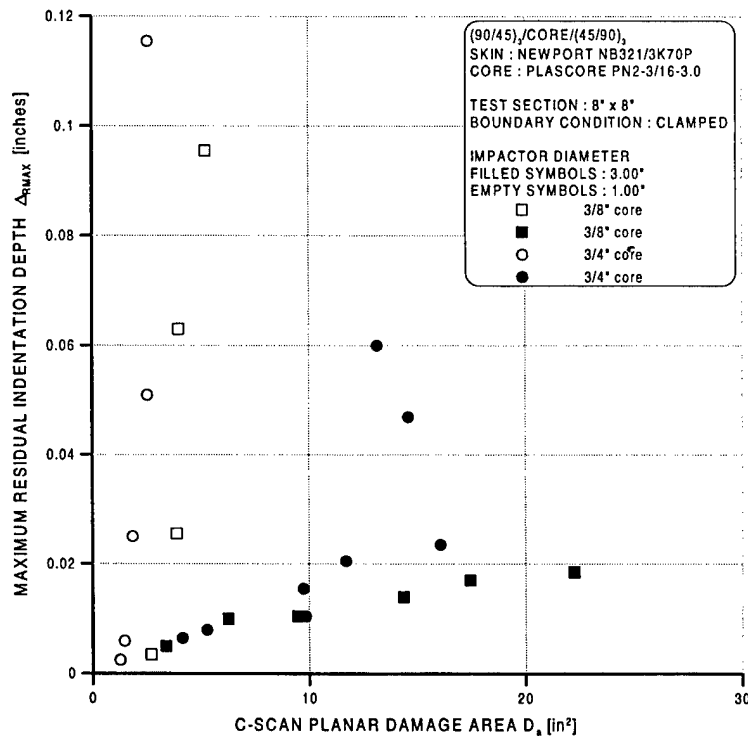


FIGURE 78c. MAXIMUM DENT DEPTH VS PLANAR DAMAGE AREA FOR [(90/45)₃/CORE/(45/90)₃] PANELS

The variation of CAI strength with the planar damage area for different sandwich configurations and impactor diameters is summarized in figures 79a to 79c. It can be observed that the CAI strengths decrease with increase in planar damage area. In fact, there is a change in failure mode from compressive failure of the skins (similar to open-hole specimens) to a local buckling initiated failure of the skins. The CAI strengths dropped to as much as 40% of the respective virgin strengths, as shown in figures 79a to 79c.

The variation of the CAI strengths with the maximum residual indentation depth for different sandwich configurations and impactor diameters is summarized in figures 80a to 80c. The trends clearly underline the disadvantage of using the dent depth as an indicator of severity of damage.

The specimens with higher dent depths possessed higher CAI strengths which corresponded to compressive failures while the specimens with significantly smaller dent depths (but had large damage areas) possessed lower CAI strengths corresponding to a local buckling induced failure mechanism.

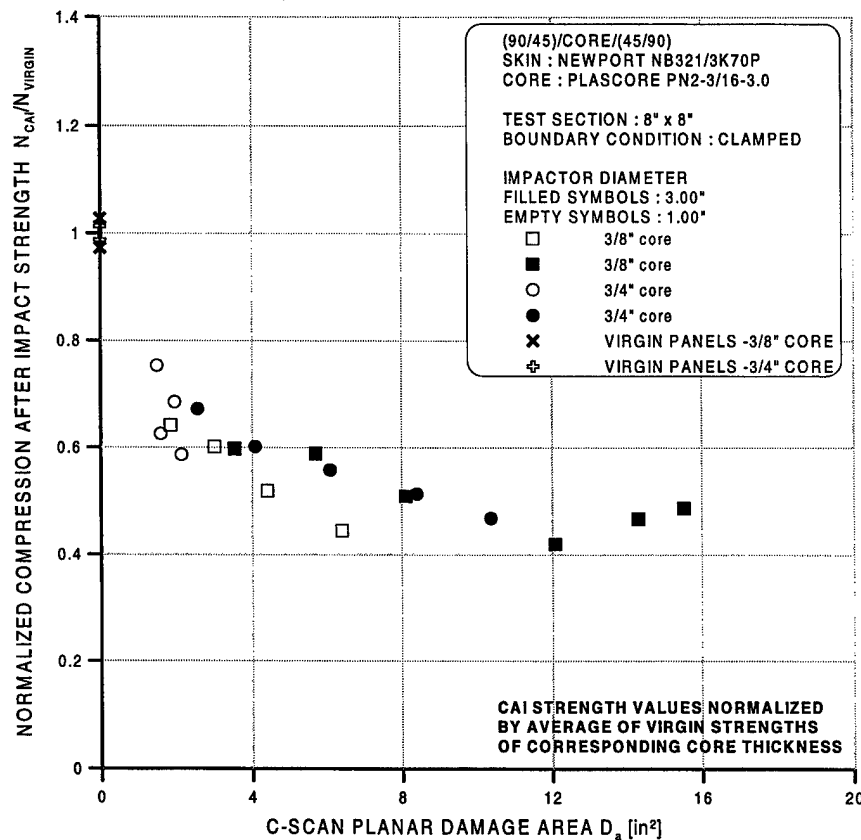


FIGURE 79a. COMPRESSION AFTER IMPACT STRENGTH VS PLANAR DAMAGE AREA FOR [(90/45)/CORE/(45/90)] PANELS

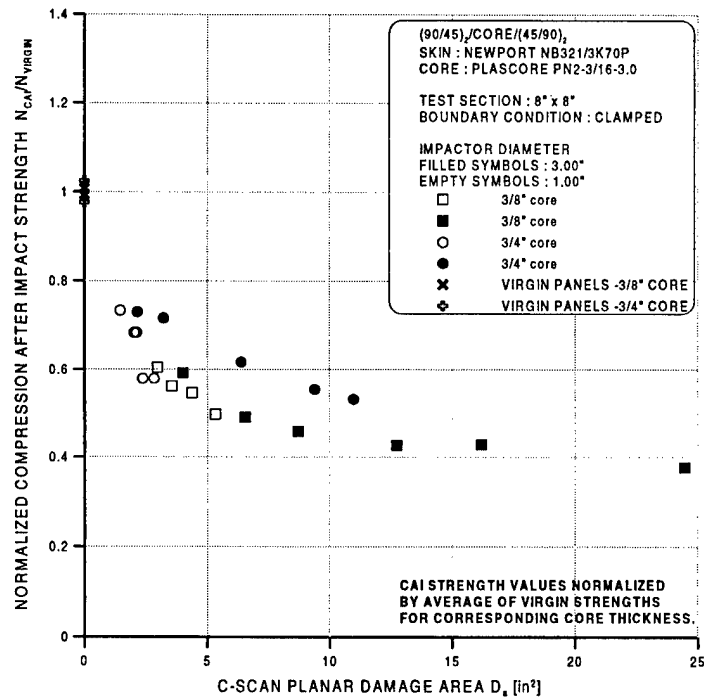


FIGURE 79b. COMPRESSION AFTER IMPACT STRENGTH VS PLANAR DAMAGE AREA FOR [(90/45)₂/CORE/(45/90)₂] PANELS

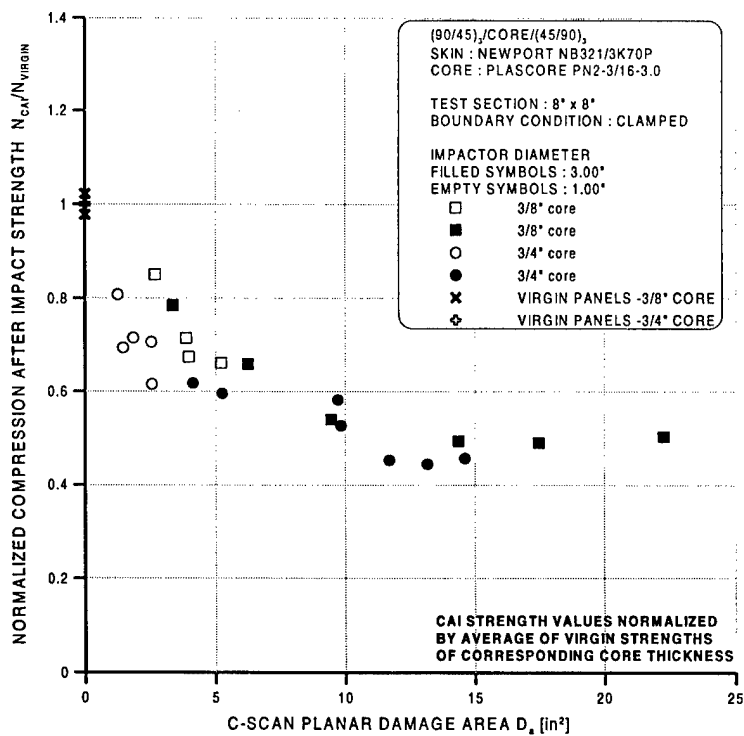


FIGURE 79c. COMPRESSION AFTER IMPACT STRENGTH VS PLANAR DAMAGE AREA FOR [(90/45)₃/CORE/(45/90)₃] PANELS

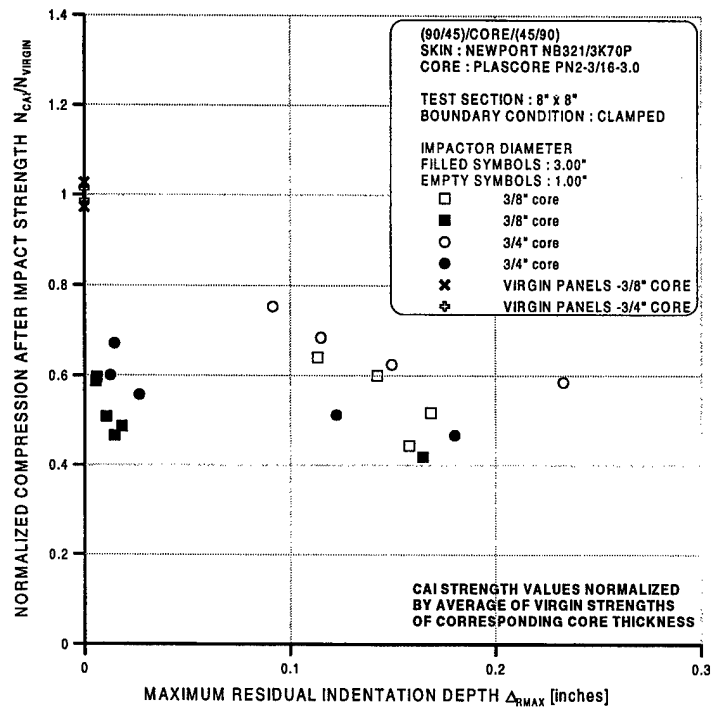


FIGURE 80a. COMPRESSION AFTER IMPACT STRENGTH VS MAXIMUM DENT DEPTH FOR [(90/45)/CORE/(45/90)] PANELS

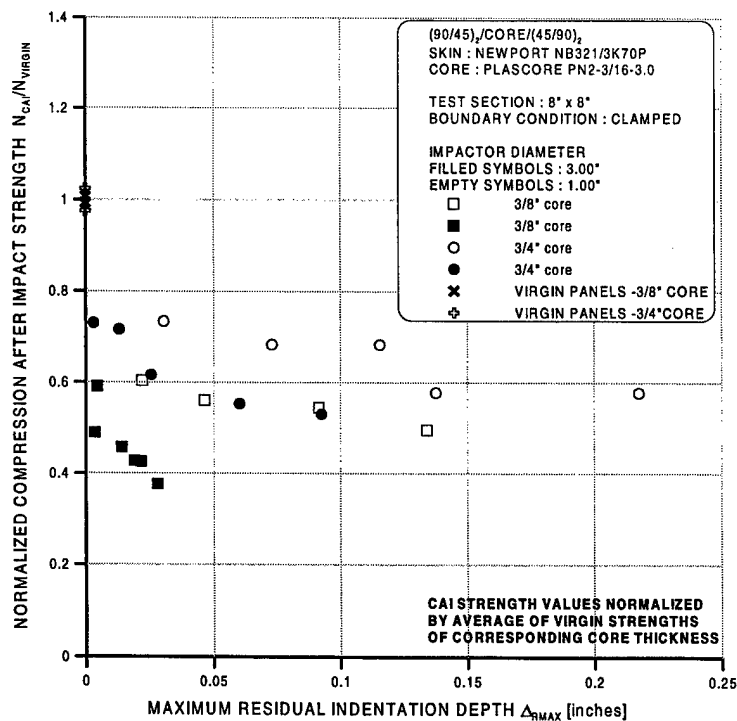


FIGURE 80b. COMPRESSION AFTER IMPACT STRENGTH VS MAXIMUM DENT DEPTH FOR [(90/45)₂/CORE/(45/90)₂] PANELS

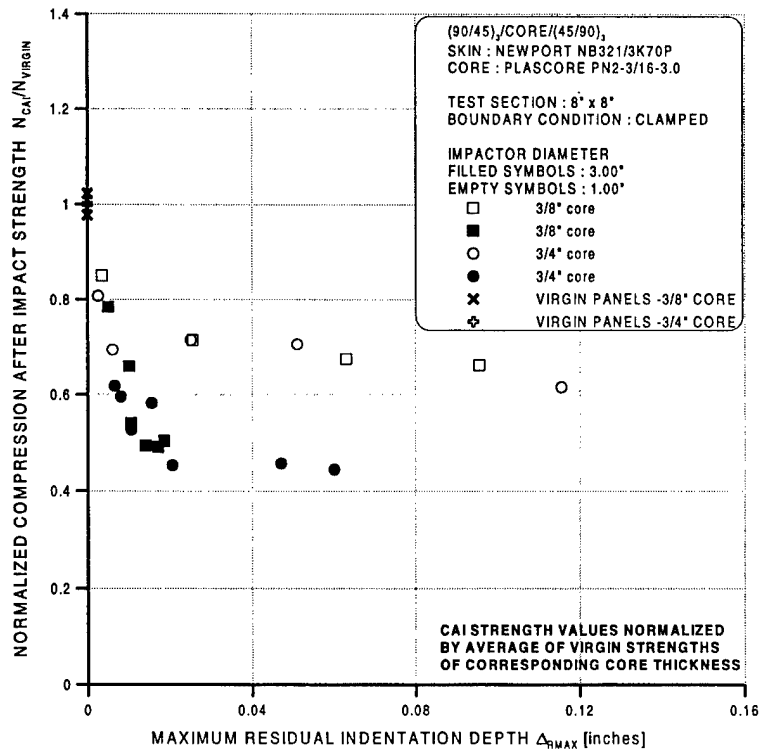


FIGURE 80c. COMPRESSION AFTER IMPACT STRENGTH VS MAXIMUM DENT DEPTH FOR [(90/45)₃/CORE/(45/90)₃] PANELS

7. CONCLUSIONS AND RECOMMENDATIONS.

The impact damage resistance and damage tolerance characteristics of honeycomb core sandwich specimens were studied experimentally. Three different quasi-isotropic skin lay-up sequences and two different core thicknesses ($\frac{3}{8}$ " and $\frac{3}{4}$ "), giving six sandwich configurations, were used in this study. The impact tests were conducted at a nominal constant impact velocity of 96.6 in/sec at various energy levels. Hemispherical steel impactors with diameters of 1.00" and 3.00" were used.

The impact test results indicated that the larger diameter impactor produced higher impact forces when compared to that of the small impactor. This trend was amplified at higher energy levels and tended to be negligible as the impact energy levels decreased. This can be attributed to the contrasting contact load distributions associated with the size of the impactors. Further, once core crushing was initiated, the local compliance was increased, which further contributed to load distribution over a larger area. The curvatures in the contact region tended to equal that of the impactor, which clearly explains the onset of skin fracture at lower impact energies for the small diameter impactor. Due to the load redistribution, the stiffness of the overall system tended to increase as evident from the peak impactor displacement, which was consistently less for the large impactor at all energy levels. Also, the duration of impact was shorter for the large impactor, indicating a stiffer system. However, at lower impact energies, the above trends tended to dissipate, indicating that in the regime of elastic impact, the effects of impactor diameter can be negligible.

The impacted specimens were subsequently inspected for damage using NDI methods. Damage metrics such as planar damage area (using TTU C-scan) and residual indentation depths were used to implicitly quantify the damage state. The results indicated that the large diameter impactor produced a very benign appearing damage state, wherein, no surface fracture or cracks nor visually perceptible levels of indentation existed, but the NDI did indicate a very large damaged region. A select number of impact experiments were repeated, the energy levels chosen from the current experience, and the specimens were subjected to destructive sectioning to study the true nature of the damage. It was observed that for specimens impacted with the large diameter impactor, the sandwich core had undergone localized crushing close to the impacted skin over a considerable area. However, the impacted skin, which had not suffered any noticeable damage, thus retaining most of its original stiffness (and aided by the now more compliant damaged core), had sprung back close to its original state. This damage scenario proved to be the most elusive when the impacted specimens were inspected using a typical visual inspection protocol. It is conclusively shown that the visual inspection methods are very misleading and the residual indentation cannot be used as a reliable damage metric for static ultimate strength and damage tolerance criteria for sandwich structure.

It is recommended that other damage metrics (e.g., planar damage size) need to be considered in addition to visual dent depth, when generating a database to support development and certification of composite sandwich structure. It is crucial to understand the effects of impact damage on static ultimate strength and damage tolerance criteria crucial to safety, as well as the implications to maintenance. One method for characterizing damage that is not clearly visible could be a simple manual tap, which is well within the capability of field inspections.

The effects of various damage states on the performance of the sandwich panels under load were quantified using a uniaxial edgewise compression test, popularly known as a CAI test. The CAI test results revealed that the damage states due to the large diameter impactor behaved as geometric imperfections leading to a local stability governed failure mode. Further, the failure loads corresponding to the buckling mode were well below that corresponding to a pure compressive failure of the skins associated with damage states which were more representative of stress raisers, due to the small diameter impactor.

Another important exercise that was conducted as part of this program was the investigation of finite width and length effects in the residual strength specimens. The results of the program indicated that the current specimen size (8.00" wide \times 10.50" high) was generally free of any significant finite length effects, i.e., there was no evidence of shear lag phenomenon in the experimental results. A very slight finite width effect was observed for the specimen with the largest damage size (core crush area) with facesheet disbond and fracture.

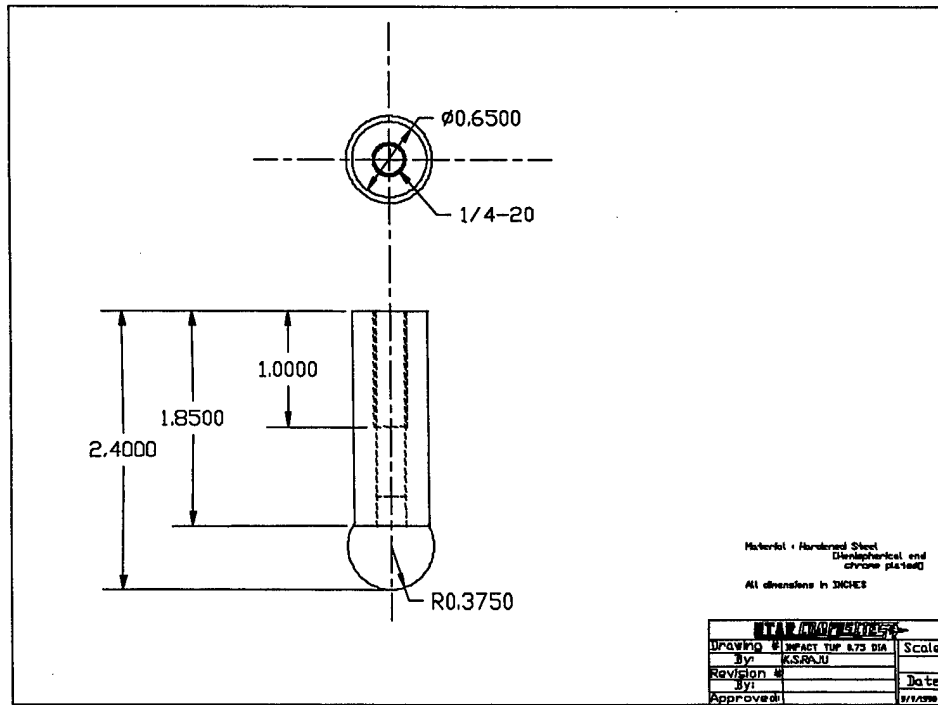
8. REFERENCES.

1. J. Tomblin, T. Lacy, B. Smith, S. Hoopes, A. Vizzini, and S. Lee, "Review of Damage Tolerance for Composite Sandwich Airframe Structures," Final Report, DOT/FAA/AR-99/49, August 1999.
2. R.C. Moody and A.J. Vizzini, "Damage Tolerance of Composite Sandwich Structures," Final Report, DOT/FAA/AR-99/91, January 2000.
3. Rhodes, M.D., "Impact Fracture of Composite Sandwich Panels," AIAA 1975-748, NASA Langley Research Center, Hampton, VA 23665.
4. Sharma, A.V., "Damage Tolerance of Composite Sandwich Structures Subjected to Projectile Impact," 11th National SAMPE Technical Conference, November 13-15, 1979.
5. C. Kassapoglou, P.J. Jonas, and R. Abbott, "Compressive Strength of Composite Sandwich Panels After Impact Damage: An Experimental and Analytical Study," Journal of Composite Technology & Research, Vol. 10, No. 1, Summer 1988, pp. 65-73.
6. M.L. Bernard and P.A. Lagace, "Impact Resistance of Composite Sandwich Plates," JI. of Reinforced Plastics and Composites, Vol. 8, September 1989.
7. S. Llorente, D. Weems, and R. Fay, Structures Technology, Boeing Helicopters, Philadelphia, PA "For Improved Durability and Damage Tolerance," 46th Annual Forum, American Helicopter Society, Washington, DC, May 21-23, 1990.
8. P.H.W. Tsang, and J. Dugundji, "Damage Resistance of Graphite/Epoxy Sandwich Panels Under Low Speed Impacts," 46th Annual Forum, American Helicopter Society, Washington, DC, May 1990.
9. T. Saczalski, B. Lucht, and D. Steeb, "Advanced Experimental Design Applied to Damage Tolerance of Composite Materials," 23rd International SAMPE Technical Conference, October 21-24, 1991.
10. C. Hiel and O. Ishai, NASA Ames Research Center, CA, "Design of Highly Damage-Tolerant Sandwich Panels," 37th International SAMPE Symposium, March 9-12, 1992.
11. O. Ishai and C. Hiel, "Damage Tolerance of a Composite Sandwich With Interleaved Foam Core," JI of Composites Technology & Research, JCTRER, Vol. 14, No. 3, Fall 1992, pp. 155-168.
12. S.G. Russell, W. Lin, H.P. Kan, and R.B. Deo, "Damage Tolerance and Fail-Safety of Composite Sandwich Panels," SAE 942159, 1994.
13. R.A.W. Mines, C.W. Worrall, and A.G. Gibson, "The Static and Impact Behaviour of Polymer Composite Sandwich Beams," Composites, Vol. 25, No. 2, 1994.

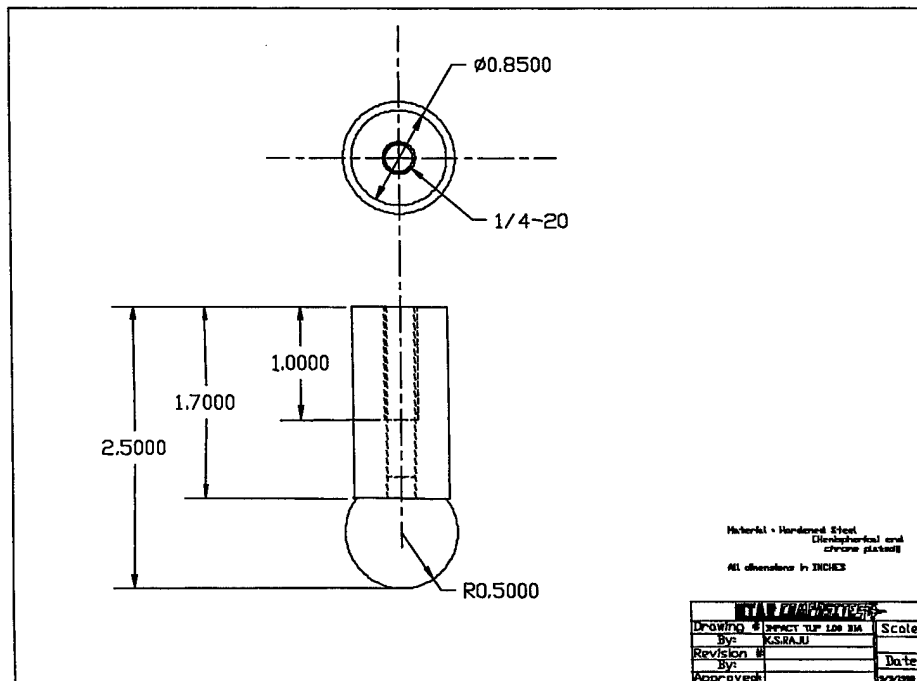
14. W.G. Baron, W.G. Smith, and G.J. Czamecki, "Damage Tolerance of Composite Sandwich Structure," AIAA-95-1324-CP.
15. O. Ishai, C. Hiel, and M. Luft, "Long-Term Hygrothermal Effects on Damage Tolerance of Hybrid Composite Sandwich Panels," *Composites*, Vol. 26, No. 1, 1995.
16. C. Kassapoglou, "Compression Strength of Composite Sandwich Structures After Barely Visible Impact Damage," *Jl of Composites Technology & Research, JCTRER*, Vol. 18, No. 4, October 1996, pp. 274-284.
17. D.M. McGowan and D.R. Ambur, "Damage Tolerance Characteristics of Composite Fuselage Sandwich Structures With Thick Facesheets," NASA Technical Memorandum 110303, February 1997.
18. E.F. Dost, W.B. Avery, S.R. Finn, D.H. Grande, A.B. Huisken, L.B. Ilcewicz, D.P. Murphy, D.B. Scholz, B.R. Coxon, and R.E. Wishart, "Impact Damage Resistance of Composite Fuselage Structure," NASA Contractor Report 4658, April 1997.
19. D.M. McGowan and D.R. Ambur, "Damage Characteristics and Residual Strength of Composite Sandwich Panels Impacted With and Without Compression Loading," AIAA 98-1783.
20. M.S. Rosenfeld and L.W. Gause, "Compression Fatigue Behavior of Graphite/Epoxy in the Presence of Stress Raisers," ASTM STP 723, ASTM, 1981, pp. 174-196.
21. E.G. Guynn and T.K. O'Brien, "The Influence of Lay-Up and Thickness on Composite Impact Damage and Compression Strength," AIAA 85-0646.
22. H.Y.T. Wu and G.S. Springer, "Impact Induced Stresses, Strains and Delaminations in Composite Plates," *Jl. of Composite Materials*, Vol. 22, pp. 533-560, June 1988.
23. H.Y.T. Wu and G.S. Springer, "Measurements of Matrix Cracking and Delamination Caused by Impact on Composite Plates," *Jl. of Composite Materials*, Vol. 22, pp. 518-532, June 1988.
24. D. Liu, "Impact Induced Delamination—A View of Bending Stiffness Mismatching," *Jl. of Composite Materials*, Vol. 22, pp. 674-692, July 1988.
25. C. C. Poe, Jr., "Relevance of Impactor Shape to Nonvisible Damage and Residual Tensile Strength of a Thick Graphite/Epoxy Laminate," ASTM STP 1110, T. K. O'Brien ed., ASTM, 1991, pp. 501-527.
26. R.B. Bucinell, R.J. Nuismer, and J.L. Koury, "Response of Composite Plates to Quasi-Static Impact Events," ASTM STP 1110, T. K. O'Brien ed., ASTM, 1991, pp. 528-549.

27. S. Girshovich, T. Gottesman, H. Rosenthal, E. Drukker, and Y. Steinberg, "Impact Damage Assessment of Composites," ASTM STP 1128, J. E. Masters, ed., ASTM, 1992, pp. 183-199.
28. R.J. Chester and G. Clark, "Modeling of Impact Damage Features in Graphite/Epoxy Laminates," ASTM STP 1128, J. E. Masters, ed., ASTM, 1992, pp. 200-212.
29. D.R. Ambur and J.H. Starnes, Jr., "Effect of Curvature on the Impact Damage Characteristics and Residual Strength of Composite Plates," AIAA 98-1881.
30. D.R. Ambur and H.L. Kemmerly, "Influence of Impactor Mass on the Damage Characteristics and Failure Strength of Laminated Composite Plates," AIAA 98-1784.
31. E. Wu and Ling-Cheng Chang, "Loading Rate Effect on Woven Glass Laminated Plates by Penetration Force," Journal of Composite Materials, Vol. 32, No. 8, 1998.
32. H.D. Espinosa, H.C. Lu, and Y. Xu, "A Novel Technique for Penetrator Velocity Measurement and Damage Identification in Ballistic Penetration Experiments," Journal of Composite Materials, Vol. 32, No. 8, 1998.
33. E. Demuts and R. B. Sandhu, "Barely Visible Damage Threshold in a BMI," Wright Laboratory, Flight Dynamics Directorate, WL/FIBEC, Wright-Patterson AFB, Ohio 45433.
34. D. Liu and L.E. Malvern, "Matrix Cracking in Impacted Glass/Epoxy Plates," JI. of Composite Materials, Vol. 21, pp. 594-609, July 1987.
35. "Standard Tests for Toughend Resin Composites," NASA Reference Publication 1092, May 1982.
36. ATCAS Monthly Technical Progress Reports No. 44, 49.

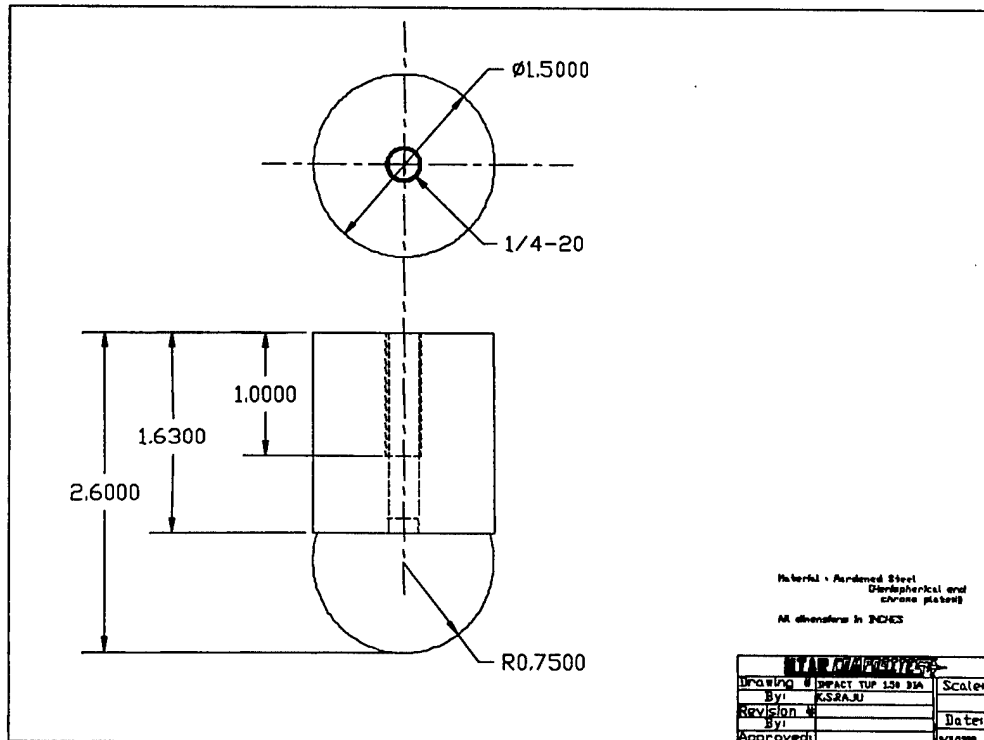
APPENDIX A—DETAILED DRAWINGS OF IMPACT TUPS



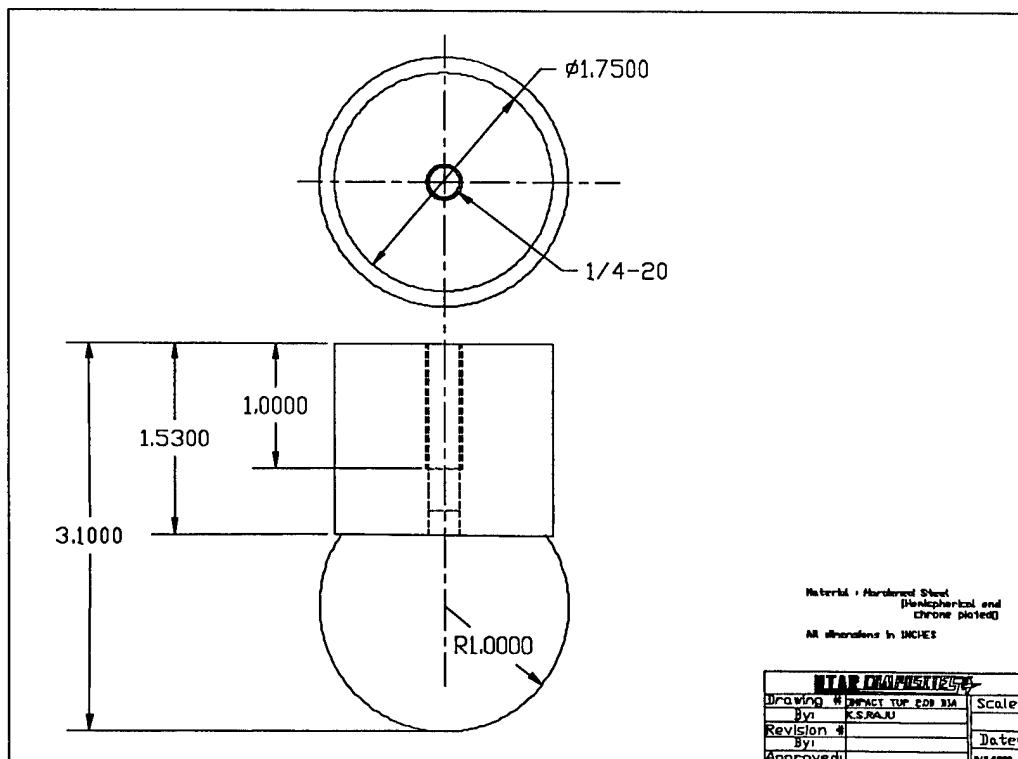
A-1. IMPACT TUP 0.75" DIAMETER



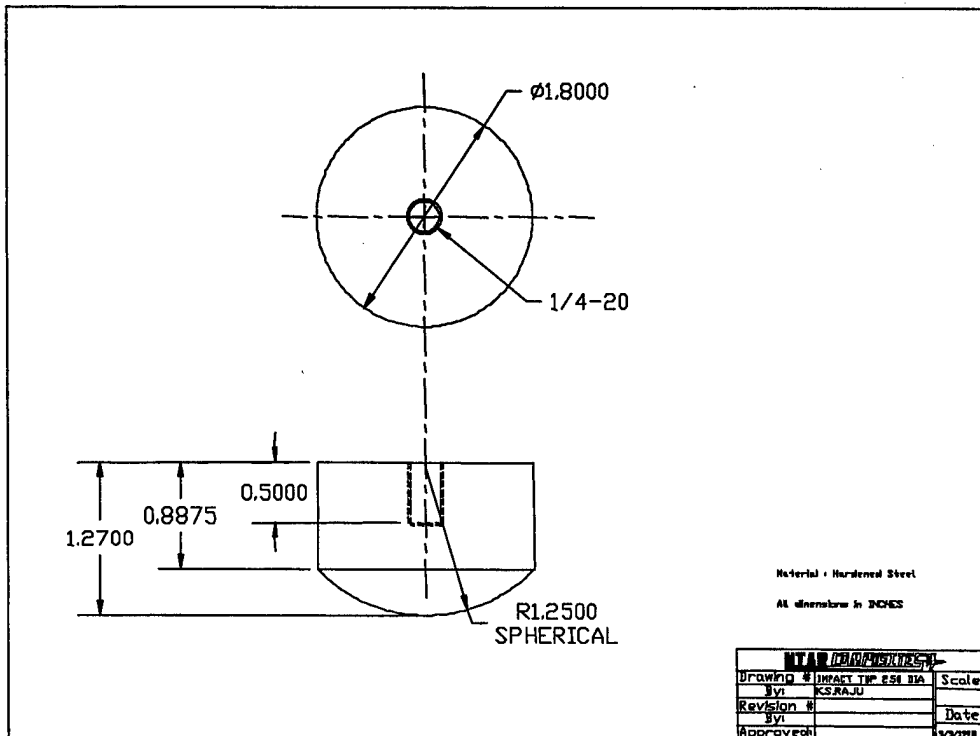
A-2. IMPACT TUP 1.00" DIAMETER



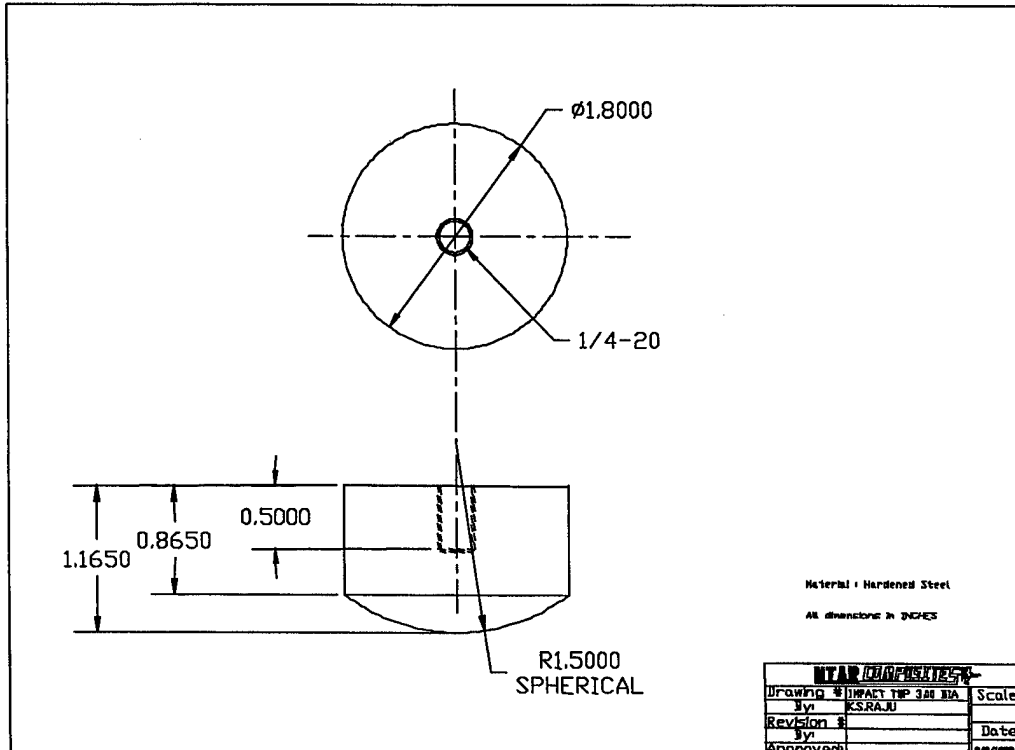
A-3. IMPACT TUP 1.50" DIAMETER



A-4. IMPACT TUP 2.00" DIAMETER

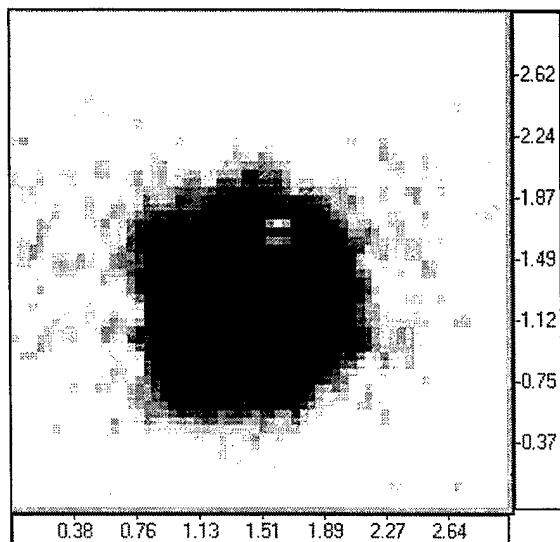


A-5. IMPACT TUP 2.50" DIAMETER

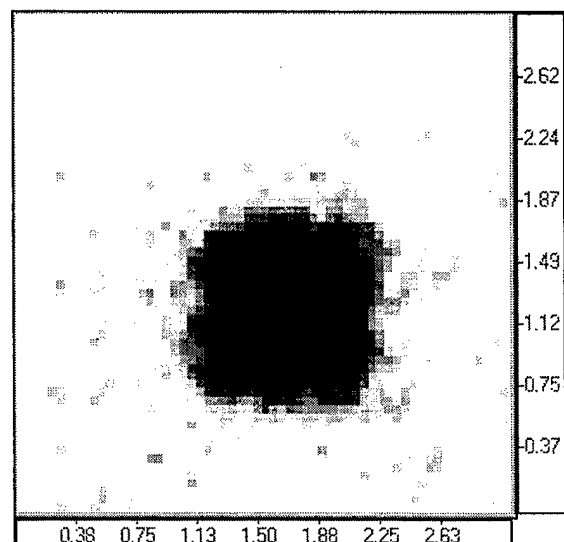


A-6. IMPACT TUP 3.00" DIAMETER

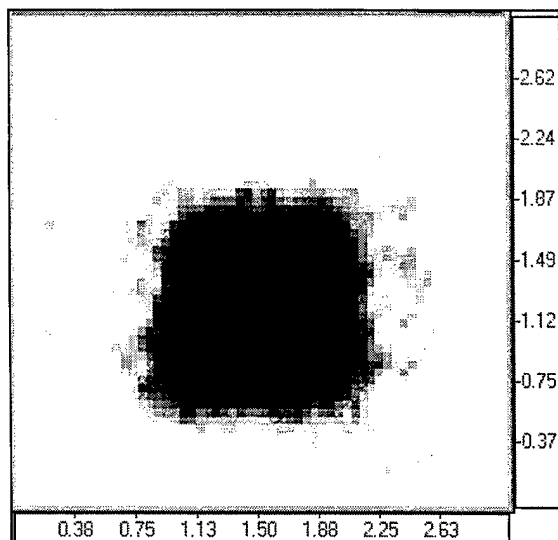
APPENDIX B—THROUGH TRANSMISSION ULTRASONIC (TTU) C-SCAN DAMAGE
MAPS OF IMPACTED SANDWICH PANELS



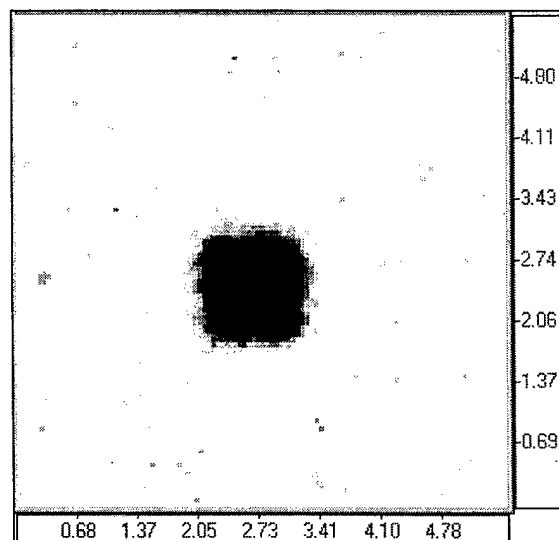
WXC11C



WXC13C

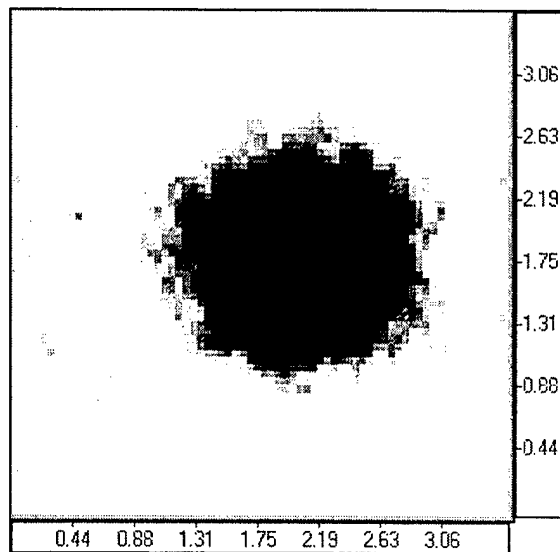


WXC12C

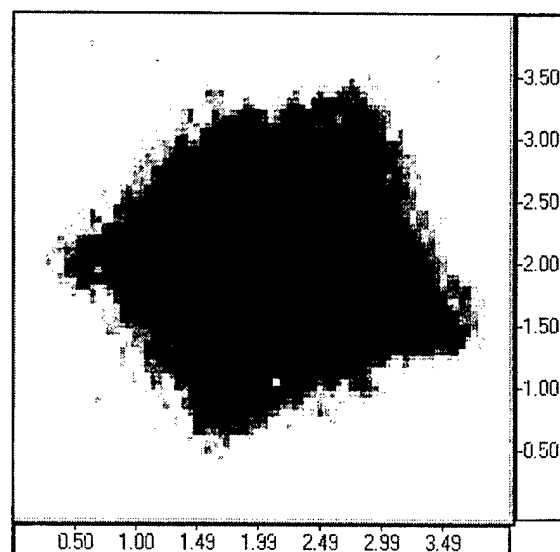


WXC14C

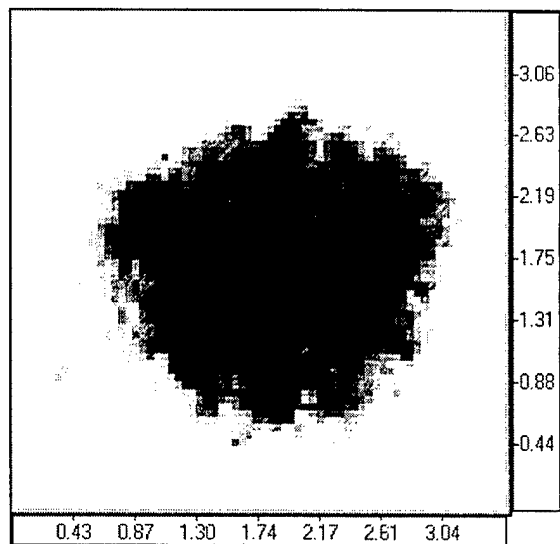
FIGURE B-1. TTU C-SCAN DAMAGE MAPS OF WXC11C, WXC12C, WXC13C, AND
WXC14C PANELS



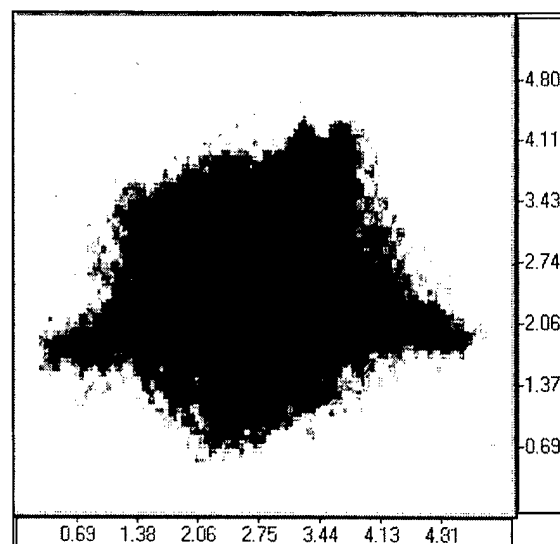
WXC11D



WXC13D

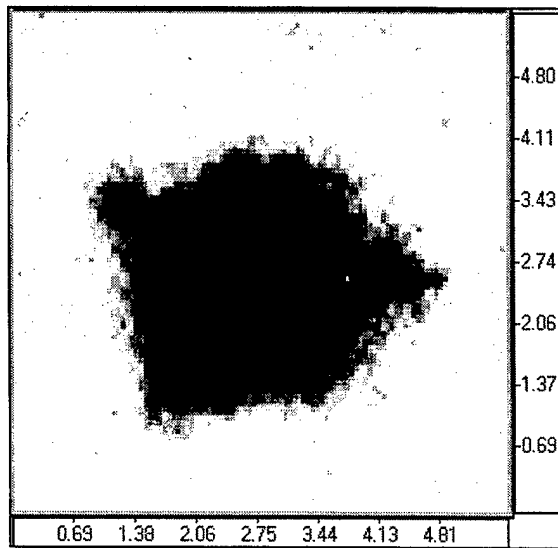


WXC12D

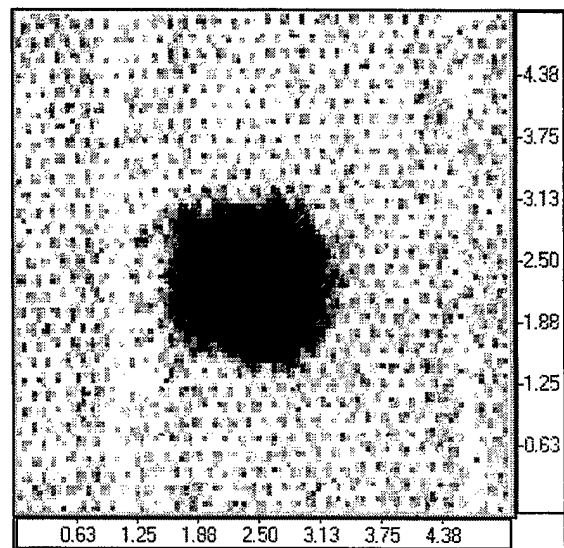


WXC14D

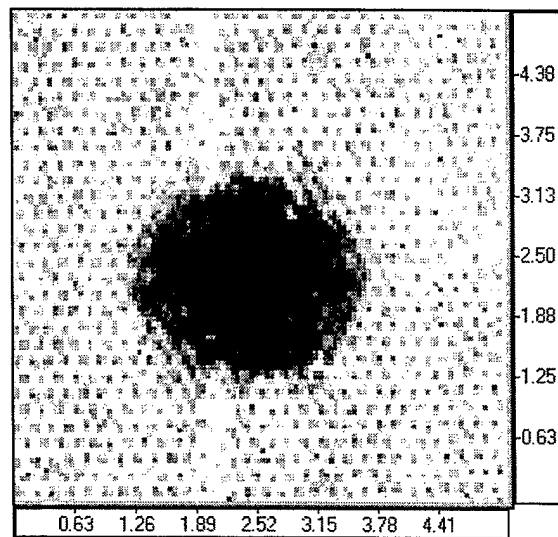
FIGURE B-2. TTU C-SCAN DAMAGE MAPS OF WXC11D, WXC12D, WXC13D, AND WXC14D PANELS



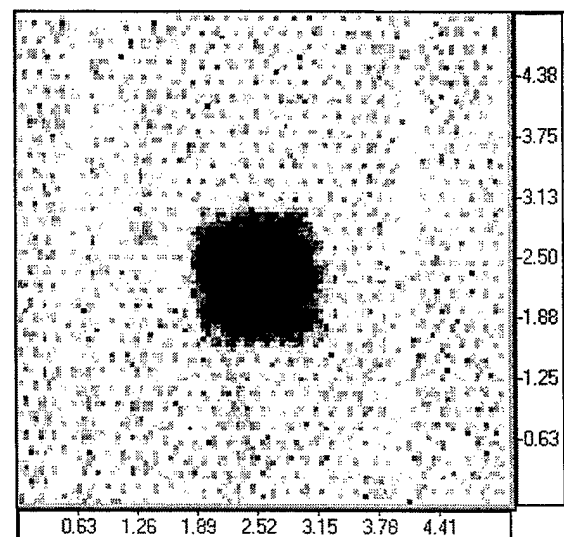
WXC15D



WXC12B

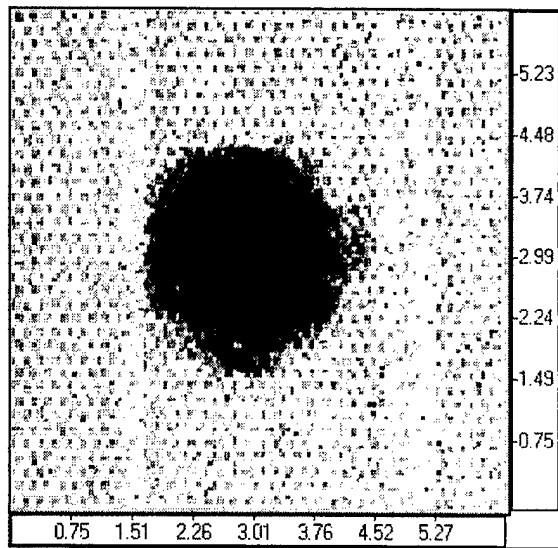


WXC11B

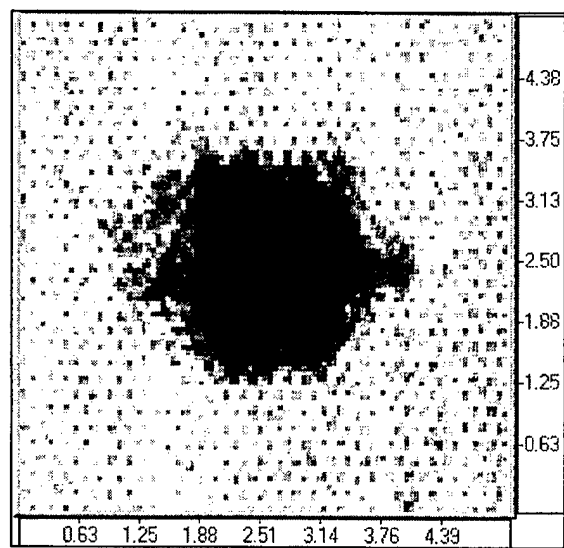


WXC13B

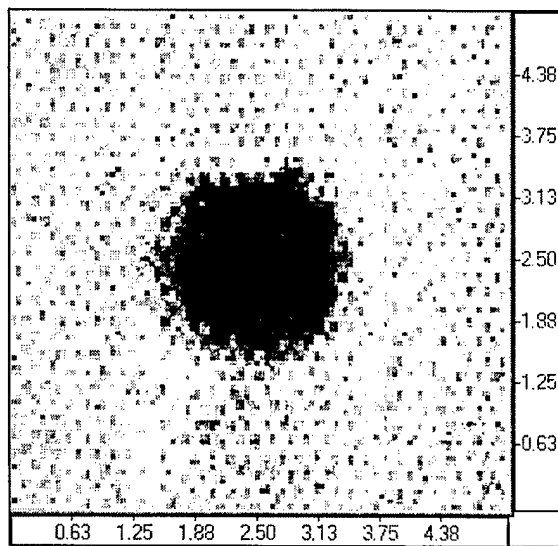
FIGURE B-3. TTU C-SCAN DAMAGE MAPS OF WXC15D, WXC11B, WXC12B, AND WXC13B PANELS



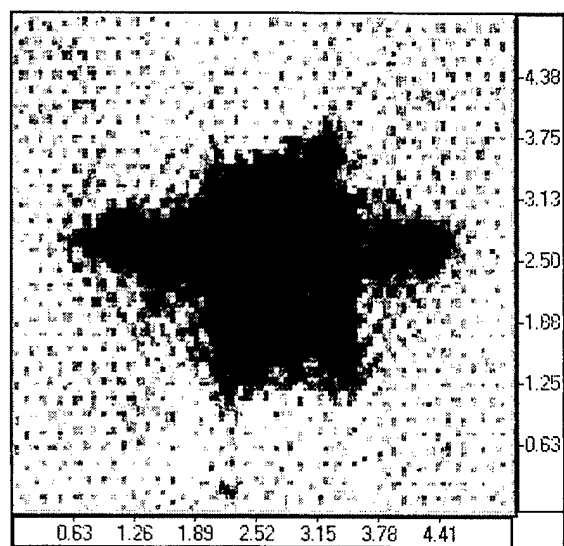
WXC14B



WXC12A

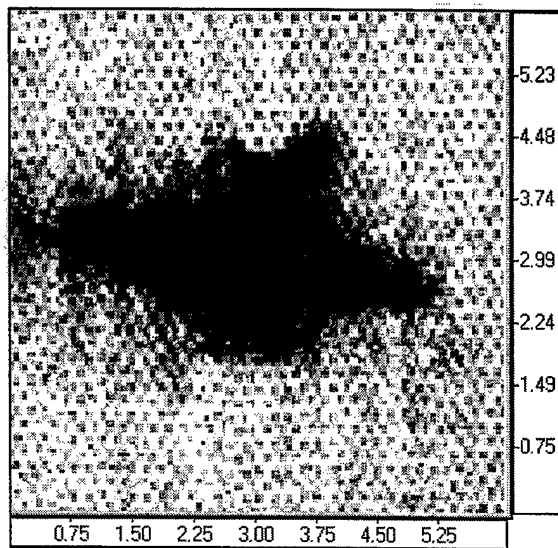


WXC11A

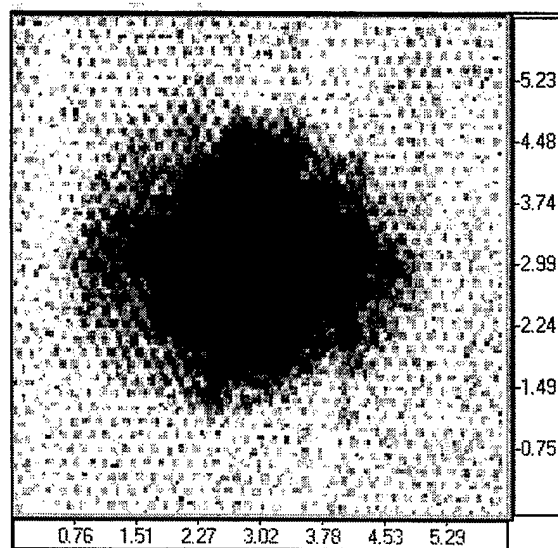


WXC13A

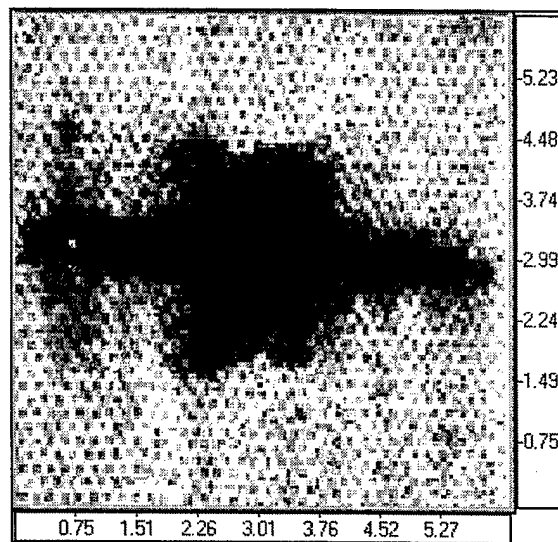
FIGURE B-4. TTU C-SCAN DAMAGE MAPS OF WXC14B, WXC11A, WXC12A, AND WXC13A PANELS



WXC14A

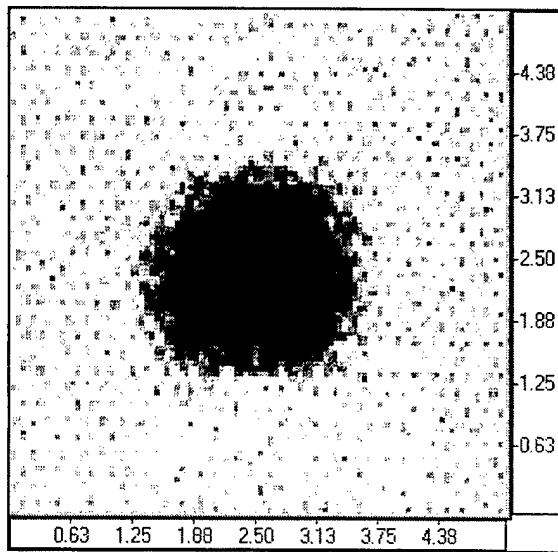


WXC15B

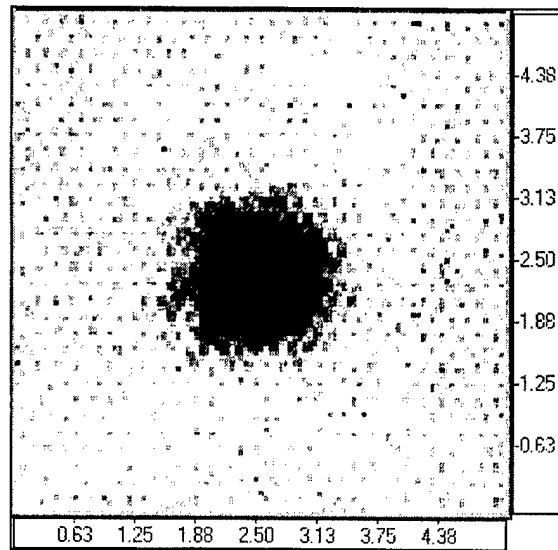


WXC15A

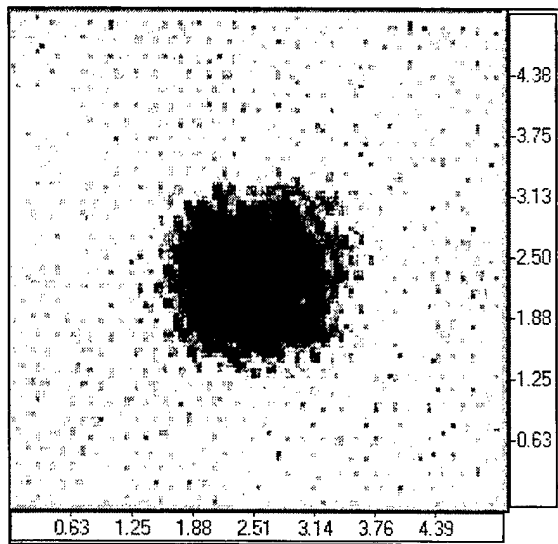
FIGURE B-5. TTU C-SCAN DAMAGE MAPS OF WXC14A, WXC15A, AND WXC15B PANELS



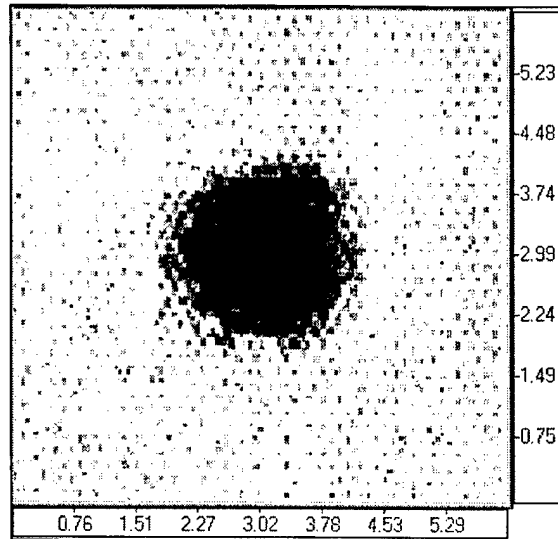
WXC21E



WXC23E

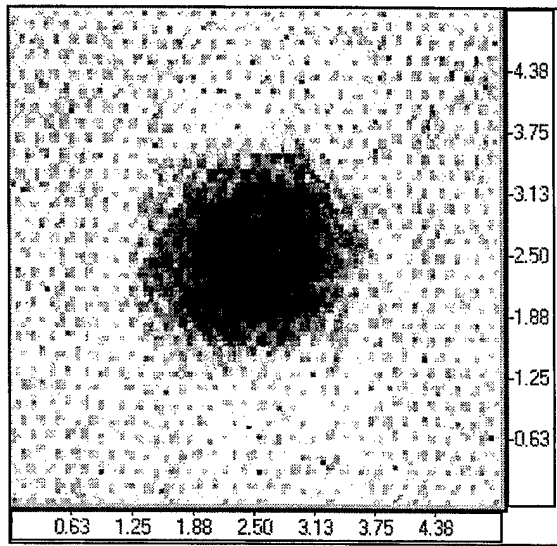


WXC22E

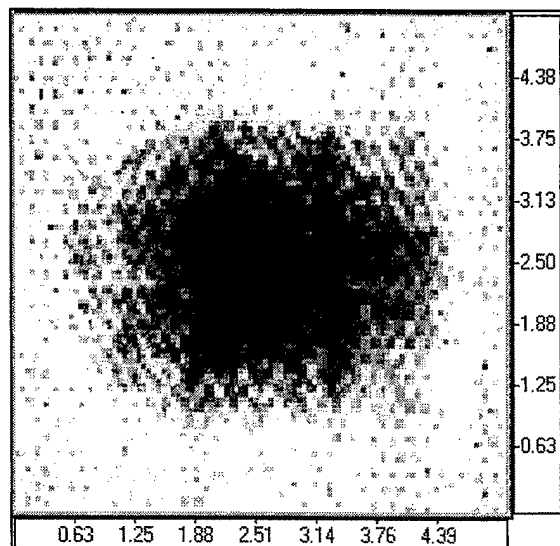


WXC24E

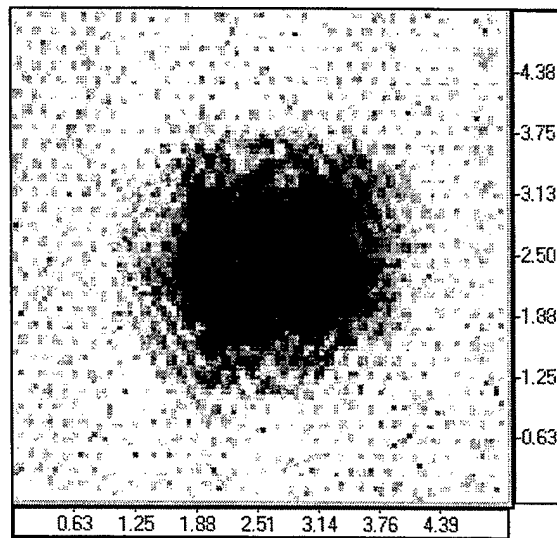
FIGURE B-6. TTU C-SCAN DAMAGE MAPS OF WXC21E, WXC22E, WXC23E, AND WXC24E PANELS



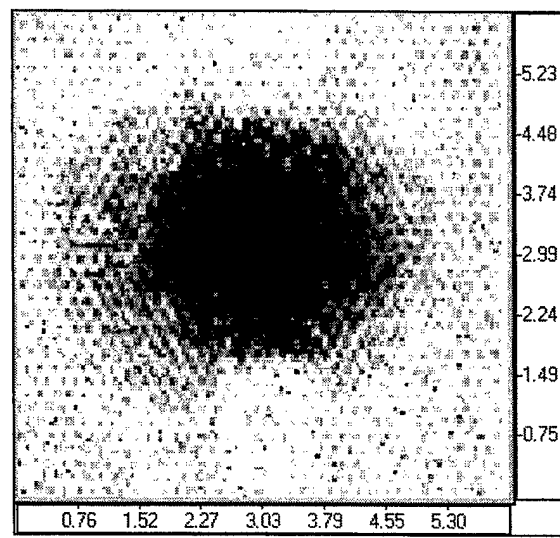
WXC21F



WXC23F

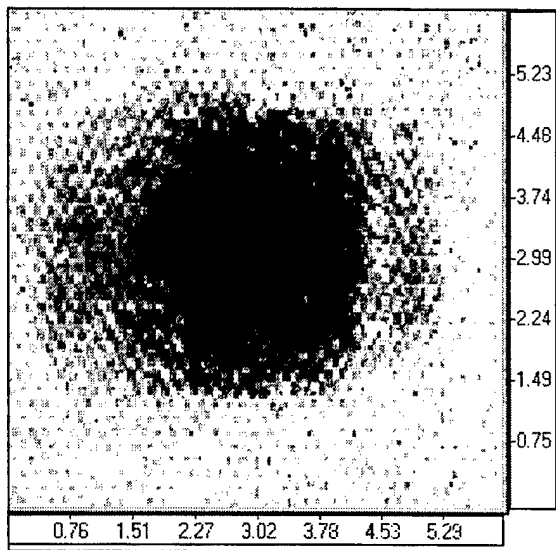


WXC22F

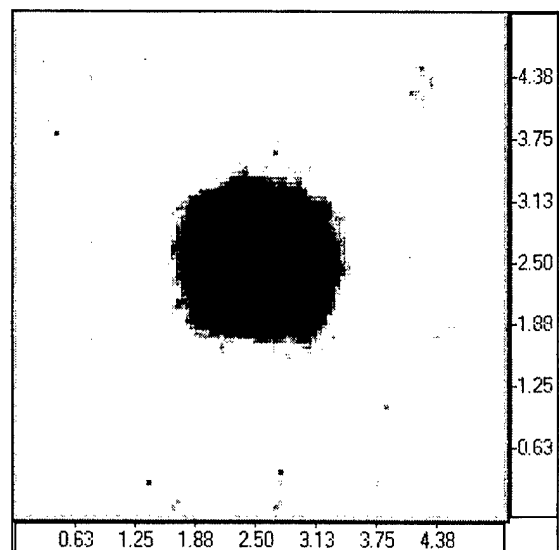


WXC24F

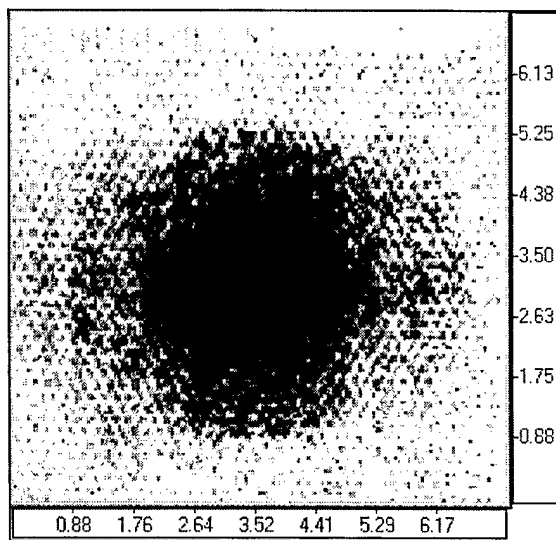
FIGURE B-7. TTU C-SCAN DAMAGE MAPS OF WXC21F, WXC22F, WXC23F, AND WXC24F PANELS



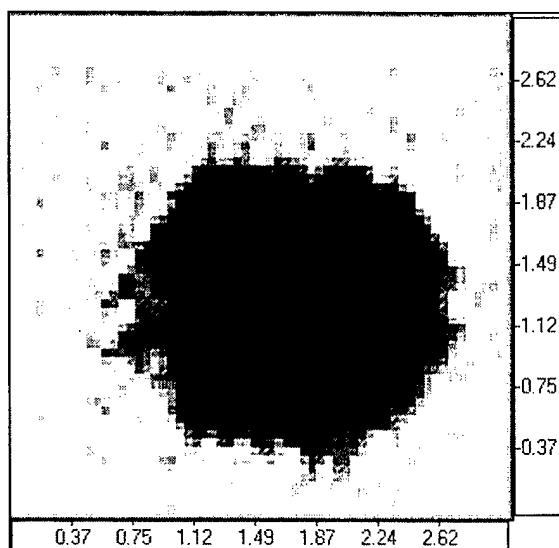
WXC25F



WXC21H

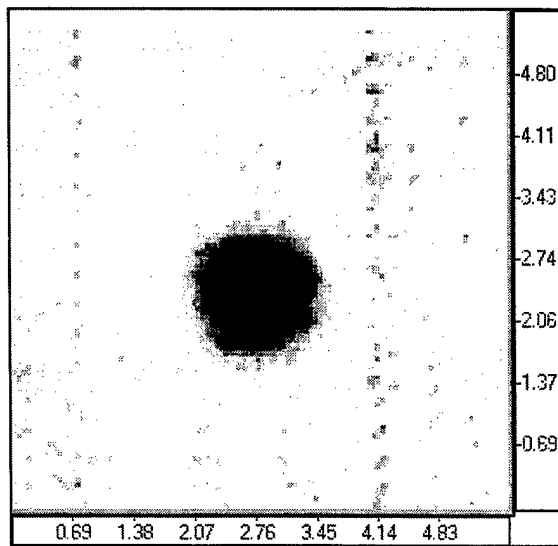


WXC25E

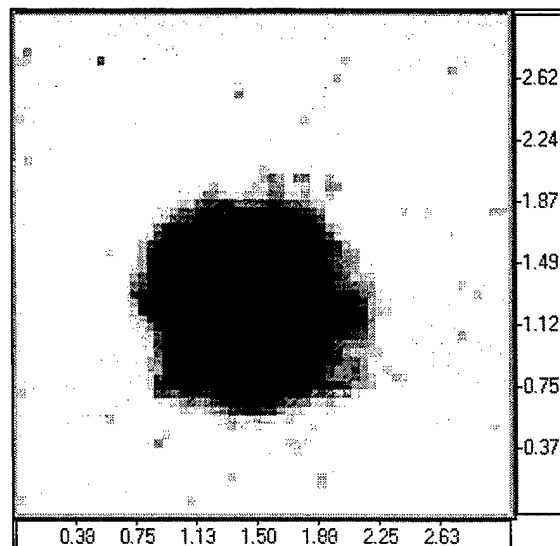


WXC22H

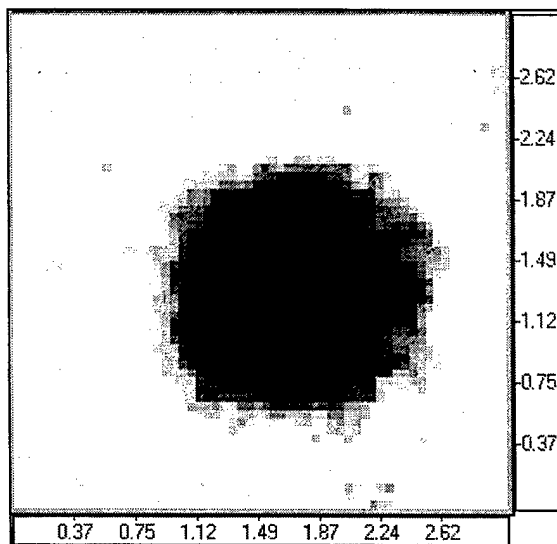
FIGURE B-8. TTU C-SCAN DAMAGE MAPS OF WXC25F, WXC25E, WXC21H, AND WXC22H PANELS



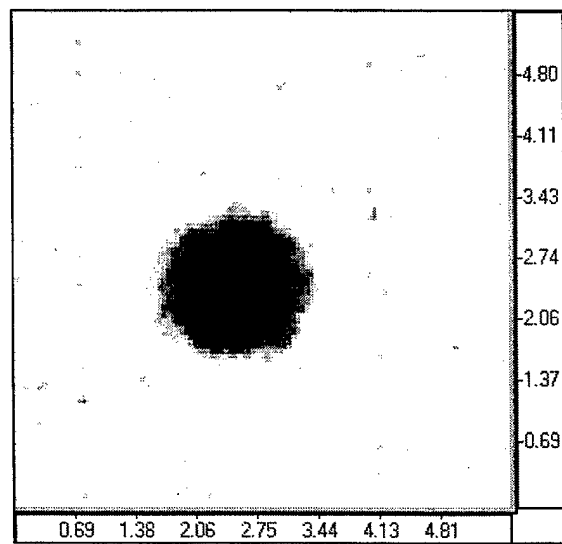
WXC23H



WXC25H

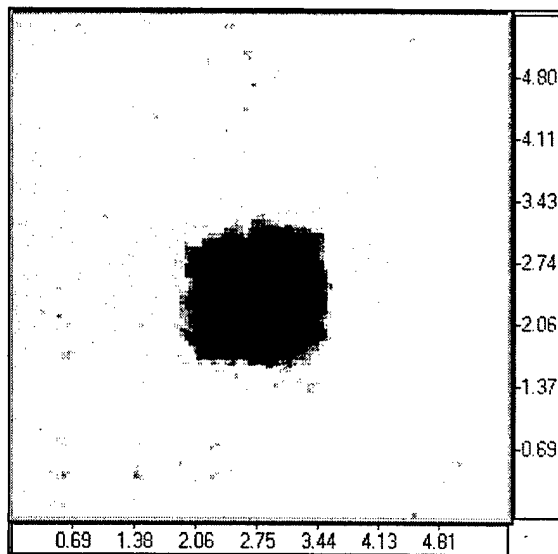


WXC24H

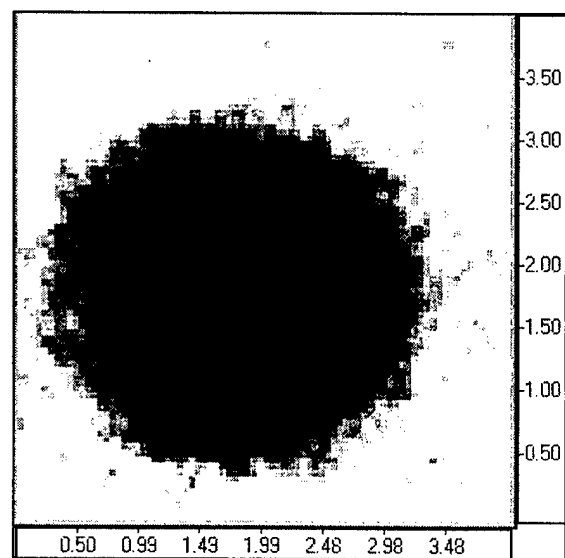


WXC26H

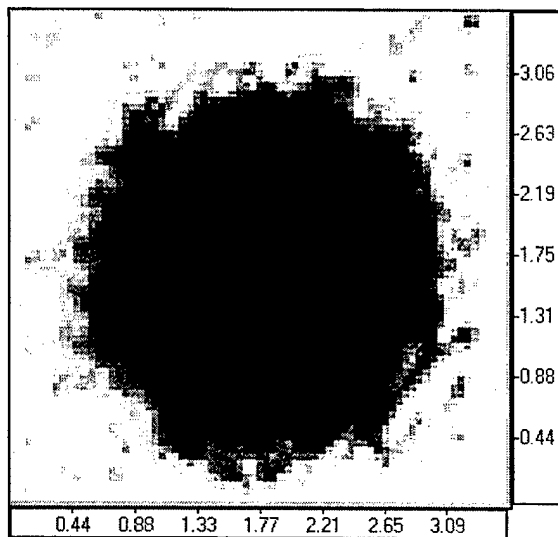
FIGURE B-9. TTU C-SCAN DAMAGE MAPS OF WXC23H, WXC24H, WXC25H, AND WXC26H PANELS



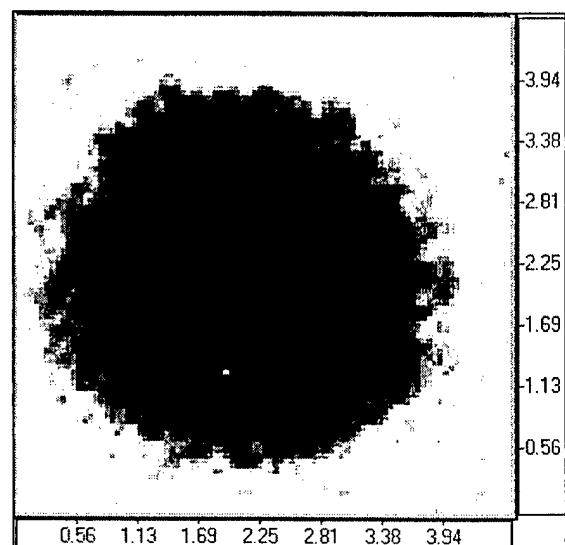
WXC27H



WXC21G

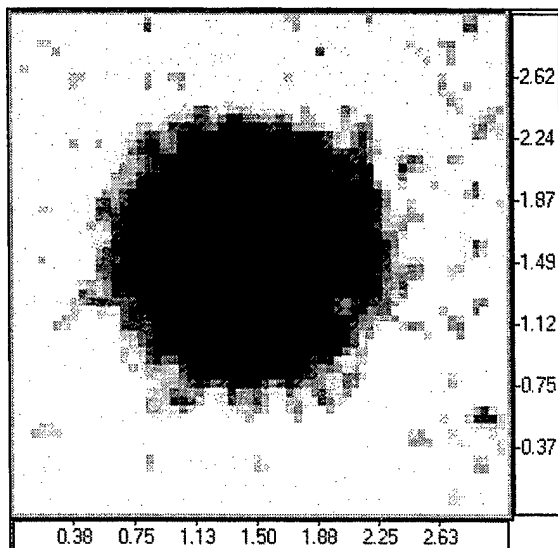


WXC21L

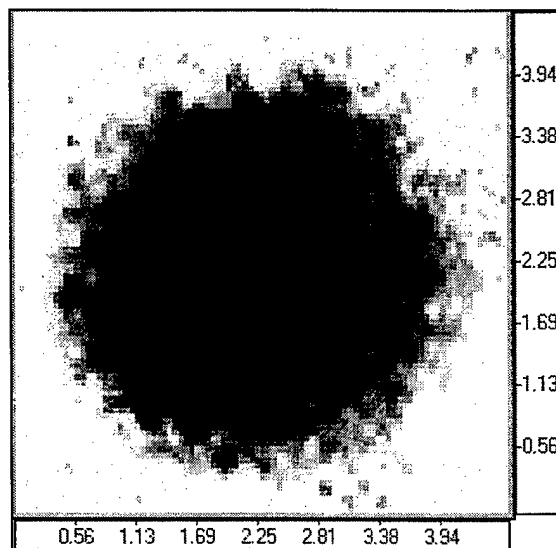


WXC22G

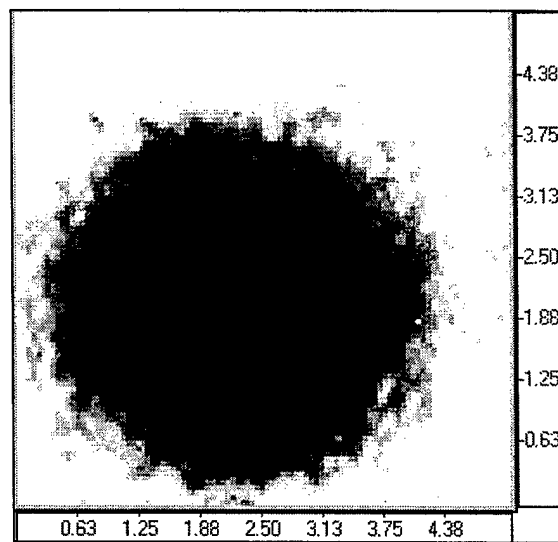
FIGURE B-10. TTU C-SCAN DAMAGE MAPS OF WXC27H, WXC21L, WXC21G, AND WXC22G PANELS



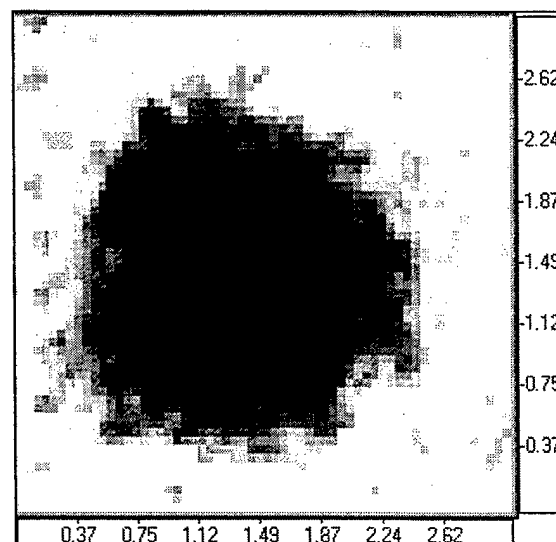
WXC23G



WXC24L

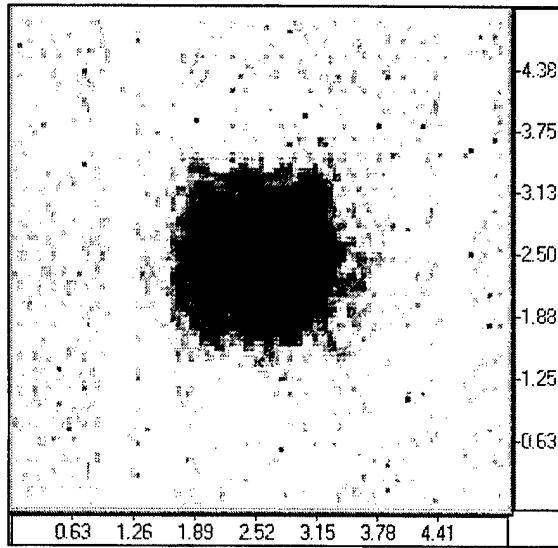


WXC24G

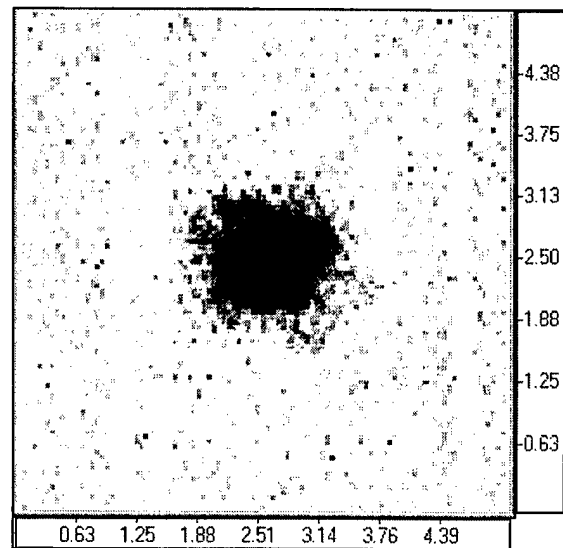


WXC25G

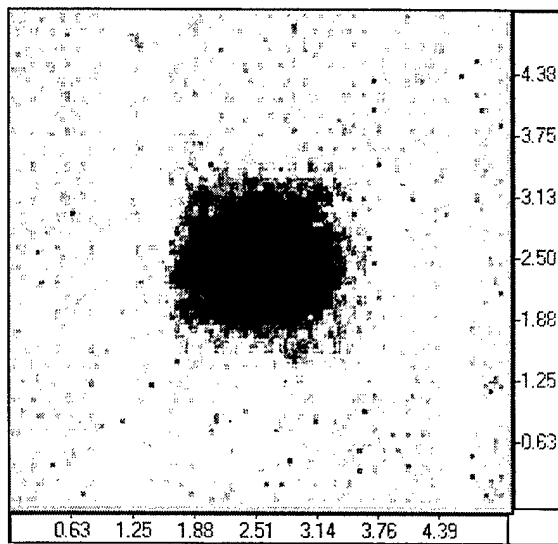
FIGURE B-11 TTU C-SCAN DAMAGE MAPS OF WXC23G, WXC24G, WXC24L, AND WXC25G PANELS



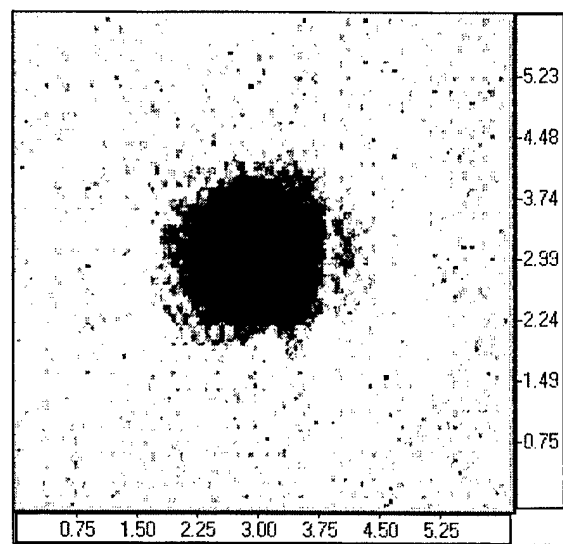
WXC31M



WXC33M

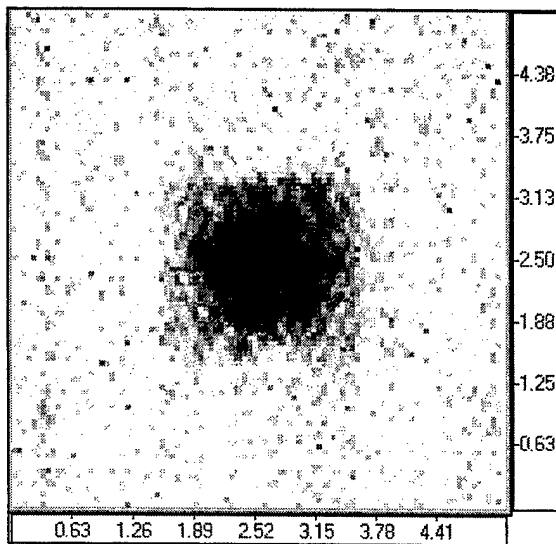


WXC32M

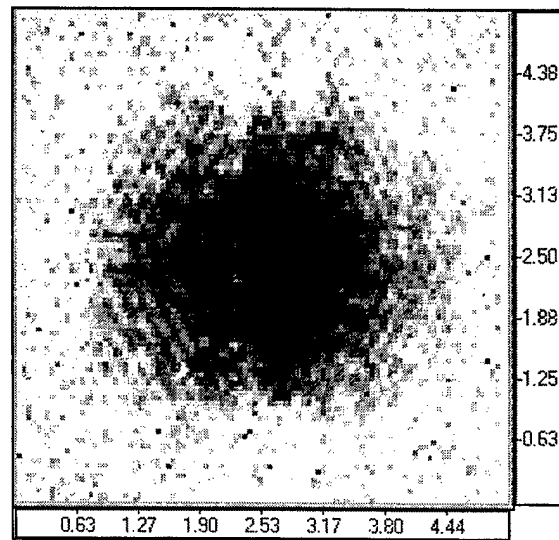


WXC34M

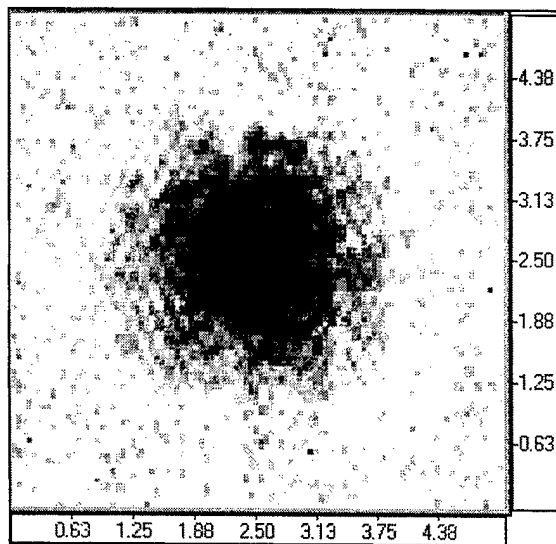
FIGURE B-12 TTU C-SCAN DAMAGE MAPS OF WXC31M, WXC32M, WXC33M, AND WXC34M PANELS



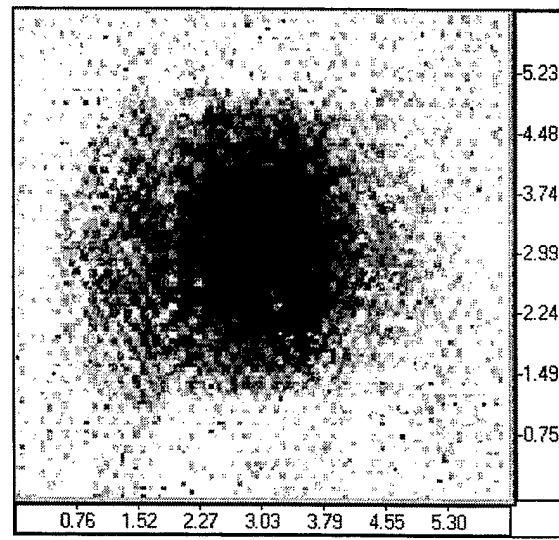
WXC31N



WXC33N

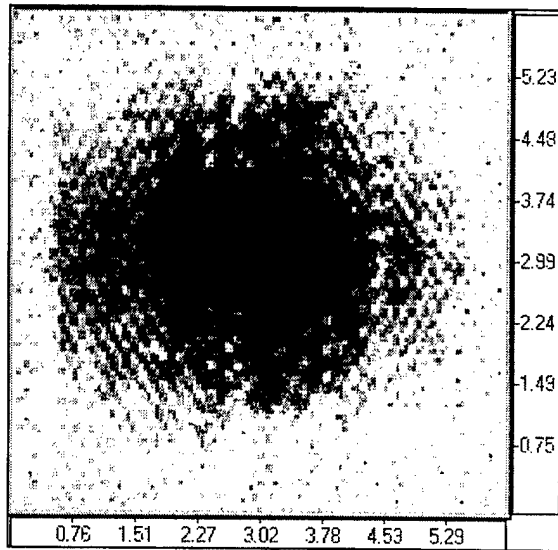


WXC32N

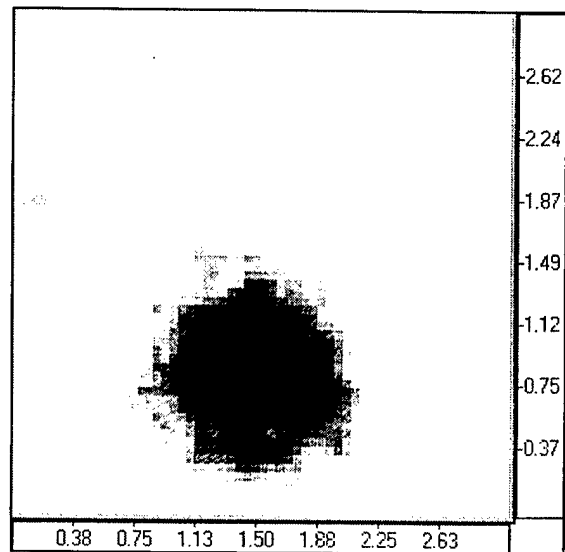


WXC34N

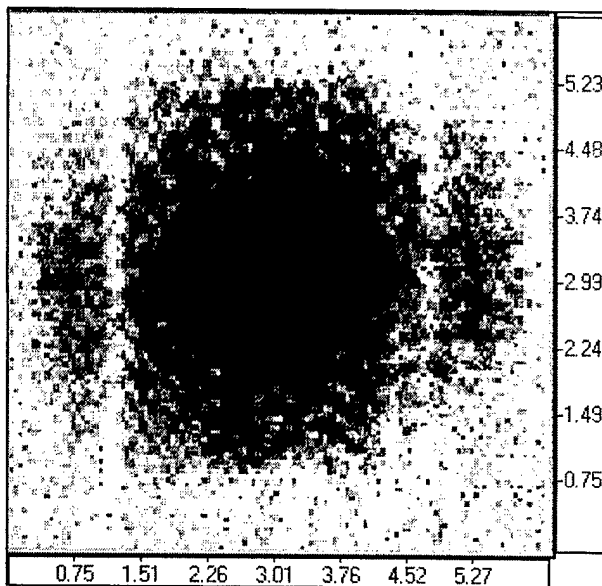
FIGURE B-13. TTU C-SCAN DAMAGE MAPS OF WXC31N, WXC32N, WXC33N, AND WXC34N PANELS



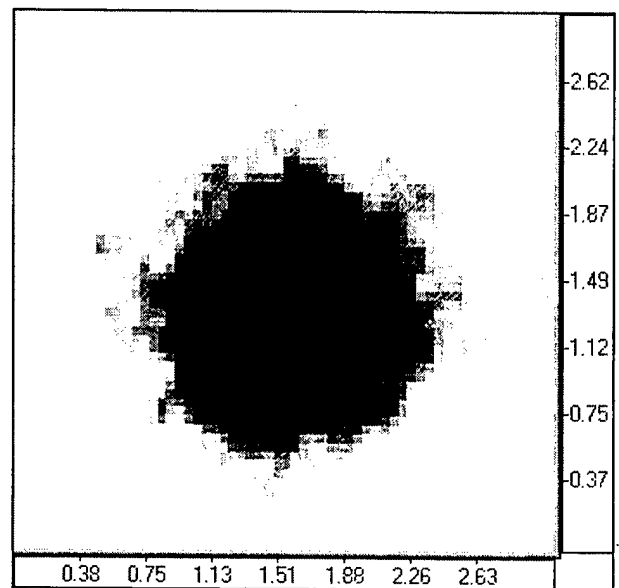
WXC35N



WXC31O

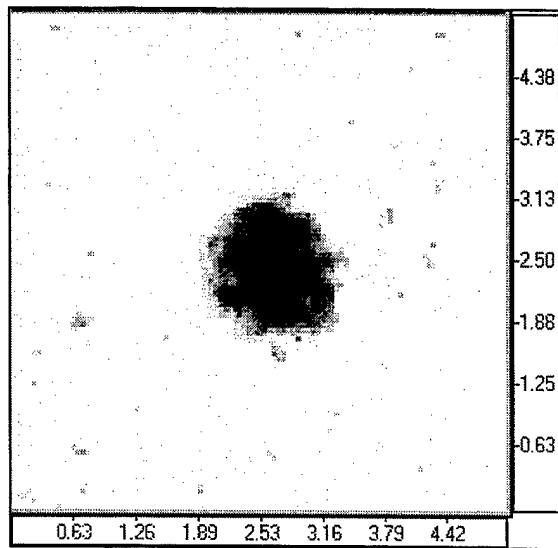


WXC35M

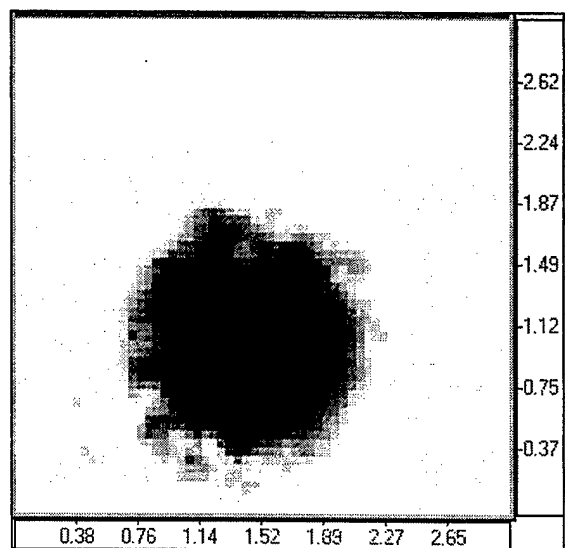


WXC32O

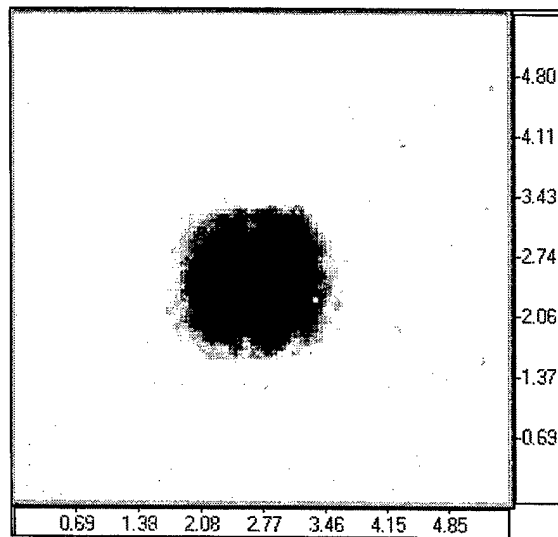
FIGURE B-14. TTU C-SCAN DAMAGE MAPS OF WXC35N, WXC35M, WXC31O, AND WXC32O PANELS



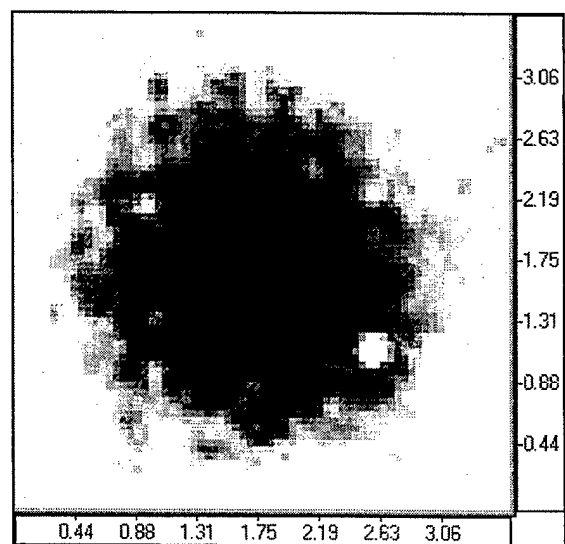
WXC330



WXC350

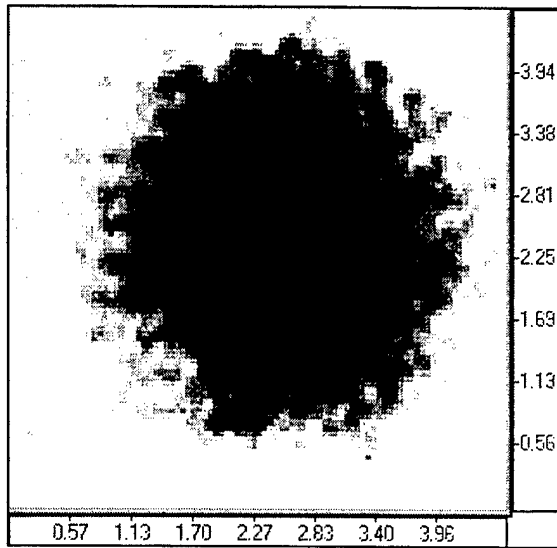


WXC340

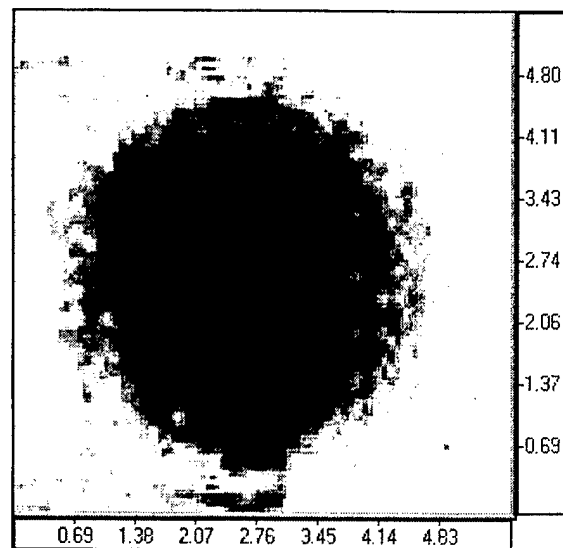


WXC31P

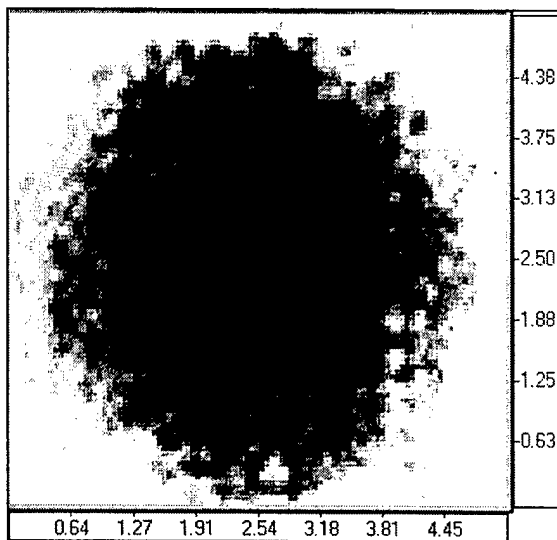
FIGURE B-15. TTU C-SCAN DAMAGE MAPS OF WXC330, WXC340, WXC350, AND WXC31P PANELS



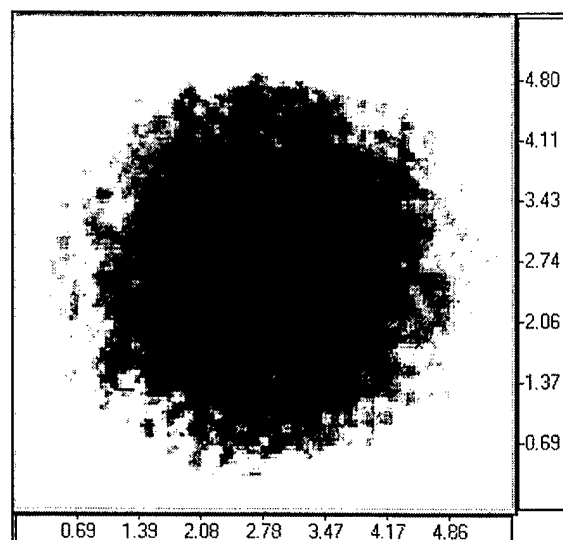
WXC32P



WXC34P

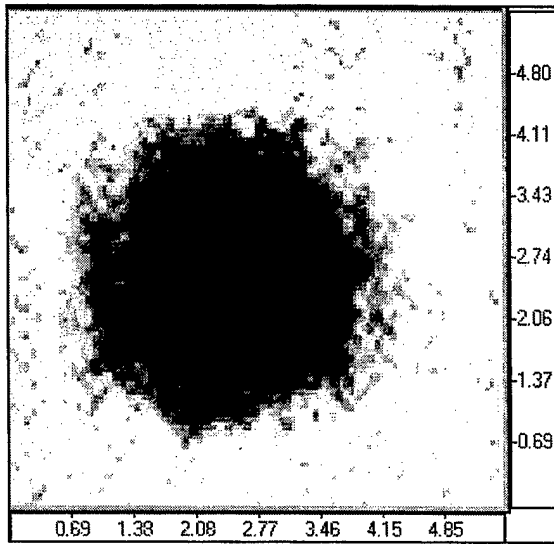


WXC33P

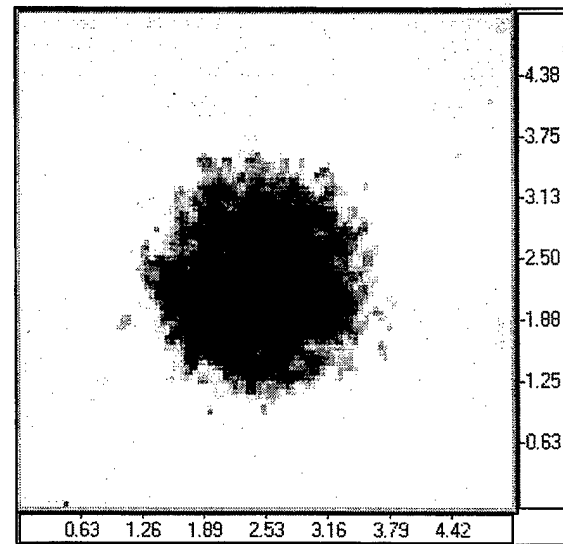


WXC35P

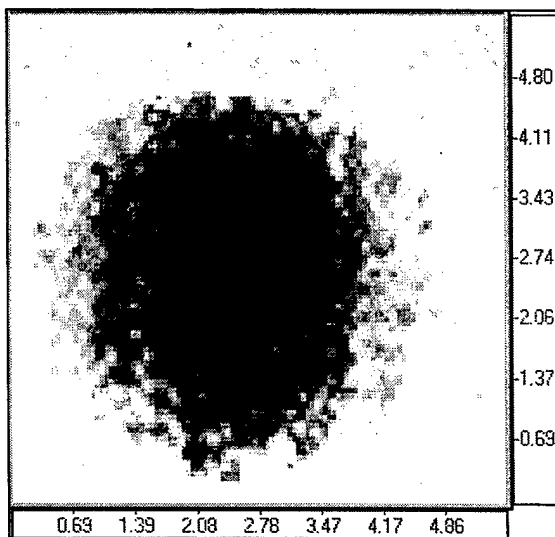
FIGURE B-16. TTU C-SCAN DAMAGE MAPS OF WXC32P, WXC33P, WXC34P, AND WXC35P PANELS



WXC36P



WXC38P



WXC37P

FIGURE B-17. TTU C-SCAN DAMAGE MAPS OF WXC36P, WXC37P, AND WXC38P PANELS

APPENDIX C—DESTRUCTIVE INSPECTION OF SELECTED SANDWICH PANELS

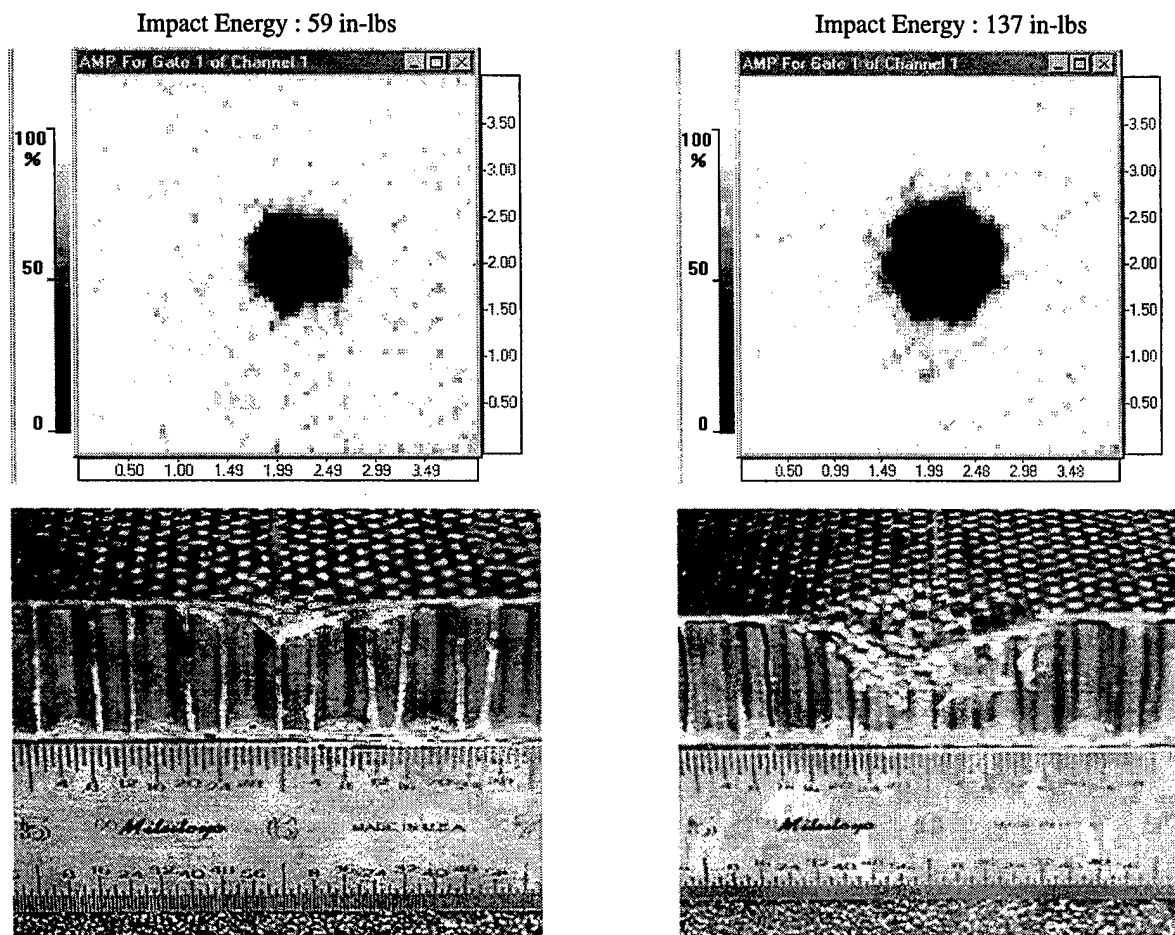


FIGURE C-1. DAMAGE IN PANELS [90/45/CORE 45/90]; $\frac{3}{4}$ " THICK CORE;
1.00" DIAMETER IMPACTOR

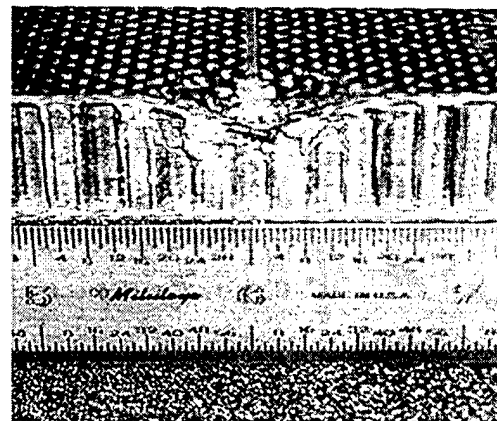
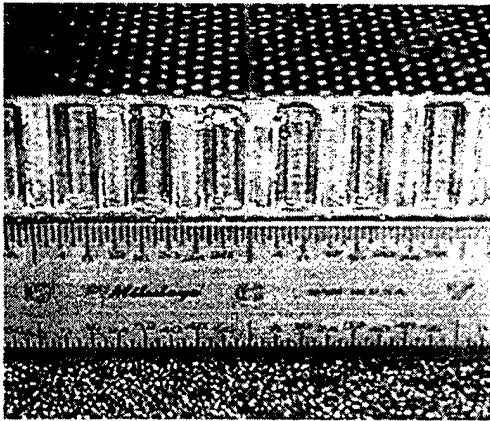
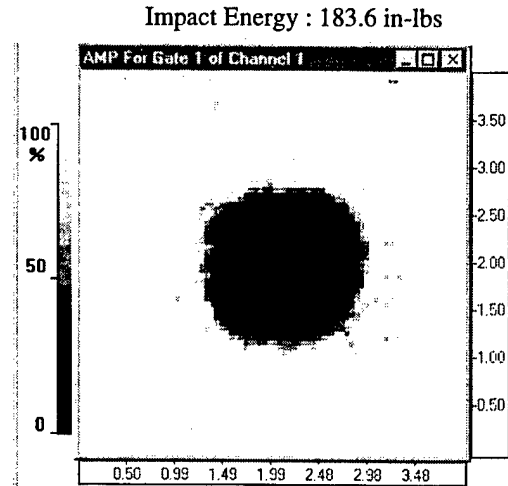
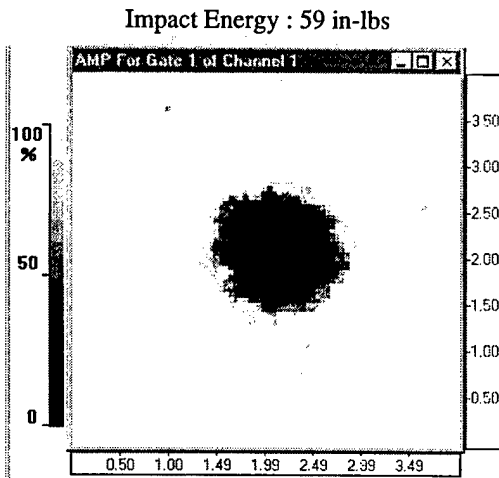


FIGURE C-2. DAMAGE IN PANELS $[(90/45)_2/\text{CORE}/(45/90)_2]$; $\frac{3}{4}$ " THICK CORE;
1.00" DIAMETER IMPACTOR

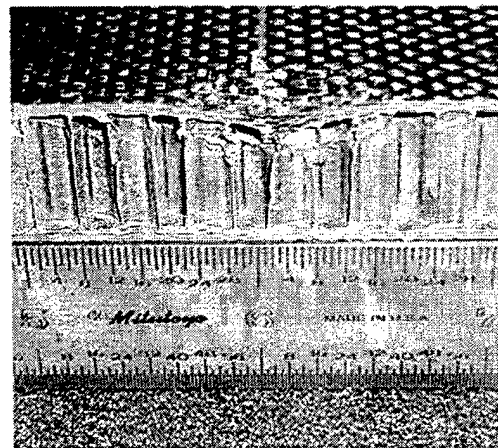
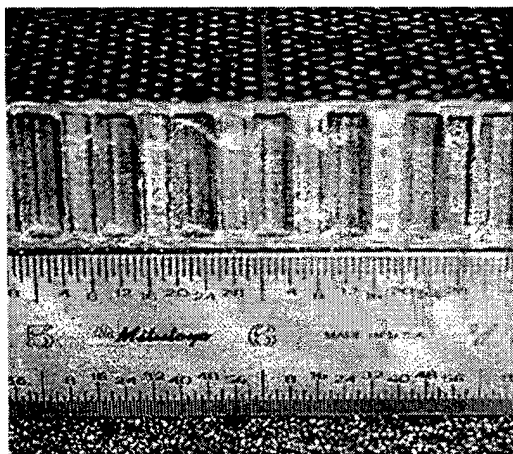
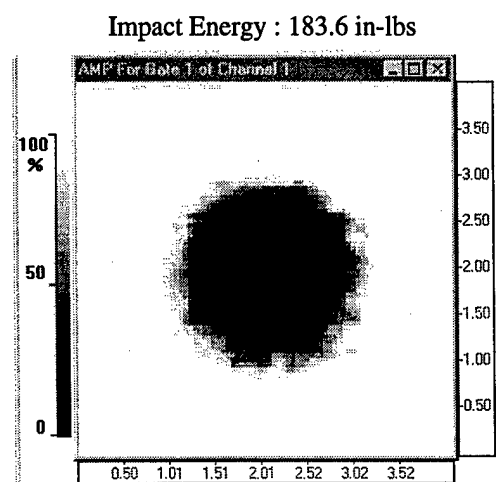
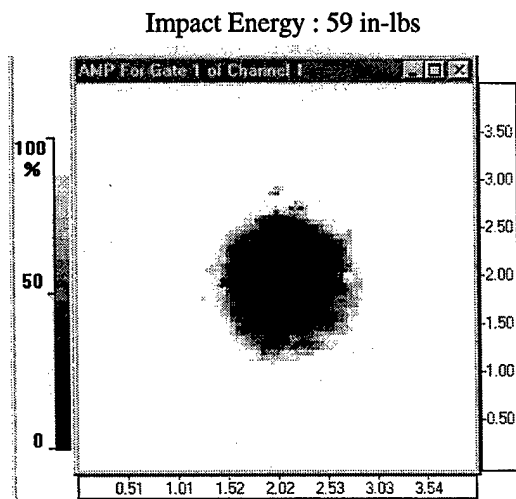


FIGURE C-3. DAMAGE IN PANELS $[(90/45)_3/\text{CORE}/(45/90)_3]$; $\frac{3}{4}$ " THICK CORE; 1.00" DIAMETER IMPACTOR

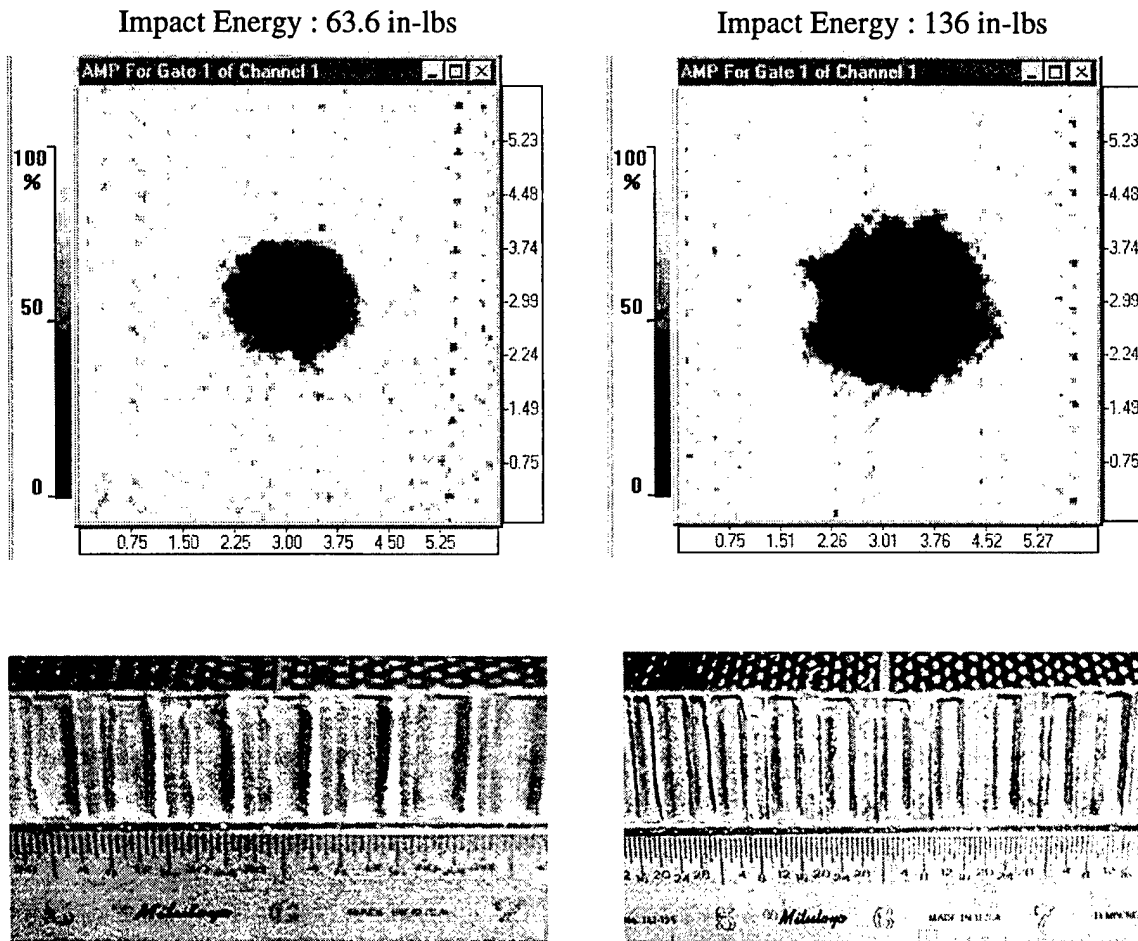


FIGURE C-4. DAMAGE IN PANELS [90/45/CORE/45/90]; $\frac{3}{4}$ " THICK CORE; 3.00" DIAMETER IMPACTOR (Impact Energy: 63.6 in-lbs and 136 in-lbs)

Impact Energy : 224 in-lbs

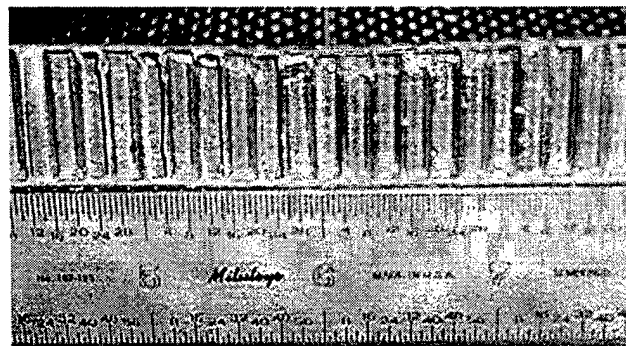
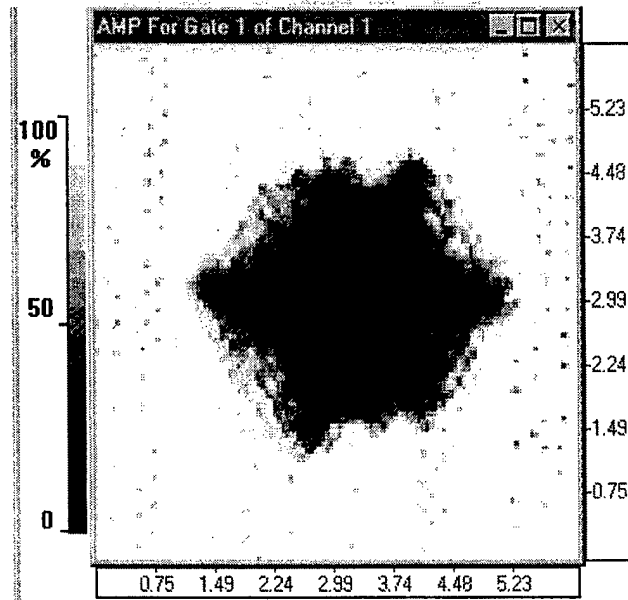


FIGURE C-5. DAMAGE IN PANELS [90/45/CORE/45/90]; $\frac{3}{4}$ " THICK CORE;
3.00" DIAMETER IMPACTOR (Impact Energy: 224 in-lbs)

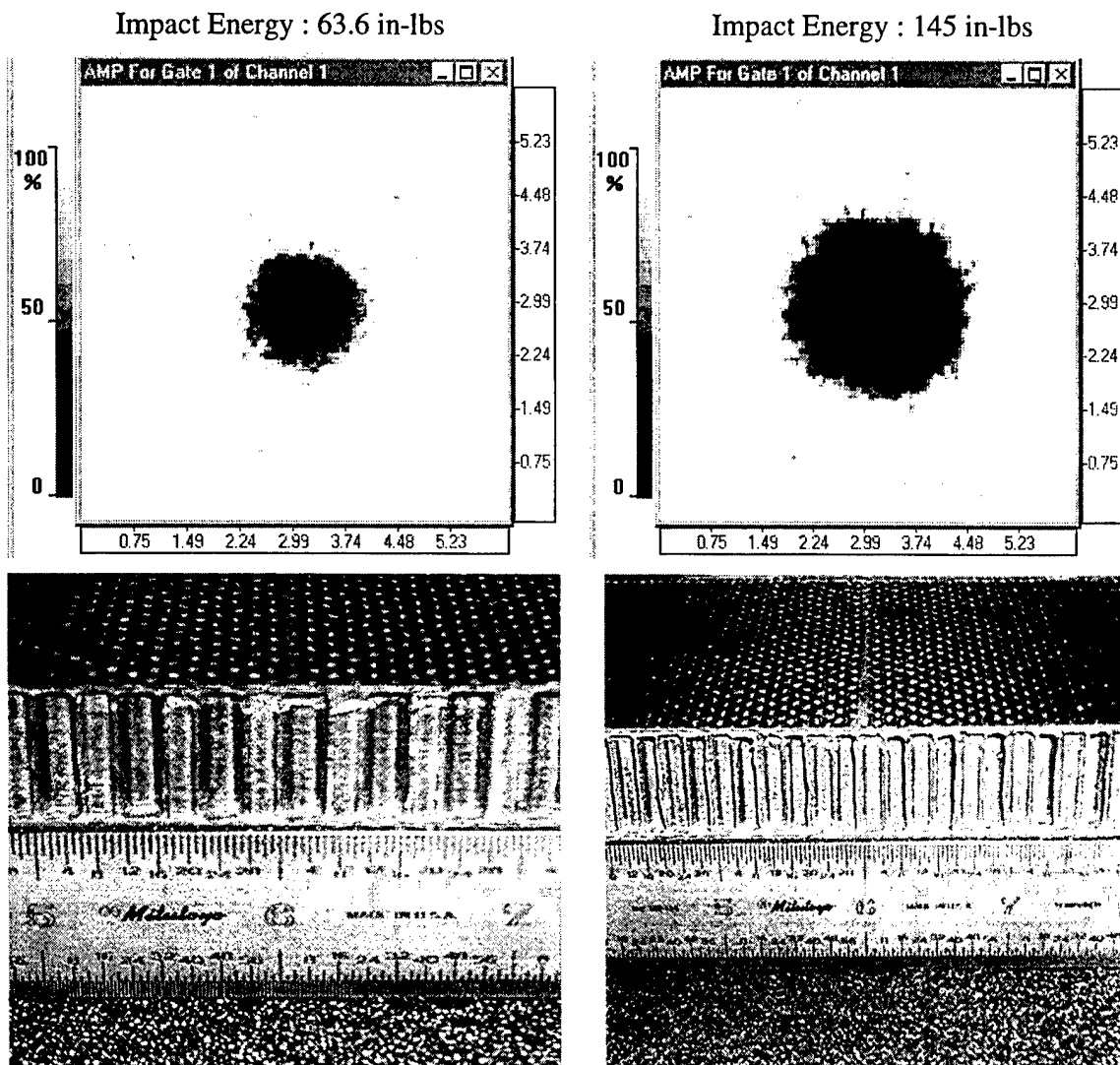


FIGURE C-6. DAMAGE IN PANELS $[(90/45)_2/\text{CORE}/(45/90)_2]$; $\frac{3}{4}$ " THICK CORE; 3.00" DIAMETER IMPACTOR (Impact Energy: 63.6 in-lbs and 145 in-lbs)

Impact Energy : 318 in-lbs

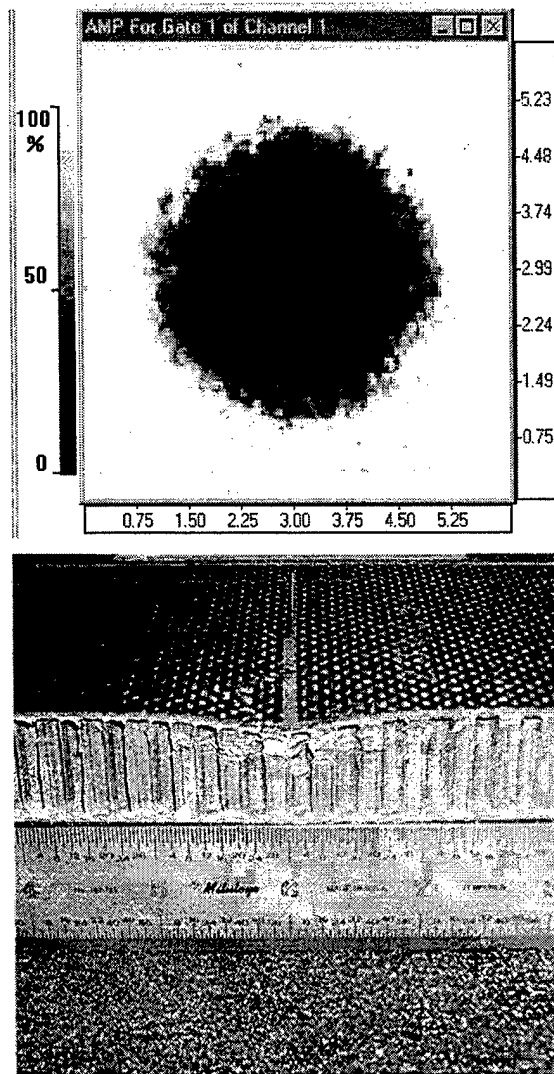


FIGURE C-7. DAMAGE IN PANELS $[(90/45)_2/\text{CORE}/(45/90)_2]$; $\frac{3}{4}$ " THICK CORE; 3.00" DIAMETER IMPACTOR (Impact Energy: 318 in-lbs)

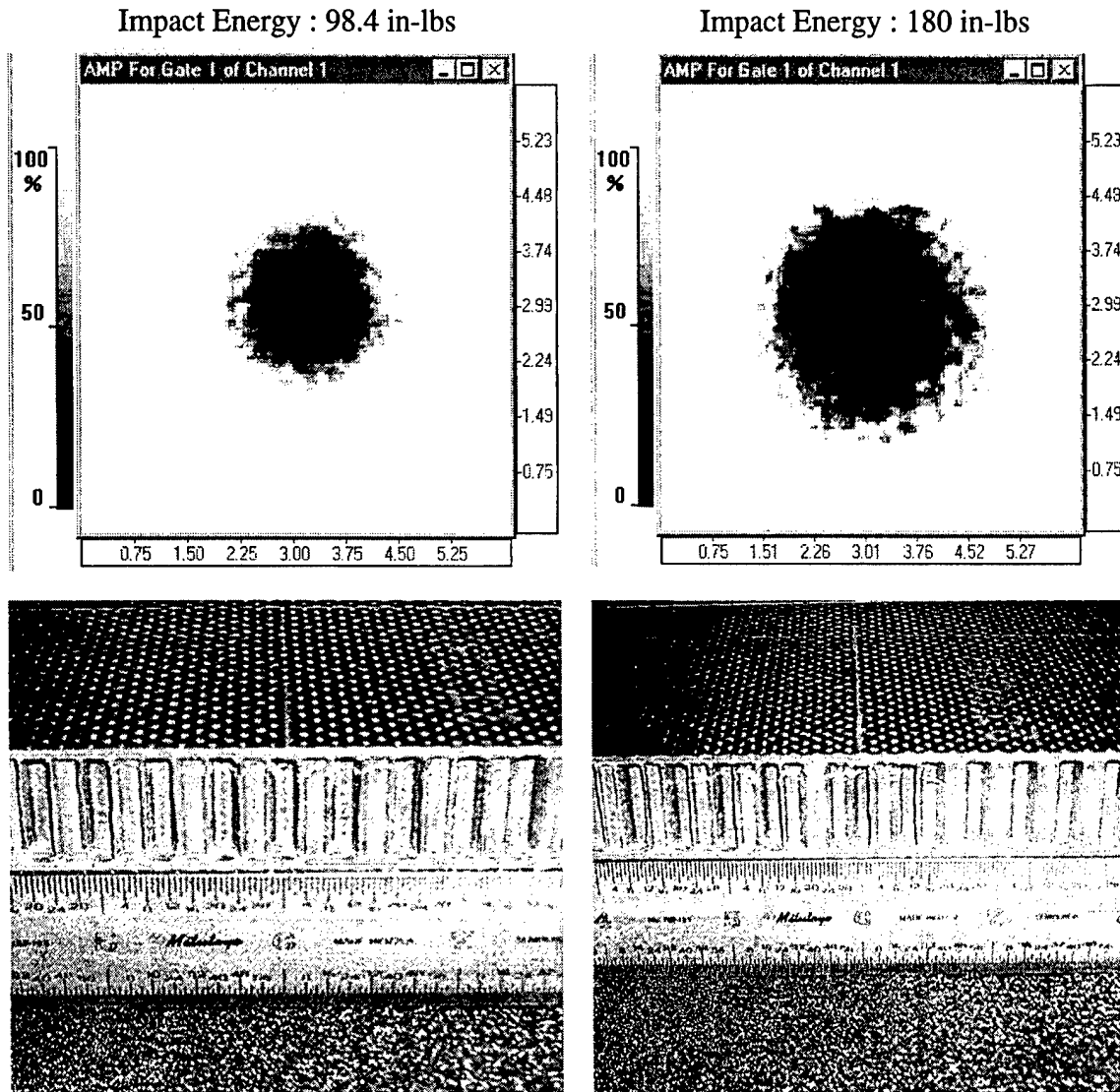


FIGURE C-8. DAMAGE IN PANELS $[(90/45)_3/\text{CORE}/(45/90)_3]$; $\frac{3}{4}$ " THICK CORE; 3.00" DIAMETER IMPACTOR (Impact Energy: 98.4 in-lbs and 180 in-lbs)

Impact Energy : 320 in-lbs

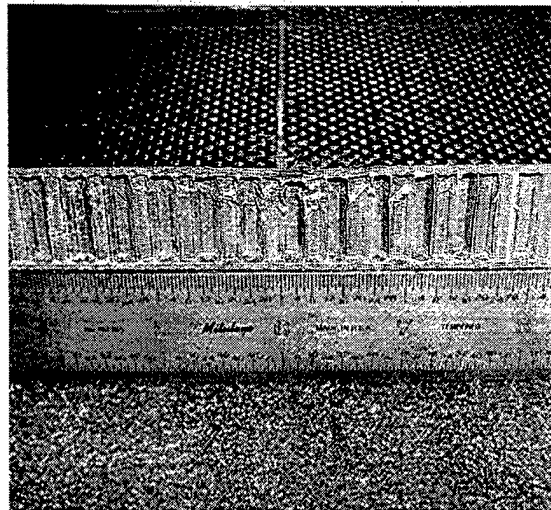
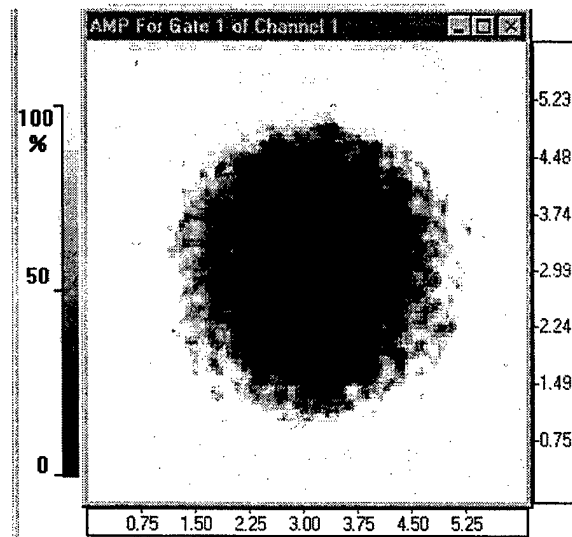


FIGURE C-9. DAMAGE IN PANELS [(90/45)₃/CORE/(45/90)₃]; 3/4" THICK CORE; 3.00" DIAMETER IMPACTOR (Impact Energy: 320 in-lbs)

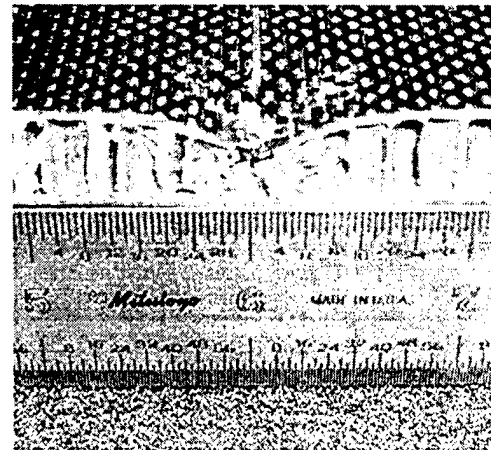
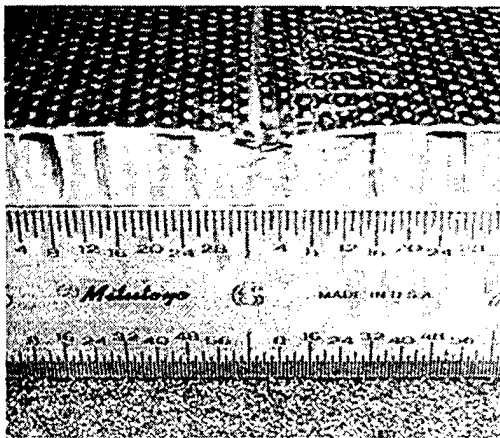
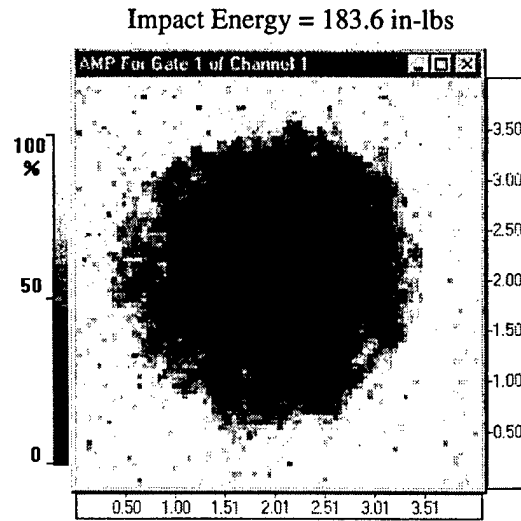
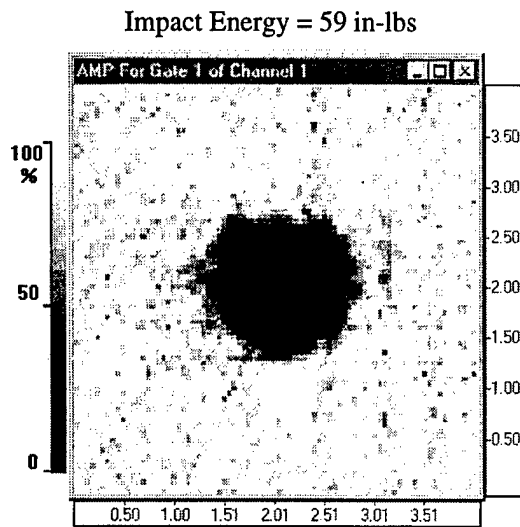


FIGURE C-10. DAMAGE IN PANELS [90/45/CORE/45/90]; $\frac{3}{8}$ " THICK CORE; 1.00" DIAMETER IMPACTOR

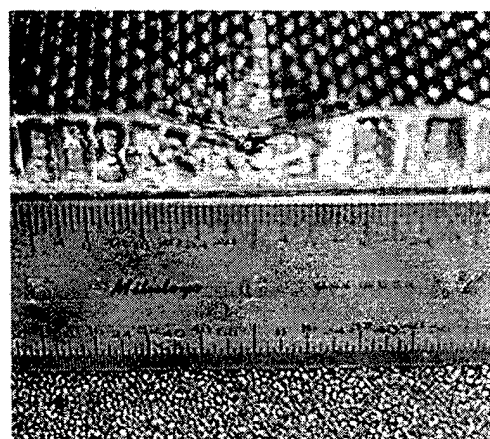
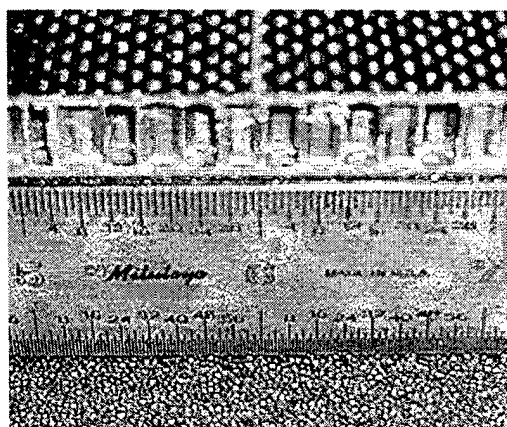
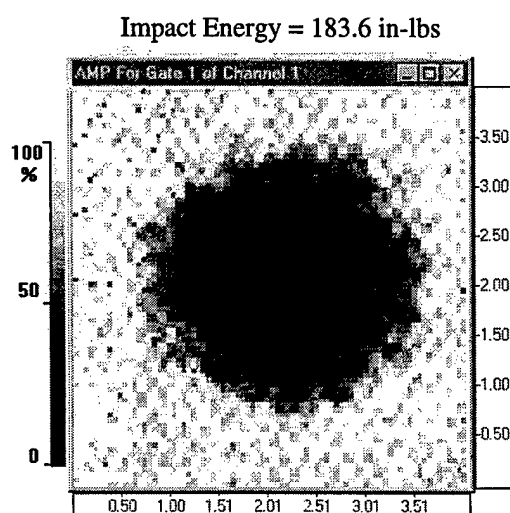
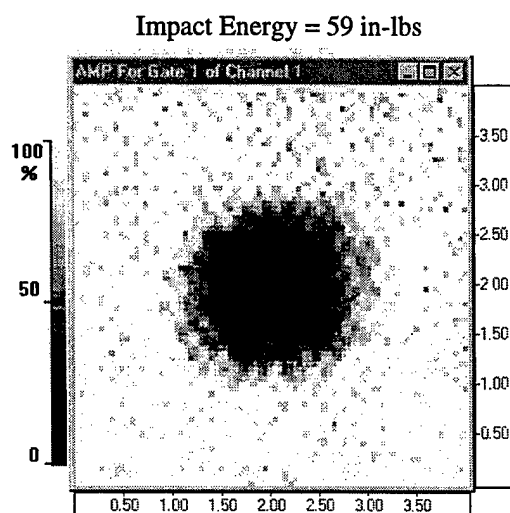


FIGURE C-11. DAMAGE IN PANELS $[(90/45)_2/\text{CORE}/(45/90)_2]$; $\frac{3}{8}$ " THICK CORE;
1.00" DIAMETER IMPACTOR

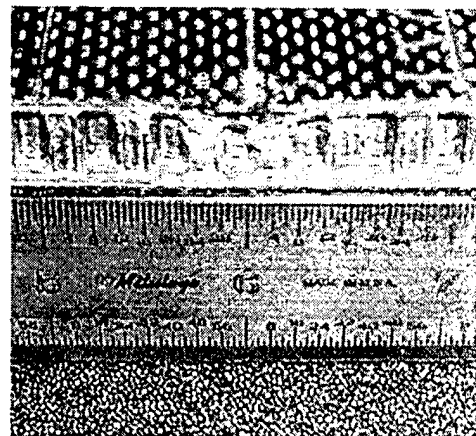
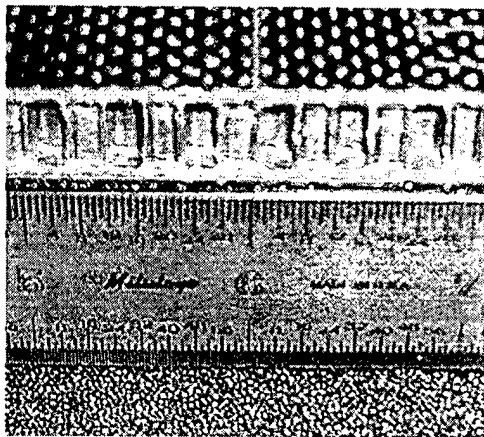
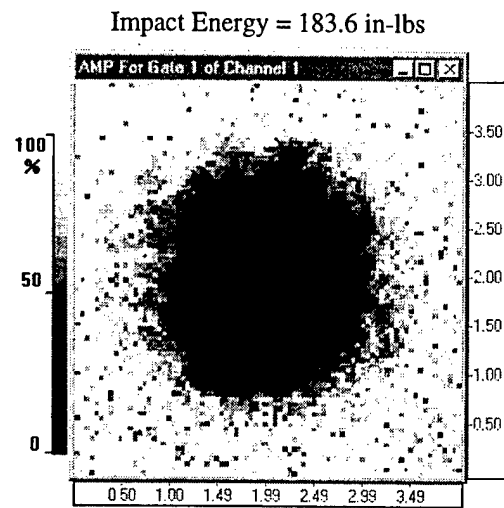
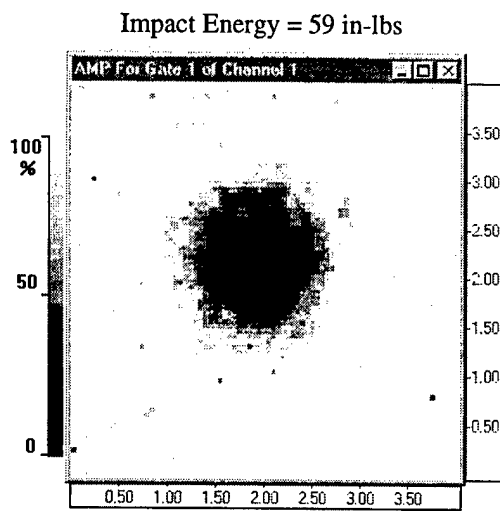


FIGURE C-12. DAMAGE IN PANELS $[(90/45)_3/\text{CORE}/(45/90)_3]$; $\frac{3}{8}$ " THICK CORE; 1.00" DIAMETER IMPACTOR

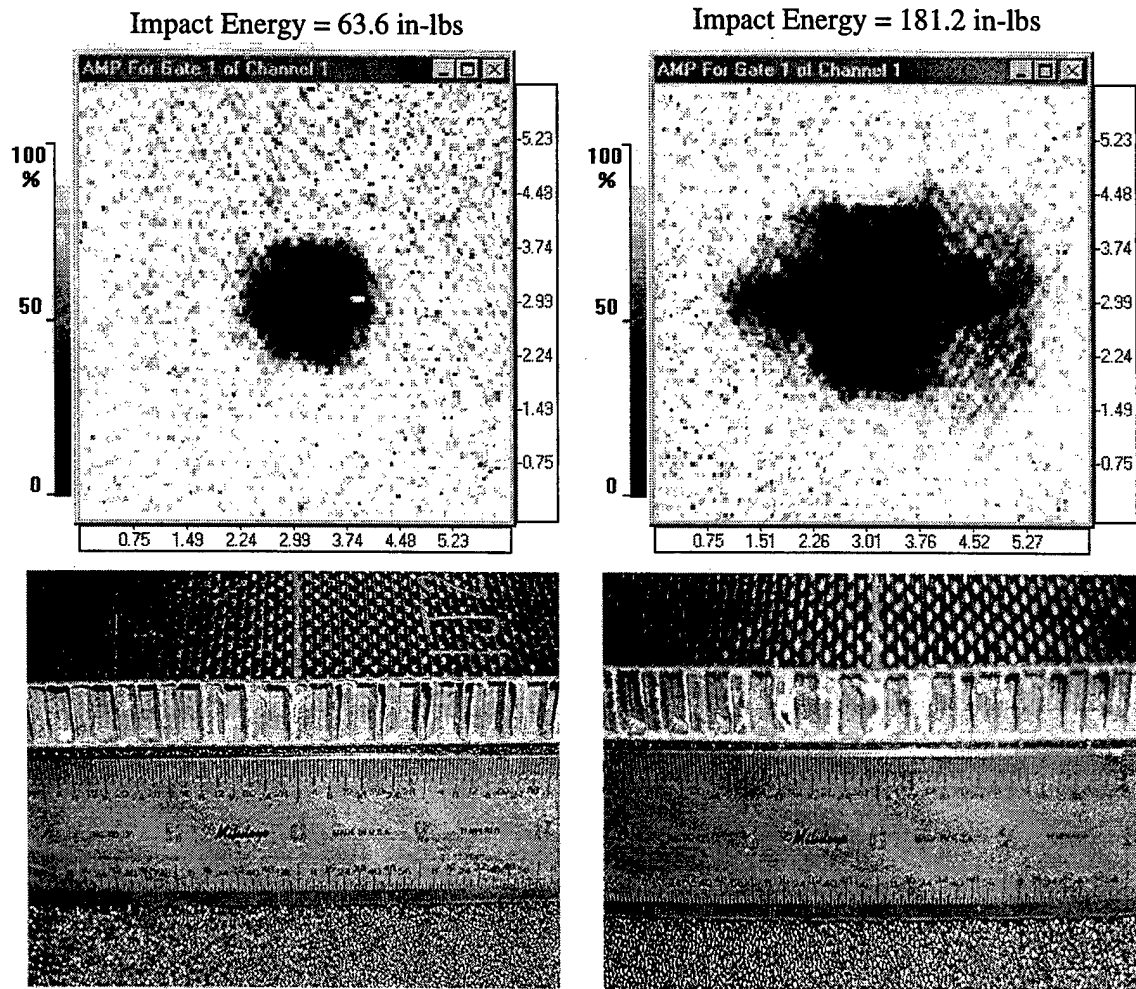


FIGURE C-13. DAMAGE IN PANELS [90/45/CORE/45/90]; $\frac{3}{8}$ " THICK CORE;
3.00" DIAMETER IMPACTOR (Impact Energy: 63.6 in-lbs and 181.2 in-lbs)

Impact Energy = 279 in-lbs

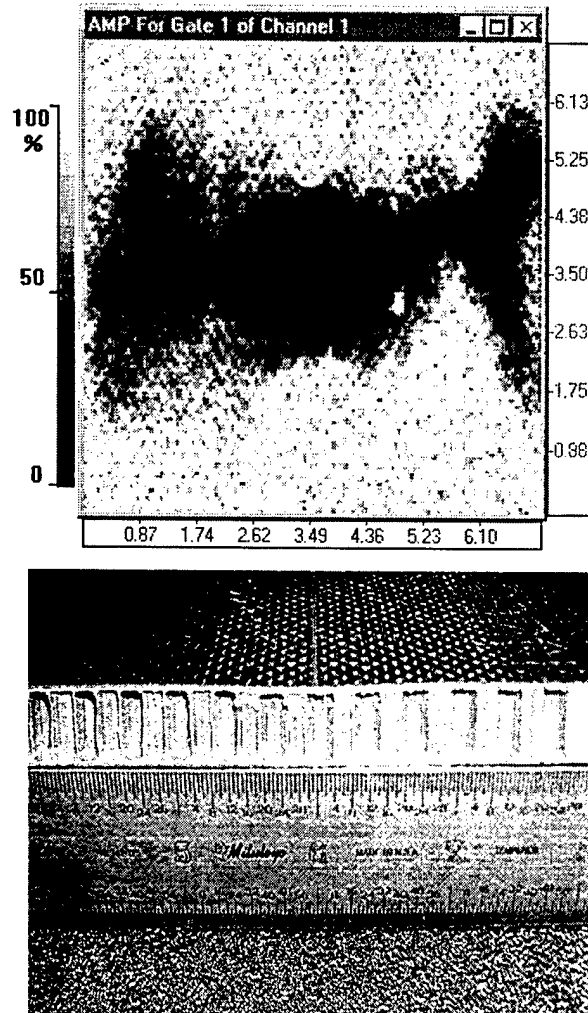


FIGURE C-14. DAMAGE IN PANELS [90/45/CORE/45/90]; $\frac{3}{8}$ " THICK CORE;
3.00" DIAMETER IMPACTOR (Impact Energy: 279 in-lbs)

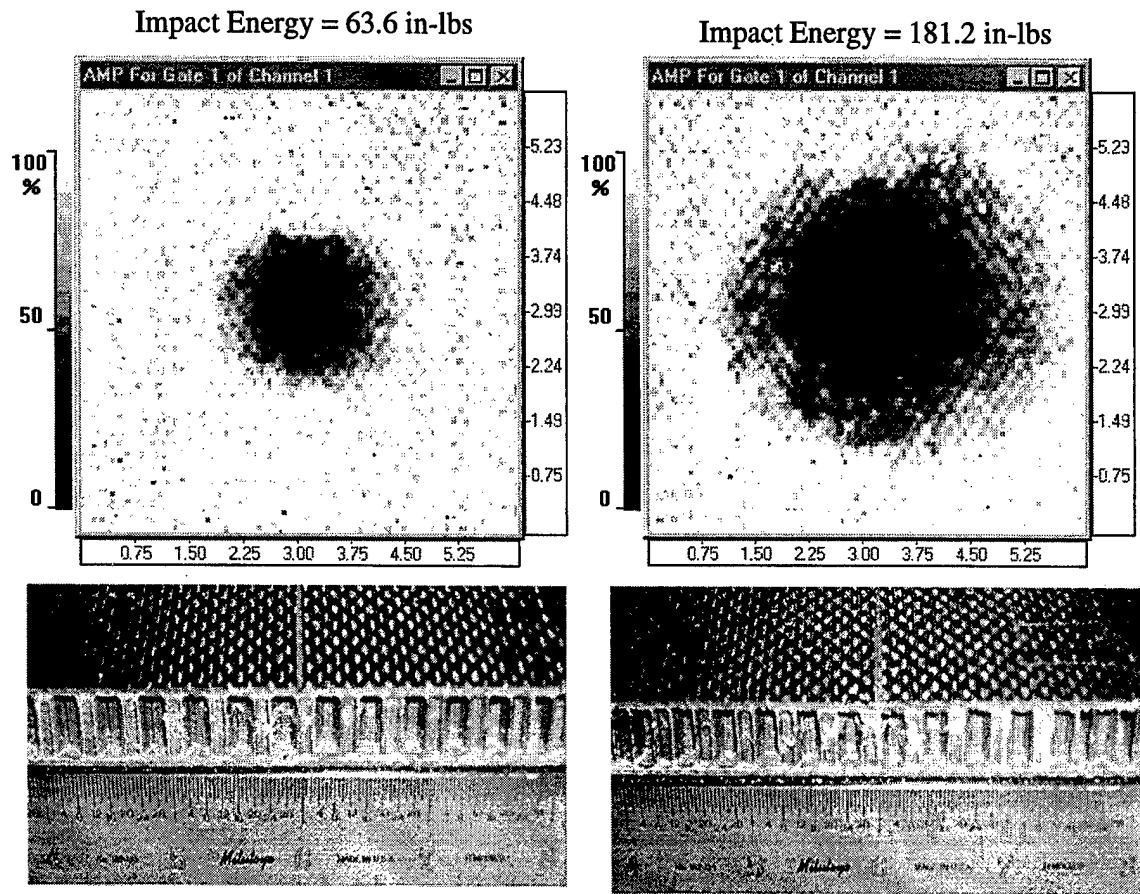


FIGURE C-15. DAMAGE IN PANELS $[(90/45)_2/\text{CORE}/(45/90)_2]$; $\frac{3}{8}$ " THICK CORE; 3.00" DIAMETER IMPACTOR (Impact Energy: 63.6 in-lbs and 181.2 in-lbs)

Impact Energy = 279 in-lbs

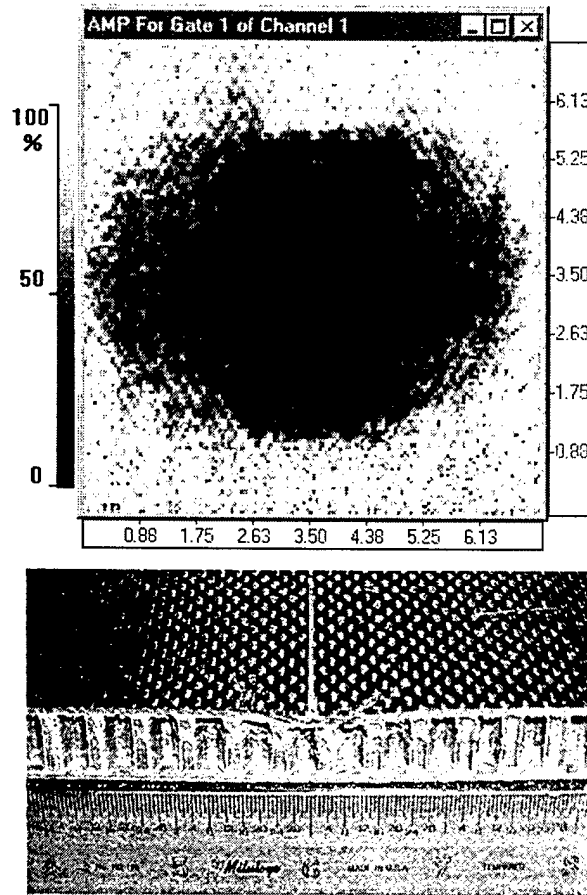


FIGURE C-16. DAMAGE IN PANELS $[(90/45)_2/\text{CORE}/(45/90)_2]$; $\frac{3}{8}$ " THICK CORE;
3.00" DIAMETER IMPACTOR (Impact Energy: 279 in-lbs)

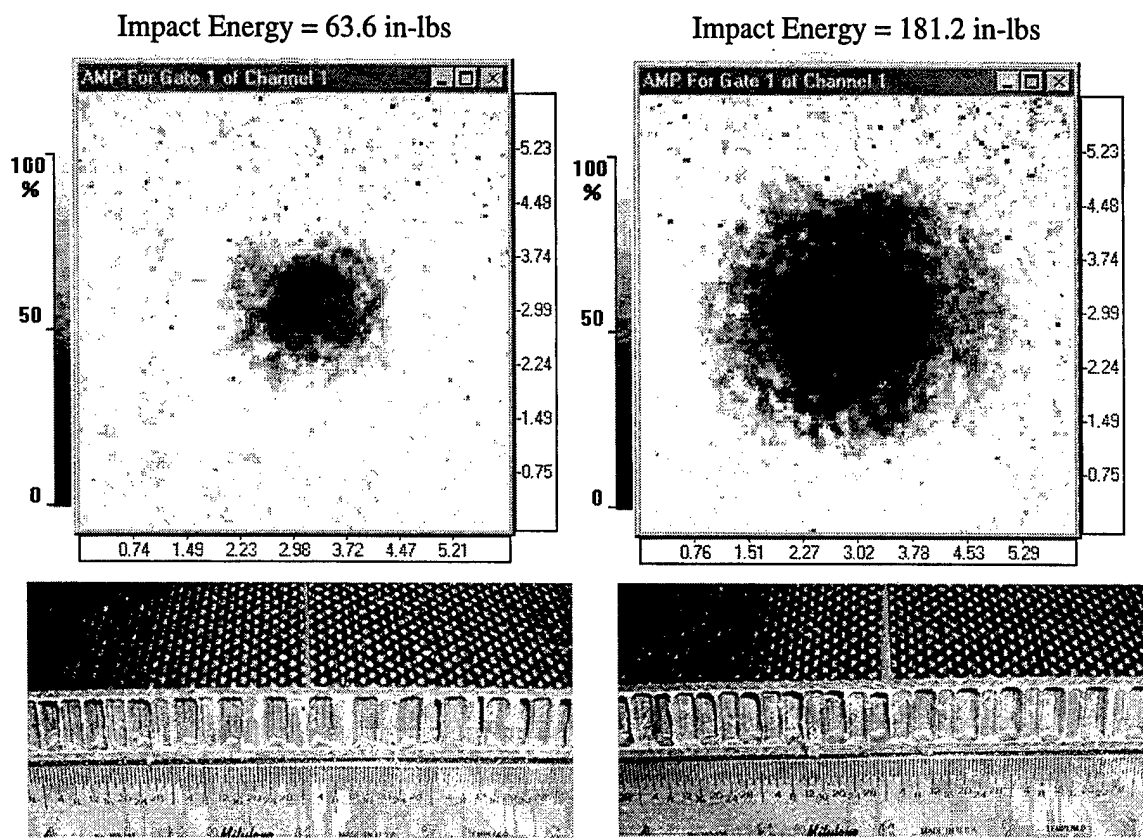


FIGURE C-17. DAMAGE IN PANELS $[(90/45)_3/\text{CORE}/(45/90)_3]$; $\frac{3}{8}$ " THICK CORE; 3.00" DIAMETER IMPACTOR (Impact Energy: 63.6 in-lbs and 181.2 in-lbs)

Impact Energy = 279 in-lbs

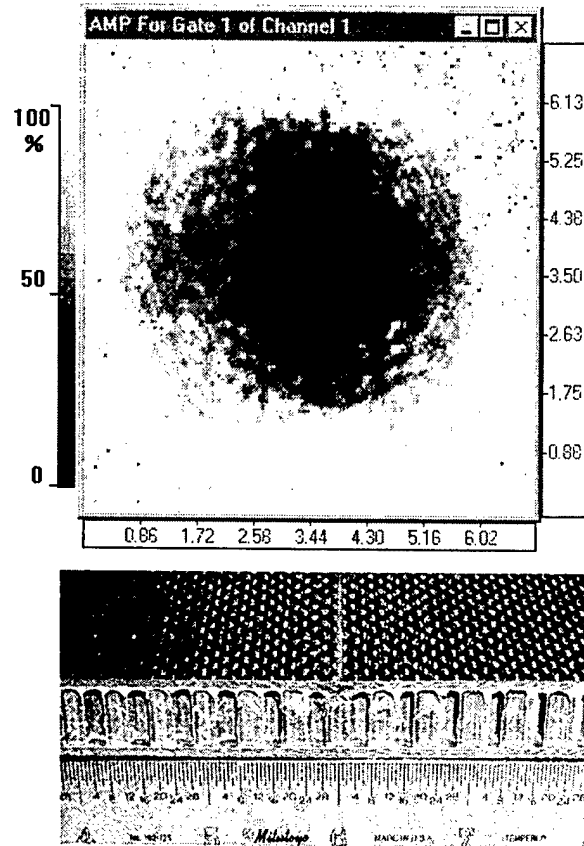


FIGURE C-18. DAMAGE IN PANELS $[(90/45)_3/\text{CORE}/(45/90)_3]$; $\frac{3}{8}$ " THICK CORE; 3.00" DIAMETER IMPACTOR (Impact Energy: 279 in-lbs)

APPENDIX D—FORCE RESULTANT VERSUS STRAIN GAGE RENDERING PLOTS

